Universitat Politècnica València

Departamento de comunicaciones

Development of Integrated Silicon Photonics Modulation Devices for Digital and Analog Applications

Ana María Gutiérrez Campo

Supervisor: Dr. Pablo Sanchis Kilders

Tesis presentada para la obtención del grado de Doctor en Telecomunicaciones de la Universitat Politècnica de València.

Thesis submitted to the Universitat Politècnica de València in partial fulfillment of the requirements for the degree of Doctor of Philosophy in Telecommunications engineering.

Junio 2013

Acknowledgements

En primer lugar agradecer a mi director Pablo Sanchis por la confianza depositada en mí, por estar siempre pendiente de mi trabajo, valorándolo y aconsejándome cómo mejorarlo, y por enseñarme en todo momento prestándome la ayuda necesaria siempre que lo he requerido. Como bien dices "os tengo muy mal acostumbradas". Es cierto, por ello y por todo lo anterior, puedo decir que no podría haber tenido un mejor director de tesis. En segundo lugar, agradecer también a Antoine todo el tiempo que me ha dedicado a lo largo de estos 4 años, enseñándome y aconsejándome desde el primer momento y siempre con una sonrisa. Gran parte de esta tesis es tuya por toda tu implicación en ella. Muchísimas gracias de corazón porque sin ti me hubiera sido mucho más complicado llegar hasta aquí. También agradecer al director del centro, Javier Martí, por darme la oportunidad de realizar el doctorado en el NTC. Gracias a Javi Herrera por su ayuda en este último año. Y a Galán por los principios. Sois dos grandes.

Agradecer a Mariam por su inestimable ayuda, cualquier duda que he tenido la has hecho tuya para poder darme la mejor solución posible. Soy muy afortunada por haberte tenido todo este tiempo de compañera de trabajo. Pero mi agradecimiento a ti va más allá de lo laboral. No tengo palabras para describir tu calidad como persona y como amiga. Has sido uno de mis mayores apoyos en los momentos difíciles y siempre has estado ahí de manera incondicional sin esperar nada a cambio. Nunca podré llegar a agradecerte como te mereces todo lo que has hecho por mí. Ni que decir tiene que empezaste siendo sólo una compañera de trabajo pero hoy día eres una gran amiga y puedo afirmar que para toda la vida. Te quiero muchísimo "mori".

Albita y Marta, mis amores, toda una vida juntas contra viento y marea. Sois parte de mí y por tanto parte de esta tesis. Muchas veces os amenazaba con que si no os portabais bien no apareceríais en estos agradecimientos. Sabéis que eso es imposible, tengo mucho que agradeceros. Cuando uno tiene que llevar a cabo un trabajo como es esta tesis y todo se vuelve negro, la realización de dicho trabajo se vuelve muy complicada. Pero vosotras siempre habéis estado ahí para darme esa luz que se necesita para seguir adelante. A cualquier hora, en cualquier momento y cualquier lugar, sea como fuere, una llamada ha bastado para que vinierais corriendo a brindarme vuestro hombro. Eso no se olvida nunca. Sois amigas, confidentes, hermanas y todo por lo que alguien debe dar gracias todos los días de tener a su lado. Gracias por todo chicas, os he querido os quiero y os querré toda mi vida.
Por supuesto que no me olvido del resto de "Femeninas Emprendedoras". Ana, Patri y Elia. Esas quedadas semanales han sido durante la realización de esta tesis. Esas noches

de “marujeo” y de “terapia” han sido de lo mejor de estos 4 años, siempre las recordaré con una sonrisa todas y cada una de ellas aunque no voy a hablar en pasado porque espero que sigamos haciéndolas. Risas aparte, también he tenido la suerte de contar con vuestro apoyo y cariño en los peores momentos, siempre pendientes de mis “problemillas” y de mi estado de ánimo. Sois buenas personas, buenas amigas y espero teneros siempre a mi lado. Os quiero mil chicas. Pedrito, literalmente, una página de este tesis es “teua”, gracias, eres un crack. Rubén, decirte que estás lejos pero estás cerca, mi mayor regalo de la carrera es haberte conocido.

También quiero agradecer a Javi García, Josema y Pak por los grandes y buenos momentos vividos en estos últimos meses de desesperación durante la fase final de escritura de la tesis la cual me alegro que haya coincidido en tiempo con la vuestra. Por fin somos doctores chicos y parecía que no iba a llegar nunca. El humor que le habéis puesto y las risas que me habéis hecho sacar son de mucho agradecer. Os deseo de corazón muchísima suerte a todos allá donde vayáis.

Eva, Jose, Belén, Pepa, mis “Wasay”. Que sepáis que esa “secta” es de lo mejor que me ha pasado en estos 2 últimos años. Como sé que vosotros no sois mucho de leer en inglés he hecho los agradecimientos (acknowledgements) en castellano para que no os quejéis y porque sé que me lo habríais estado recordando durante mucho tiempo. Vuestra “coles”, “cables”, “chispas”, “cani”, “tocineta”,…, o sea yo, os quiere agradecer vuestros ánimos y apoyo durante esta tesis, y deciros que soy feliz de tener esa segunda familia llamada “Wasay”. Os quiero.

Gracias a mis tíos Seve, Choni y Antonio por vuestro apoyo incondicional y vuestro continuo interés en esta tesis.

Finalmente, lo que más quiero en el mundo, MI FAMILIA. Mi hermana, mi padre y mi madre y desde hace dos años y medio, mis “pollitos”. No sé por dónde empezar a agradeceros ya que todo lo que soy os lo debo a vosotros. Gracias por el continuo apoyo en todo lo que hago, por cómo se os “llena la boca” cuando habláis de mí, por sobrevalorarme siempre, por estar en todo momento orgullosos de mí, por confiar plenamente siempre en mis criterios y mis decisiones. Que sepáis que cuando todo se derrumba, cuando todo se vuelve negro, cuando todo sale mal, cuando tengo miedo, cuando parece que no hay ninguna salida, el pensar en vosotros y en lo mucho que os quiero me ayuda a cargarme de fuerzas para seguir para adelante. Nunca me cansaré de luchar por vosotros. Estos últimos 4 años no han sido precisamente fáciles para nosotros, de hecho podemos decir que han sido los más duros de nuestra vida pero ¿sabéis qué?, que a pesar de todos los obstáculos, lo hemos conseguido. Hemos conseguido superar un cáncer y hemos conseguido terminar esta tesis y además la vida nos ha recompensado con dos maravillosos niños. Queda mucho por superar y mucho por afrontar, pero sé que también lo conseguiremos porque sois ejemplo de superación, y sé que algún día volveremos a sonreír los cuatro juntos, ese es mi mayor deseo. Lo sois todo para mí, y esta tesis, y todo lo que hago, es por y para vosotros. Os amo.

Resumen

La fotónica de silicio es una de las tecnologías fotónicas que está experimentando un crecimiento más excitante y rápido en los últimos años. La característica más destacada de esta tecnología es su compatibilidad con las maduras técnicas de fabricación de circuitos integrados de silicio basadas en los procesos "complementary metal-oxide semiconductor" (CMOS) ampliamente utilizados en la industria microelectrónica. Otra motivación es la disponibilidad de circuitos de guía de ondas planas de silicio sobre aislante (SOI) de alta calidad que ofrecen un fuerte confinamiento óptico debido al alto contraste índices entre el silicio (n=3,45) y el SiO_2 (n=1,45). Esto abre las puertas a la miniaturización y a la integración a gran escala de dispositivos fotónicos lo que resulta en circuitos fotónicos integrados para una amplia gama de aplicaciones y mercados, desde telecomunicaciones ópticas a dispositivos bio-fotónicos o sensores de fibra precisos. Los moduladores ópticos son elementos básicos fundamentales para la transmisión de señales a alta velocidad y el procesado de información en cualquier solución de interconexión fotónica. El trabajo desarrollado en esta tesis, como parte del los objetivos del proyecto Europeo HELIOS en el que está enmarcada, se centra fundamentalmente en realizar moduladores compactos y eficientes, integrados en chips de silicio.

La tesis consiste en 3 capítulos principales así como una sección de conclusiones del trabajo conseguido. El capítulo uno está destinado a dar una descripción general de los beneficios del uso de la fotónica de silicio, mostrando sus retos y oportunidades, así como a dar una visión profunda de todos los aspectos relacionados con la modulación electro-óptica. El capítulo dos está dedicado a desarrollar moduladores de silicio de altas prestaciones para aplicaciones digitales. Específicamente, se presentan nuevas estructuras ópticas diferentes a las convencionales con el objetivo de mejorar el rendimiento de la modulación o al menos algunos parámetros críticos en la modulación. El tercer capítulo se dedica a las aplicaciones analógicas. Se describe el concepto de la fotónica de microondas, así como diferentes investigaciones llevadas a cabo en el ámbito analógico para su aplicación en el campo de la fotónica integrada de microondas, todas ellas usando moduladores electro-ópticos de silicio compatibles con los procesos de fabricación CMOS, lo que valida el potencial de la fotónica de silicio como un prometedor enfoque para permitir el desarrollo de aplicaciones de la fotónica integrada de microondas. Por último, las conclusiones sobre el trabajo realizado se proporcionan en el Capítulo 4.

Resum

La fotònica de silici és una de les tecnologies fotòniques que está experimentant un creixement més excitant i rápit en els últims anys. La característica més destacada d'aquesta tecnología és la seua compatibilitat amb les madures tècniques de fabricació de circuits integrats de silici basades en els processos "complementary metal-oxide semiconductor" (CMOS) ampliament utilitzats en la indústria microelectrònica. Una altra motivació és la disponibilitat de circuits de guía d'ones planes de silici sobre aïllant (SOI) d'alta calitat que oferix un fort confinament òptic degut a l'alt contrast índex entre el silici (n=3,45) i el SiO_2 (n=1,45). Açò obri les portes a la miniaturització i a la integració a gran escala de dispositius fotònics, el que resulta en circuits fotònics integrats per à una àmplia gamma d'aplicacions i mercats, desde telecomunicacions òptiques fins a dispositius bio-fotònics o sensors de fibra precissos. Els moduladors òptics són elements básics fonamentals per à la transmisió de senyals a alta velocitat i el processat d' informació en qualsevol solució d'interconnexió fotònica. El treball desenvolupat en aquesta tesi, com part dels objectius del projecte Europeu HELIOS en el que está emmarcada, es centra fonamentalment en realitzar moduladors compactes y eficients, integrars en xips de silici.

La tesi consisteix en 3 capítols principals així com una secció de conclusions del treball aconseguit. El capítol un está destinat a donar una descripció general dels beneficis de l'us de la fotònica de silici, mostrant els seus reptes i oportunitats, així com a donar una visió profunda de tots els aspectes relacionats amb la modulació electro-òptica. El capítol dos está dedicat a desenvolupar moduladors de silici d'altes prestacions per à aplicacions digitals. Específicament, es presenten noves estructures òptiques diferents a les convencionals amb l'objectiu de millorar el rendimient de la modulació o al menys alguns parámetres crítics en la modulació. El tercer capítol es dedica a les aplicacions analògiques. Es descriu el concepte de la fotònica de microones, així com diferents investigacions dutes a terme en l'àmbit analògic per à la seua aplicació en el camp de la fotònica integrada de microones, totes elles usant moduladors electro-òptics de silici compatibles amb els processos de fabricació CMOS, el que valida el potencial de la fotònica de silici com un prometedor enfocament per à permetre el desenvolupament d'aplicacions de la fotònica integrada de microones. Per últim, les conclusions sobre el treball realitzat es proporcionen en el Capítol 4.

Abstract

Silicon photonics is one of the most exciting and fastest growing photonic technologies in recent years. The salient feature of this technology is its compatibility with the mature silicon IC manufacturing based on complementary metal-oxide semiconductor (CMOS) processes widely used in microelectronic industry. Another motivation is the availability of high-quality silicon-on-insulator (SOI) planar waveguide circuits that offer strong optical confinement due to the high index contrast between silicon (n=3.45) and SiO_2 (n=1.45). This opens up miniaturization and very large scale integration of photonic devices allowing photonic integrated circuits for a wide range of applications and markets, from optical telecommunications to bio-photonic devices or precise fibre sensors. Optical modulators are key building-blocks for high speed signal transmission and information processing in any photonic interconnection solution. The work developed in this thesis, as part of the objectives of the European project HELIOS in which it is framed, is essentially focused on realizing compact and efficient modulators integrated on silicon chips.

The thesis consists of three main chapters as well as the concluding section on the work accomplished. Chapter one is aimed at giving a general description of the benefits of using silicon photonics, showing its challenges and opportunities as well as at giving a deeply overview of all issues related to the electro-optic modulation. Chapter two is devoted to develop silicon modulators with high features for digital applications. Specifically, new optical structures different to the conventional ones are presented with the aim of enhancing the modulation performance or at least several critical parameters in the modulation. Chapter three is dedicated to the analog applications. The concept of microwave photonics is described as well as different researches carried out in the analog scope for application in the field of integrated microwave photonics, all of them using CMOS-compatible electro-optic silicon modulators which validate the potential of silicon photonics as a promising approach for enabling the development of integrated microwave photonics applications. Finally, conclusions on the work realized are provided in Chapter 4.

Contents

Chapter 1

Introduction

1.1. Silicon photonics

Optics is and old and venerable subject involving the generation, propagation and detection of the light. Three major developments, which have been achieved in the last thirty years, are responsible for the rejuvenation of the Optics, nowadays under the denomination of Photonics, and its increasing importance in modern technology: the invention of the laser, the fabrication of low-loss optical fibers and the introduction of semiconductor optical devices. So, Photonics is the science and technology of light, with an emphasis on applications. At the heart of photonics are technologies for generating, transmitting, amplifying, modulating and detecting light, and particularly using light for practical purposes. It thus builds heavily on optical technology but reflects the growing tie between optics and electronics forged by the increasing role that semiconductors materials and devices play in optical systems. For all, Photonics is considered as one of the key technologies of the 21st century. It supplements electronics in the form of optoelectronics and exhibits a strong market growth, which is expected to continue for the foreseeable future. Typical Photonics application areas are: information and communication technologies (ICTs), health care and life sciences, optical metrology, sensing and biosensors, defense and space technology.

Among all these main application areas, the field of ICTs is witnessing a development speed unprecedented in history. Internet traffic grows by 40-60% per year, almost unchanged for >10 years, driven by new user applications and user access data rates by 42% per year [OCL11]. So, as traffic demands are growing much more rapidly than revenues, service providers must continually seek ways to carry the traffic more efficiently. The idea of using light beams to replace wires has been dominating during

the last decades all long-distance communications but the trend nowadays is progressively taking over in networks over increasingly shorter distances: from optical fiber communications to optical interconnect computing; and silicon photonics seems to be the most effective technology for such purpose.

Signal transmission and processing by means of optical beams rather than electrical currents or radio waves has been a very interesting topic since the 1960s [KAO66]. Low loss, high data rate capabilities, noise rejection and electrical isolation are just a few of the important features that make fiber optic technology ideal for the transport of information in communication networks [GAM00]. In current telecom and datacom networks, the optical fibers are used to transport the information in the form of light and are usually installed in the intermediate links between the core networks and between networks and small sub-networks, whilst copper wire or coaxial cable is commonly used in the access network which connects subscribers to their immediate service provider. Replacing at least part of these links with fiber shortens the remaining copper segments and allows them to run much faster. Following this approach, new emerging technologies such as FTTH (Fiber-To-The-Home) started to arouse the interest of telecom operators many years ago. The key objective of FTTH technology is to be able to offer to the customers a higher speed and broadband access, by bringing the fiber link directly to their homes. However, even in FTTH technology, the network equipment mainly remains electronic circuitry, and the optical signals are just used to transport the data, nor for data processing. So, in the network nodes, the routing and signal processing is performed electrically, and the electrical signal is converted back into light and sent on the output fiber and transport it towards the next node. These optoelectronic conversions cause an increase of the latency of the whole transport network, and the benefits of high velocity capability of using optical fibers is unfortunately wasted. This fact represents a real bottleneck in current communication networks. The most efficient way for making the most of optical fiber advantages is to replace microelectronic circuitry with optical circuits capable for all-optical signal processing. Fortunately, besides the main function of guiding light, optical fibers can also be developed as attractive photonic components performing desired optical signal processing, through corresponding modifications on the fiber core. So, Photonics has seen a big development in the last years at the request of this communication market. Nowadays, the capacity of optical communication on long hauls is reaching some Tbit/s over thousands of kilometres. And all these are thanks to the progress in optical fibre fabrication, the use of erbium-doped-fiber-amplifiers (EDFA) and Raman amplifiers, modulators and single frequency lasers. However, these optical fiber-based devices result in high cost and large discrete elements. The key to make more advanced and cheaper components is the integration of these optical components on a single chip.

On the other hand, as the first semiconductor transistor was demonstrated in 1943, and the later invention of integrated circuit (IC), microelectronics has kept developing in a very fast pace. The size of complementary metal-oxide-semiconductor (CMOS) transistors, as a key factor concerning the computer performance, has been continuously

scaled following the Moore's Law, which states that the number of transistors on an integrated circuit doubled approximately every two years [MOO65]. However, conventional copper electronic interconnects are not suitable for the ultra-high bandwidth on-chip communication in future so, a significant performance limitation in ICs has become the metal interconnect. For that, a big driving force is the need to replace electronic interconnects in today's microprocessors, which has become the bottleneck that limits the operating speed of microelectronic devices. Optical or photonics interconnects seems to be the better solution to overcome such bottleneck due to its larger bandwidth, lower power consumption, smaller interconnect delays, and better resistance to electromagnetic interference. When one speak about optical interconnects, one may think in four levels of interconnects which can be easily identified: rack-to-rack, board-to-board, chip-to-chip and on-chip. These optical interconnects are the main motivation to look for silicon photonics.

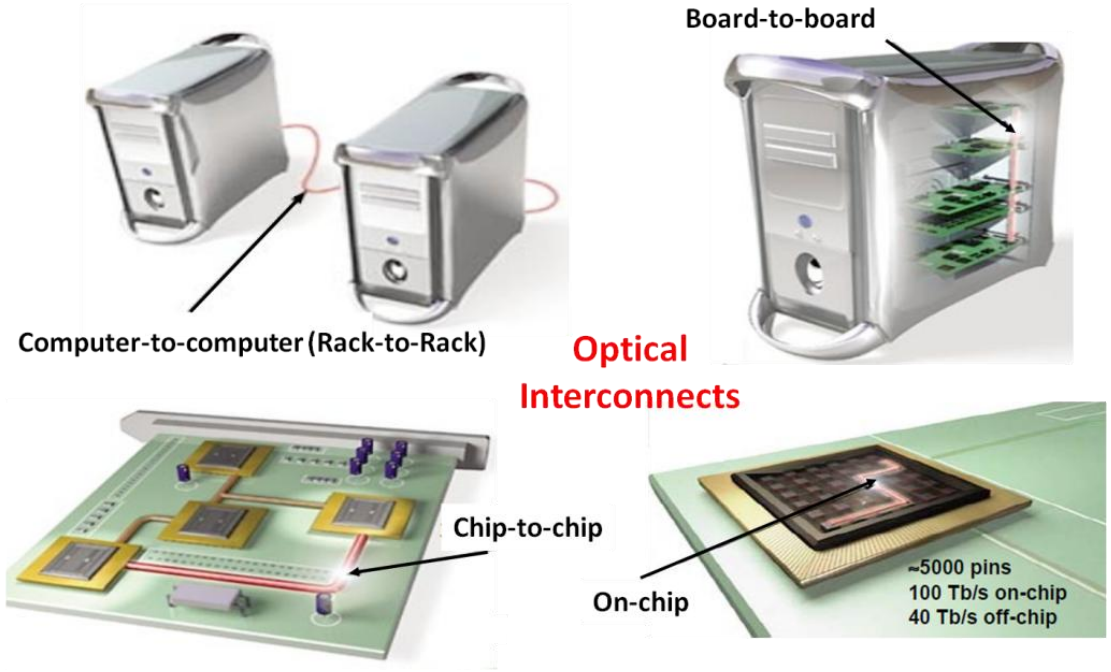

Figure 1-1: Optical interconnects, "This approach to signal transfer is moving from longer-distance applications, such as linking separate computers, to joining chips within a computer" [SAV02].

So, the key to face the actual trend is to make advanced and cheap components towards the integration of optical components on a single chip. When the optical components are integrated on chip, we talk about photonic integrated circuits (PICs). Following same approach as in microelectronic devices, the commitment towards a process of photonic device integration and miniaturization has attracted the interest of industry which has allowed the emergence of integrated photonics. So, the main objective is to find a technology in which a variety of PICs can be easily fabricated in a generic foundry process. This concept is well known in silicon microelectronics. As happened with silicon microelectronics, photonic technology to the mass market may happen only if one can bring high volume manufacturing at low cost. It was possible

because microelectronic integration processes support the integration of a set of basic building blocks, which make possible more complex circuits by simple interconnection between them. So the idea of using silicon and its mature technologic platform for developing photonics started to make sense driven by the increasing demand for low-cost mass-production.

Thus, the traditional argument in favour of silicon photonics is based on its compatibility with the mature silicon CMOS microelectronic manufacturing. Silicon wafers have the lowest cost (per unit area) and the highest crystal quality of any semiconductor material. It can also be used for optical interconnects due to its transparency in the range of optical telecom wavelengths which will enable a platform for a monolithic integration of optics and microelectronics. So, creating low-cost photonics for mass-market applications by exploiting the mighty IC industry has been the traditional motivation for silicon photonics researchers. Another motivation is the availability of high-quality silicon-on-insulator (SOI) wafers, an ideal platform for creating planar waveguide circuits. The strong optical confinement offered by the high index contrast between silicon (n=3.45) and SiO2 (n=1.45) makes it possible to scale photonic devices to the hundreds of nanometre level. Such lateral and vertical dimensions are required for true compatibility with IC processing.

Changing the field but without departing from the scope of the photonic, the area of microwave photonics (MWP) has evolved in parallel to the development of optical communication, as optical components have become available at microwave frequencies and beyond. We refer to MWP as the study of photonic devices operating at microwave frequencies and their applications in microwave and optical systems. The interdisciplinary field of MWP covers research within a frequency span from MHz to THz. The flexibility of microwave technology in combination with the low loss, large bandwidth and the insensitivity to electromagnetic disturbances of photonics, create a solid foundation for a vast number of MWP applications. These applications span from common antenna TV, to antenna remoting of communication systems and radars and to signal generation and signal processing. Further, a particular aspect that recently gains significant interests is the use of PIC technology in the microwave photonics (MWP) field, technology known as integrated microwave photonics (IWMP), for enhanced functionalities and robustness as well as the reduction of size, weight, cost and power consumption. IMWP is an emerging field, in which analog radio frequency (RF) signals are generated, distributed, processed and analyzed using the strength of photonic techniques. It is a technology that enables various functionalities which are not feasible to achieve only in the microwave domain. The past years have also seen significant increase of silicon photonics technology for MWP systems.

After presenting all challenges and opportunities of silicon photonics, one can imagine that tremendous amount of progress has been reported in the last decade in individual photonic components on silicon, including hybrid lasers, fast and low-power silicon electro-optic modulators, and high-speed photodetectors or even transceivers,

since significant global companies such as IBM or Intel, have included the silicon photonics technology among his main lines of research. As a matter of fact, the integration of modulators and photodetectors (the two key interfaces bridging the electrical and optical domains) on the same chip, enabling a fully PIC with high speed electronics, is one crucial step towards a fully functional optical interconnect system.

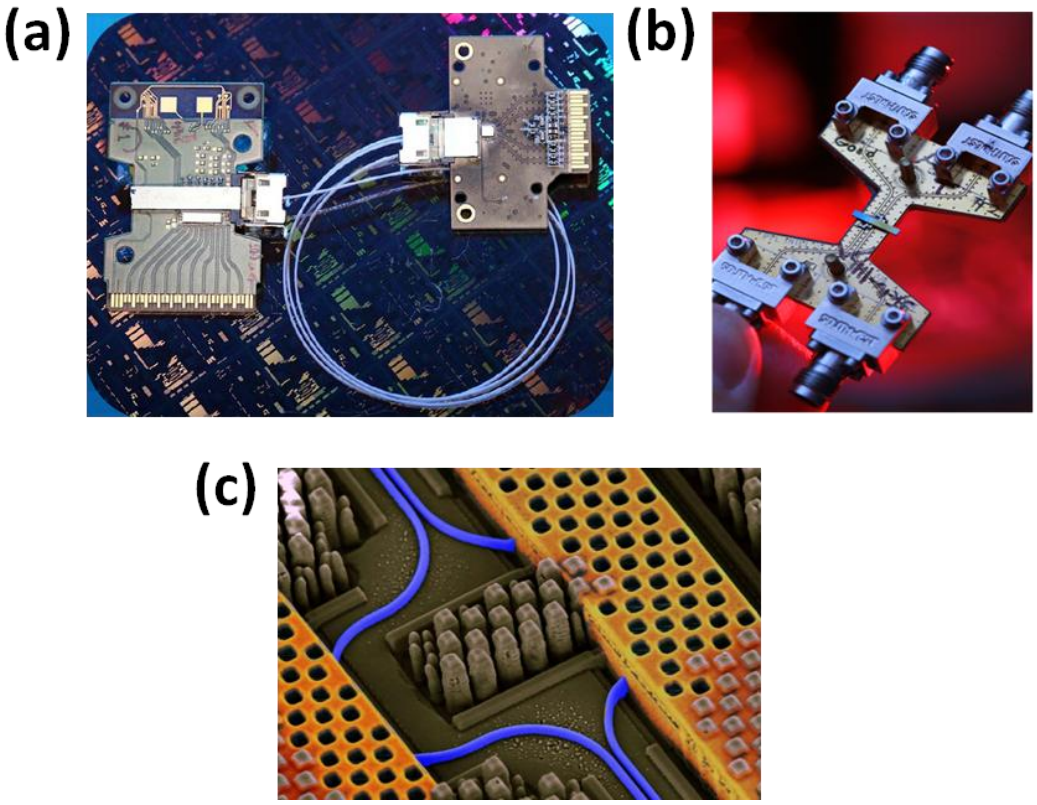

Figure 1-2: (a) Intel Silicon photonics-based 50 Gbit/s link (5 channels @12.5Gbps) with a bit of scaling: 1 Terabit/s link forecasted (25 channels @40Gbit/s) (b) Intel's packaged 40Gbit/s modulator [INT], (c) angled view of a portion of an IBM chip showing blue optical waveguides transmitting high-speed optical signals and yellow copper wires carrying high-speed electrical signals [IBM].

In this thesis, the previously introduced SOI technology is employed to develop one of these key building blocks. This device, as already abovementioned, is the electro-optic modulator which links the electrical and optical domain. So, as proof of concept, this thesis intends to be a contribution to the field of silicon photonics through the demonstration of high-speed modulation in silicon devices to achieve more complex building blocks and thus going one step further towards a fully integration of modulators devices in the CMOS-compatible silicon photonics platform for digital and analog applications for future inter/intra-chip interconnect applications.

This thesis is framed in the European project called HELIOS [HEL] (pHotonics ELectronics functional Integration on CMOS). The HELIOS consortium has developed innovative means to combine a photonic layer with a CMOS circuit, using microelectronics fabrication processes. HELIOS has gathered 19 partners among the

major European CMOS Photonics and Electronics players and potential users. It has driven the European RTD in CMOS Photonics and has paved the way for industrial development [HEL].

The objectives of HELIOS have been the following:

- Development of high performance generic building blocks that can be used for a broad range of applications such as wavelength-division multiplexing (WDM) sources by III-V/Si heterogeneous integration, fast modulators and detectors, passive circuits and packaging.
- Building and optimization of the whole "food chain" in order to fabricate complex functional devices.
- Demonstrating the power of this proposed "food chain" by realizing several complex PICs addressing different industrial needs, including a 40Gbit/s modulator, a 10x10Gbit/s transceiver, a photonic 10Gbit/s wireless transmission and a mixed analog and digital transceiver module for multifunction antennas.
- Road mapping, dissemination and training to strengthen the European research and industry in this field and to raise awareness of new users about the interest of CMOS Photonics.

Specifically, HELIOS work package 3 (WP3), in which this thesis is concretely framed, is dedicated to the developing high speed plasma dispersion effect based SOI modulators and part of the work is to find a way to increase the linear interaction between charges carriers and the optical mode. One of the most promising options is to take advantage of the slow-wave and resonant enhancement, which allows for more compact and less power consuming electro-optic modulators.

1.2. Electro-optic modulation in silicon

Optical modulators are key building-blocks for high speed signal transmission and information processing in both analog and digital scopes. The work developed in this thesis is essentially focused on the design, fabrication and characterization of these building-blocks in order to make possible the realization of compact and efficient modulators integrated on silicon chips and its application to digital and analog optical communications.

This section introduces all the issues related to electro-optic modulation effect. The definition of optical modulators, as well as different ways to classify them, is introduced. Moreover, the basic principles and performance analysis of a Mach-Zehnder Interferometer (MZI) modulator are discussed in order to get a comprehensive picture of the mechanisms taking place in silicon to achieve phase and amplitude modulation which are also described. Finally, a description of the complete development process of is reviewed.

1.2.1. Optical modulators

An optical source can be either directly or externally modulated. External modulation offers several advantages compared to direct modulation: the optical source can be relatively inexpensive and its operation does not need to be compromised by direct modulation, modulation speeds can be higher, and optical isolation and wavelength stabilization need to be performed only once for the entire system. Furthermore, a single light source can feed multiple channels via individual modulators, thus reducing the total power budget of the system [REE10]. This thesis focuses on the development of external modulators.

An optical modulator is a device that is used to modulate (that is, vary the fundamental characteristics of) a light beam propagating either in free space or in an optical waveguide. These devices can alter different beam parameters, allowing them to be categorized as either amplitude, phase or polarization modulators. The modulating signal may come in several forms such that modulation may be carried out either via electro-optical, magneto-optical, mechano-optical or acousto-optical effects. The prefix placed before "optical" defines the nature of the modulating signal [BRI11B]. In addition, modulators can be also classified as either electro-refractive or electro-absorptive modulators. Applying an electric field to a material may change both real and imaginary coefficients of the refractive index. A change in the real coefficient of the refractive index (Δn) with an applied electric field is known as electro-refraction, whereas a change in the imaginary coefficient of the refractive index ($\Delta \alpha$) is known as electro-absorption. Another main classification of modulators can be defined by the signal type of the modulating signal.

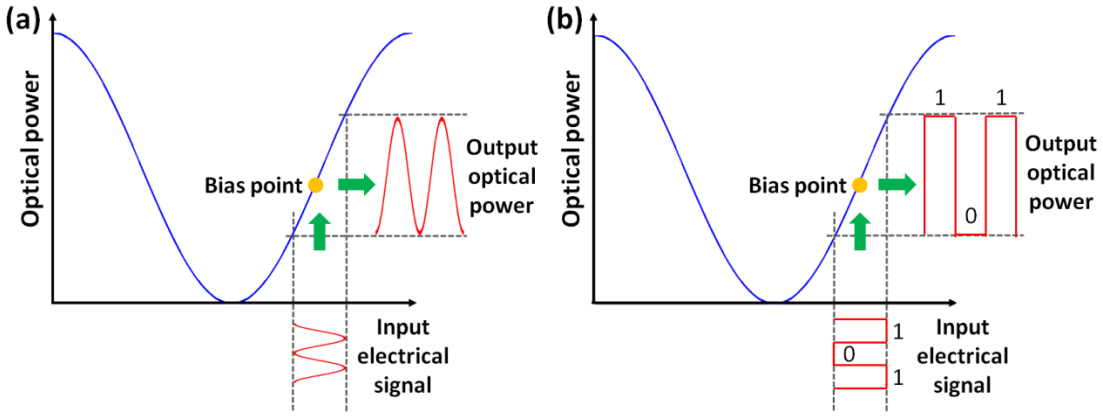

Figure 1-3: (a) Analog (b) digital amplitude modulation in a MZI modulator.

On one hand, we can talk about analog optical modulation, where the optical carrier is gradually modulated in phase or intensity via a continuous electrical signal and on the other hand, digital optical modulation, which converts a continuous light waveform (containing no information) into a discontinuous carrier that carries information in a binary form, that is, '1's and '0's referred to as 'bits'. These binary states correspond to

the case when light is respectively switched on and off. Specifically, in this thesis electro-optical modulators are developed for both digital and analog applications, so the modulating signal will be respectively, a set of bits and a continuous RF signal. Figure 1-3 illustrates an example of analog and digital amplitude modulations of a MZI modulator.

1.2.2. Modulation in silicon: the plasma dispersion effect

In the field of light modulation in silicon, the challenging aspect is to alter the refractive index as silicon does not exhibit any linear electro-optic (Pockels) effect, classically used in III-V semiconductors [BAH01]. Alternative ways to alter the refractive index in all-silicon structures have been proposed [BRI11B]. So far, the most viable mechanism to achieve multi-GHz modulation in all-silicon devices is proven to be the plasma dispersion effect. This physical effect is basically based on free carrier concentration variation in a semiconductor, which alters both the real and imaginary coefficients of the refractive index. These parameters were derived experimentally by R. A. Soref [SOR87] from the Drude-Lorenz equations at the specific telecommunication wavelengths (1.3μm and 1.55μm). His conclusions led to the following empirical equations for λ= 1.55 μm, which is the desirable wavelength in this work:

$$\Delta n = -[8.8\times10^{-22}\Delta N_e + 8.5\times10^{-18}(\Delta N_h)^{0.8}] \quad (1.1)$$

$$\Delta \alpha = 8.5\times10^{-18}\Delta N_e + 6.0\times10^{-18}\Delta N_h \quad (1.2)$$

where ΔN_e and ΔN_h are respectively the variations in concentration of electrons and holes in cm^{-3}.

Let us consider now that light coming up from a continuous wave laser can be confined and guided by total internal reflection (mechanism through which light can be confined and hence guided within the central layer of the silicon waveguide) in a single mode silicon waveguide. As for electronic devices, silicon needs to be doped with elements from the third and fifth columns of the periodic classification of elements to form a semiconductor junction capable of injecting, depleting or accumulating charge carriers (electrons and holes). This enables to accurately control the electrical response. Such control is required to realize diodes, transistors, detectors, and others devices. Conveniently using this existing technology, it becomes possible to combine an optical structure guiding the propagating mode with an electrical structure in charge of injecting, depleting or accumulating a plasma of free carriers overlapping the mode in question. The next section deals with this issue.

1.2.3. Phase modulation: electrical structures

As already discussed, the refractive index as well as the absorption of silicon can be altered varying the density of charges carriers within a silicon waveguiding structure through the plasma dispersion effect. To achieve such variations, the silicon waveguiding structure must be mandatorily doped to form an electrical structure where charge carrier motion can be produced under an applied electric field. Such application of an external electrical field in form on a direct current (DC) voltage modifies the refractive index profile of silicon in the waveguide region and ultimately the optical phase of light passing through it, thus acting as a phase modulator. So, if the Δn index varies by plasma dispersion effect, there will be a change Δn_{eff} in effective index of the propagating mode. Therefore, the injection of an electric field causes a change in the effective refractive index of the guided mode, which in turn induces a change in the accumulated phase, defined by Equation (1.3):

$$\Delta\Phi = \frac{2\pi}{\lambda}\Delta n_{eff} L_{ACT} \tag{1.3}$$

where Δn_{eff} is the effective index change, λ is the wavelength and L_{ACT} is the length of the active region. By embedding such optical phase modulation in a MZI structure, it is possible to convert the phase modulation into intensity modulation as we will discuss in the section 1.2.4.

The speed of the optical modulation is directly related to the intrinsic speed of charge carrier motion, but however may be limited by other effects. Since the first GHz modulator [LIU04] was demonstrated in 2004, a variety of designs were reported, each of them involving specific charge carrier motion in an appropriate electrical structure. So, electrical manipulation of the charge density with the propagation light is achievable through mechanism such as carrier injection, accumulation or depletion. An overview on each of them is hereinafter given.

The first electrical mechanism used for achieving high-speed modulation was the carrier accumulation. In such case, carrier density modulation is obtained by driving a metal-oxide-semiconductor (MOS) capacitor (Figure 1-4(a)) into the accumulation mode of operation. A thin insulating layer of oxide, SiO_2 (p-type doped) is used to isolate two halves of the waveguide (slightly n-type doped) to create a capacitor structure. When a positive voltage is applied between the contacting pads, electrons and holes accumulate at the gate oxide layer, that is, at the Si/SiO_2 interface. This change in charge density causes the optical mode propagating to overlaps with those accumulated electrical charges, leading to a variation in its effective index of refraction. Carrier-accumulation modulators are not limited by the relatively long minority carrier lifetime in silicon, which is the case of carrier-injection modulators, but are instead dominated by the device resistance and capacitance. Thus, these modulators generally suffer from high capacitance and the lack of modulation efficiency due to the low amount of carrier involved.

On the other hand, carrier injection-based modulators are usually based on forward biased *PIN* diode (Figure 1-4(b)). The basic *PIN* structure architecture consists of a silicon optical waveguide embedded into highly p- and n-type doped silicon regions. When the junction is forward biased, minority charge carrier motion through the intrinsic silicon region, where the mode propagates, is produced. So, forward-biasing the device causes free electrons and holes to be injected into the intrinsic waveguide region. The optical mode is confined into the intrinsic silicon region to avoid high losses due to heavily doped p- and n-type regions and overlaps with the current of charge carriers injected through the intrinsic region.

There is a trade-off between the intrinsic silicon region width, meaning higher modulation speed and optical losses induced by heavily doped regions. Because of the slow carrier/generation recombination process modulation are in principle limited to 1 GHz. To counteract such a fundamental limitation, a pre-emphasis driving scheme consisting in applying short peaks of current at the beginning of each electrical bits to accelerate the carrier generation process and followed by a reverse bias operation to extract carriers more efficiently, may been employed which adds complexity to the overall device. Moreover, the advantage of *PIN* diode architectures is the high amount of charge carriers involved in the electrical process leading to strong change in silicon refractive index. Therefore, smaller modulation lengths at the expense of non negligible power consumption unless low driving voltages are used. So, special care must be taken to minimize the insertion losses and power consumption.

Finally, depletion modulators are based on the change in space charge region depletion width of a *PN* junction, that is, slightly doped p- and n-type regions in the waveguide to form a *PN* diode (Figure 1-4(c)). The diode's depletion width, and therefore the free-carrier density in the waveguide, varies with the applied reverse bias in such a way that, the depletion area of the diode becomes larger with increasing reverse bias voltage.

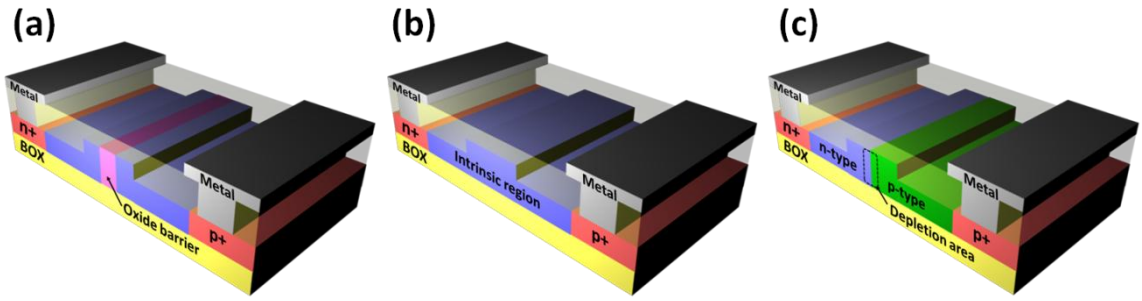

Figure 1-4: Cross section of typical phase shifters to implementing the (a) carrier accumulation mechanism through a *MOS* structure, (b) carrier injection mechanism through a *PIN* structure, (c) carrier depletion mechanism through a *PN* structure, used to electrically manipulate the free-carrier concentrations in plasma dispersion based silicon optical modulators.

Due the fact that depletion modulators are based on the change in space charge region depletion width of a PN junction and hence involve only majority carriers, no generation/recombination process takes place since the modulator behaves as a RC

circuit with specific rise and fall time constant. This effect is intrinsically fast but involves a lower amount of carriers than in the case of the injection regime, which implies that carrier depletion-based modulator are generally less efficient than their injection counterparts. Despite this drawback, the carrier depletion mechanism is the technique that manipulates free-carrier densities in a modulator avoiding the speed limitation posed by the minority carrier lifetime. So, modulation speeds in excess of 30 GHz can be reached by using carrier depletion modulators, but at reduced efficiency as mentioned above. For all, the challenge remains to improve efficiency while maintaining other performance metrics. Special care in decreasing the access (or series) resistance and decreasing the junction capacitance must be taken into account.

Apart from these three main electrical structures, with the increasing develop in the fabrication processes, evolution of them or new electrical structures have been proposed in the last years. For example, a *PIPIN* (used in this thesis) structure which allows achieving low loss optical modulator working at the same cut-off frequency than a *PN* diode [RAS10]. A high-speed silicon MZI modulator was proposed, in [XU12], based on interleaved *PN* junctions. This doping profile enabled both high modulation efficiency and low doping-induced loss. Moreover, in [AKI12A, BAB12 and AKI12B] the authors presented high-speed operation of *PIN* diode-based silicon MZI modulators that have side-wall gratings on both sides of the waveguide core. In [THO10], a new design of high speed carrier depletion silicon optical modulator was introduced which featured the use of a self-aligned fabrication process to form the *PN* junction.

1.2.4. Intensity modulation: Mach-Zehnder Interferometer (MZI)

As already discussed, the electrical structures presented in the previous section are phase shifters since they only alter the phase of the propagating wave. This optical phase modulation can be converted into an amplitude modulation by integrating a phase shifters into one or both arms of an interferometer structure. The most frequently used interferometer is the Mach–Zehnder type being the basis of several other devices such as switches and filters. Some of the advantages of the MZI are its simplicity, its large optical bandwidth and the fact that they are temperature independent. In contrast the relatively large phase shifter length required in a MZI silicon modulator is the main drawback. This device is schematically shown in Figure 1-5.

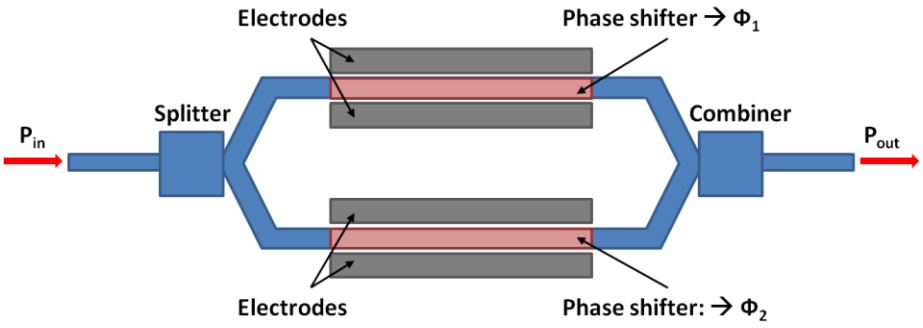

Figure 1-5: Basic schematic of the MZI modulator

It consists of an input waveguide, a splitter, two waveguide with integrated phase shifters into one or both them and an output combiner. The splitter and combiner function can be based on Y-junctions or multimode interference (MMI) couplers.

Let us briefly review the basic operation of the interferometer acting as electro-optic modulator: the incoming light is split into two waveguides under the influence of conducting electrodes, as shown in Figure 1-7. The electro-optical effect (the plasma dispersion effect in the case of a silicon phase shifter) induces a change in the refractive index of one or both interferometer arm and phase-modulates the light propagating into that arm (modifying the values of Φ_1 and/or Φ_2) according to the electric voltage applied to each electrode. By combining the two paths with different phase modulations, this phase modulation is turned into an intensity modulation in such a way that the power at the output can be defined as:

$$P_{out} = P_{in} \cos^2\left(\frac{\Delta\Phi}{2}\right) \tag{1.4}$$

where P_{in} is the power input and $\Delta\Phi=\Phi_2-\Phi_1$ is the phase difference between both arms.

The ideal working principle of this amplitude modulator is based on the fact that the active part of the first arm shifts the phase of the incoming wave by π (by applying a suitable voltage V_π) with respect to the second arm. As a result, the splitted waves interfere destructively, leading ideally to no optical signal at the output. The modulator is in turned off and a "0" is transmitted (Figure 1-6(a)). On the contrary, if no voltage is applied to the phase shifter, the phase of the wave remains unchanged and hence the two waves interfere constructively at the output leading to no alteration of the optical signal. The modulator is turned on and a "1" is transmitted (Figure 1-6(b)).

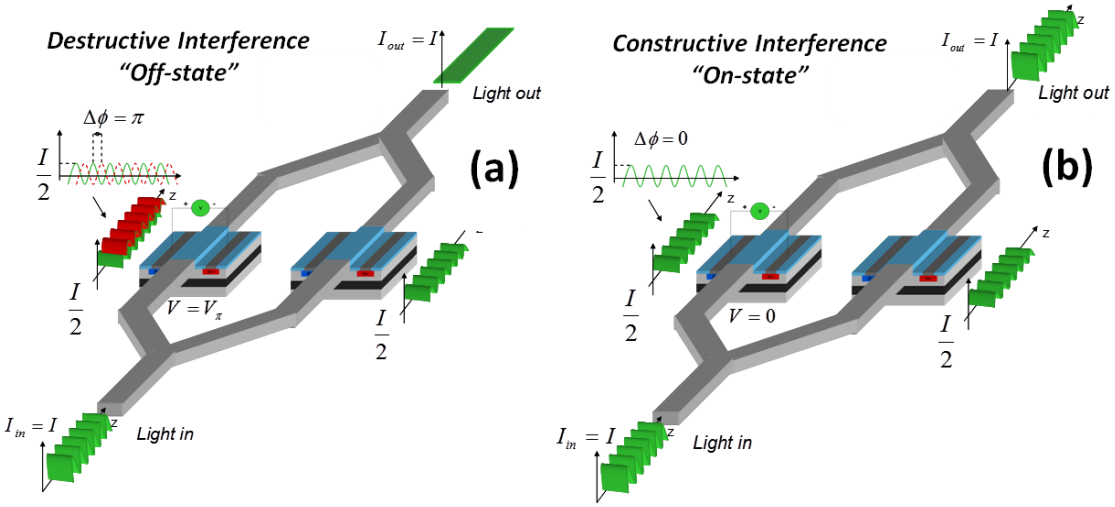

Figure 1-6: Ideal MZI amplitude modulator consisting of two phase shifters integrated into both arms of the device. The operation principle is shown.

The efficiency of the modulator active region is defined by the $V_\pi L_\pi$ product, where V_π is the bias voltage applied to the junction, and L_π is the length of the active region that leads to a π-phase variation. The better efficiency is obtained when $V_\pi L_\pi$ is minimal, that is, when the active region length is the shortest and/or the applied bias voltage is the lowest. Thus, this $V_\pi L_\pi$ product can also be read as a footprint indication.

Two basic types of MZI modulators with different configurations can be defined:

- Single drive: this type of modulator has a single access to both branches. By introducing an electrical signal in such single access, it will affects in the same way to both electrodes but with opposite sign. This modulator can only works in a *push-pull configuration,* which is obtained by applying data and bias voltage in one arm and inverted data and inverted bias voltage in the other arm.
- Dual drive: this kind of modulators has two accesses, one for each of the two branches. So it is possible to work in *asymmetric configuration,* besides in a *push-pull configuration,* where the modulating signal and the bias voltage are applied to only one of the interferometric branches, either to the same or to different branches.

Finally, there are several figures of merit that are used to characterize a modulator [REE10]:

- The modulation speed or bandwidth: is usually defined by the frequency at which the modulation is reduced to 3dB (roll-off frequency) of its maximum value. The speed of the modulator is characterized by its ability to carry data at a certain rate. High modulation speeds are required for interconnection applications in which high data rates are imperative.
- Modulation depth or extinction ratio (ER): is defined as the ratio of the output power in the "on" state to the output power in the "off" state. A large modulation depth is useful for long transmission distances, good bit error rates and high receiver sensitivity.
- On-chip insertion losses (On-chip IL): takes into account the optical power that is lost when the modulator is added to a photonic circuit, so, it can be defined as the ratio between the optical input power before entering the modulator and the "on" state.
- Optical bandwidth: refers to the useful operational wavelength range of the modulator, that is, to the range of wavelengths in which the performance of the modulator is maintained.
- Drive voltage: is the voltage peak-to-peak required by the modulator to achieve the desired level of performance in terms of ER. The drive voltage determines the power consumption of the modulator which is the energy expended in producing each bit of data (energy per bit).

1.3. Development process of photonic structures

A complete development process of any photonic structure can be split into four basic steps: design (including modelling, simulation and analysis), mask generation, fabrication and characterization. In this section, we are going to describe in broad terms each of them as well as the contribution of this thesis at each step.

1.3.1. Design

When talking about light propagation in optical integrated waveguides, one must be thinking in two physical approaches which are presented in such mechanism: on one hand the ray optics approach or geometrical optics, which enables light propagation along an optical waveguide by total internal reflection [REE04] (in silicon this mechanism is highly effective due to the high index contrast effect); and on the other hand, the electromagnetic approach (by means of Maxwell's equations), which allows to derive the guided modes and the field patterns. Maxwell's equations enable to make a rigorous study of the mode profiles propagating along the considered waveguide.

First, the designer must try to model the performance of the device under study. The modeling of photonic structures may not always be carried out in an analytic way, especially when one deals with high index contrast structures with non uniform refractive index profiles all over the propagation length. In this case, the device under study must be simulated to analyze its performance.

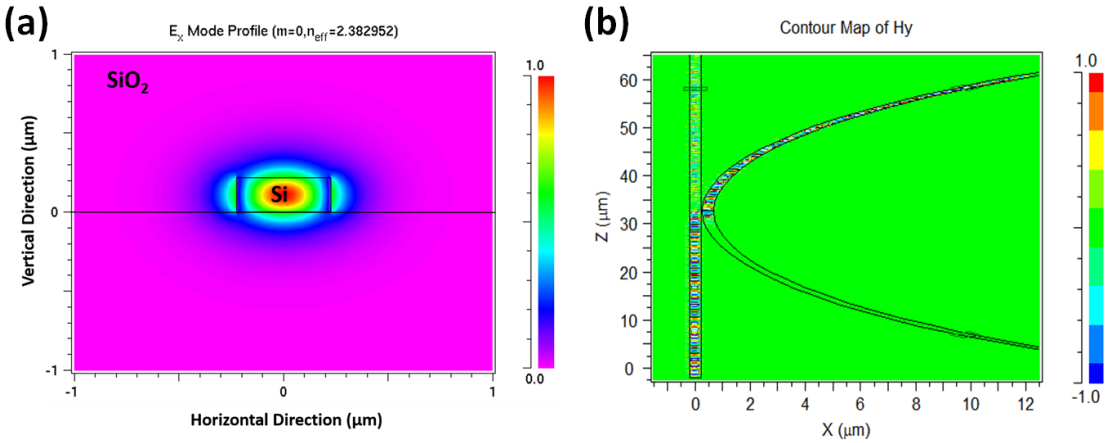

Figure 1-7: (a) BeamPROP simulation of the fundamental mode in a silicon waveguide of 220nm height and 450nm width, (b) FullWAVE simulation on a waveguide-ring resonator structure with a distance between them of 200nm in the coupling region. The power density trough the ring and the waveguide is represented.

Several techniques exist to perform these simulations. Among them, some of those that have been employed to simulate the behaviour of our photonic modulators are: the finite time difference domain (FDTD) method, which consists in discretizing Maxwell's equations via finite differences, the plane wave expansion (PWE) method, which, in

contrast with FDTD, computes the electromagnetic field as a superposition of planes waves, which are straightforward solutions of Maxwell's equations in an uniform medium or beam propagation method (BPM) used for some structures which are uniform in the propagation direction. The simulation tools used in the Nanophotonics Technology Center to carry out the above mentioned methods are, respectively: FullWAVE, BandSOLVE and BeamPROP from RSOFT^{TM} [RSO00]. Figure 1-7 shows two simulation examples.

Besides from the abovementioned optical modelling, also the electrical modelling must be taken into account when working with the electro-optic modulators based on the plasma dispersion effect. In this case, an extra semiconductor device simulation is needed to simulate the electrical structures which compound the phase shifters of the electro-optical modulators under study. Specifically, in this thesis, ATLAS simulation tool from SILVACO has been used. It predicts the electrical behavior of specified semiconductor structures and provides insight on the internal physical mechanisms associated with device operation. DC, alternating current (AC) and transient behavior of a given device may be modelled via solving the discretized Poisson's equation (derived from Maxwell's law), which basically relates variations in electrostatic potential to local charge densities.

All the simulations carried out to finally designing the electro-optical modulators used in this thesis have been developed under the framework of the work package 3 of HELIOS project partnered by the University of Surrey (UNIS), the Université Paris-Sud (UPS) and the Nanophotonics Technology Center in the Universitat Politècnica de Valencia (UPVLC).

1.3.2. Mask generation

Once the designer is in possession of appropriate design parameters derived from the modelling and simulation process, the mask design for the fabrication must be generated. When generating the mask layout, the designer should consider the specific lithography process limitations, essentially given by the wavelength of the illuminating radiation. Usually, a set of photonic structures are designed varying the parameters in a wide range. Moreover, each several repetitions of the same mask are positioned at different locations on the wafer since the deep-UV (used for lithography) incident dose, and therefore the waveguide width (as the resist is more exposed) depends on positioning on the wafer.

In the Nanophotonics Technology Center, *Raith150* lithography software it is used [RAI150]. This tool generates the graphic database system (GDS) final file of the mask which, finally is sent to the fabrication foundry. The electro-optic modulators involved in this thesis are divided into two main masks: on one hand, slow-wave modulators (Figure 1-8(a)) and on the other hand ring-resonator modulators (Figure 1-8(b)).

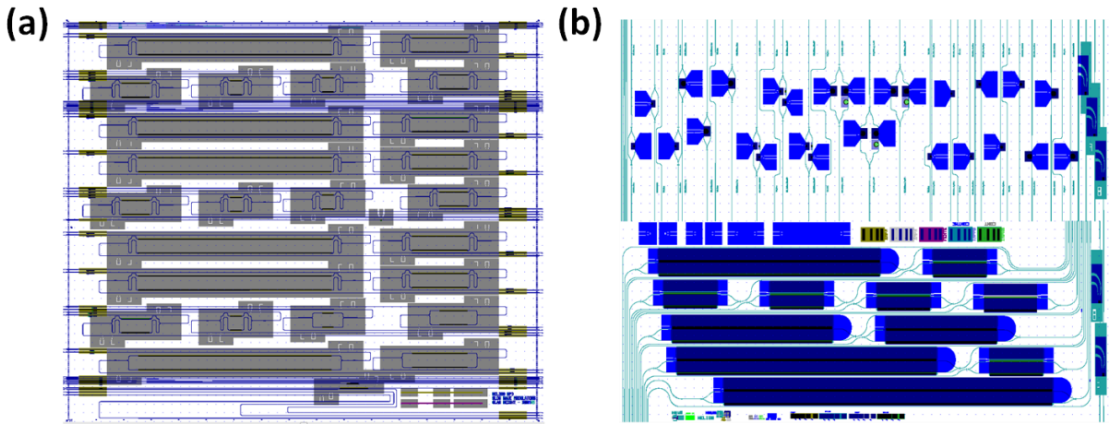

Figure 1-8: Final GDSs mask layers of the fabricated modulators used in this thesis, (a) MZIs and slow-wave MZI modulators and (b) micro-ring and ring-assisted MZI modulators.

1.3.3. Fabrication

Today's trend in silicon photonics is demonstrating that any new device design may be mass produced in CMOS foundries. Such entities consist of advanced nanofabrication tools and highly experienced engineers. Working in a controlled environment gives the designer the opportunity to be aware of the reality of fabrication constraints and capabilities.

The complexity of active silicon devices requires numerous demanding fabrication steps, which must be handled cautiously to avoid time and money consuming errors. For the abovementioned reasons, a CMOS foundry provides a suitable platform to realize complex active silicon devices. In Europe, one of the most standardized foundry models relies on the use of the ePIXfab platform [EPI] within the FP7 European Commission Program. ePIXfab organizes multi-project wafer-scale fabrication services of silicon PICs and partners three institutions: CEA-LETI [MIN], IMEC [IME] and IHP [IHP], with similar standard fabrication capabilities summarized below. Design rules and guidelines are provided in the technology paper standard of both CEA-LETI and IMEC [EPI]. In addition to passive technology, ePIXfab offers ion implantation services to realize silicon active devices based on the plasma dispersion effect. The most common impurities used to dope silicon are boron and phosphorus, which are respectively situated in the III column and V column of the periodic table. Finally, silicide and metallization are also available processes to form low loss contacting electrodes. Specifically, the fabrication of all silicon-based modulators involved in this thesis was carried out at CEA-LETI on 8 inches wafer, with 193 nm deep-UV lithographic process.

Figure 1-9: (a) Photograph of an 8-in SOI wafer with hundreds of photonic components and circuits and (b) picture of a single silicon chip fabricated in CEA-LETI consisting of 26 electro-optical modulators.

1.3.4. Characterization

The main task of this thesis is focused at this step of the device processing. The characterization in the laboratory of all electro-optic silicon-based modulators developed and presented along the thesis has been carried out entirely at the NTC facilities. Several types of characterization processes have been performed: passive, RF, high speed, small signal. All of them are deeply explained in each section, as well as, the characterization set-up and the equipment used and obviously the obtained results.

1.4. Objectives and outline of the thesis

Over the last decade, the advancement in realizing efficient silicon or silicon-based active components has shown that silicon photonics is reaching a degree of maturity never imagined so far. Indeed, the potential commercial impact is motivating research efforts towards creating highly reliable integrated lasers, optical modulators, detectors, and all types of passive elements such as multiplexers, demultiplexers, splitters, directional couplers and delay lines to eventually realize complex optical functions. The key to success is integrating all these building blocks on a standard CMOS-processed silicon wafer while achieving ultra-low footprints. Among them, optical modulators, which handle electrical-to-optical data conversion, are of paramount importance. In such a way, this thesis is intended to be a contribution to the field of silicon photonics through demonstrating high speed modulation in silicon devices featuring small footprints and thus going one step further towards a fully integration of modulators devices in the CMOS-compatible silicon photonics platform. So, the thesis focuses on the development of silicon-based electro-optic modulators with applicability in wide application areas, in both analog and digital scopes, which are the two main chapters in which this work is structured.

This introductory chapter 1 is aimed at giving a general description of the benefits of using silicon photonics, showing its challenges and opportunities as well as at giving a deeply overview of all issues related to the electro-optic modulation. The concept of an optical modulator is given, as well as different classifications of them. Furthermore, a description of the main physical mechanism used for optical modulation in silicon is presented in order to make possible to also give an overview of the phase and intensity modulation in silicon. Moreover, a summary of the main steps followed to developing any photonic structure is presented and the contribution of this thesis in each step is highlighted. Chapter 2 is devoted to develop silicon modulators with high features for digital applications. Specifically, new optical structures different to the conventional MZI are presented with the aim of enhancing the modulation performance or at least several critical parameters in the modulation as the speed or the drive voltage. On one hand, slow-wave structures and, on the other one, resonant structures, are presented theoretically and then demonstrated experimentally. The state-of-the-art of silicon-based modulators is also provided in both cases. Chapter 3 is dedicated to the analog applications. The concept of microwave photonics is described as well as different researches carried out in the analog scope for application in the field of, IMWP all of them using CMOS-compatible electro-optic silicon modulators which validate the potential of silicon CMOS photonics as a promising approach for enabling the development of IMWP applications. A study of nonlinear distortion produced by a silicon MZI is presented leading analytical expressions. Moreover, two silicon-based modulators are used each one to carry out two important analog applications as frequency mixing and microwave filtering. Again the state-of-art of silicon-based modulators reported in such tasks is provided. Finally, conclusions on the work realized are provided in Chapter 5.

Finally, the specific objectives of this thesis can be summarized as follow:

- To demonstrate high-speed and low-drive voltage slow-wave silicon-based electro-optical modulators.
- To propose and demonstrate a method for obtaining the propagation losses parameter. The method will be firstly developed for conventional rib waveguides and then extended to slow-wave waveguides.
- To demonstrate high-speed silicon ring resonators-based electro-optical modulators.
- To develop analytical expressions for the nonlinear distortion in a silicon electro-optic modulator.
- To demonstrate a silicon photonic mixer based on an electro-optic modulator for high quality frequency conversion analog application.
- To demonstrate microwave filtering application by using a single silicon electro-optic modulator.

Chapter 2

Digital applications

2.1. Introduction: state-of-art of plasma dispersion effect-based MZI

The emerging research conducted on silicon photonics has emphasized its potential to utilize low cost, mature and mass productive CMOS processes. The goal of integrating photonics together with electronic devices has become one of the major possibilities to provide higher capacity for future computation. Among all of the silicon photonics devices, the silicon modulator is one of the key building blocks. So, silicon-based modulators could possibly be key elements for high speed, less consuming and low cost optical solutions for the future optical on-chip interconnections. Despite silicon natural inability to produce electro-optical effects (neither Pockels nor Kerr effects) researches an engineers discovered several mechanisms to turn optical modulation in silicon into reality. Based on the two decade old Soref's predictions [SOR87], the refractive index of silicon can be altered varying the density of charge carriers within a silicon waveguide structure. This effect is known as the plasma dispersion effect, as we already presented in Chapter 1. Since the first GHz modulator [LIU04] was demonstrated in 2004, a variety of designs have been reported, each of them involving specific charge motion in an appropriate electrical structure. Following, we review the state of the art of silicon (featuring the plasma dispersion effect) electro-optical modulators for applications in the digital field and all of them based on a MZI structure. Its advantages and disadvantages using different electrical structures are summarized and compared.

The electrical mechanism less used to modulating light consists on carrier accumulation. As already mentioned in the previous chapter, in this configuration a thin insulating layer of SiO_2 is used to isolate two halves of the waveguide to form a capacitor structure. These modulators are based on biased metal-oxide-semiconductor

(*MOS*) structure. The advantage of a *MOS* structure is its process similar to a transistor. This is precisely the desired property for future photonic and electronic integration. The drawback is that the modulation based on a *MOS* structure is limited by the RC delay. Furthermore, a modulator with low capacitance has a wide bandwidth but requires a higher radio-frequency (RF) voltage to achieve the same amount of charge. Therefore, is a trade-off between speed and voltage (and efficiency). The first modulator based on a MOS structure was proposed and demonstrated in February 2004 by Intel [LIU04]. Moreover, this modulator was the first one based on the plasma dispersion effect. The length of the device was 2.5mm and results showed that the optical output signal faithfully reproduced the 1 Gbit/s electrical input data stream. The modulator efficiency was 8V.cm and it presented a high insertion losses (IL) of 13.5dB (4.3dB per interface coupling loss to and from the waveguide and 6.7dB on-chip loss). Later, in 2005, the same authors achieved an increased speed of 10Gbit/s with 3.8dB of extinction ratio (ER) [LIA05]. The modulator was 3.5mm which a better modulation efficiency of 3.3V.cm although higher IL of 19dB (10dB of on-chip loss and 9dB of coupling loss). Further, NEC Corporation group recently demonstrated a high speed of 12.5Gbit/s operation in case of 120μm phase-shift length, high optical modulation efficiency of 0.5-0.67V.cm and lower IL of 7.5dB, by using a projection *MOS* junction structure designed to maximize the overlapping between the optical field and the carrier modulation region by using a compact rib waveguide with highly-efficient optical confinement [FUJ10].

Otherwise, injection modulators are usually based on forward biased *PIN* diode; highly doped p- and n-regions are separated by an 'intrinsic region' in which the waveguide is formed and forward-biasing the device causes free electrons and holes to be injected into the 'intrinsic' waveguide region. The advantage of this type of structure is that it can provide electrical injection of carriers to further increase the refractive index change respect to other structures, which in turn provide much lower $V_\pi L_\pi$. However, there is a main drawback associated with this type of structure. It is the modulation speed typically determined by the free carrier's lifetime. Therefore, pre-emphasis (PE) (which consists on apply short peaks of current at the beginning of each electrical bit to accelerate the carrier generation process and followed by a reverse bias operation to extract carriers more efficiently) is a commonly used technique for successfully mitigating this fundamental limitation enabling broadband operation. In such configuration, a 200μm MZI modulator operating at 10Gbit/s was reported in 2007 by IBM research group [GRE07]. The short modulation length is due to the low device modulation efficiency of 0.036V.cm. However, a large measured on-chip loss of 12dB was presented in the work. In January 2012 a *PIN*-diode-based silicon Mach-Zehnder modulator with side-wall gratings on both sides of the waveguide core has been presented by the Photonics Electronics Technology Research Association (PETRA) and others research groups in Japan [AKI12A]. A $V_\pi L_\pi$ 0.29V.cm was obtained at 12.5Gbit/s using the fabricated modulator and the PE technique. The ultra short modulator (250μm) showed low IL of 4.2dB compared with the IBM modulator. Latter, in May 2012, the authors achieved a higher modulation speed of 25Gbit/s in a shorter

modulator with a phase shifter length of 100μm by optimization of the doping profile. The modulator showed similar IL and lower dynamic ER [BAB12]. Finally, the same groups enhanced again these results, in August 2012, showing an operation speed of 50Gbit/s in a 250μm-length modulator with similar results of both ER and IL. They designed a doping profile of the *PIN* diodes to operate the MZI at a higher speed than in their previous works [AKI12B].

Since 2004, Mach-Zehnder modulators using reverse-biased *PN* diodes have been the most commonly investigated for near-future applications. In these diodes lightly doped p- and n- type are in contact in the waveguide forming the *PN* diode. This mechanism is called depletion and the depletion area of the diode becomes larger with increasing reverse bias voltage. Among the previous mentioned, carrier-depletion on a reverse-biased *PN* junction has been shown to be the best option for high speed operation and this kind of modulator has already exhibited as high-speed operation as 50Gbit/s. However, typically the density of carriers, mostly provided by donors and acceptors is low and a large doping may introduce more optical loss. This change can only provide carriers refractive index change around $\Delta n \sim 10^{-4}$ resulting in a large efficiency $V_\pi L_\pi$. This great efficiency requires a length of several millimetres of the phase shifter, therefore a good design of travelling wave electrode is required to achieve a high modulation speed. In 2007, Intel demonstrated the highest modulation speed until that moment; it was 40Gbit/s with 30GHz of bandwidth in a 1mm travelling device with a low ER of 1dB and a large $V_\pi L_\pi$ of 4V.cm. Moreover, the total on-chip optical loss was less than 4 dB [LIA07]. From that moment, many works have been published improving these parameters. We are going to review the modulation performance of the reported carrier depletion MZIs with speeds up to 40GHz of the most important research groups. In 2001, researchers of the Advanced Technology Institute in University of Surrey demonstrated 40Gbit/s optical modulation in silicon is demonstrated with a large ER for the first time. Phase modulators with an efficiency of 2.7V.cm were incorporated into MZIs with 3.5mm and 1mm length arms. ERs of up to 10dB were demonstrated at 40Gbit/s from the 3.5mm MZI, with a corresponding optical loss of approximately 15dB [THO11]. On the other hand, the most recent modulator presented by this research group achieves a modulation speed of 50Gbit/s also in a 1mm travelling device [THO12]. The bandwidth showed by the modulator is 40GHz and a dynamic ER of 3.1dB. With the progress in the fabrication processes, in recent years some works have presented with optimized electrical structures based on reverse biased carrier depletion. For example, in April 2012, the research group Institut d'Electronique Fondamentale (IEF) showed a reverse biased *PIPIN* modulator operating at 40Gbit/s. Two devices were presented, one with an ER of 3.2dB and an optical loss of 4.5 dB, and another one with an ER of 6.6dB and an optical loss of 6dB. The bandwidth of the larger was 20GHz and both showed an efficiency of 3.5V.cm [ZIE12]. Also in 2012, Bell Labs. & Alcatel-Lucent research group reported a 2 mm-long device, whose switching speed reached 50 Gbit/s with an ER of 4.7 dB [DON12]. Finally, very recently, the State Key Laboratory on Integrated Optoelectronics in China demonstrated in February 2013 a very high speed of 60Gbit/s in a 750μm MZI modulator with doping optimization of the

PN junction [XIA13]. The next Table 2-1 summarizes the above mentioned metrics of the silicon-based MZI modulators reported.

Electrical mechanism	Research group	[ref]	VπLπ [V.cm]	BW [GHz]	Data rate [Gbit/s] @Vpp	Dyn. ER [dB]	Length [µm]	Insertion losses [dB]
Carrier Accumulation (MOS)	Intel	[LIU04]	8	2.5	1		2500	15.3
		[LIA05]	3.3	10	10@3.5	3.8	3450	19
	NEC Corp.	[FUJ10]	0.5-0.67	-	12.5@3.5	3-6	120	7.5
Carrier Injection (PIN)	IBM	[GRE07]	0.036	-	10@7	-	200	12
	PETRA et al.	[AKI12A]	0.29	7.89	12.5@2.3	8	250	4.2
		[BAB12]	-	20	25@3.7	4.3	100	4.7
		[AKI12B]	1.3	25	50@4.35	4.2	250	4
Carrier depletion (PN and others)	Intel	[LIA07]	4	30	40@6	1	1000	4
	Surrey	[THO11]	2.7	47(*3)	40@4 40@6.5	10 7.5	3500 1000	15 8
		[THO12]	2.4	40(*2)	50@6.5	3.1	1000	7.4
	IEF	[ZIE12]	3.5	20(*1)	40@6-7	6.6 3.2	4700 950	6 4.5
	Bell Labs.	[DON12]	2.4	>20	50@4.5	4.7	2000	4.1
	State Key Lab.	[XIA13]	2.05	28	60@6.5	3.6	750	6.5(*4)

Table 2-1: The most important parameters of the last published MZI modulators based on the plasma dispersion effect, (*1) for the 4700µm length, (*2) BW_{6dB}, (*3) predicted, (*4) at 50Gbit/s.

Building a modulator that simultaneously features high speed (40Gbit⁄s) maintaining high dynamic extinction ratio, small footprint (a few hundred micrometers), low IL (<6dB), and low drive voltage (~1V) to meet the stringent values required for monolithic integration with CMOS transistors , represents the main target of silicon modulator designers. As may be seen in Table 2-1, conventional MZI modulators featuring high modulation speeds with high ERs, generally require large footprints, which results in turn in large optical losses. So, the main issue encountered in MZI based devices is the needed interaction length to achieve the π-phase shift in one arm with respect to the other. As an alternative, decreasing the interaction length to reduce the on-chip IL would require to operate the diodes under higher voltage leading to higher injection current (*PIN*), faster depletion (*PN*), more accumulated carriers (*MOS*) as well as the reduction of the extinction ratio.

Therefore, it is clear that there is a clear trade-off in conventional MZM between the drive voltage, modulation speed and IL. On one hand, high modulation speeds are achieved by minimizing the modulation length, which also contributes to reduce IL, but increases the required drive voltage. On the other hand, low drive voltages are achieved by increasing the modulation length which penalizes the IL and modulation speed. Overall, although tremendous efforts have been carried out over the last years, the trade-off between, IL, high speed and drive voltage inherent to silicon-based modulators seems to persist.

This is the reason for that new optical structures different to the MZI one have been proposed in the last years improve the modulation efficiency or device footprint. Part of the work to overcome such issues is to find a way to increase the interaction between charges carriers (refractive index variation) and the propagating optical mode. Two of the most promising solutions for such purpose are to take advantage of slow-wave and resonant structures modulation enhancement, which allow for more compact and less power consumption electro-optic modulators.

In this way, the objective of this chapter is to develop silicon modulation structures in order to enhance the performance of conventional MZI modulators and to demonstrate that the incorporation of optical phase modulators into slow-wave and resonant structures can offer advantages in both reduced device footprint and power consumption in terms of required drive voltage meanwhile high speed operation is maintained and offer the prospect of compact optoelectronic devices integrated with CMOS circuits on the same silicon substrate.

First of all, a MRR electro-optic modulator device using the free-carrier-plasma-dispersion effect [4] is briefly theoretical presented and then experimental results are presented. Despite such modulator can be consider as a promising as it exhibit beyond-GHz-speed, low drive voltage and offer the prospect of compact optoelectronic devices, modulation is usually achieved by shifting the MRR intensity response, which constrains the MRR to be operated close to the critical coupling point to achieve a high extinction ratio, hence making the device very sensitive to temperature and fabrication deviations. For that reason, a new optical structure is proposed, presented and experimentally characterized: the so-called ring-assisted Mach-Zehnder interferometer (RAMZI) which provides a more flexible structure as the MRR just needs to be over-coupled, thus not requiring critical coupling, which in turn offers a higher robustness and the potential for achieving a higher modulation speed.

Second, the enhancement introduced by slow-wave structures is briefly introduced. It is shown that for a given perturbation of the refractive index, the size of the device scales linearly with the group velocity. A review of state of the art of modulators based on slow-wave structures is then carried out. Then, the characterization results of two fast and compact silicon slow-wave-based electro-optic modulators are presented. Finally a method for obtaining the propagation losses in conventional rib waveguides is presented and later extended for obtaining the IL of slow-wave structures.

2.2. Micro-ring resonator structures

Micro-ring resonators (MRRs) have been extensively studied due to their high degree of compactness which makes them suitable for large scale integration in silicon photonic circuits. In this section, different configurations of ring resonator structures have been investigated to enhance modulators performance in terms of extinction ratio, required

external voltage and device size. Modulation based on the intensity and phase response of a ring resonator is considered and analyzed. In the latter, phase modulation is converted to an intensity modulation by using a Mach-Zehnder interferometer structure, which provides a more flexible structure as the ring resonator just needs to be over-coupled, thus not requiring critical coupling, which in turn offers a higher robustness and the potential for achieving a higher modulation speed.

2.2.1. Introduction: state-of-art

Active high-speed ring resonators were first introduced in 2005 by the School of Electrical and Computer Engineering in Cornell University [XU05]. They introduced a *PIN* diode based carrier injection scheme into sub-micrometre waveguide-based ring resonator structures, and achieved an initial data rate of 1.5Gbit/s. The ring had a radius of 6μm, giving a device footprint far smaller than any MZI-based modulator reported so far. The same authors later reported improved results in January 2007 of 12.5Gbit/s with high ER >9dB using a PE driving signal in a ring resonator with the radius of 5μm [XU07]. Then, also in 2007 they achieved an improved operation rate of 18Gbit/s at an ER of 8dB in a ring with diameter of 12μm [MAN07].

This method for modulating was also used by Kotura Inc. & Sun Labs, which in May 2010 obtained a data rate of 12.5Gbit/s with a ring radius of 5μm and a driving voltage of $3V_{pp}$ to achieve ~6dB of extinction ratio. The modulator consisted on an asymmetric lateral *PN* junction [DON10A]. Later, in October 2010, they presented a silicon racetrack resonator modulator with radius of 10.4μm and a straight coupling length of 5μm which achieves over 8dB of modulation depth at also 12.5 Gbit/s with a lower driving voltage of 1V. The design improvement was the *PN* junction embedded along the entire circumference of the resonator, including the coupler part of the resonator and the bus waveguide. The modulator efficiency was of 0.71V.cm [DON10B].

Also in 2010, Sun Labs & Luxtera demonstrated, for the first time, a flip-chip integrated all-CMOS photonic modulator with driver using a carrier-depletion ring modulator and CMOS driver circuits. It showed a 3dB ER and was operated error-free at a data rate of 5Gbps. Small signal measurements of the CMOS ring modulator showed a 3dB bandwidth in excess of 15GHz at 1V of reverse bias, indicating that further increases in transmission rate is possible while retaining compatibility with CMOS drive voltages [ZHE10].

In 2011, the Oracle Labs group published a work reporting a very efficient silicon ring modulator with a ring radius of 7.5μm. Its high-speed section, employing *PN* junction working in carrier-depletion mode, enabled a very high speed operation of 25Gbit/s modulation and an ER >5dB with only $1V_{pp}$ driving [LI11].

Also in 2011, IBM group demonstrated a silicon carrier depletion microring modulator utilizing IBM CMOS Silicon Nanophotonics technology (that has been shown to be fully compatible with fabrication of monolithically integrated optical

transceiver chips), achieving 30Gbps operation with reasonable ER of 3.5dB at very low power consumption in a device suitable for monolithic integration [ROS11]. Finally, special mention has the fastest speed operation so far of 50Gbit/s (with a driving voltage of $1.96V_{pp}$) which has been achieved in 2013 by PETRA research group with a ring-resonator-based silicon modulator for the first time [BAB13].

Group	[ref]	Electrical structure	Q factor	BW_{3dB} [GHz]	Data rate [Gbit/s]@V_{pp}	Dyn.ER [dB]	Ring radius [μm]
Cornell	[XU05]	PIN injection	39350	-	1.5@6.9	6.9	6
	[XU07]	PIN injection (PE)	20000	-	12.5@8	9	5
	[MAN07]	PIN injection (PE)	12000	-	18@6	3	6
Kotura Inc & Sun Labs	[DON10A]	PN depletion	9000	-	12.5@3	6	5
	[DON10B]	PN depletion	10000	20	12.5@1	8	10.4
Sun Labs & Luxtera	[ZHE10]	PN depletion	8300	15	5@2	3	15
Oracle Labs	[LI11]	PN depletion	8000	16.3	25@1	5	7.5
IBM	[ROS11]	PN depletion	9800	-	30@1.6	3.5	300.8(*)
PETRA	[BAB13]	PIN injection (PE)	4300	-	50@1.96	4.58	67.4(*)

Table 2-2: State-of-art of ring resonators-based silicon electro-optical modulators, (*) Racetrack add-drop configuration with a 300.8μm and 67.4 μm circumference, (PE) Pre-emphasis.

As an alternative to intensity modulation, the so-called RAMZI optical structure provides a more flexible and robust structure as the MRR [GUT12A]. In 2010, the first RAMZI silicon modulator was demonstrated in CMOS-compatible technology [GIL10]. Modulation was based on carrier-depletion in a *PIN* diode and 10Gbit/s data transmission with 2dB ER was demonstrated using an interaction length of 680 μm.

2.2.2. Micro-ring resonator-based (MRR) modulators

In this point, theory of micro-ring resonator (MRR) based modulator is reviewed for later demonstrate a silicon microring modulator based on carrier depletion in a *PIPIN* structure.

2.2.2.1. Basic principle of MRR modulators

The basic configuration, which consists of a ring resonator (resonant at a wavelength λ_i) coupled to a straight waveguide, is shown in the Figure 2-1. Key parameters are the separation between waveguide and ring in the coupling region (d), the ring radius (R) and the losses in the ring in dB/cm (α). If the wavelength, for example, λ_i satisfies the resonant condition, that is,

$$n_{eff} L = m\lambda_i \tag{2.1}$$

the coupling of the wave with wavelength λ_i will be enhanced and all others will be suppressed. As a result, only λ_i will resonate inside the ring, while the rest of the wavelengths will pass through and output. In this way, a ring resonator modulator can be consider as a Notch filter. Here n_{eff} is the effective index of the bending waveguide, $L=2\pi R$ is length of the ring, and m is an integer.

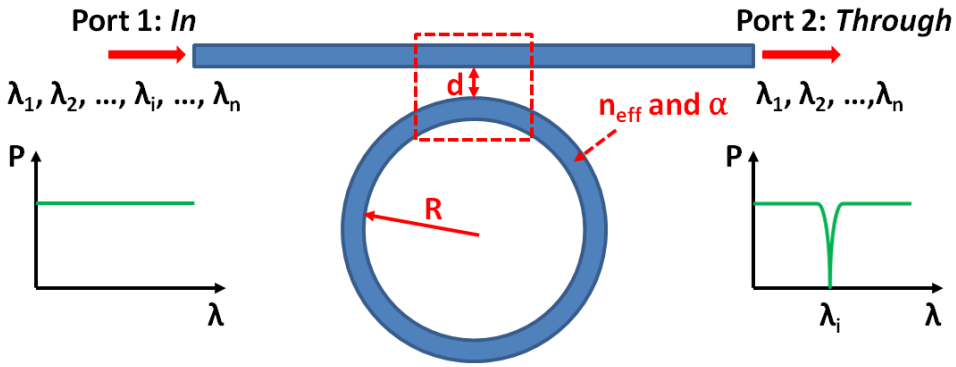

Figure 2-1: Ring resonator in Notch filter configuration and the most important design parameters.

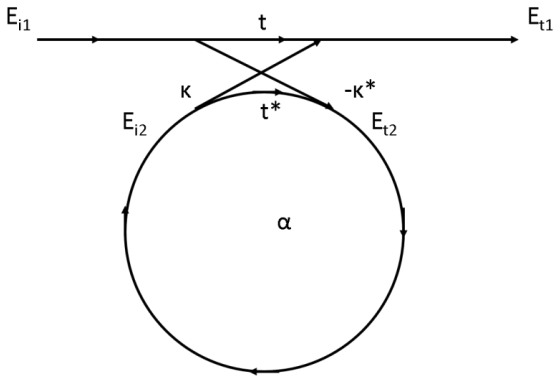

Figure 2-2: Model of a single ring resonator with coupled to one waveguide.

Defining that a single unidirectional mode of the resonator is excited, the coupling is lossless, single polarization is considered, and taking into account that the different kinds of losses in the ring resonator are incorporated in the attenuation constant, the interaction can be described by the matrix relation:

$$\begin{pmatrix} E_{t1} \\ E_{t2} \end{pmatrix} = \begin{pmatrix} t & \kappa \\ -\kappa^* & t^* \end{pmatrix} \begin{pmatrix} E_{i1} \\ E_{i2} \end{pmatrix} \tag{2.2}$$

The complex mode amplitudes are normalized, so that their squared magnitude corresponds to the modal power. The coupler parameters t and κ depend on the specific coupling mechanism used. The "$*$" denotes the conjugated complex value of t and κ, respectively. The matrix is symmetric because the networks under consideration are reciprocal. Therefore:

$$\left|\kappa^2\right| + \left|t^2\right| = 1 \tag{2.3}$$

In order to simplify the model, E_{i1} is chosen to be equal to 1. Then the round trip in the ring is given by:

$$E_{i2} = \alpha \cdot e^{j\theta} \cdot E_{t2} \tag{2.4}$$

where α is the loss coefficient of the ring (zero loss: α=1) and $\theta=\omega L/c$, being L the length of the ring which is given by $L=2\pi R$, where R is the radius of the ring measured from the center of the ring to the center of the waveguide, c the phase velocity of the ring mode ($c=c_0/n_{eff}$) and the fixed angular frequency $\omega=k.c_0$, c_0 refers to the vacuum speed of light. The vacuum wave-number k is related to the wavelength λ through: $k=2\pi/\lambda$. Using the vacuum wave-number, the effective refractive index n_{eff} can be introduced easily into the ring coupling relations by:

$$\beta = k \cdot n_{eff} = \frac{2\pi \cdot n_{eff}}{\lambda} \tag{2.5}$$

where β is the propagation constant. This leads to

$$\theta = \frac{\omega L}{c} = \frac{k c_0 L}{c} = k \cdot n_{eff} \cdot 2\pi R = \frac{2\pi \cdot n_{eff} \cdot 2\pi R}{\lambda} = 4\pi^2 n_{eff} \frac{R}{\lambda} \tag{2.6}$$

From Equations (2.2) and (2.4) we obtain:

$$E_{t1} = \frac{-\alpha + t \cdot e^{-j\theta}}{-\alpha t^* + e^{-j\theta}} \tag{2.7}$$

$$E_{i2} = \frac{-\alpha \kappa^*}{-\alpha t^* + e^{-j\theta}} \tag{2.8}$$

$$E_{t2} = \frac{-\kappa^*}{1 - \alpha t^* e^{j\theta}} \tag{2.9}$$

This leads to the transmission power P_{t1} in the output waveguide, which is:

$$P_{t1} = |E_t|^2 = \frac{\alpha^2 + |t|^2 - 2\alpha|t|\cos\ \theta + \varphi_t}{1 + \alpha^2|t|^2 - 2\alpha|t|\cos\ \theta + \varphi_t} \tag{2.10}$$

where $t=|t|exp(j\varphi_t)$, $|t|$ representing the coupling losses and φ_t the phase of the coupler.

The circulating power P_{i2} in the ring is given by:

$$P_{i2} = |E_{i2}|^2 = \frac{\alpha^2\ \ 1 - |t|^2}{1 + \alpha^2|t|^2 - 2\alpha|t|\cos\ \theta + \varphi_t} \tag{2.11}$$

On resonance, $(\theta+\varphi_t)=2\pi m$, where m is an integer, we obtain that:

$$P_{t1} = \left|E_t\right|^2 = \frac{\alpha - \left|t\right|^2}{1-\alpha\left|t\right|^2} \tag{2.12}$$

and

$$P_{i2} = \left|E_{i2}\right|^2 = \frac{\alpha^2\ 1-\left|t\right|^2}{1-\alpha\left|t\right|^2} \tag{2.13}$$

A special case happens when $\alpha=|t|$ in Equation (2.12), when the internal losses are equal to the coupling losses, so the transmitted power equals zero, which is known in literature as critical coupling, due to destructive interference. By using the above equations, the behaviour of a basic ring resonator filter configuration consisting of only one waveguide and one ring can be taken. This model can be extended to suit the requirement of various types of ring resonator configurations.

Ring resonator filters can be described by some figures of merit which will be explained in the next paragraphs. The first figure is free spectral range (*FSR*), which represents the distance between resonance peaks. By using the propagation constant from Equation (2.5), neglecting the wavelength dependency of the effective refractive index, a simple approximation can be obtained for the *FSR*

$$\frac{\partial\beta}{\partial\lambda} = -\frac{\beta}{\lambda} + k\frac{\partial n_{eff}}{\partial\lambda} \approx -\frac{\beta}{\lambda} \tag{2.14}$$

which leads to the $FSR=\Delta\lambda$ expressed in Equation (2.15), which is the difference between the vacuum wavelengths corresponding to two resonant conditions.

$$FSR = \Delta\lambda = -\frac{2\pi}{L}\left(\frac{\partial\beta}{\partial\lambda}\right)^{-1} \approx \frac{\lambda^2}{n_{eff}L} \tag{2.15}$$

Note that the equation above is for the resonant condition next to a resonance found for the used propagation constant. If the wavelength dependence of the effective index is not neglected, we will obtain a modified version of Equation (2.14):

$$\frac{\partial\beta}{\partial\lambda} = -\frac{k}{\lambda}n_g \tag{2.16}$$

where n_g is the group refractive index, which is defined as:

$$n_g = n_{eff} - \lambda\frac{\partial n_{eff}}{\partial\lambda} \tag{2.17}$$

The group refractive index can be used instead of the effective index in order to obtain accurate values when avoiding approximation is important. The modified FSR $\Delta\lambda$ is then given by:

$$FSR = \Delta\lambda = \frac{\lambda^2}{n_g L} \tag{2.18}$$

The next parameter of importance is the resonance width which is defined as the full width at half maximum (*FWHM*) or 3 dB bandwidth ($2\delta\lambda$) of the resonance line-shape. Using Equations (2.6) and (2.14) and assuming real coupling coefficients, no coupling losses and without phase term, after some operations, we obtain that:

$$2\delta\lambda = \frac{\lambda^2}{\pi L n_{eff}} \frac{1-t^2}{t} \tag{2.19}$$

The expression which is commonly used can be obtained by assuming weak coupling and $\lambda >> \delta\lambda$:

$$FWHM = 2\delta\lambda = \frac{\kappa^2 \lambda^2}{\pi L n_{eff}} \tag{2.20}$$

The finesse *F* of the ring resonator filter, which is defined as the ratio of the FSR and the width of a resonance for a specific wavelength (*FWHM*) is another parameter which can now be directly calculated from the parameters defined previously is:

$$F = \frac{FSR}{FWHM} = \frac{\Delta\lambda}{2\delta\lambda} = \pi \frac{t}{1-t^2} \simeq \frac{\pi}{\kappa^2} \tag{2.21}$$

if we consider that $\kappa << 1$.

A parameter which is closely related to the finesse is the quality factor *Q* of a resonator, which is a measure of the sharpness of the resonance. It is defined as the ratio of the operation wavelength and the resonance width:

$$Q = \frac{\lambda}{\delta\lambda} = \pi \frac{n_{eff} L}{\lambda} \frac{t}{1-t^2} = \frac{n_{eff} L}{\lambda} F \tag{2.22}$$

One key figure of merit of resonators is their bandwidth, which is inversely proportional to the quality factor defined in Equation (2.22). While a narrow bandwidth (high *Q*) is suitable for enhancing light–matter interactions such as lasing [REI06] and sensing [ARM06], a wide bandwidth (low *Q*), on the other hand, allows for optical signals of a broader spectrum and higher speed [LEE06] and is more tolerant to variations in the environment.

Once the most important parameters of a MRR have been presented we are going to explain the basic performance of a MRR based modulator in silicon. The refractive

index in the ring can be modified by means of the plasma dispersion effect. The change of the real part of the refractive index induces a change in the effective refraction index which shifts the spectral response of the ring. This property can be used to implement an intensity modulator. Basic performance of an intensity modulator based on a single ring resonator is shown in Figure 2-3. A continuous wave (CW) of a certain wavelength is injected into the ring resonator. Minimum transmission is achieved when the wavelength is located at a resonance. Furthermore, this transmission is ideally zero when the ring operates at critical coupling, i.e. when the coupled power is equal to the power lost in the ring (*critical coupling condition*) as it has been explained previously:

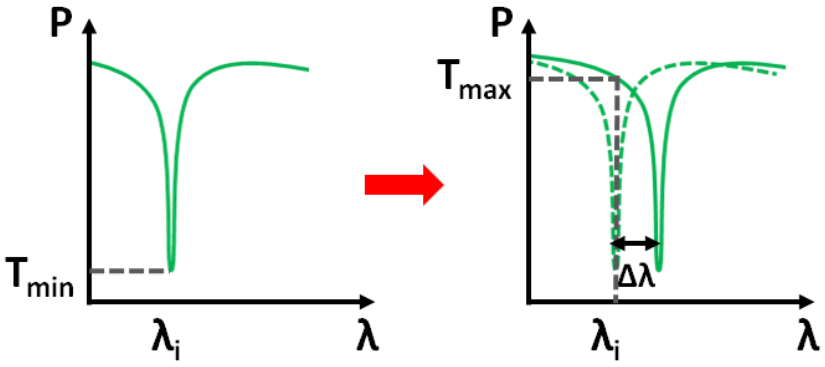

Figure 2-3: Basic performance of an intensity modulator based on a ring resonator.

The spectral response of the ring resonator is shifted when the effective index is modified. Thus, the output power increases up to a maximum value when the frequency shift is enough to move the resonance out of the working wavelength. Therefore, to optimize the performance of the intensity modulator, we are interested in the lowest transmission at resonance to maximize the extinction ration and the narrowest spectrum to minimize the required frequency shift, i.e. the required external voltage.

Figure 2-4 shows the full-width at half maximum (*FWHM*) and transmission of a ring resonator as a function of ring losses and power coupling and taking into account different radii. In the upper plots, power coupling is chosen for each radius to operate at critical coupling while in the lower plots losses are 10dB/cm. The operating wavelength is 1550nm and the effective index is 2.76.

It can be seen that the FWHM increases as the losses (Figure 2-4(a)) and coupling (Figure 2-4(b)) increase. Furthermore, it is also interesting to notice that the FWHM is lower for higher radii and that it converges to a constant value. This constant value is determined by the FSR, which is higher for higher radius, so the FWHM cannot be increased more than the FSR value.

On the other hand, the transmission as a function of losses is the same for the three different radii, as shown in Figure 2-4(c), because the power coupling is changed in each case to operate at critical coupling considering 10dB/cm losses. The different power coupling value for each radius is shown in the transmission plot as a function of the power coupling in Figure 2-4(d). In both cases, it can also be seen that the variation

of the transmission with power coupling and losses is more abrupt, and therefore undesired for the intensity modulator, when the ring is smaller and the ring is under coupled, i.e. when the coupled power is lower than the power lost in the ring.

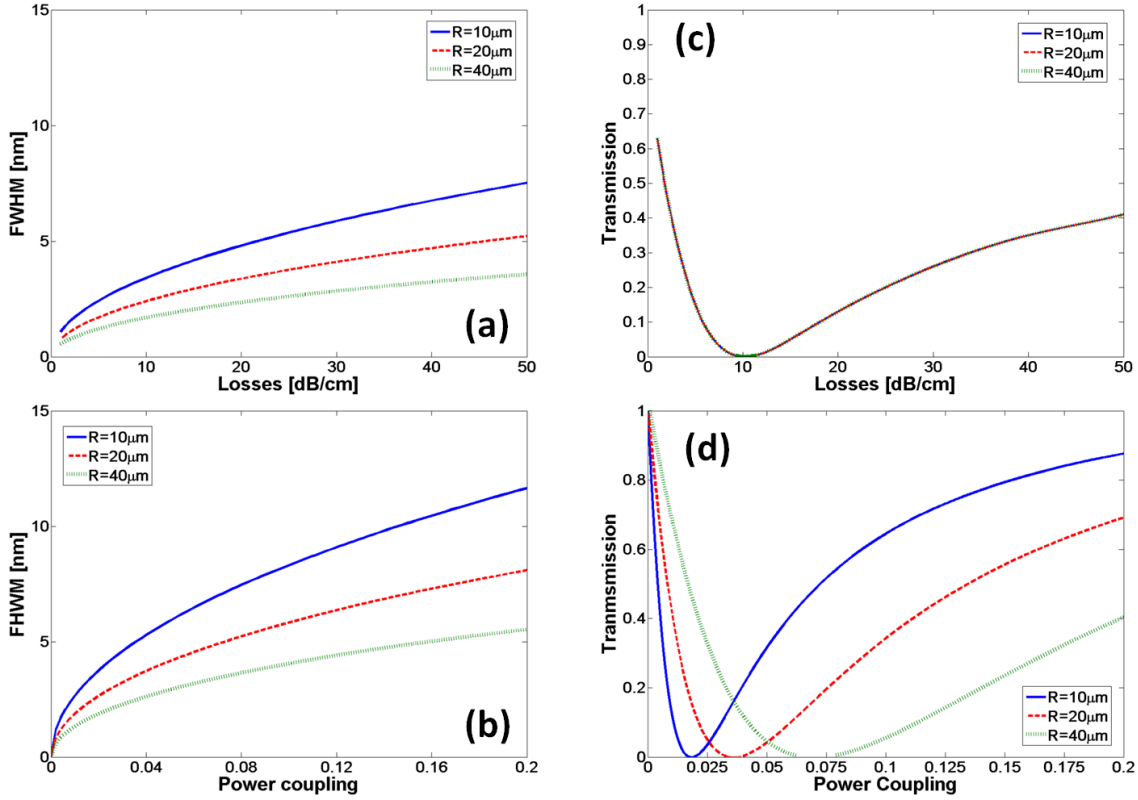

Figure 2-4: FWHM and transmission of a ring resonator as a function of ring losses and power coupling and taking into account different radii. In the upper plots, power coupling is chosen for each radius to operate at critical coupling while in the lower plots losses are 10dB/cm.

In summary, we should work with big radii and close to the critical coupling point for optimizing the performance of the intensity modulator, i.e. maximum extinction ratio and minimum frequency shift. Furthermore, a ring with a higher radius is more robust against coupling variations than a ring with a lower radius.

2.2.2.2. Experimental MRR modulator

The modulator consists of a MRR embedded in a *PIPIN* diode structure and coupled to a straight waveguide, as shown in Figure 2.5(a), fabricated on a silicon-on-insulator (SOI) wafer. The ring and input waveguide of dimensions of 420nm x 390nm have been partially dry etched to leave a 100nm thick slab as shown Figure 2-5(b). As it can be observed, a p-doped slit has been inserted in the intrinsic region in order to act as a source of holes. When a reverse bias is applied on the diode, holes are swept out of the central p-doped region by carrier depletion, leading to a refractive index change. Figure 2-5(c) shows a scanning electron microscope (SEM) picture of some of the fabricated structures and Figure 2-5(d) depicts a zoomed-in view of a MRR. Doping

concentrations in the -*p* and -*n* parts of the diode are 8.10^{17} and $1.10^{18}cm^{-3}$ respectively. Within the 100nm-wide p-doped slit, doping concentration reaches $3.10^{17}cm^{-3}$. The lumped electrodes, placed 0.5µm away from the rib edges to minimize the overlap between the optical mode and so the optical losses, are formed by highly doped *p*+ and *n*+ regions with concentrations of $1.10^{19}cm^{-3}$ in order to decrease the access resistance between the active region and the metal contacts. For the same reason, the waveguide was only etched in an 800nm-wide region on each side of the rib [RAS11A, RAS11B].

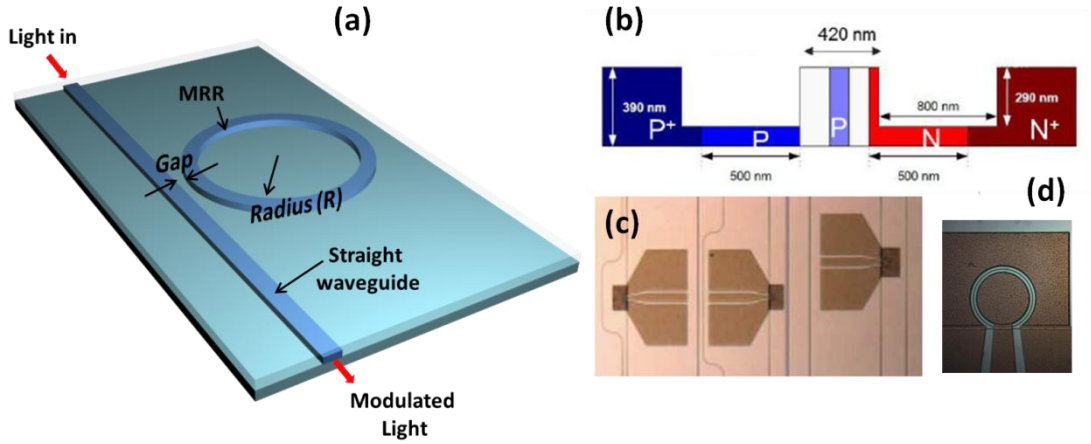

Figure 2-5: (a) Schematic of the MRR silicon-based electro-optic modulator, (b) cross section of the device active region with a *PIPIN* diode (c) top view of some of the fabricated MRR modulators and (d) close up view of the 40µm radius MRR.

As already mentioned, carrier depletion is the mechanism used to electrically manipulate the free carrier concentrations in the investigated plasma-dispersion-based silicon optical modulator. Therefore, with no applied bias voltage, holes are confined in the p-doped slit. Then, when a reverse bias is applied to the diode, they are swept out of the active region. As we already know from Chapter 1, this hole concentration variation produces an effective index variation based on Soref's equations [SOR87], which in turn induces a phase shift following the equation:

$$\Delta\Phi = \frac{2\pi}{\lambda} L \Delta n_{eff} \tag{2.23}$$

where λ is the operation wavelength, L is de ring length ($L=2\pi R$) and Δn_{eff} is the effective index change due to the plasma dispersion effect.

The optical modulator is fabricated on a 200mm SOI wafer with a 2 µm-thick buried oxide layer and a 400nm-thick crystalline silicon film. Deep-UV optical lithography and ion implantation is used to obtain the highly doped *p*+ and *n*+ regions. For hard mask purpose, SiO_2 is then deposited by LPCVD. The waveguides and the slits are patterned using deep-UV lithography. After hard mask etching by reactive ion etching, Boron implantation (*p* in the slit) is performed to obtain the doped layer in the middle of the waveguide and *n* and *p* doped regions are then obtained by lithography and ion implantation, followed by thermal annealing. Finally, metal stack is deposited onto the

wafer, and the electrodes are patterned and etched down to the SiO_2 cap layer. The process used is fully compatible with SOI CMOS technology and could be transferred in high-volume microelectronic manufacturing.

We first carried out passive measurements with the aim of designing the optimum parameters of the MRR structures around the operating wavelength of 1550nm. Optical measurements have been performed with an external cavity laser (ECL) having tuneable range from 1500 to 1580nm. Light was butt-coupled to the chip via a lensed fiber (details of horizontal coupling and passive characterization can be found in appendix A).

Optimum modulation performance is achieved when the ring works at critical coupling, so the ER is maximized, and the ring resonance bandwidth is reduced. As a result, the power consumption may be significantly reduced as small resonance shifts (produced by low applied voltages) will give rise to large extinction ratios. The critical coupling condition is achieved by choosing the optimum waveguide to ring separation depending on the losses of the MRR structure. On the other hand, the resonance bandwidth is inversely proportional to the ring radius. However, large radii also affect the modulation bandwidth owing to the higher RC constant of the lumped electrodes. Hence, a MRR modulator with smaller radius is expected to achieve higher modulation rates at the expense of higher required drive voltages (under the same coupling condition with respect to a higher ring radius). Therefore, although the waveguide to ring separation can be designed to maximize the modulation depth, the ring radius will yield to a trade-off between the modulation bandwidth and power consumption.

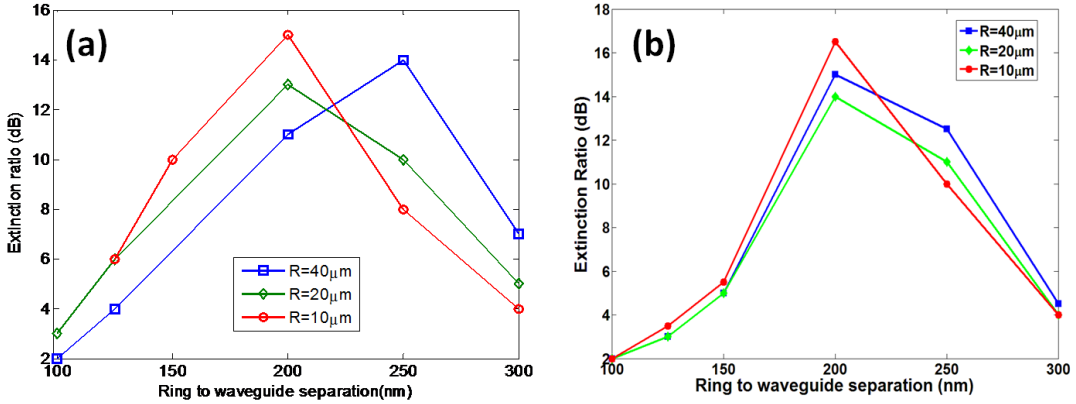

Figure 2-6: (a) Experimental and (b) simulated ER as a function of the ring to waveguide separation.

Figure 2-6(a) shows the experimental ER as a function of the ring to waveguide separation of MRR structures with different radii. It can be seen that the maximum ER (around 15dB) is given for a separation around 200nm for R=10μm and R=20μm and for a separation of s=250nm for R=40μm. On the other hand, propagation losses of around 10dB/cm were also estimated by means of the cut-back method. Taking into account the measured propagation losses and the power coupling as a function of the

waveguide to ring separation, obtained by means of 2D-FDTD simulations and the effective index method, the maximum ER should be given for a waveguide to ring separation of around 200nm for the three radii considered, as depicted in Figure 2-6(b).

Therefore, although there is a slight discrepancy for the optimum separation for the ring with R=40µm probably due to fabrication deviations, in general a good agreement between experimental and simulation results is achieved. Finally, a MRR with big radius (R=40µm) and waveguide to ring separation of 200nm point has been chosen for optimizing the performance of the intensity modulator, i.e. maximum extinction ratio and minimum frequency shift required. Furthermore, a ring with a higher radius is more robust against coupling variations than a ring with a lower radius.

Once the optimum MRR parameters were designed based on previous passive measurements, the ring modulator was characterized under static and high speed regimes. Static measurements for varying applied voltages were realized to estimate the DC ER as well as the modulation efficiency deduced from the achieved phase shift. High speed tests were carried out to evaluate the MRR modulator performance. In both cases the diode was electrically biased via 40 GHz electric probes. The spectrum of the MRR with 40µm radius shows a free-spectral range of 2.5nm and a 9dB drop in transmission at the resonant wavelength around 1556.17nm. The 3-dB bandwidth of such resonance $\Delta\lambda$ is 0.075nm measured from the spectrum, corresponding to a quality factor of around Q~20750 (from Equation (2.22)).

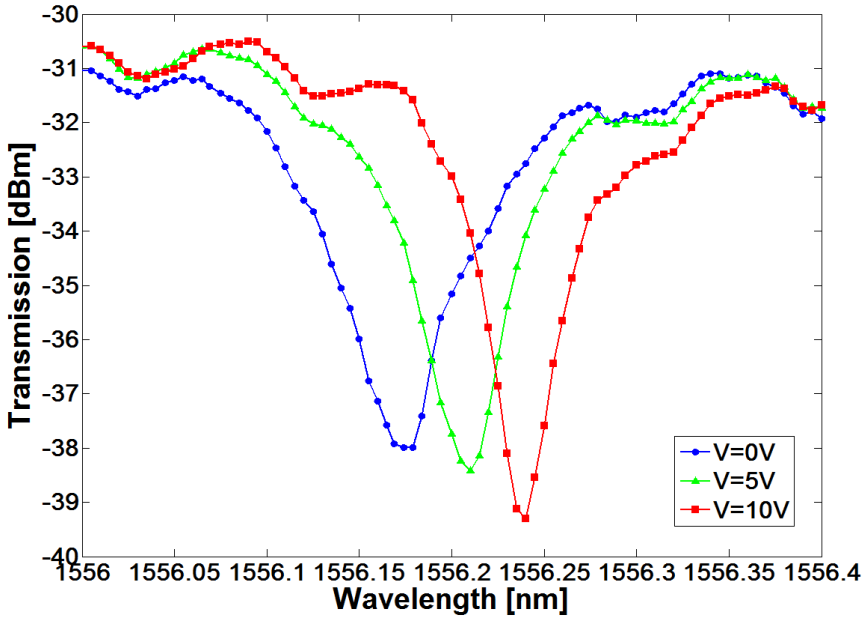

Figure 2-7: Transmission spectrum as a function of the wavelength for different applied bias voltages.

Figure 2-7 shows transmission spectrum under different bias voltages. It can be observed that a DC ER of 4dB is achievable at a bias voltage of 5V while it improves up to 7dB when the bias voltage increases to 10V.

On the other hand, the voltage-induced wavelength shift ($\Delta\lambda$) in the ring resonator modulator output spectrum can be used to extract the effective index variation (Δn_{eff}) as follows:

$$\Delta n_{eff} = \lambda \frac{\Delta\lambda}{FSR \cdot L_A} \tag{2.24}$$

where L_A is the active length that, in our case, is slightly smaller than the MRR perimeter (L_A=207μm<L_{MRR}=251μm), λ is the operation wavelength and *FSR* is the free spectral range.

Figure 2-8 shows the effective index variation as a function of applied bias voltage for the measured MRR.

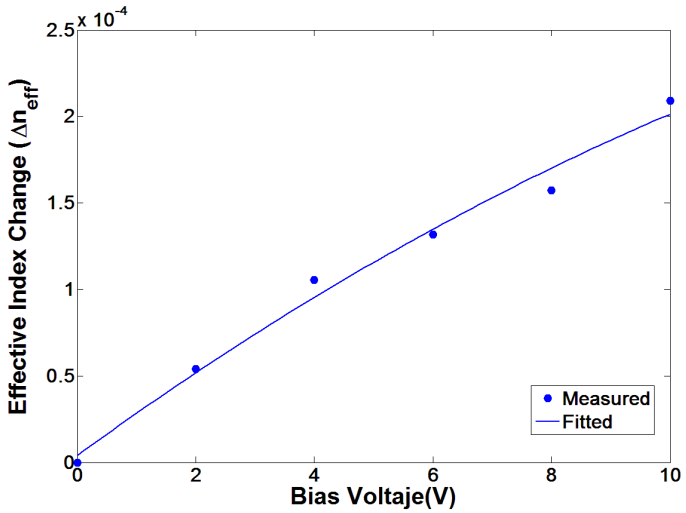

Figure 2-8: Effective index variation as a function of applied bias voltage.

A modulation efficiency $V_\pi L_\pi$ of 2.8V.cm has been calculated from such effective index variation by means of Equation (2.25):

$$\Delta\Phi = \pi \rightarrow L_\pi = \frac{\lambda}{2\Delta n_{eff}} \tag{2.25}$$

where L_π is the interaction length required to achieve a π-phase shift.

Finally, high speed performance of the silicon ring modulator was characterized by measuring the data transmission capability by using the set-up shown in Figure 2-9. The ring modulator with 40μm radius was driven with a nonreturn-to-zero (NRZ) pseudorandom bit sequence (PRBS) of length 2^{31}-1 delivered by a bit pattern generator (BPG), which is connected to an external clock. The electrical signal is amplified through a high-speed RF amplifier to achieve the desired voltage swing (V_{pp}=8V) and combined to a -4V DC bias voltage (in order to ensure reverse bias operation) using a bias-Tee. The modulating signal is applied by a high-speed ground-signal-ground (GSG) RF probes to the lumped electrodes, which are not required to be terminated externally by a 50Ω load. The output modulated optical signal is then optically

amplified by an erbium-doped fiber amplifier (EDFA), filtered via an optical filter (OF) and finally photo-detected by a digital communication analyzer (DCA). Details of model equipments and pictures of the real set-up are given in section 2.4.

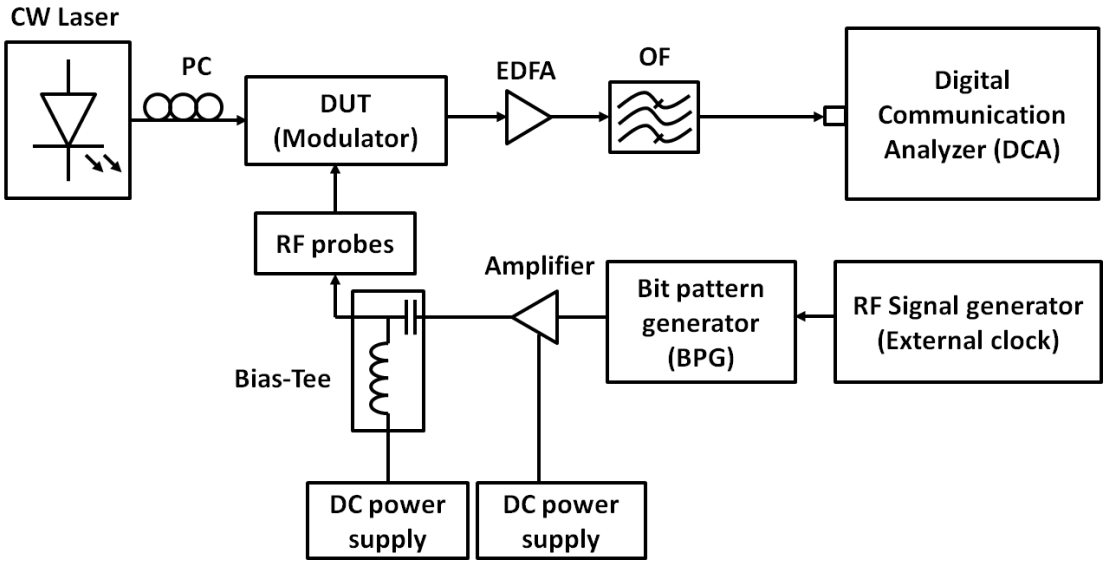

Figure 2-9: Schematic of the characterization setup for the data transmission measurements.

Figure 2-10 shows the obtained eye diagrams. The ER is 4.5dB at bit rates of 5Gbit/s and 10Gbit/s and 3.5dB at 12.5Gbit/s.

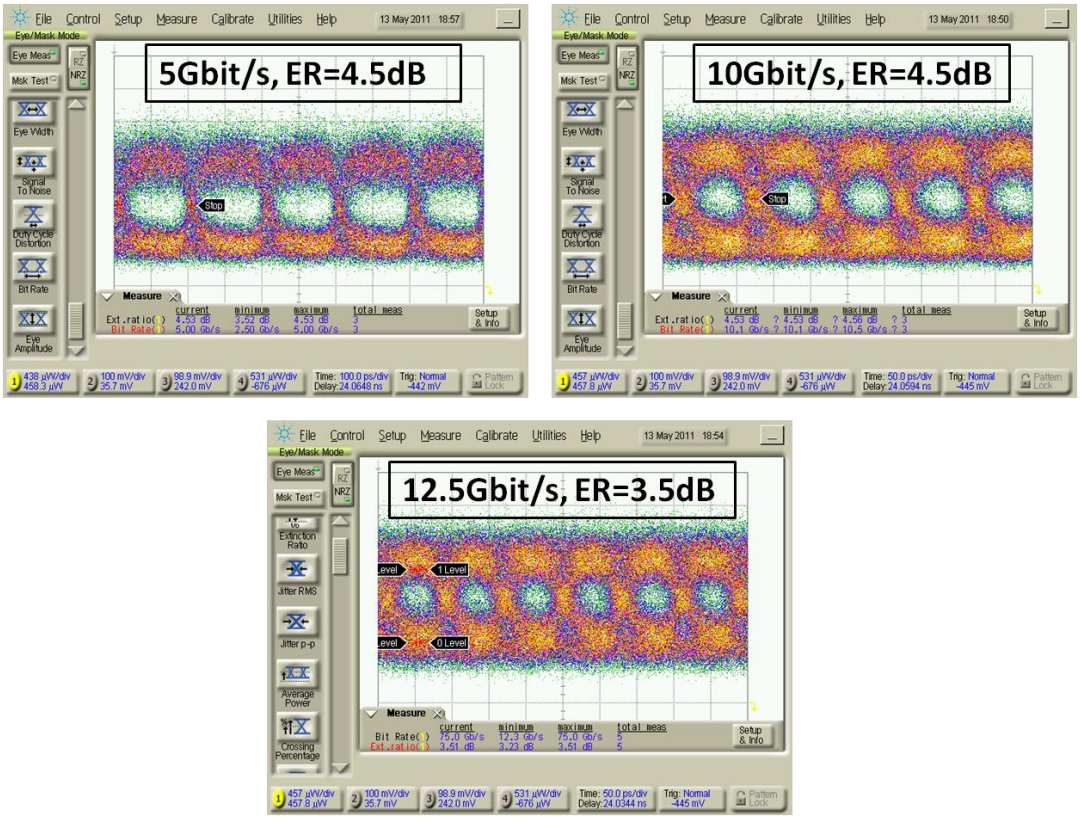

Figure 2-10: Optical eye diagrams with an ER of 4.5dB at 5Gbit/s and 10Gbit/s and with an ER of 3.5dB at 12.5Gbit/s.

In conclusion, we have presented a high speed 40µm radius ring resonator modulator in which the modulation is achieved by carrier depletion effect in a *PIPIN* diode structure. The modulator exhibited an ER of 4.5dB at a data transmission of 5Gbit/s and 10Gbit/s and 3.5dB at 12.5Gbit/s with a drive voltage of $8V_{pp}$.

2.2.3. Ring-assisted MZI (RAMZI) modulators

This point is devoted to report and experimentally demonstrate a high-speed RAMZI silicon modulator. It is shown that, the RAMZI optical structure relaxes the optimum coupling condition of the ring without degrading the modulator performance, which therefore improves the modulator robustness against fabrication deviations and could eventually lead to an enhanced modulation bandwidth [GUT12A]. First, a brief theoretical explanation about the RAMZI basic operation principle is given.

2.2.3.1. Operation principles of RAMZI modulators

The phase response of the MRR can also be used to achieve phase modulation. This phase modulation is converted to an intensity modulation by using a MZI structure, as it is shown in Figure 2-11(a).

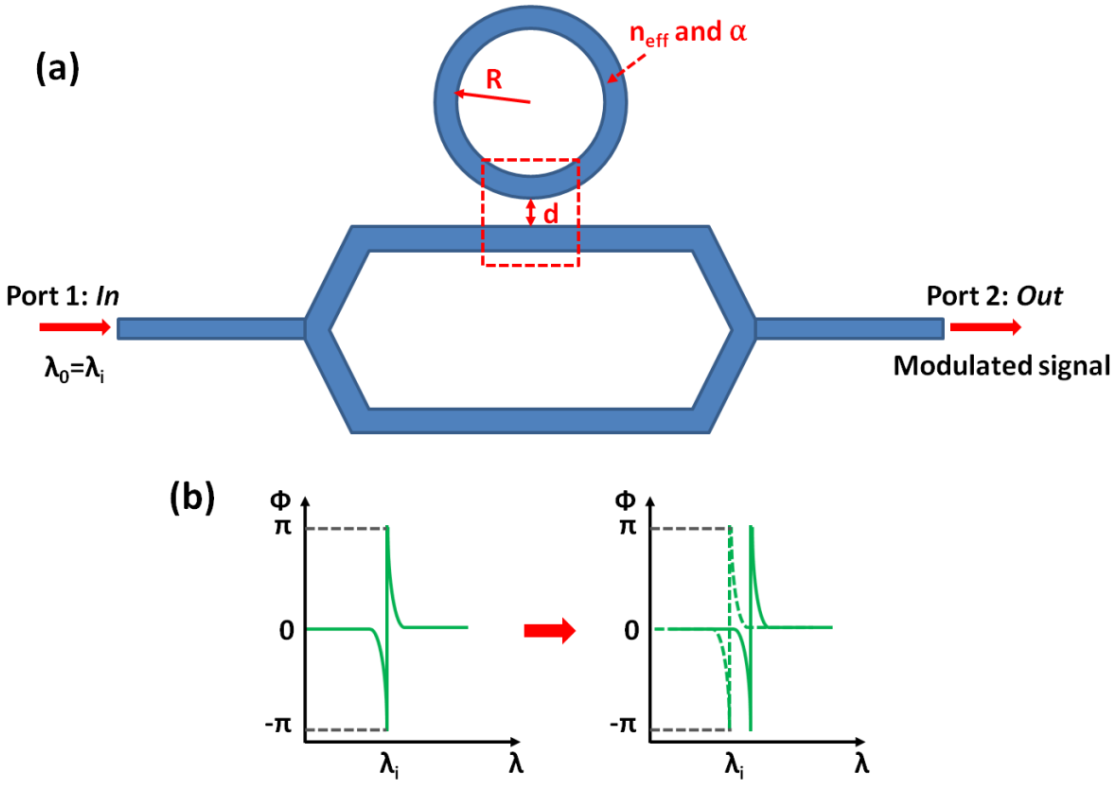

Figure 2-11: (a) Schematic of the RAMZI modulator with the parameters of the MRR and (b) Basic performance of a phase modulator based on a MRR.

To explain the basic performance of the RAMZI optical structure, which is depicted in Figure 2-11(b), it is assumed that the input signal is a CW located at the MRR resonance. The side-coupled MRR induces a π-phase shift to the signal that travels through one arm of the MZI which will interfere destructively with the signal that propagates through the other arm of the MZI. This π-phase shift is thus responsible for minimum transmission at the MZI output. When the spectral response of the MRR resonator is shifted due to the effective index variation and the frequency shift is enough so that the operation wavelength is now out of the resonance, the MRR will not introduce any additional phase shift and the signals at both arm ends will interfere constructively, leading to maximum transmission at the MZI output.

The ER of the modulator is ideally infinite if the attenuation at both arms of the MZI is the same. However, it is worth noting that the intensity response of the MRR resonator will also vary when the effective index is modified (assuming losses are not negligible, which is usually the case). This will introduce additional attenuation to the signal travelling through the arm with the MRR at resonance, which could in turn deteriorate the ER of the modulator due to the power unbalance between both arms of the MZI. This power unbalance will be lower as the power coupling factor, i.e. the fraction of power coupled from the waveguide into the MRR, increases. Therefore, the MRR does not need to be operated at the critical coupling point and just over-coupled. However, it should be realized that too high power coupling factors could increase the IL as the change of the MRR phase response for a given effective index variation will be smaller.

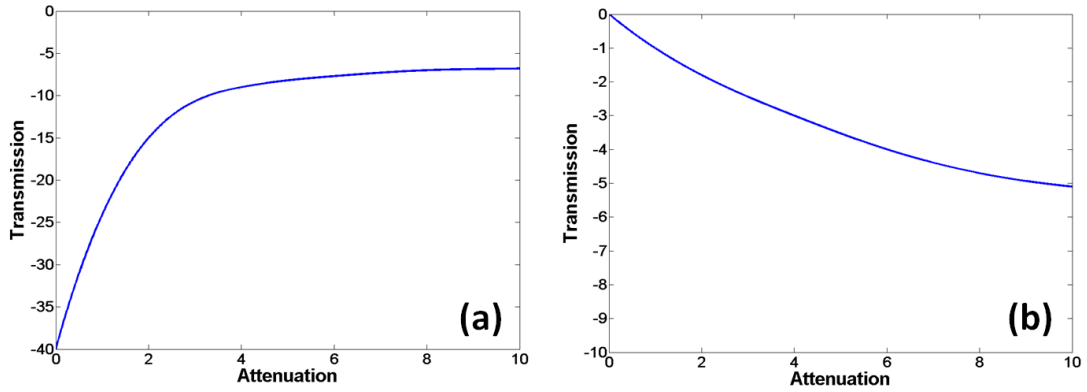

Figure 2-12: Transmission at the MZI output as function of the difference in attenuation between arms when the MZI is operating at (a) minimum transmission (π-phase shift) and (b) maximum transmission (0-phase shift).

Figure 2-12 shows the transmission at the MZI output as function of the difference in attenuation between arms when the MZI is operating at (a) minimum transmission (π-phase shift) and (b) maximum transmission (0-phase shift). First of all, it can be seen that at minimum transmission, the performance of the MZI is much more sensible to attenuation differences than at maximum transmission. As the attenuation increases, the minimum transmission is higher while the maximum transmission is lower so the ER

will decrease. For instance, if the attenuation difference is 3dB, the ER is degraded to 9.57dB.

2.2.3.2. Experimental RAMZI modulator

The RAMZI modulator consists of a MRR embedded in the same *PIPIN* diode structure (Figure 2-13(b)) with the same doping levels than previous MRR modulator but this time coupled to one arm of a MZI, as shown in Figure 2-13(a). The MZI consists of two arms of equal lengths of 215µm with 3dB star coupler splitters and combiners. Figure 2-13(c) shows an optical microscope image of the fabricated device. The overall footprint of the modulator without probe pads is 680µm x 125µm.

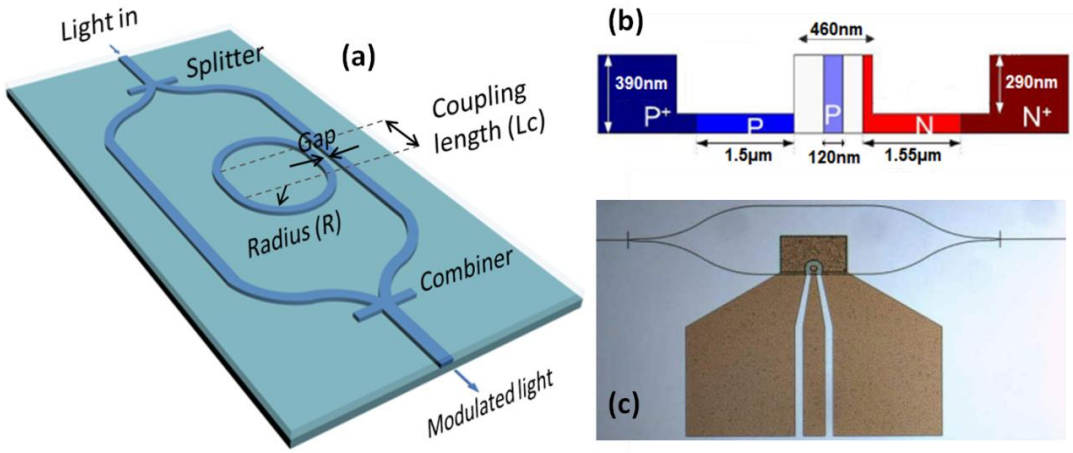

Figure 2-13: (a) Schematic of the fabricated ring-assisted MZI modulator, (b) cross section of the device active region, (c) top view of fabricated modulator.

The fact that the MRR does not need to be operated at the critical coupling factor (which we have already explained in the previous point) implies that modulator robustness against fabrication deviations could be significantly improved with respect to standalone MRR based intensity modulators. Fabrication deviations could lead to both variations on the MRR losses as well as variations in the designed separation between the waveguide and the MRR and therefore in the power coupling factor. Figure 2-14 shows the theoretical ER as a function of the coupling factor and the ring losses for the standalone MRR based intensity modulator and taking into account different effective index variations. The MRR radius is 40µm. The same plot is shown in Figure 2-15 for the RAMZI modulator. IL, i.e. losses at on-state, are lower than 5dB in the values shown in Figures 2-14 and 2-15. Results in such figures were calculated by using the transmission Equation (2.10) of the ring resonator.

Comparing the results shown in Figure 2-14 and 2-15 the enhanced performance achieved by the RAMZI modulator can be clearly seen. High ER values in the standalone MRR modulator are only achieved when there is a correspondence between the MRR losses and the coupling factor, i.e. the critical coupling condition, and therefore undesired variations in the MRR losses or coupling factor significantly

degrade the ER even though the effective index variation is increased. The ER in the RAMZI modulator is much less sensitive to variations in losses and coupling factor and is always improved for coupling values above the critical coupling condition when the effective index variation increases.

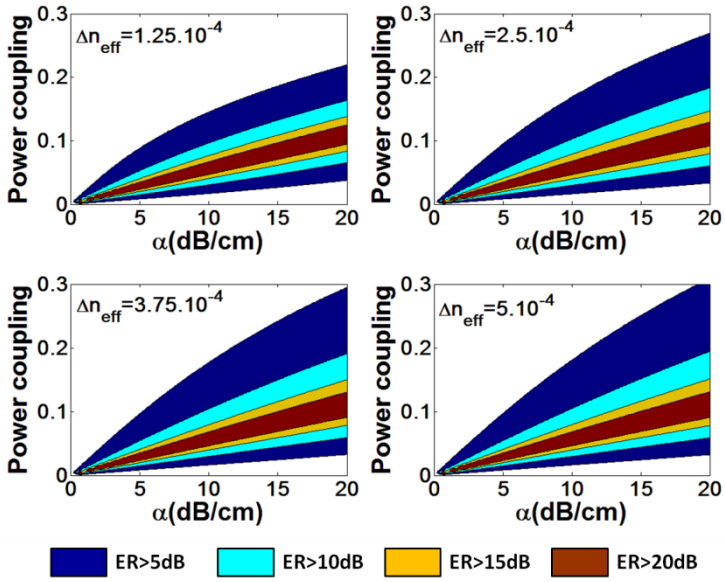

Figure 2-14: Theoretical ER as a function of the coupling factor and the ring losses for the MRR based intensity modulator for different effective index variation. IL are lower than 5dB for the values shown, where the ER is higher than 5dB (dark blue), 10dB (light blue), 15dB (yellow) and 20dB (brown).

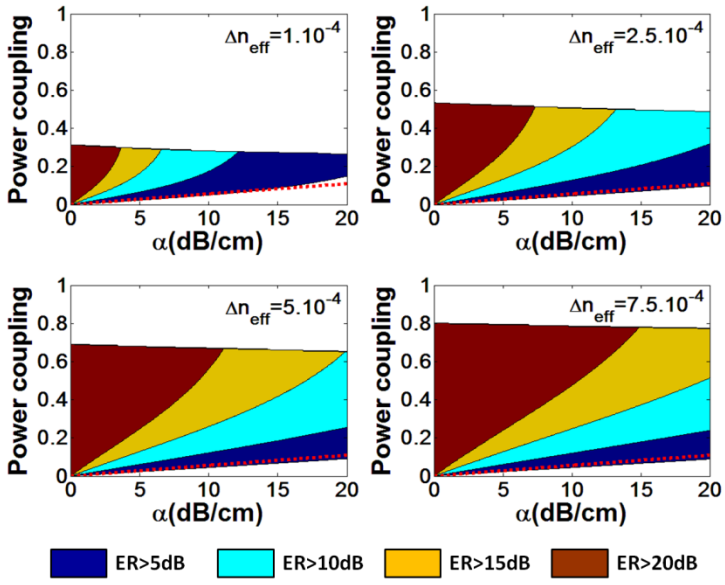

Figure 2-15: Theoretical ER as a function of the coupling factor and the ring losses for the RAMZI modulator for different effective index variation. IL are lower than 5dB in the values shown, where the ER is higher than 5dB (dark blue), 10dB (light blue), 15dB (yellow) and 20dB (brown). The dotted red line shows the critical coupling condition.

Furthermore, it should be remarked that the ER could also be improved by conveniently adjusting the splitting ratio of the couplers in the MZI to counteract the power unbalance between arms (as it will be shown in section 2.3.4.1). On the other hand, the main contribution to the IL in the RAMZI modulator is the insufficient phase shift rather than the power unbalance between the MZI arms. A similar performance is achieved for both modulators when the MRR radius is modified.

The fabricated RAMZI modulator has a 1µm coupling length and 150nm waveguide to MRR separation dimensions. The power coupling factor has been calculated to lie around 0.3 for such coupling length and waveguide to MRR separation based on 2D-FDTD simulations and the effective index method. Such value has been chosen as a trade-off between large robustness and high extinction ratio-low IL performance.

The RAMZI modulator was characterized under passive (details of horizontal coupling in Appendix A), DC and high speed regimes. DC measurements for varying reverse applied voltages were realized to estimate the DC ER as well as the modulation efficiency, which was deduced from the spectral shift of the modulation response, while high speed tests were carried out to evaluate the radio-frequency RAMZI modulator performance.

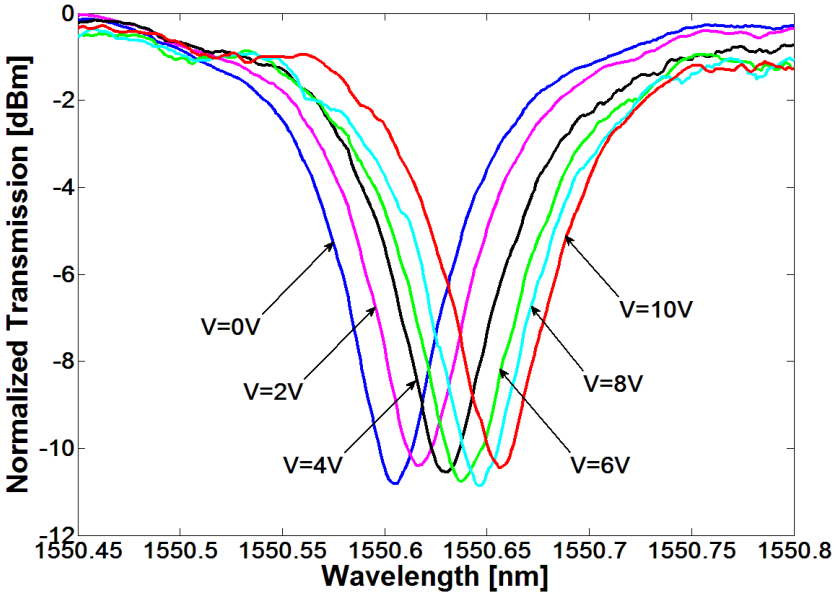

Figure 2-16: Transmission spectrum of the RAMZI modulator as a function of the wavelength for different applied bias.

The spectrum of the RAMZI exhibits a FSR of 2.4nm and a 10dB drop in transmission at the resonant wavelength around 1550.6nm. Figure 2-16 shows the RAMZI transmission spectrum for varying bias voltages. The voltage-induced wavelength shift ($\Delta\lambda$) in the RAMZI modulator output spectrum can be used to extract the effective index variations (Δn_{eff}) using the Equation (2.24) with L_A=208µm ($<L_{MRR}$=253µm). Figure 2-17(a) depicts the deduced effective index variations as a function of applied bias voltage. The $V_\pi L_\pi$ product has also been calculated from such effective index variations through Equation (2.25). Its evolution as a function of the

applied voltage is shown in Figure 2-17(b). Nearly constant $V_\pi L_\pi$ around 4.3V.cm for reverse bias voltages ranging from 2V to 10V is found.

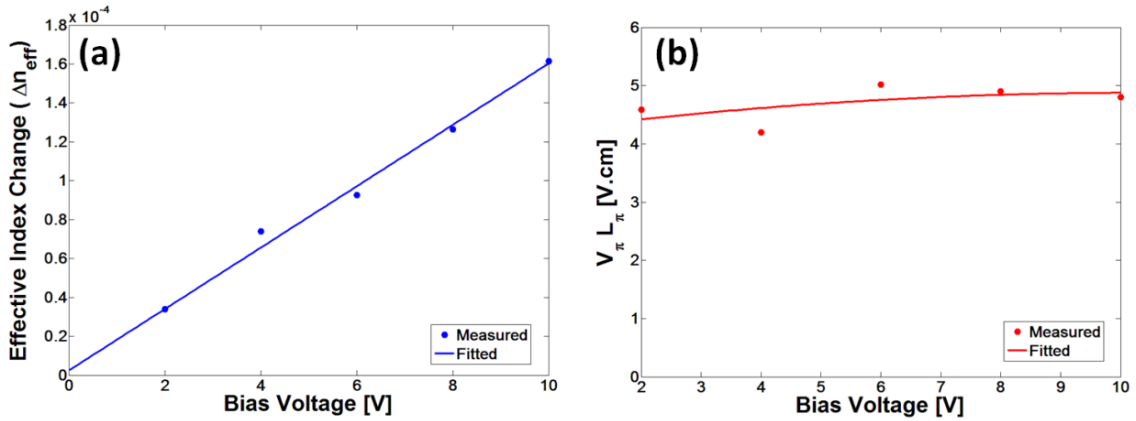

Figure 2-17: (a) Modulation efficiency as a function of applied bias voltage and (b) Effective index variation as a function of applied bias voltage.

Additionally, to deepen our DC analysis depicted in Figure 2.16, we have compared experimental and simulated ER and IL under an 8V reverse bias voltage. Figure 2-18 shows the obtained results. Experimental results are in good agreement with our theoretical ones assuming ring losses of 20dB/cm, the simulated coupling factor and the effective index change ($\Delta n_{eff}=1.25.10^{-4}$) for 8V reverse bias voltage depicted in Figure 2-17(a). Hence, an ER of approximately 7dB with IL below 4.5dB is achieved in our device. Higher ER values would be achieved by lowering ring losses or increasing the effective index change.

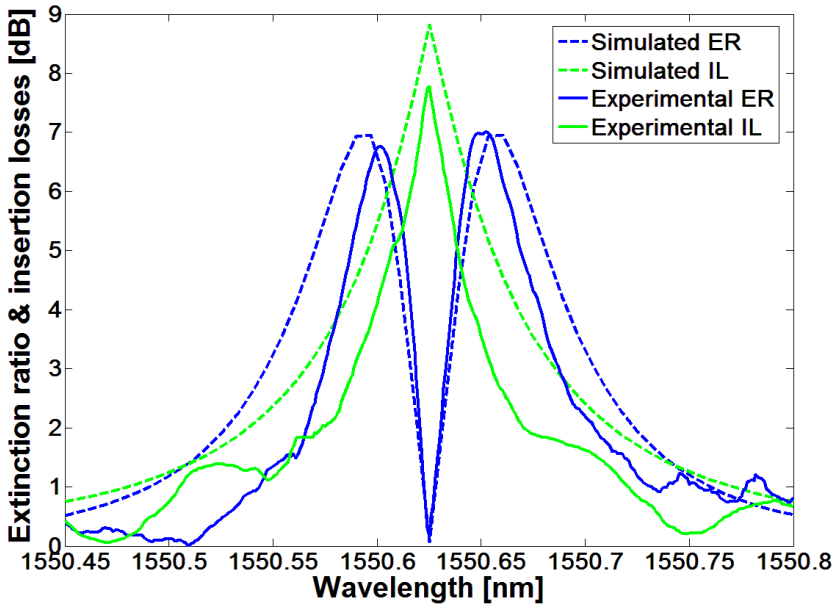

Figure 2-18: Simulated and experimental RAMZI ER and IL versus wavelength under an applied voltage of 8V.

The high speed performance of the RAMZI modulator has been characterized by measuring both its 3dB frequency roll-off and data transmission capability. Figure 2-19 shows the experimental set-up for measuring the high speed optical frequency response.

Light is coupled from an ECL to the chip via a lensed fiber after polarization control. The small electrical signal delivered by the RF port 1 of the vectorial network analyzer (VNA) is coupled a -4V DC bias via a bias-Tee and applied to the lumped electrodes through high speed GSG probes to the RAMZI modulator. The output modulated signal is amplified with an EDFA and photo-detected by a photodiode connected to the port 2 of the VNA in order to extract the electro-optical S_{21} transfer function. Details of model equipments and pictures of the real set-up are given in section 2.4.

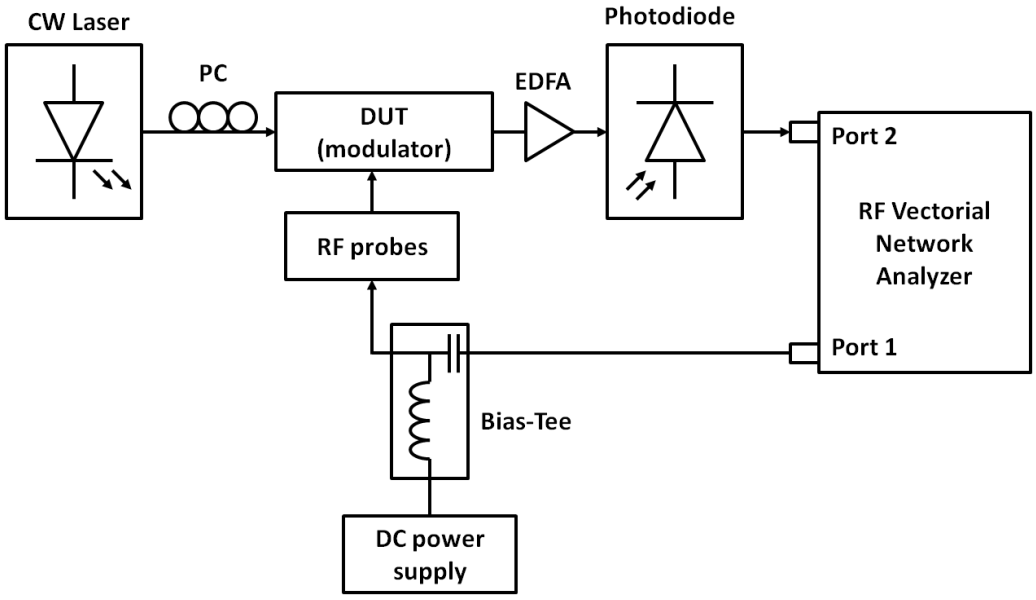

Figure 2-19: Experimental setup for measuring the high speed optical frequency response of the RAMZI modulator.

The resulting data is given in Figure 2-20, which shows that the RAMZI modulator has a 3-dB roll-off frequency as high as 19GHz so the fabricated device displays a promising figure in terms of frequency of operation.

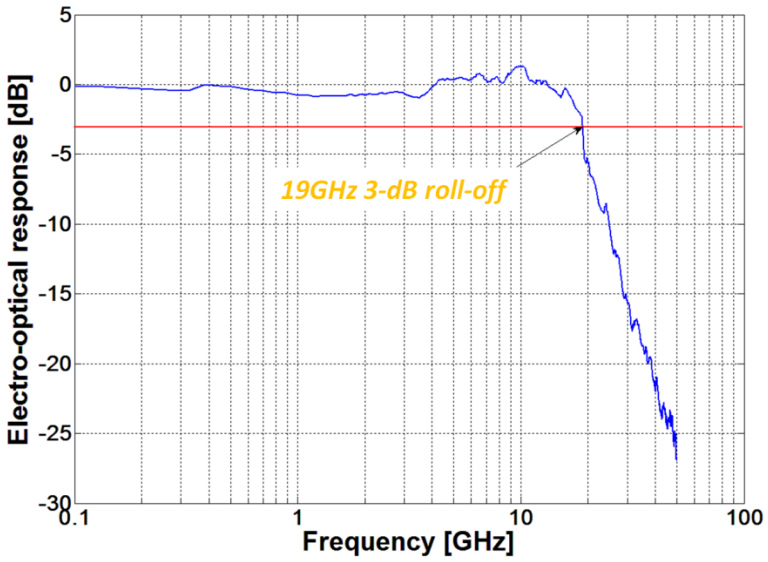

Figure 2-20: Electro-optical response of the RAMZI modulator. It is show a 3dB roll-off frequency of 19GHz.

It should be noticed that over-coupling the MRR makes the modulator faster when cavity photon lifetime is the limiting factor of the modulation speed. In our case, the cavity photon lifetime is around 15ps and the measured 3-dB modulation bandwidth is 19GHz, which are in good agreement with the theoretical results reported in [BEA10].

To characterize the high speed data transmission performance, the RAMZI modulator was driven in a lumped configuration in the same way than the MRR modulator (set-up in Figure 2-9). A -4V DC bias was applied to the modulator to ensure reverse bias operation over the entire voltage swing. Figure 2-21 shows the obtained eye diagrams. The ER is 6.7dB at a bit rate of 10Gbit/s and 2.6dB at 20Gbit/s. IL at on-state, which include losses at the input/output couplers and propagation losses outside the MRR, are around 6dB. Despite the lower ER at 20 Gbits/s, which is attributed to the limited bandwidth (12GHz) of our driver amplifier, the 3-dB roll-off frequency of 19GHz shown in Figure 2-20, indicates that our modulator is capable of transmitting data above 20Gbits/s.

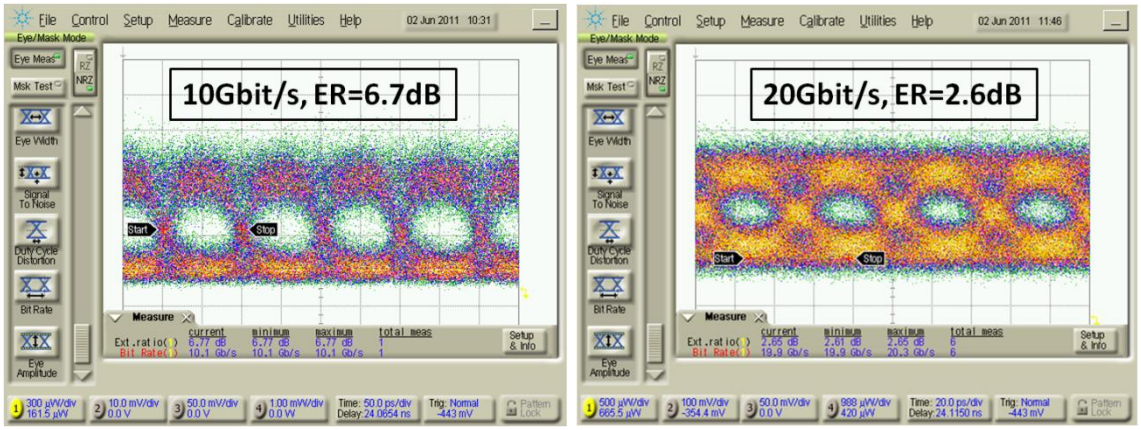

Figure 2-21: Eye diagram of the RAMZI modulator with an ER of 6.7dB at 10Gbit/s and 2.6dB at 20Gbit/s.

Overall, we have reported a high speed silicon RAMZI modulator fabricated with a standard CMOS-compatible process. The RAMZI modulator features the potential for high speed performance and higher robustness against fabrication deviations than its standalone MRR based intensity modulator counterpart as the MRR does not require being at the critical coupling operation point to achieve enhanced performance in terms of ER and IL. In our device, modulation is achieved by carrier depletion in a *PIPIN* diode structure over a RF/optical interaction length of only ~200µm featuring a 3-dB electro-optical bandwidth as high as 19GHz and a data transmission rate up to 20Gbit/s.

2.3. Slow-wave structures

This section is devoted to the description of the slow-light phenomenon and the justification of slow-light structures capability for enhancing electro-optical modulation based on the plasma dispersion effect in silicon-based modulators due to its unique feature of increasing the linear interaction between charges carriers and the optical mode. This ability allows for more compact and less power consuming electro-optic modulators. So, the main characteristic of such structures is their capability to decrease the group velocity of the propagating wave strengthening the interaction between the optical mode and the depleted, injected, or accumulated charge carriers. This can leads to a significant reduction of the interaction length and hence allows for device shrinking down to a few hundred microns. The choice of corrugated waveguides for slow light enhancement among others architectures is justified by the following points:

- Standard CMOS compatible process fabrication.
- Squared geometry as for conventional SOI rib waveguides.
- Impedance mismatch between rib and slow mode can be compensated by convenient linear tapering of the structure [POV05].
- High dispersion due to the slow mode can be compensated by combining slow and fast light sections.
- High bandwidth achievable for 40 Gbits/s modulation [GAR08].
- High overlap achievable between charge carriers and the optical mode due to high mode confinement.

So, the chapter is structured as follows. First of all, a review of state-of-the art of modulators based on slow-wave structures is provided. Second, the basic theory of the slow-light effect is briefly introduced as well as the basic design procedure of the slow-wave waveguide used latter for the experimental modulators. The proposed slow-wave corrugated waveguide was originally proposed in [BRI11B] for enhancing modulation and this point is a simple summary of the design procedure followed in such work. The next point is devoted to the characterization of two silicon-based slow-light Mach-Zehnder Interferometer (SL-MZI) modulators, one showing a high speed of 40Gbit/s [BRI12B] and the other a low-drive voltage operation [BRI12A].

Finally a method for measuring the propagation losses, since it is one of the main drawbacks derived by the use of the slow-light structures, is developed. Such method is proposed and demonstrated experimentally to be independent of the fiber-waveguide coupling losses, so that identical coupling conditions for each measurement were not required. The method is based on the analysis of the transmission spectra of asymmetric MZIs, which enables the calculation of the propagation losses as well as the power imbalance of the branching structure of a MZI. The main contribution of the author is the proposed method for measuring the propagation losses, which was originally proposed and developed for conventional rib waveguides [GUT12B] and then it was extended for corrugated waveguides [BRI12A] in collaboration with A. Brimont.

2.3.1. Introduction: state-of-art

The ability to slow-down the velocity of light has been foreseen as a very useful mechanism for enhancing performances in numerous applications ranging from telecom and datacom to sensing via enlarged light–matter interactions [KRA08, BAB08, BOY09]. In particular, slow-light achieved by means of nanostructured periodic waveguides has been demonstrated as an effective mechanism for pushing forward the limits mentioned in the introduction of this chapter of free-carrier-based electro-optical phenomena in silicon.

The first silicon electro-optical modulator based on photonic crystals (PhCs) was demonstrated in 2005 [JIA05] and showed low speed operation (300KHz) under a drive voltage of 7.5mV and for an active length of 80µm. The modulation was achieved via free holes injected through a *PIP* diode integrated into a MZI. Two years later, the same group followed up on these results [GU07] and reported high-speed operation using a PhC-based MZI having similar dimensions. The active element is made up of a *PIN* diode in one arm of a MZI. The authors reported a modulation bit rate of 1Gbit/s with ER of ~3dB. Another PhC-based modulator embedded in a capacitor was also demonstrated [CHE09]. The device features a figure of merit of 0.18V.cm, which means that for a 6V applied voltage, a π-phase shift is achieved over a length of 300µm. This reduced interaction length is approximately one order of magnitude lower than for conventional rib waveguide MOS and depletion modulators. The modulator was driven at 1.6Gbits/s with 3dB ER and with n_g~50. In 2011, pre-emphasized 10Gbits/s operation with 7.2 dB ER in a 200 µm-long PhC modulator embedded in *PN* junction has been reported [NGU11] in spite of a 3dB roll-off frequency of 3GHz. The device feature modulation efficiencies of $V_\pi L_\pi$~0.056V.cm and 0.016V.cm when respectively operated in both depletion and injection regimes and only in the injection regime at a group index of ~18. In 2012, the same authors reported the demonstration of 40 Gbit/s modulation in a sub-100µm MZI with an acceptable drive voltage of $5.3V_{pp}$ [NGU12B]. Meanwhile, researches of this group, with a high experience in slow-light phenomenon [BRI09, BRI10], demonstrated the first carrier depletion-based slow- wave modulator as a means to enhance the modulation efficiency [BRI11A] The device is based on a 500 µm long periodic laterally corrugated waveguide (LCWG) embedded in a self aligned *PN* junction [THO10]. It combines the attractive properties of slow-light propagation in a nanostructured periodic waveguide together with a high speed semiconductor *PN* diode, and exhibits error free modulation up to 20 Gbit/s with 6.3dB ER at group index of n_g~11. The longer phase shifter features 10Gbit/s error free operation with 9.5dB ER at the same group index. These results are supported by modulation rate capabilities reaching 40 Gbit/s (ER~3dB). Modulation efficiencies are $V_\pi L_\pi$ ~1.27V.cm is obtained for a group index of 11 and as low as ~0.45V.cm when the group index increases up to ~22, which is respectively 2 and 5 times greater than in a 400nm reference rib waveguide modulation. The following Table 2-3 summarizes the all these results of the slow-wave modulators reported.

[ref]	Electrical structure	VπLπ [V.cm]	Data rate [Gbit/s]	Drive Voltage/V_{pp} [V]	Dyn.ER [dB]	Length [µm]
[JIA05]	PIP injection	-	300KHz	7.5mV	6.9	80
[GU07]	PIN injection	-	1	3	3	80
[CHE09]	PCP Accumulation(*)	0.18	1.6	6	3	300
[NGU11]	PN depletion	0.016	10	4	7.2	200
[NGU12B]	PN depletion	-	40	5.3	-	90
[BRI11A]	PN depletion	0.45	40/20	5	3/6.3	500

Table 2-3: State-of-art of silicon-based slow-wave electro-optic modulators, (*) Lateral capacitor-embedded PhC. The waveguide comprises a p-type doped silicon PhC slab with a center slot working as the vertical gate oxide.

As we has commented in the Introduction chapter, in the SOI technology the high refractive index contrast between silicon (n=3.5) and silica (n=1.45) enables the realization of integrated waveguides with submicron cross-sections. The extreme light confinement in SOI optical waveguides paved the way toward the realization of ultra-dense photonic integrated circuits on a single silicon chip but may result in higher propagation losses due to the increased interaction of the optical mode with sidewall roughness [LEE00]. This issue is, in fact, the main limitation of slow-wave based devices as increasing the group index and therefore decreasing the group velocity will lead to higher losses.

From 1980 to 1990 these were usually high; about 5-20dB/cm [SOR86], based on ridge waveguides modulators, and have been reduced to less than 1dB/cm [GAR05] based on buried waveguides modulators after 2000. Because high losses are prohibited for the majority of applications, smoothing techniques have been successfully developed to reduce light scattering [LEE01]. During years, numerous methods have been developed to estimate this critical parameter. Some of them, such as the two-prism and three-prism methods [WEB73, WON80, OKA83], consist in measuring the light scattered above the waveguide under study. The advantage of these techniques is that no constant coupling conditions are required. However, the quality of the wafer surface is crucial, which limits therefore the measurement accuracy. Other methods are based on measuring the absorbed optical power [TIT93], but in this case, the coupling efficiency is critical. Moreover, the well-known cut-back method, which is based on a comparison of the transmission through waveguides of different lengths, has been widely employed owing to its ease of use. However, it requires identical coupling conditions, which is difficult to achieve in practice [VLA04, REE92]. As an alternative, the Fabry–Perot method and modified versions have been proposed to estimate the propagation losses independently of the coupling losses. Nevertheless, this method is based on the use of reflective facets, which are avoided in practical devices where high efficiency coupling techniques are precisely used to reduce the facet reflections and improve coupling [REG85, ROE11].

2.3.2. Theory of slow-wave effect

The slow wave phenomenon has attracted numerous researchers in the last few years due to the deeper control on light it offers. The following equation, which was derived in [SOL02], depicts the required length to achieve a π-phase shift.

$$\frac{L}{\lambda} \approx \frac{1}{2\sigma}\left(\frac{n}{\delta n}\right)\left(\frac{v_g}{c}\right) \tag{2.26}$$

This equation shows that for a given perturbation of the refractive index (δn) the size of the device scales linearly with the group velocity of light (v_g). The group velocity of light, defined by $v_g=c/n_g$, where n_g is the group index, provides an estimation on how much the group velocity of a wavepacket propagating through a dispersive material is reduced compared to the speed of light in a vacuum c. Another important parameter is the overlap factor (σ) which stands for the fraction of the total energy of the mode that is stored in the region where is being applied. Therefore, for instance, for $\delta n=10^{-3}$, n=3.47 and λ=1550nm, size device can be decreased below 100μm if group velocities lower than 0.04c (n_g=25) can be achieved and σ=1.

2.3.2.1. Basic concepts of slow-light effect

Following, we are going to define some basic concepts which are necessary to know and understand the slow-light effect:

- Bands diagram: The structures are characterized by periodic bands diagram (or dispersion relation) which is a 2D or 3D representation of the relationship between the frequency (normalized units ωΛ/2πc being 'Λ' period) and the wave vector (k normalized units/π). Another typical definition of the bands diagram is a representation of the frequency or energy of the allowed modes in a periodic structure as a function of wave vector.

- Photonic Band-Gap (FBG): ranges of frequencies or energies for which there is no propagation mode (the light does not propagate) independently of the incidence direction, that is, regardless of the wave vector. Higher index contrasts provide wider band-gaps. Outside the band-gaps, the periodic stack supports truly-propagative modes with a real propagation constant (k_z is real).

- Bloch modes: periodic structures allow the existence of propagating electromagnetic modes: lossless, Bloch waves shaped and displayable on a band diagram. So, a Bloch mode is an allowed propagating mode.

- Brillouin Zone: The importance of the Brillouin zone stems from the Bloch wave description of waves in a periodic medium, in which it is found that the solutions can be completely characterized by their behaviour in a single

Brillouin zone. So, due to the periodicity of the structure, the band diagram is repeated with a period $G_z=2\pi/\Lambda$, therefore, it suffices to represent the wave vectors in the space $-G_z/2<k<G_z/2$ $(-\pi/\Lambda<k<\pi/\Lambda)$ and this region is called Brillouin zone.

2.3.2.2. Basic operation principle of slow-light effect

Once established the theoretical basis, we already are able to explain the basic operation of the slow light effect. The form in which SOI technology produces slow light "on-chip" is via the use of in 1, 2 or even 3 dimensional periodic structures, where the dielectric periodicity is usually achieved via ordered nano-structuring [VLA05]. Indeed, slow-wave structures, due to their periodic nature, present the great advantage of slowing down the propagation of light. So, incorporating these slow-wave structures in optical modulators can provide advantages in the reduced length of the device as well as in the power consumption, all this determined by such reduction in the group velocity. The period, size and shape of the repeated pattern of such periodic nano-structure define the frequency at which the speed of light theoretically drops inside the waveguide, thus providing complete liberty for the designer. The nature of slow light, which consists in the coupling in phase and amplitude between successive back and forth reflections experienced by the propagating wave at each unit cell, can intuitively be described with the ray optics theory in mind. Here, we focus on a 1 dimensional (1D) laterally corrugated periodic structure (LCWG), although the slow wave propagation principle remains the same for the other types of PhCs. A typical band diagram of a deep-etched 1D LCWG is depicted in Figure 2-22(a). There are two slow light propagation mechanisms: by omnidirectional reflection or backscattering. Here, we are interested in the last mechanism which is produced in the band edge ($k=0.5*2\pi/\Lambda$, $\Lambda\approx\lambda/2$).

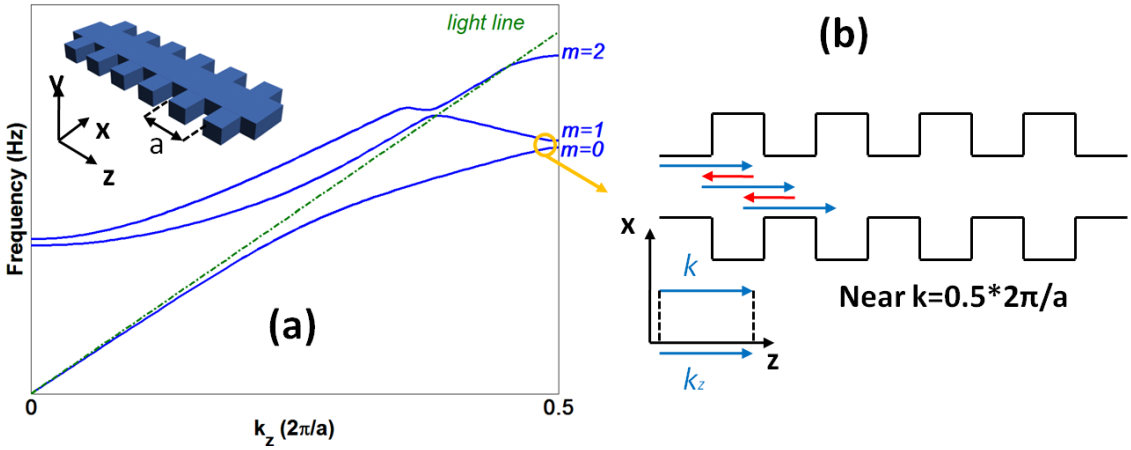

Figure 2-22: (a) Band diagram of a 1D laterally corrugated waveguide. The blue solid lines represent the first three modes of the optical structure of which only those located below the light line (green dashed) propagate through the optical structure theoretically without losses, (b) Slow light propagation by backscattering [BRI11B].

Light propagating at parallel incidence (that is, $k_z=0.5*2\pi/\Lambda$) experiences multiple reflections at each unit cell due to the periodic grating. The coherent interaction in phase and amplitude between the forward and backscattered propagating modes forms a standing wave with zero group velocity. When light propagates at nearly parallel incidence, i.e. within the vicinity of the Brillouin zone edge, that is within the vicinity of the Brillouin zone edge, the forward and backward travelling components still interact but slightly out of phase, giving rise to a slowly forward moving interference pattern: a slow mode. This may be pictured as a three steps forward and two steps backward motion as illustrated in Figure 2-22(b). As one moves further away from the Brillouin zone the forward and backward travelling components are almost completely out of phase and total internal reflection becomes the dominant propagation mechanisms as in straight waveguides with regular group velocity.

From such physical insight, one may think that slow light occurs only at the edge of the Brillouin zone in a reduced bandwidth which is one of the two main drawbacks associated to the slow-light effect. However, recent works on 2D PhCs with line defect, that is a 2D PhCs with a single line of missing hole, [FRAN06, KUB07, SET07] refuted this hypothesis showing that slow light may also be achieved inside the Brillouin zone over a wide bandwidth by increasing the coupling between modes of different orders naturally interacting with each other. These so-called engineered PhCs are of great interest for electro-optic modulation applications owing to their artificially increased optical bandwidth.

The possibility of obtaining low group velocity values is one of the most attractive features of the structures possessing periodicity in the propagation direction. A direct application of this low group velocity is the possibility to create compact delay lines, which is a fundamental element to the creation of more complex optical devices. Besides the increasing delay experienced by the signal when propagates through the structure, the reduction in the group velocity of the guided mode also causes a high interaction between the electromagnetic energy of the guided mode and the structure itself. Such increased field-material interaction will increase the efficiency of any effect in the structure, either as the positive character as the non-linear effects in the material, amplification, phase changes, etc., or negative as the structure heating, absorption material, losses due to sidewall roughness, etc. So, other of the most important negative effects derived by the use of slow-light structures is the associated propagation losses due to roughness and positional disorder when the group velocity of the guided mode is low. Despite the great advance in the last years of the integrated photonic devices fabrication processes, there is a limitation in the minimum achievable roughness. Such roughness is mainly responsible for the propagation losses in the photonic structures. For the case of slow-wave structures, losses will also be influenced by the low group velocity. In this case there will also be a greater interaction between the guided mode and fabrication deviations. It is clear that, to reduce propagation losses will be necessary to perform a high accuracy fabrication process with the aim of decreasing the imperfections created in the sidewall waveguide. One way to achieve greater precision

in the manufacturing will be using the simplest possible designs in which the limitations of the available fabrication process are not as critical.

In summary, both PhCs and LCWGs are subject to optical propagation losses usually inherent to the fabrication deviations (roughness, disorder...) and specific waveguide geometry. In the fast light regime, state of the art devices were reported to feature propagation losses as low as 4.1±0.9dB/cm [FAO06] and 0.92±0.14dB/cm [GNA08] for PhCs and 1D deep-etched LCWG, respectively. Still, some doubts about the loss dependency against group velocity subsist when entering in the slow light regime. Some authors have suggested that the propagation losses have a proportional relation with $(1/v_g)$ in the case of PhCs [KUR05]. However, other studies conclude that this relationship is not so simple and losses are scaled approximately by a factor $(1/v_g)^2$ [HUH05] near the band edge, that is, for very low group velocity (i.e. below c/100). And even further studies indicate that these losses are proportional to $(1/v_g)^{1/2}$ [FAO07]. Interestingly, the need for such very low group velocity is not mandatory required for modulation applications due the trade-off arising between useful optical bandwidth (i.e. the wavelength/frequency interval where the expected performance of the device is maintained), loss and low group velocity. Namely, the group velocity dependence upon frequency usually features a steep slope limiting the useful operating bandwidth. For lower group velocities, i.e. as we move closer to the band edge, this restriction becomes more severe, which clearly impairs potential applications.

2.3.2.3. Corrugated slow-light waveguide design

This point reports on the designing of 1D slow-wave LCWG for electro-optical modulation enhancement. As already commented in the introduction of this section, the original LCWG was proposed and designed in the context of [BRI11B] and here we only show a summary of the design results. Such LCWG considered in this thesis to demonstrate high speed and low-drive voltage electro-optic modulation is shown in the Figure 2-23. It is shallow-etched waveguide which consists on an etched silicon epilayer of height H and a slab (which corresponds to the remaining silicon layer) of height h, forming an alternation of narrow and wide sections of respective widths *W* and *We*, repeated over a period Λ. This periodical repetition of the identical transversal corrugations gives rise to slow light propagation in form of Bloch modes at the edge of the Brillouin zone and hence a PBG (range of frequencies where light propagation is not allowed). Depending on such transversal elements dimensions (W, W_i, W_e), the bands are flattened or elevated and the band-gap becomes wider or narrower. Obviously, a flat band is required since the flatter the band, the lower the group velocity. On the other hand, a very low group velocity can lead to undesirable effects such as high losses as discussed in the previous point. Concerning the band gap, though this is not of a vital importance here, the wider the band gap is, the less sensitive the device is to fabrication variation and the more likely the device is to be single mode. Therefore, a trade-off has to be found to take advantage of the corrugated waveguides smart properties while the

undesired effects above mentioned are eliminated or at least reduced. It must be stated here that, the reason for using a shallow-etched version of the LCWG instead the deep-etched one (without silicon slab) is because silicon modulators require contacting regions located on both side of the waveguide to allow contact with the electrodes to electrically tune the refractive index.

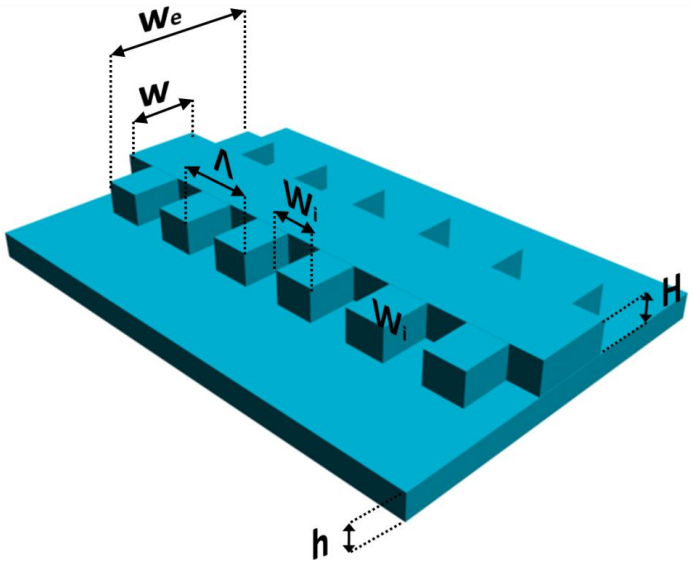

Figure 2-23: Schematic of the shallow-etched LCWG with slab height (h) considered in this thesis to enhanced modulation [BRI11B].

As previously seen, enabling light to propagate with slow group velocity in the form of Bloch modes is a matter of inducing multiple reflections inside any periodically patterned waveguide. Thereby, the wide variety of architectures potentially available should be only limited by the technological constraints, i.e. the resolution of the lithography process. In this way, the choice of the waveguide parameters relies mainly on the critical dimensions (CD), that is, the minimum dimensions that may be resolved by the lithography process. Since these LCWGs are expected to be fabricated with deep-UV lithography process, the corrugations dimensions must be selected with CD of about 100nm in order to address the fabrications issues. Then, this CD sets a lower limit on the minimum dimension of the corrugated slow-wave waveguide.

The design method is then to set the period (Λ) of the transversal corrugations and varying W_e and W dimensions of these elements with the aim of matching the slow wave region wavelengths around 1.55μm. For such task, the Bragg condition is used. So, we need to estimate the period at which the Bragg condition is satisfied. This condition, for the corrugated waveguide under study, is defined by:

$$\Lambda = \mathrm{m}\frac{\lambda_{Bragg}}{(n_{eff,W} + n_{eff,W_e})} \tag{2.27}$$

Where Λ is the Bragg grating period, $n_{eff,We}$ and $n_{eff,W}$ the effective index of the optical mode propagating into the wide (W_e) and narrow sections (W), m the mode order and

λ_{Bragg} is the Bragg wavelength which, in our case, must be equal to 1.55µm. So, taking into account this equation the Bragg grating period and therefore the repetition period of the transversal corrugations in the slow-light waveguides can be obtained.

In the other hand, the corrugated waveguide dimensioning consists on performing a scanning of both the width (W_e) and the length (W_i) parameters which completely define the transversal elements size. For such calculations, the band diagram is elaborated for each combination of these parameters through the BANDSOLVE™ software package from RSOFT™ [RSO00]. Both parameters values are chosen, as commented at the beginning of this point, as a function of the fabrication capabilities, taking into account the maximum resolution in the lithography process (deep-UV in this case). So, considering that the period is fixed to be 310nm, then they are to be varied over a certain range, which boundaries are mainly delimited by the seeming fabrication constraints the minimum separation (Λ-W_i) between two consecutive transversal elements should be 100 nm as well as the minimum length W_i should not be lower than 100nm. In addition, the distance between the thin and wide waveguide edges should be as large as possible to minimize proximity effects (which occur when the pattern of an illuminated structure interfere constructively of destructively with that of neighbouring elements, modifying therefore its size) while maintaining the waveguide operation around 1.55µm wavelength. In order to work out the Bragg wavelength λ_{Bragg}, i.e. the wavelength at which multiple back and forth reflections start taking place into the periodic waveguide, a 2D scan was performed over the range W_i=[150-200nm] and W_e=[500-800nm]. The Bragg wavelength corresponds to the photonic band edge operating point, that is, when the group velocity of the propagating wave theoretically vanishes. The calculation results for the fundamental mode, depicted in the next Figure 2-24, offer a set of parameter combinations (W_i, W_e) for which the waveguide exhibits slow-light behaviour around 1.55µm.

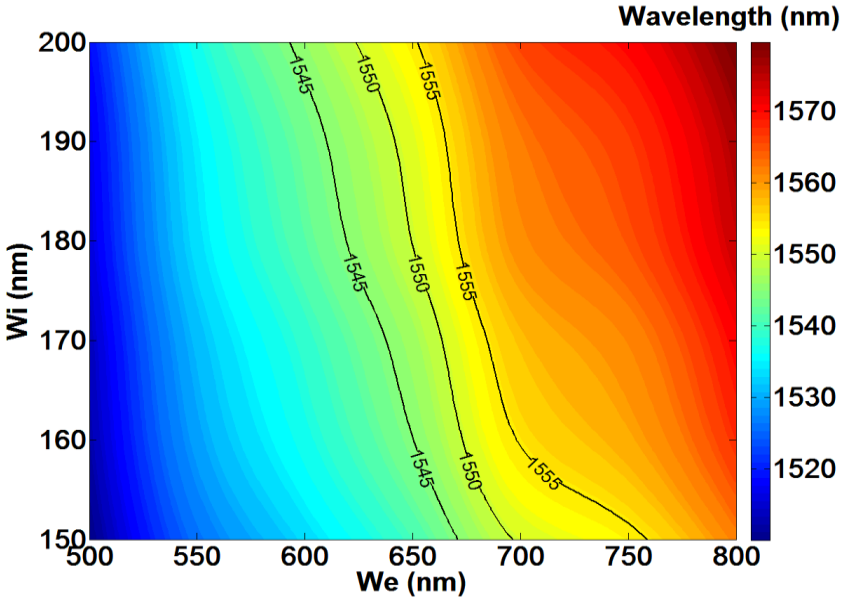

Figure 2-24: Contour plot of the Bragg wavelength @ the photonic band edge versus width (W_e) and length (W_i) of the transversal corrugations for the fundamental mode of with Λ=300nm, W=300nm and h=100nm [BRI11B].

The interesting result here is that the wavelength-sensitivity of the waveguide to W_e or W_i depends on the size of these parameters. As a matter of fact, for large W_i values, (top-middle of Figure 2-24), the device becomes more wavelength-sensitive to W_e and vice-versa, for larger W_e (bottom-right of Figure 2-24) the device becomes more wavelength sensitive to W_i. Furthermore, increasing the value of one parameter implies decreasing the size of the other to maintain the slow wave propagation (at the band edge) at constant wavelength (along the 1550nm isoline). But the most interesting feature of such plot is that it gives the entire range of parameters (W_i, W_e) for which the edge of the band matches the wavelengths of interest (around 1550nm in our case), despite that it is impossible in practice for the fabricated waveguide to fit rigorously the design. This implies that the parameters (W_i, W_e) should be chosen along or nearly along the 1550nm isoline. In [BRI11B] one can find the more complete description of the overall design process.

Finally, taking into account everything mentioned along the point, the final passive structure, which is shown in the Figure 2-25, consists on a rib single mode waveguide of W=300nm x H=220nm with a thick slab of h=100nm with corrugated elements of W_e=650nm of width and W_i=100nm of length which are repeated periodically every Λ =310nm. These parameters are summarized in Table2-4 and are used in the slow-light silicon-based modulators demonstrated in the following section.

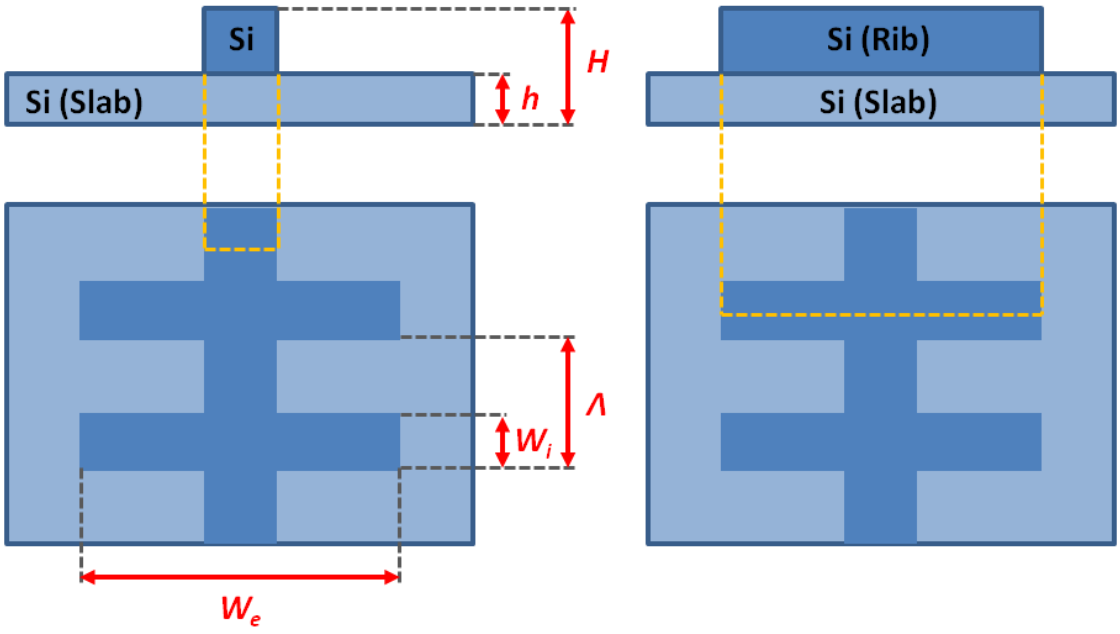

Figure 2-25: Corrugated waveguide design parameters

W (nm)	Wi (nm)	We (nm)	Λ (nm)	Slab height (nm)
300	100	650	310	100

Table 2-4: Summary of the final shallow-etched LCWGs parameters of the corrugated waveguide chosen for the slow-wave electro-optic modulator.

2.3.3. Experimental slow-light (SL-MZI) MZI modulators

In this point, we show highly efficient, compact, high-contrast and low-loss silicon slow-wave modulators carrier depletion based-MZIs. It must be pointed out here that the contribution of the author in this work consists on the collaboration in the experimental characterization together with A. Brimont [BRI11A, BRI11B].

On one hand, a high speed operation with high efficiency and ER at quadrature and with a relatively low on-chip IL is shown [BRI12B] enhancing previous results reported in [BR111A]. On the other hand, the use of slow-light is exploited to reduce the driving voltage [BRI12A]. So, we take advantage of the high modulation efficiency achievable in slow-light modulators in order to lower the drive voltage down to values that fulfil current CMOS requirements, again enhancing previous results reported in [BR111A].

Moreover the variation of the IL with a group index is also analyzed and discussed in other point dedicated entirely to present a method for calculating the propagation losses, first in MZIs with conventional rib waveguides [GUT12B] and second with corrugated one [BRI12A]. As a result, relatively compact single-drive phase shifters featuring low drive voltage, moderate IL, and high-speed performance are demonstrated assuring the benefits of slow-light as a means to enhance the performance of silicon modulators based on the plasma dispersion effect.

2.3.3.1. High-speed SL-MZI modulator

Figure 2-26(a) shows the schematic of the slow-wave modulator. Both arms of the MZI consist of two identical 500 μm long slow-wave phase shifters to balance the optical power and thus maximize the notch depth. An extra 900 μm long rib waveguide section has been added on one arm of the MZI to allow the operating point of the modulator to be precisely set.

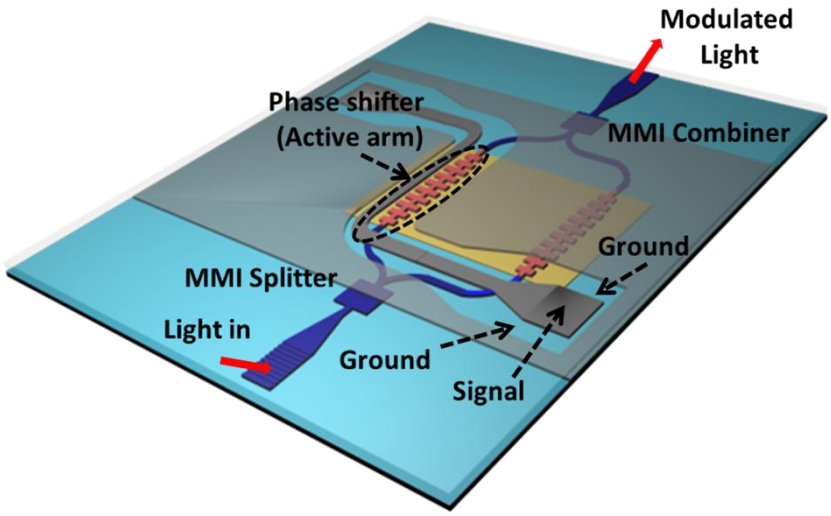

Figure 2-26: Schematic of the high-speed slow-wave modulator.

Optical phase modulation is achieved by depleting the majority carriers from a reverse-biased *PN* junction positioned in the middle of the waveguide and connected to highly doped p+ and n+ regions. As depicted in Figure 2-27(a), these are situated respectively at a distance of S_n=550nm and S_p=500nm from the edge of the narrow waveguide section and metalized with compound AlCu electrodes as shown in Figures 2-27(b) and 2-27(c). Net doping concentrations in the p- and n- type regions reached respectively $4.10^{17}cm^{-3}$ and $5.10^{17}cm^{-3}$. Highly p+ and n+ doped regions were implanted, both at a concentration of $1.10^{20}cm^{-3}$.

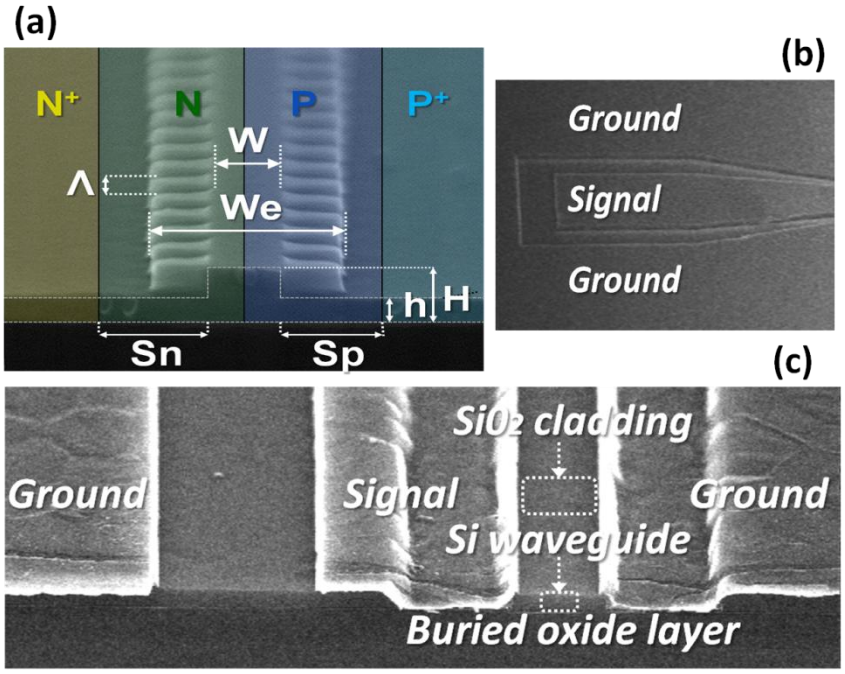

Figure 2-27: Scanning electron microscope images of (a) the corrugated waveguide, (b) the contacting AlCu pads and (c) the travelling wave coplanar electrodes.

To assess the performance of the slow-light modulator, a careful DC characterization process was carried out. Figure 2-28(a) shows the optical spectra of both the MZI modulator and the corresponding 500µm long phase shifter. Both spectra were normalized with a straight waveguide of identical length containing the same number of bends and tapers. As it can be observed on the right of the Figure 2-28(a), the loss of the single slow-light phase shifter in the fast light region (n_g~4.4) lies around 1.5dB and gradually increases as we move toward the slow-light region. Because the group index dependence cannot be directly extracted from the interference fringes of this MZI because both arms contain identical phase shifters, an asymmetric version was simultaneously characterized so the group index could be extracted from the FSR variations across wavelength [BRI11A].

Figure 2-28(b) depicts a close-up portion of the slow-light region (n_g~8) of the MZI modulator under reverse bias voltages varying between 0V, −3V, and −5V. The maximum transmission of the MZI is situated around −6 dB at 0 V, corresponding to a net on-chip loss of 6dB, from which 5dB arise from the slow-wave phase shifter

(coupling loss and propagation loss included) and 1 dB is due to the tapered multimode interference (MMI) structures (0.5dB/MMI). As can be observed, a DC ER (referred to as ER in Figure 2-28(b)) of around 7dB may be achieved at the quadrature point, designated "A" and located at 1547.7nm wavelength. At this point, the maximum transmission is situated at −9dB, which means that the IL penalty at the "1 1evel" is 9dB, including the 1dB loss arising from the two MMIs. The latter is extracted from the difference between the two curves shown in Figure 2-28(a). With an additional loss penalty of 2dB (point "B"), leading to an overall IL of 11dB, the ER increases up to ~11dB. Additionally, the effective index change as a function of the applied reverse was determined experimentally and supported by numerical calculations based on Soref and Bennett's empirical equations [SOR87].

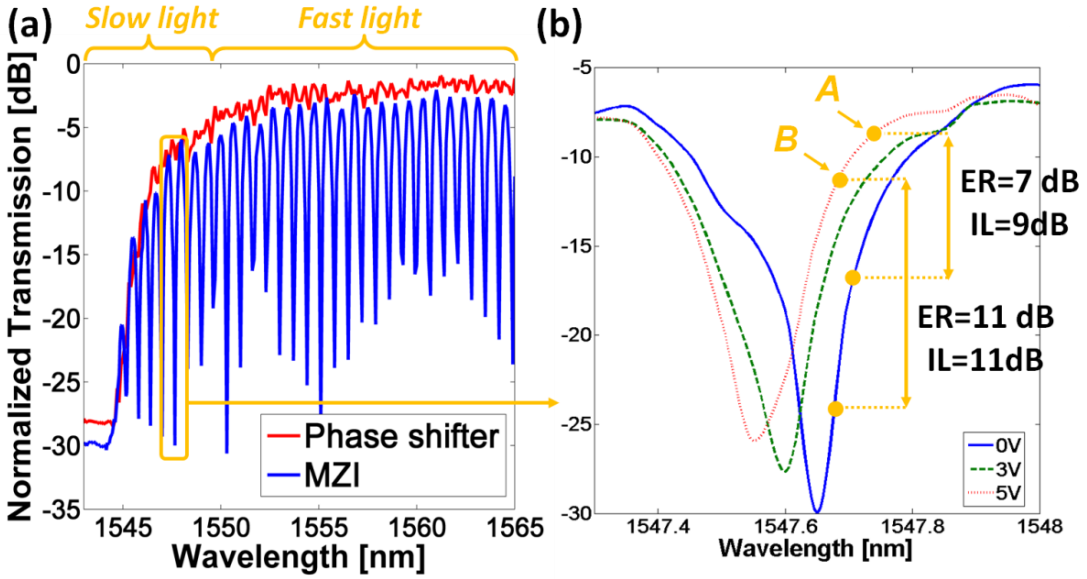

Figure 2-28: (a) Respective normalized spectra of the phase shifter (red curve, top) and the MZI (blue curve, bottom), (b) close-up view of the MZI spectrum for biases of 0, −3, and −5 V [BRI12B].

Figure 2-29 confirms that both experimental and numerical calculations are in good agreement, regardless of the small variations that may appear owing to the error in determining the notch shift across wavelength for varying reverse bias voltage. A clear enhancement of the modulation efficiencies ($V_\pi L_\pi$) between the fast (n_g~4.4) and slow (n_g~8) light regimes may be observed. It should be noticed that even in the fast light regime, the slight increase in group index compared to a conventional rib waveguide (n_g~3.8) already provides a small but noticeable enhancement. Overall, for a group index of ~8, the modulation efficiency is improved by a factor of ~2 compared to a conventional silicon modulator with identical doping conditions. In the slow-light regime (n_g~8), experimental modulation efficiencies of 0.58V.cm and 0.85V.cm for reverse biases of 1V and 5V were respectively calculated. By contrast, in the fast light regime (n_g~4.4), modulation efficiencies of 0.95V.cm and 1.62V.cm were extracted for the same corresponding reverse biases.

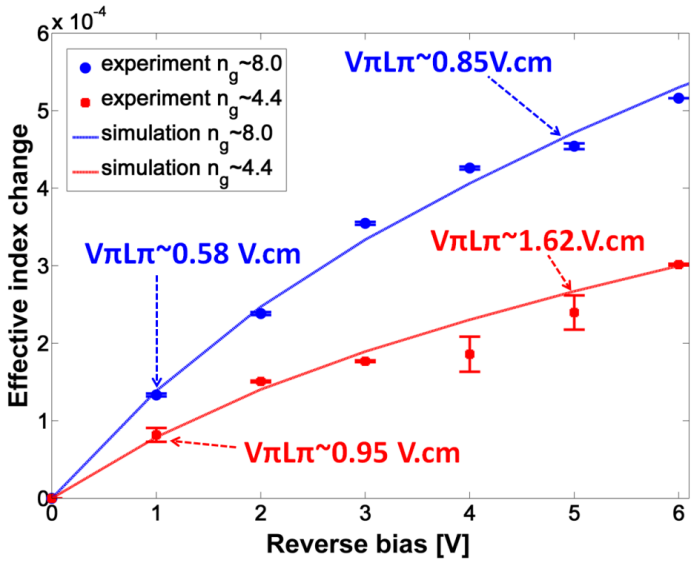

Figure 2-29: Effective index change as a function of reverse bias for group index values of ~4.4 (fast light; red curve) and ~8 (slow light; blue curve). Modulation efficiencies $V_\pi L_\pi$ are pointed by the arrows [BRI12B].

To evaluate the high-speed performance and the data transmission capability of the slow-wave modulator, we used the same set-up as in previous section 2.2 for the MRR modulators (it is shown in Figure 2-9) with the differences that the coupling is vertical instead horizontal (details in Appendix A) and the electrodes are in a travelling wave instead lumped configuration, so the modulating signal is applied to the travelling-wave electrodes, which are required to be terminated externally by a 50Ω load coupled to a DC-block. Details of model equipments and pictures of the real set-up are given in section 2.4.So, to evaluate the high-speed performance of the slow-wave modulator, 40Gbit⁄s eye diagram acquisitions at quadrature and 2dB below quadrature were carried out under a $5V_{pp}$ drive voltage, as respectively depicted in Figures 2-30(a) and 2-30(b). The measured extinction ratios are 6.6dB and 8.5dB at quadrature and 2dB below quadrature, respectively.

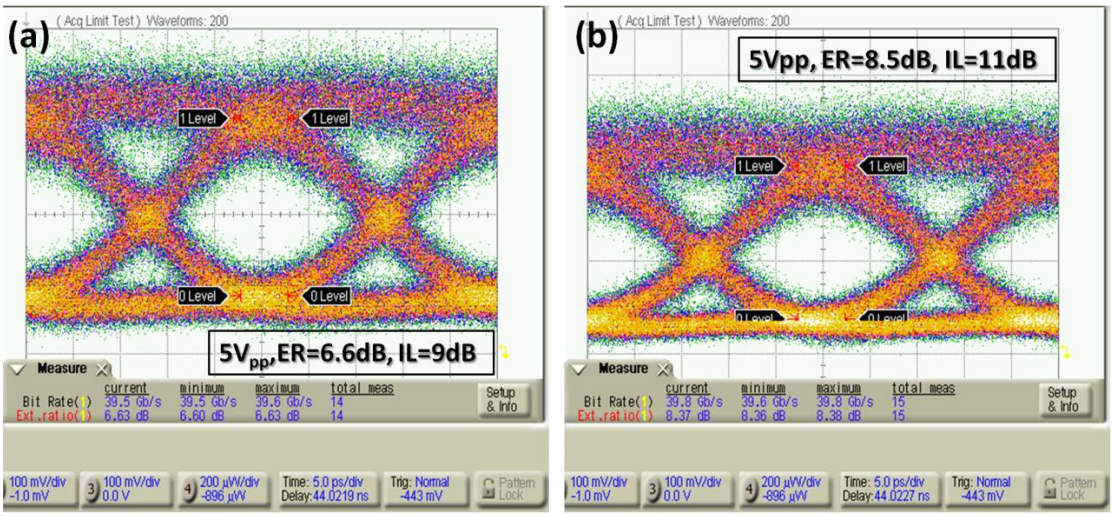

Figure 2-30: 40Gbit/s eye diagram (a) at quadrature and (b) 2dB below quadrature [BRI12B].

One should be aware that the group index at which the modulator is operated is slightly lower (n_g~8) than that used in [BRI11A] (n_g~11). Besides the lower optical losses, the choice of using such a group index value is motivated by the possibility of achieving a better electro-optical velocity matching and thus a higher modulation bandwidth. Although additional effects such as the microwave attenuation and impedance mismatch also contribute to the bandwidth reduction, the velocity mismatch between the electrical and optical signals plays a major role, especially as the group index increases [BRI11A]. However, it is important to remark that to sustain the performance in terms of extinction ratio, the phase shifter length maybe reduced according to the increase in group index. In this way, the higher velocity mismatch is partly counteracted by the shorter electro-optical interaction length.

On the other hand, the optical bandwidth of our slow-light modulator, defined as the wavelength range over which the group index variations remain within 10% of the target value [BRI10], is around 1.3nm [BRI11A]. This value is far inferior to that of conventional MZI modulators (~20-30nm). The last challenge that will definitely allow slow-light to win its spurs is showing a sustained performance over a broad optical bandwidth using engineered slow-light structures [BRI10]. Interestingly, the relatively low optical loss value positions our slow-light modulator among the state of the art of current 40Gbit⁄s modulators from an IL and footprint point of view.

In conclusion, we have demonstrated high-contrast 40 Gbit/s operation in a compact and low-loss slow-light modulator. The device features an on-chip IL of only 6dB, including the 1dB loss of the two MMI structures. The enhanced modulation efficiency (0.85V.cm) enabled 40 Gbit/s data transmission with 6.6dB ER (respectively, 8.5dB) achieved at quadrature (respectively, 2dB below quadrature) and with 9dB (respectively, 11dB) optical loss in a MZI with two identical 500μm long phase shifters. These results provide significant improvements in the field of silicon modulators at large, showing that slow light brings once more exciting prospects for silicon photonics.

2.3.3.2. Low-drive voltage SL-MZI modulator

As in the previous point, the device under study is again an asymmetric carrier depletion MZI which converts the optical phase modulation in the slow-light waveguide into amplitude modulation. Unlike the previous one, this time one arm of the MZI consists of a 1mm-long slow-light phase shifter, whereas the other arm contains a rib waveguide having the same length and doping conditions. The rest of parameters, both corrugated waveguide dimensions and doping concentrations, are the same than section 2.2.3.1.

Figure 2-31(a) shows the MZI slow-light modulator spectra under varying reverse-bias voltage. The bias voltage is varied between +0.5 and -2.5 V. The modulation efficiency increases with the group index, but using higher group indices will also have a negative impact on the IL, as we will be demonstrate in the next section dedicated to

the propagation losses measurements. Nevertheless, a fairly low IL of 12dB was measured for a moderate group index value of ~9.5 at 1546.9nm wavelength, which corresponds to the quadrature point indicated in Figure 2-31(b).

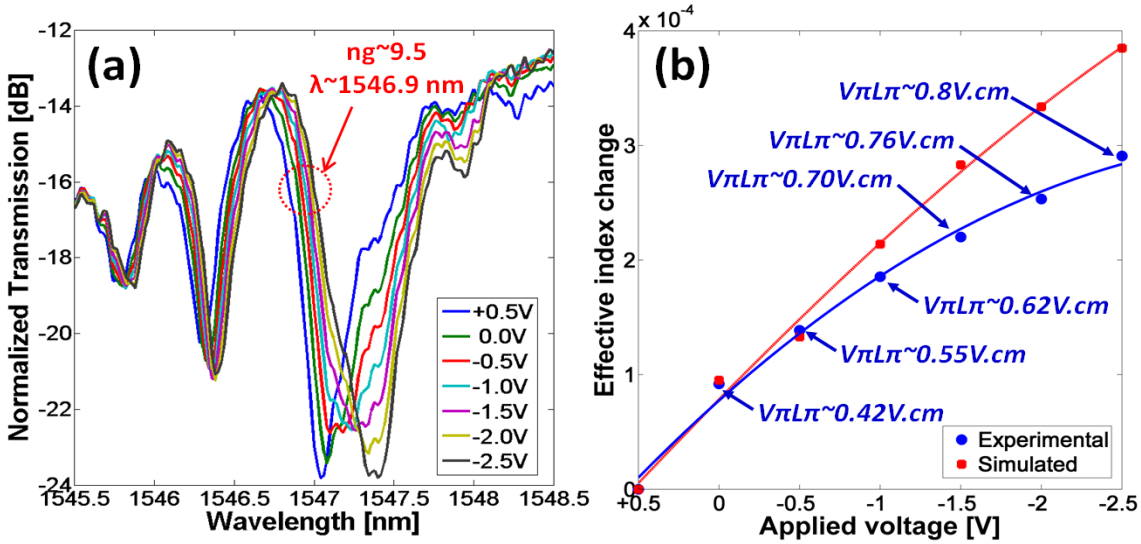

Figure 2-31: (a) Close-up view of the slow-light region for bias voltages varying from +0.5 to -2.5V. The dotted circle is the quadrature point, (b) Experimental (blue solid line) and simulated (red dashed line) effective index change versus applied voltages at 1546.9nm wavelength (measured at the quadrature point). Measured modulation efficiencies $V_\pi L_\pi$ for each corresponding applied voltage and taking +0.5 V as a reference are also shown [BRI12A].

Such Figure 2-31 shows the experimental and simulated effective index change and modulation efficiency for varying reverse-bias voltage at the quadrature point. As can be observed, the modulation efficiency varies strongly for increasing reverse-bias voltage due to the nonlinear behaviour of the *PN* junction. Modulation efficiencies $V_\pi L_\pi$ as low as 0.42, 0.55, 0.62, 0.7, and 0.8V.cm have been respectively extracted for 0.5, 1, 1.5, 2, and 3V applied voltages at 1546.9nm wavelength. Although for bias voltage beyond -0.5V both experimental and simulated effective index changes are in good agreement, a slight discrepancy takes place below -0.5V. We believe this might be due to the fact that we assume an ideal uniform doping profile in our electrical simulations, on one hand, and/or that the actual target doping concentrations are slightly lower than expected [GAR09]. One might also put forward the fact that the slow mode distribution might be altered from the simulations to experiment, hence interacting in a slightly less efficient way with charge carriers.

On the other hand, data transmission measurements were realized in the same way by using the same set-up (Figure 2-9) that in previous section 2.3.3.1. To analyze the high-speed performance of the slow-light modulator under low drive voltages, eye diagram acquisitions at quadrature (λ=1546.9nm) from 5 to 25Gbit/s were carried out under drive voltage ranging from 1 to 4V. The results are summarized in Figures 2-32, 2-33 and 2-34.

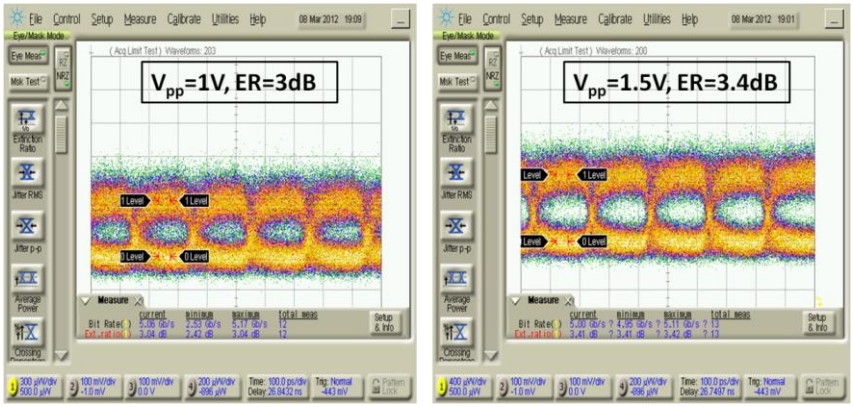

Figure 2-32: Eye diagrams at 5 Gbit/s for varying peak-to-peak drive voltage [BRI12A].

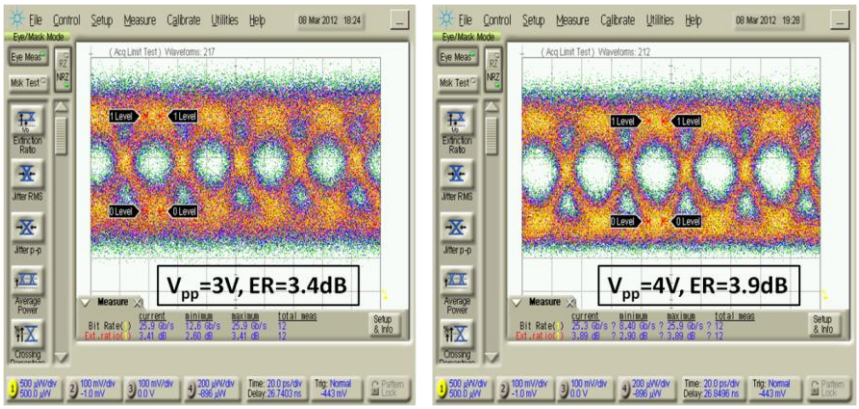

Figure 2-33: Eye diagrams at 25 Gbit/s for varying peak-to-peak drive voltage [BRI12A].

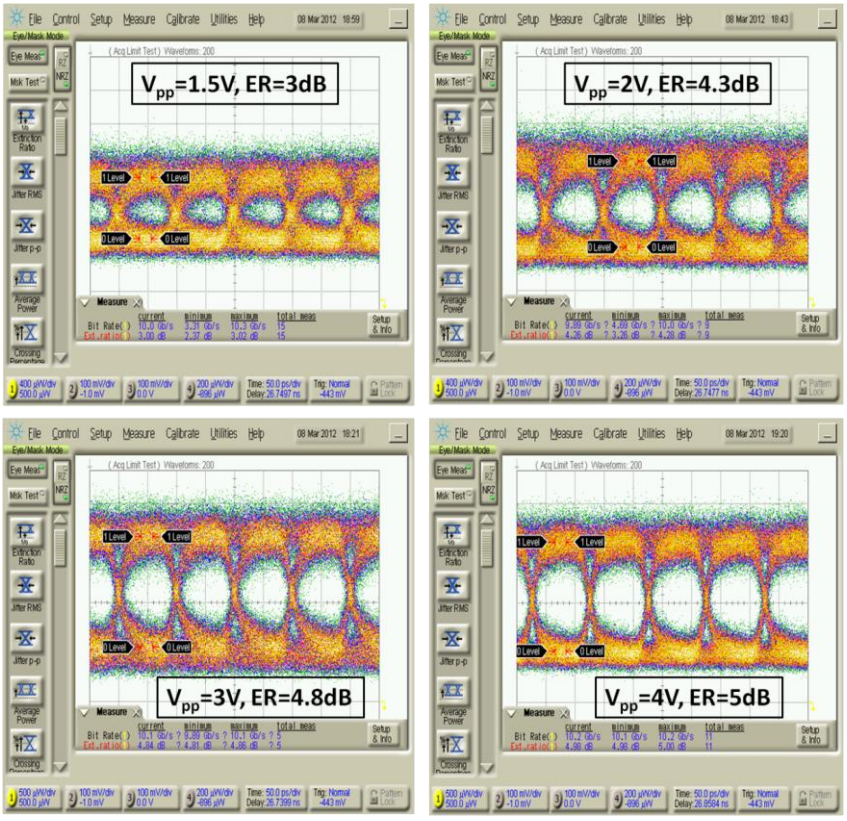

Figure 2-34: Eye diagrams at 10 Gbit/s for varying peak-to-peak drive voltage [BRI12A].

Interestingly, and as a result of the high modulation efficiencies, the eye diagram in the range 5-10Gbit/s remains open for very low drive voltages (1, 1.5, and 2V), and the corresponding ERs lie between 3dB and 4.3dB. DC bias voltages are 0, 0.25, and 0.5V, respectively. For drive voltages ranging from 3 to 4V (respective DC biases are 1 and 1.5V), the eye diagrams open up, showing that ultrahigh-speed operation at 25 Gbit/s is achieved, as shown in Figure 2-33. The relatively low ERs are due to the power unbalance between the two arms of the MZI, which produces a null height of only 10dB. Using an asymmetric MZI featuring two identical corrugated waveguides in each arm would increase the null height and lower the "0" level. This would notably increase the dynamic ERs for drive voltage beyond 2V.

In conclusion, the performance of a 1mm-long slow-light modulator has been analyzed in terms of IL, modulation efficiency, and dynamic operation under low drive voltages. The high modulation efficiency (0.55V.cm for a 1V swing) provided by the slow-light phase shifter with the *PN* junction positioned in the middle of the waveguide allowed data transmission rates from 5Gbit/s with $1V_{pp}$ up to 25Gbit/s with $3V_{pp}$ with an IL of ~12 dB. Enhanced performance (higher ER) is expected when driving the modulator in push–pull while sustaining low drive voltages. In summary, the promising combination of high modulation efficiency, low drive voltage, relatively low IL, compactness, and high-speed operation gives all the more reasons for slow-light modulators to be used in more complex silicon photonic systems.

2.3.4. Method for obtaining propagation losses

In this point, a method for measuring waveguide propagation losses by means of a MZI structure is presented, being this method the main contribution of the author to this thesis respect to slow-wave structures point. The method, based on the analysis of the transmission spectra of asymmetric MZIs, enables the propagation losses of the optical waveguides to be calculated without the requirement of identical coupling conditions for each measurement. In addition, the power imbalance of the branching structure in the MZI can also be obtained. Our theoretical analysis is supported by experimental measurements [GUT12B]. Moreover, and due to the paramount importance of this critical parameter in slow-wave elements, the method is extended and proposed to accurately measure the IL of the slow-light phase shifters presented in the previous section [BRI12A].

2.3.4.1. Rib waveguides

The passive optical component is an asymmetric MZI consisting of two identical branching elements and arms having different lengths (with ΔL of length difference). As shown in Figure 2-35, light is divided at the input and then recombined at the output

through the branching elements. The splitter and combiner components may either be Y-junctions or MMI.

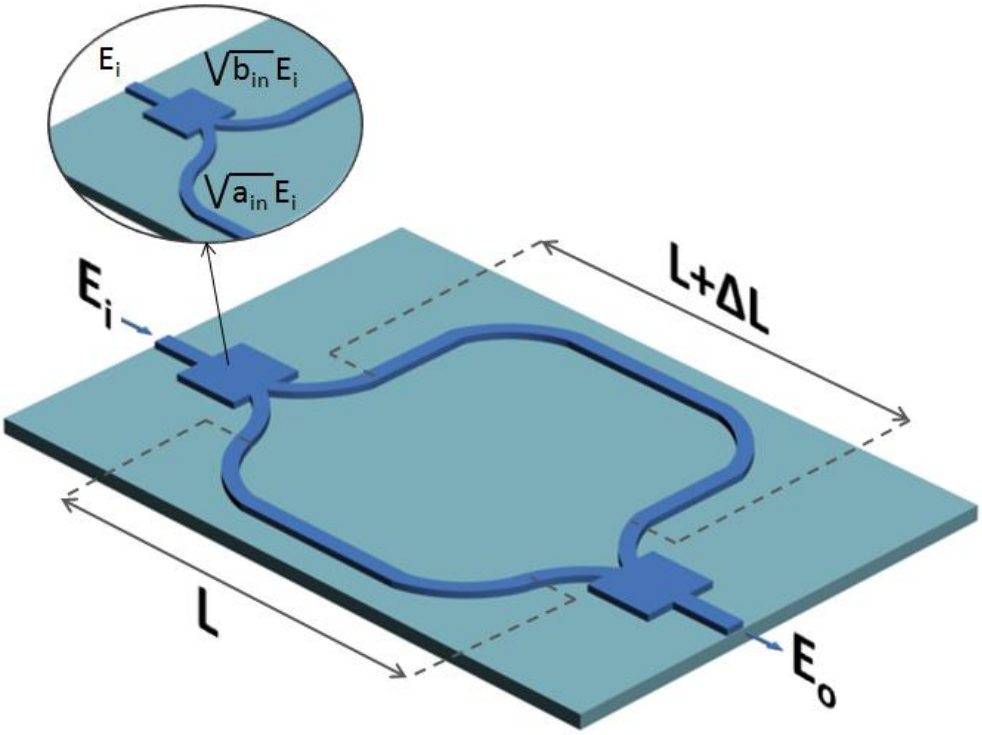

Figure 2-35: Schematic view of the MZI structure. Splitter and combiner portions are represented by a generic box.

Ideally, the branching elements should split and recombine the input power equally in both arms. However, this is not always true due to fabrication process deviations and may therefore have a significant impact on the component performance, depending on the application [CHA01]. Therefore, in our analysis, we initially consider the most general case of having branching elements with different performance at the input and output of the MZI structure. At the branching element acting as a power splitter, that is, located at the MZI input, the amount of power coupled to the shorter arm is denoted a_{in} while the amount of power coupled to the longer arm is denoted b_{in}. In a similar way, we can denote a_{out} and b_{out} the power coupling coefficients that govern the output branching element, which acts as a power combiner.

Starting from of the transfer function of a MZI and assuming the same propagation losses for both arms, we can obtain the maximum electrical field at the MZI output as:

$$E_{\max} = \mathrm{E}_i \left[\sqrt{a_{in}} \sqrt{a_{out}} e^{-\alpha L} + \sqrt{b_{in}} \sqrt{b_{out}} e^{-\alpha\ L+\Delta L} \right] \tag{2.28}$$

where E_i is the input electric field including coupling losses, $\alpha(Np/cm)$ is the propagation losses in the MZI arms, $L(cm)$ is the length of the shorter MZI arm and $\Delta L(cm)$ is the length difference between the MZI arms.

To obtain the expression for the minimum electric field, there will be an uncertainty because we do not know a priori if the output power from the longer arm is lower or higher than that from the shorter arm as it will depend on the branching elements, propagation losses and length difference between the MZI arms. Therefore, for the sake of simplicity, we can define the minimum electric field at the MZI output as:

$$E_{\min} = \mathrm{E}_i \left[\sqrt{a_{in}} \sqrt{a_{out}} e^{-\alpha L} - \sqrt{b_{in}} \sqrt{b_{out}} e^{-\alpha\ L+\Delta L} \right] \tag{2.29}$$

It should be pointed out that this value may be either positive or negative. Combining Equations (2.28) and (2.29), we can obtain the following linear equation:

$$E\ \ dB\ = \Delta L\ \ cm\ \ .\alpha\ \ dB/cm\ + R\ \ dB \tag{2.30}$$

where

$$E\ \ dB\ = 20\log_{10}\left(\frac{E_{\max} + E_{\min}}{E_{\max} - E_{\min}} \right) \tag{2.31}$$

$$R\ \ dB\ = \begin{cases} 20\log_{10}\left(\dfrac{\sqrt{a_{in}} \sqrt{a_{out}}}{\sqrt{b_{in}} \sqrt{b_{out}}} \right), E_{\min} > 0 \\ 20\log_{10}\left(\dfrac{\sqrt{b_{in}} \sqrt{b_{out}}}{\sqrt{a_{in}} \sqrt{a_{out}}} \right), E_{\min} < 0 \end{cases} \tag{2.32}$$

and *R(dB)* is denoted as the branching ratio. As can be noticed in Equation (2.32), the exact expression of the branching ratio will depend on the sign of the minimum electric field obtained from Equation (2.29). However, in both cases, the branching ratio value derived from Equation (2.30) will indicate the degree of asymmetry of the branching elements. For perfectly symmetric branching elements, R(dB)=0 while as the asymmetry in the branching elements increases *R(dB)* will give rise to values greater or lower than zero. Hence, considering a set of MZIs with different optical length differences (*ΔL*), we can represent the single parameter *E(dB)* as a function of Δ*L* for each MZI. Then, in a similar way than for the cut-back method, we linearly interpolate through these points to finally estimate the propagation losses *α(dB/cm)* of the MZI as the slope of the interpolated line. In addition, the intersection with the Y-axis (ΔL=0) of the interpolated line will give the branching ratio.

The estimation of the propagation losses and the branching ratio will be independent of the coupling loss, which is demonstrated by the fact that E_i is not present in Equations (2.30)-(2.32). Furthermore, it should be pointed out that if the branching ratio is known, for instance from previous measurements, then only one MZI structure will be required to estimate the propagation losses, which will be easily derived just by looking at the maxima and minima of the interference transmission spectrum and applying Equation (2.30).

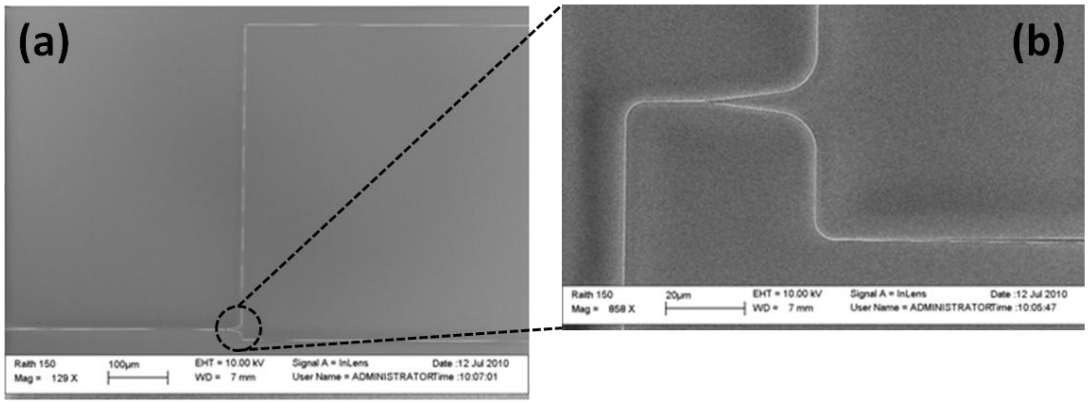

Figure 2-36: SEM picture of fabricated structures: (a) MZI, (b) Y-junction detail.

The samples were fabricated in the Nanophotonics Technology Center facilities on a 220nm thick SOI wafer. The optical waveguides were patterned by electron-beam lithography (EBL) on 100nm PMMA resist, deeply etched by Reactive Ion Etching (RIE) and covered with a roughly 2μm thick silicon dioxide layer. Figure 2-36(a) shows a SEM picture of one of the MZI and the inset (Figure 2-36(b)) depicts a zoomed-in view of the input power splitter.

To perform the experiment we fabricated three MZIs having optical length differences of ΔL=1, 2, 3mm. The optical characterization was carried out using a tunable laser as a coherent light source, which was coupled to a fiber PC. The performance of the device has been measured using vertical coupling through grating couplers over a bandwidth span of 20nm from λ=1540nm to 1560nm. The measured transmission spectra are shown in Figure 2-37.

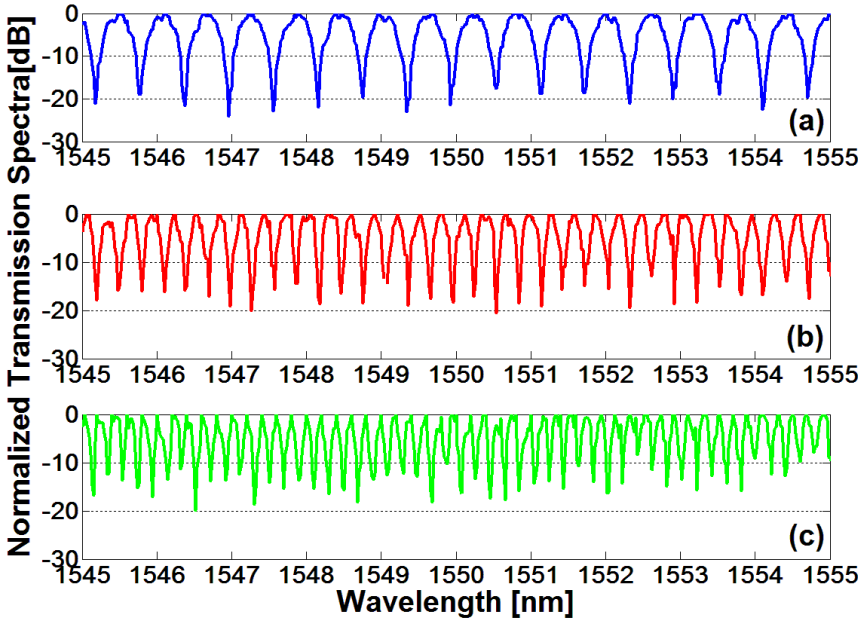

Figure 2-37: Detail of the measured transmission spectra of the MZI's with (a) ΔL=1mm, (b) ΔL=2mm, (c) ΔL=3mm. The spectral range is reduced for clarity.

As already mentioned, when the splitting and combining ratio is 50%, the MZI is balanced. In this case, we can obtain a complete destructive interference when the phases in both arms are opposite that leads ideally to an infinite extinction ratio. However, the imbalance of the splitter and combiner as well as the excess loss of one arm with respect to the other gives rise to a reduction of the extinction ratio, as occurs in Figure 2-37. The excess loss in one arm is directly responsible for the ER variation as the length difference between the MZIs changes. On the other hand, we attribute the ER variation with wavelength to the effect of stitching. It is well known that stitching originates due to offsets in the pattern at different writing fields. In our case, a writing field of 150µm x150µm has been used in the EBL process. Consequently, MZIs with longer lengths are more likely to suffer offsets in the pattern (stitching errors) and exhibit therefore more ER variability as it can be clearly seen in such Figure 2-37.

Applying the method described, we obtained that the propagation losses, shown in Figure 2-38(b), are on average 8dB/cm with a standard deviation of 3.5dB/cm for the measured wavelength range. It can be noticed here that such relatively high losses can be attributed to stitching and sidewall roughness. Roughness loss reduction can be achieved with techniques such as oxidation smoothing of the sidewalls [LEE01, SPA05] and stitching may be minimized via substrate-tilt correction procedure [GNA07A, GNA07B]. On the other hand, Figure 2-38(a) depicts the branching ratio as a function of the wavelength. It can be seen that the branching elements are not perfectly symmetric, which results in an average branching ratio of 0.83dB with a standard deviation of 0.82dB. The standard deviation is high due to the undesired ER variation with wavelength. Therefore, assuming identical branching elements at the input and output of the MZI structures ($a=a_{in}=a_{out}$ and $b=b_{in}=b_{out}$), as well as power conservation (a+b=1), it is possible to extract a and b coefficients from Equation (2.32) with acceptable accuracy and hence completely characterize the branching element performance.

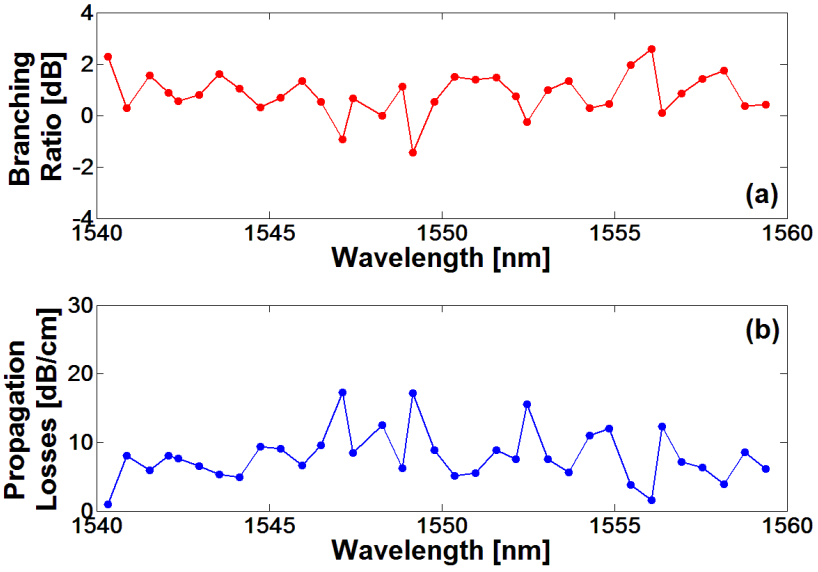

Figure 2-38: (a) Branching ratio and (b) propagation losses versus wavelength obtained from method.

The uncertainty given by the two possible solutions can be resolved by comparing the experimental ERs of the MZI transmission spectra with the theoretical ER values, both shown in Table 2-5 and calculated from Equations (2.28) and (2.29). These values take into account the propagation loss and branching ratio that were extracted from the proposed method. It can be seen that the ER values from solution a~0.52 are in very good agreement with the average ER values derived from the transmission spectra of MZIs thus demonstrating the robustness of the proposed method and indicating that more power is coupled into the shorter arm of the MZI.

	Average experimental ER	Theoretical ER a~0.52	Theoretical ER a~0.48
ΔL =1 mm	20.4 dB	21.3 dB	44.4 dB
ΔL =2 mm	17.3 dB	17.6 dB	25.7 dB
ΔL =3 mm	14.6 dB	15.1 dB	20.2 dB

Table 2-5: Average theoretical ERs and experimental ERs derived and from the transmission spectra.

In contrast to the cut-back technique, conventionally used for straight silicon waveguide [VLA04], the proposed method involves all the components of the MZI, including waveguides and branching elements (power splitter/combiner). Moreover, the alignment at the chip-input and output is not a critical issue because what matters is the relative position between the maxima and minima of the same spectrum and not the relative positions of the spectra as cut-back requires. In other words, our method is independent of the coupling losses. Finally, as already mentioned, if the branching ratio is known, then only one MZI structure will be required to estimate the propagation losses. On the other hand, if the propagation loss is known and the splitting ratio at the branching element could be tuned [FEN08], the optimum splitting ratio value, denoted b_{opt}, can be straightforwardly from Equations (2.28) and (2.29):

$$b_{opt} = \frac{1}{1+e^{-\alpha\Delta L}} \tag{2.33}$$

so that then more optical power would be forced to propagate through the longer arm of the MZI thus maximizing the extinction ratio.

Overall, the proposed method introduces interesting improvements over the cut-back method as it allows for reliably calculating the propagation losses as well as the branching asymmetry of MZI structures. The method, based on analyzing the interference fringes of the MZI spectra, avoids the requirement of constant fiber-to-chip coupling conditions, which is difficult to achieve in practice. Moreover, the proposed technique may also be of great interest to systematically estimate the performance of MZI-based structures, such as filters, switches or modulators, in which the power imbalance introduced by the branching elements as well as the propagation losses, are

of paramount importance. Finally, this method may be applied to more complex structures as MZI featuring slow wave structures as it will be described in the following point.

2.3.4.2. Corrugated waveguides

The previous method is proposed and extended to accurately measure the IL of the slow-light phase shifter [BRI12A]. In order to estimate the IL versus group index with a single measure, the method exploits again the MZI structure consisting of a slow-light waveguide in one of its arms, as illustrated in Figure 2-39(a). It should be noticed that the calculation of the group index variations has been proposed with similar procedures [GOM07, NOT01]; however, to the best of our knowledge, a method for also estimating the IL from the MZI spectrum has not yet been reported. Figure 2-39(b) shows the optical transmission spectrum of the MZI structure. The FSR changes across the spectrum as a result of the group index dependence upon wavelength, which increases as we approach the band edge of the slow-light mode.

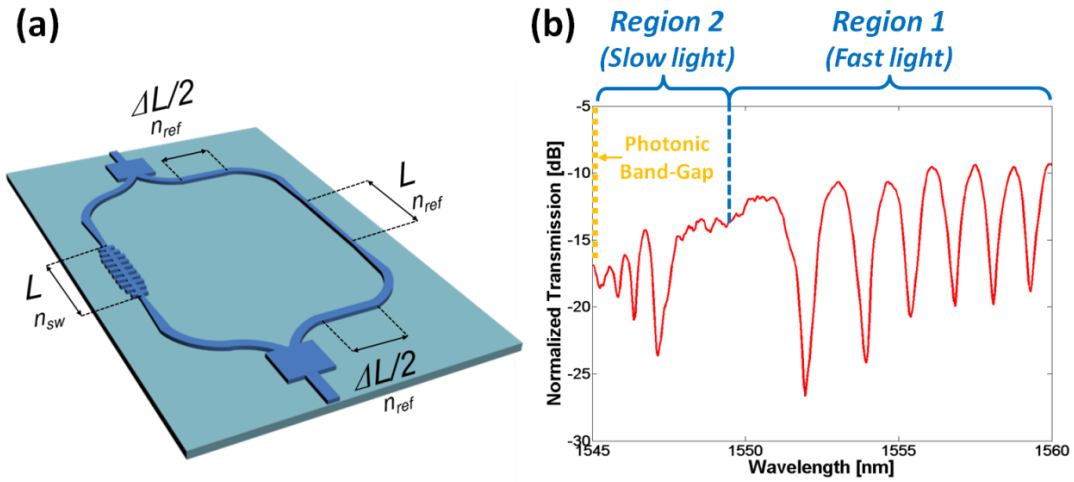

Figure 2-39: (a) Schematic of the MZI structure used in the proposed method to estimate the IL in the slow-light phase shifter, (b) normalized optical transmission spectrum of the MZI structure [BRI12A].

Therefore, the FSR variations across wavelength can be used to extract the group index from

$$FSR\ \lambda \approx \frac{\lambda^2}{n\Delta L + n_{ref} \pm n_{sw}\ \lambda\ L} \tag{2.34}$$

where λ is the central wavelength of the FSR; n_{sw}, n_{ref}, and n are the respective group indices in the slow-light, 300nm wide reference rib, and 400nm wide rib waveguides; L is the length of the slow-light and reference rib waveguides, which is the same; and ΔL stands for the length difference between the MZI arms considering only the 400nm wide rib waveguide. In our case, L=1mm, ΔL=0.9mm, n_{ref}~3.5, and n~3.7. The selection of the sign in the right-hand side of Equation (2.34) depends upon the considered

wavelength range and is related to the fact that the FSR exhibits different behaviours as we move from the fast-light region toward the PBG, as can be observed in Figure 2-39(b). In the fast-light regime (far enough from the PBG), the separation between the interference fringes remains approximately constant, which is consistent with a nearly unvarying group index value, and the negative sign must be used in the Equation (2.34). However, as we enter the slow-light regime, that is, as we move closer to PBG, the FSR increases up to a maximum value, which means that the phase difference between the MZI arms is minimized. According to (2.34), the FSR is infinite when the denominator is zero, which means that there is no phase difference between the MZI arms. It can be straightforwardly obtained that this occurs for a group index of 6.8. From this point forward, the positive sign must be used in the Equation (2.34) because higher group indices imply that the effective optical path length of the shorter arm becomes larger than that of the longer arm, thus causing the FSR to decrease.

The influence of loss variations versus group index in the slow-light waveguide is also clearly observed in Figure 2-39(b). Initially, the losses in the reference arm are higher than in the fast-light region (i.e., the region where the group index is approximately constant) of the slow-light waveguide, hence reducing the contrast ratio of the MZI interference fringes. As the group index increases, the losses in the slow-light waveguide increase accordingly, reducing further the power imbalance between arms. This, in turn, contributes to improve the contrast ratio. The maximum contrast ratio is achieved when the total losses in each of the MZI arms are similar, which takes place for wavelengths around 1552nm. At wavelengths lower than 1552nm, the power imbalance increases back again, reducing therefore the contrast ratio, though this time caused by higher losses in the slow-light waveguide. Therefore, the IL in the slow-light phase shifter can be estimated from the variation of the contrast ratio with wavelength. The proposed method for estimating the IL starts from the evaluation of the maximum and minimum electrical field at the MZI output, which can be written as

$$E_{\max}(\lambda) = E_0 \left| m_L c_p(\lambda) e^{-\alpha_{sw}(\lambda) L} + m_{L+\Delta L} e^{-\alpha_{ref} L + \alpha \Delta L} \right| \tag{2.35}$$

$$E_{\min}(\lambda) = E_0 \left| m_L c_p(\lambda) e^{-\alpha_{sw}(\lambda) L} - m_{L+\Delta L} e^{-\alpha_{ref} L + \alpha \Delta L} \right| \tag{2.36}$$

where E_o is an amplitude factor that includes the fiber-to-the-chip coupling losses, m_L and $m_{L+\Delta L}$ is the power branching coefficient of the splitter and combiner (it is assumed that both are identical), c_p accounts for the input and output coupling losses between the slow-light and rib waveguides; and α_{sw}, α_{ref}, and α are the respective propagation losses in nepers per unit length in the slow-light, reference rib, and rib waveguides. It is assumed that the propagation losses in the rib waveguides are approximately constant with wavelength. The following relation is obtained by combining (2.35) and (2.36)

$$E(\lambda) = 20\log_{10}\left(\frac{E_{\max}(\lambda) + E_{\min}(\lambda)}{E_{\max}(\lambda) - E_{\min}(\lambda)} \right) = Cte + C_p(\lambda) + \alpha_{ref} - \alpha_{sw}(\lambda) \quad L \tag{2.37}$$

where *Cte* is a constant value, which depends only on the possible splitter/combiner branching asymmetry and the $\alpha\Delta L$ losses. Thereby, we can obtain an estimation of both coupling and propagation losses within the slow-light waveguide at a given wavelength just by considering the maxima and minima or, in other words, the contrast ratio of the MZI interference fringes, which makes the proposed method independent on the external alignment and the fiber-to-the-chip coupling losses.

The IL, which include both coupling and propagation losses, can be derived as follows

$$IL\ \lambda\ = C_p\ \lambda\ + \alpha_{sw}\ \lambda\ L \approx \alpha_{fw} L + \begin{cases} \overline{E} - E\ \lambda\ , region\,1 \\ \overline{E} + E\ \lambda\ , region\,2 \end{cases} \tag{2.38}$$

where α_{fw} and $\overline{E}$ are, respectively, the propagation losses and mean value of $E(\lambda)$ in the fast-light region, where the group index is approximately constant and where the coupling losses are assumed to be negligible. The two different expressions for regions 1 and 2 depicted in Figure 2.39(b) assume that, in region 1, the output power from the longer arm is lower than that from the shorter arm, and vice versa in region 2, where the sign must be changed in the Equation (2.36) as also occurs in (2.34). The propagation losses, α_{fw}, can be estimated from Equation (2.37) giving rise to a value around 3dB/mm.

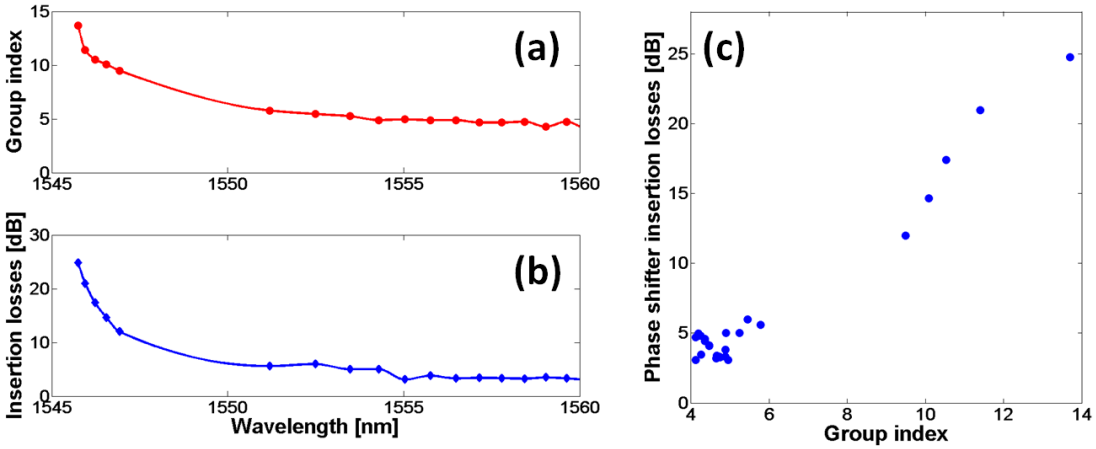

Figure 2-40: (a) Group index and (b) IL variation versus wavelength. (c) Slow-light phase shifter IL versus group index. [BRI12A]

Figure 2.40 shows (a) the group index and (b) IL dependence on wavelength, which are derived from Equations (2.34) and (2.38), respectively. Both results can be combined in order to obtain the IL versus group index of the slow-light phase shifter structure, as depicted in Figure 2-40(c). It can be seen that the IL increase for increasing group index, yielding to a trade-off between high modulation efficiency and low IL, which relies on the group index operating point [BRI11A].

The increase in loss is partly attributed to the higher free-carrier-based absorption arising from the enhanced light–matter interaction. In fact, the IL in the fast-light region are similar to those reported in other works with similar doping concentrations [KIM11,

DIN12]. Nevertheless, IL as low as ~2dB for a group index of ~28 have been reported in an MZI modulator with 200μm long slow-light phase shifters based on a 2D-PhC structure although considering lower implantation doses [NGU12A]. Overall, strategies to reduce the IL should be focused on optimizing the overlap between the active region and the slow-light mode propagating through the periodic optical waveguide. As a matter of fact, a doping compensation method in which the doping profile is optimized to reduce absorption losses without degrading the modulation efficiency and speed has been recently proposed and demonstrated for conventional silicon modulators [TU11]. Such a method could also be applied for the proposed slow-light modulator. Finally, improving the coupling technique to the slow-light mode would also be especially desirable as the group index increases.

In conclusion, a simple method has been proposed for experimentally estimating the IL versus group index of a slow-light photonic waveguiding structure. Only a single measure is required, and the loss estimation is independent of the alignment and fiber-to-the-chip coupling losses.

2.4. Active RF characterization set-ups

During the chapter, a brief overview of the set-ups used for experimental measurements has been provided. However, it is important to describe in more detail the experimental setup as well as the function of each component used for characterizing the fabricated electro-optic modulators acting in each case on different way. Two main types of active characterization set-ups have been presented and used along the chapter.

2.4.1. Data transmission measurements

The high speed performance of all silicon-based modulators (both slow-light and MRR-based modulators) presented in the chapter has been characterized by measuring their data transmission capability. For such task it is necessary to visualize and measure the eye diagram of the received signal. The main component used in this case is the digital communication analyzer (DCA) which is a powerful and versatile instrument for characterizing high-speed digital communications waveforms. We are going to explain in detail the set-up used.

Light emitted by an ECL laser is injected into the modulator via grating couplers if vertical coupling (slow-wave modulators) or lensed fiber and inverted tapers if horizontal coupling (MRR-based modulators). The transmitted power is optimized through the use of a polarization controller (PolaRITE™ General Photonics). The description of both coupling techniques as well as the passive characterizations set-ups are given in Appendix A.

Data transmission measurements are realized by driving the modulator with a NRZ PRBS of length 2^{31}-1 delivered by a BPG (SHF BPG 44E) connected to an external clock (R&S SMR RF signal generator). The electrical signal is generally amplified through a high speed RF amplifier (Picosecond Pulse lab model 5865) to achieve a decent voltage swing (V_{pp}) and combined to a DC bias supplied by a DC Power Source (Agilent E3647A) using a bias-Tee (SHF BT-110) . For consistency with S_{21} electro-optical measurements, the modulating signal is applied through a high speed GSG input probes to the electrodes (travelling wave in slow-wave modulators and lumped electrodes in the MRR-based modulators) which are terminated externally by a 50 Ω resistance coupled to a DC block (SHF DCB-110) by using a GSG output probes to avoid reflexions (in the case of travelling wave configuration).

The output modulated signal is amplified with an EDFA (Amonics AEDFA-18-B-FA), filtered by a tunable OF (Tecos bandpass-OF) to isolate the selected resonance of the modulator optical transmission spectrum and photo-detected by a DCA (Agilent Infiniium DCA-J 86100C). In the DCA we display the eye diagram and measure the dynamic ER. The next Figure 2-41 depicts again the schematic of the set-up but this time showing a real picture of each component used.

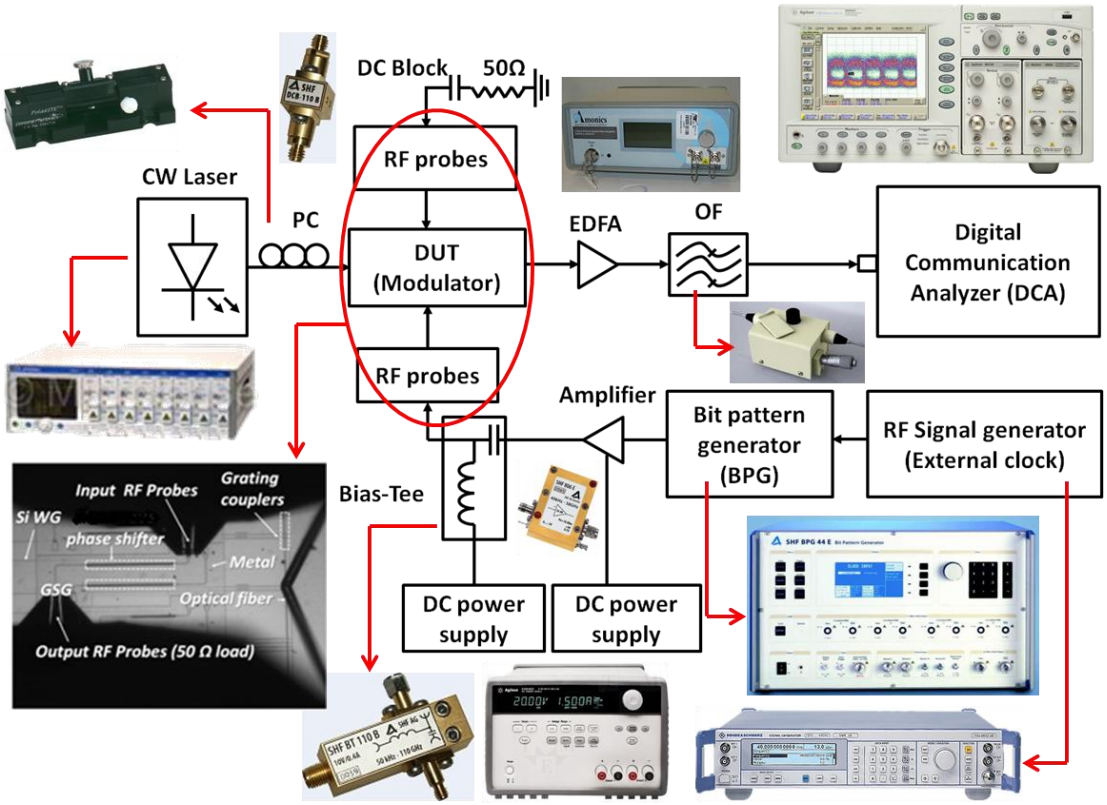

Figure 2-41: Schematic of the characterization setup and pictures of each component used in along the chapter to measure the data transmission capability of the silicon-based modulators.

For completeness, pictures of the entire real set-up used in the Nanophotonics Technology Center facilities are shown in Figure 2-42.

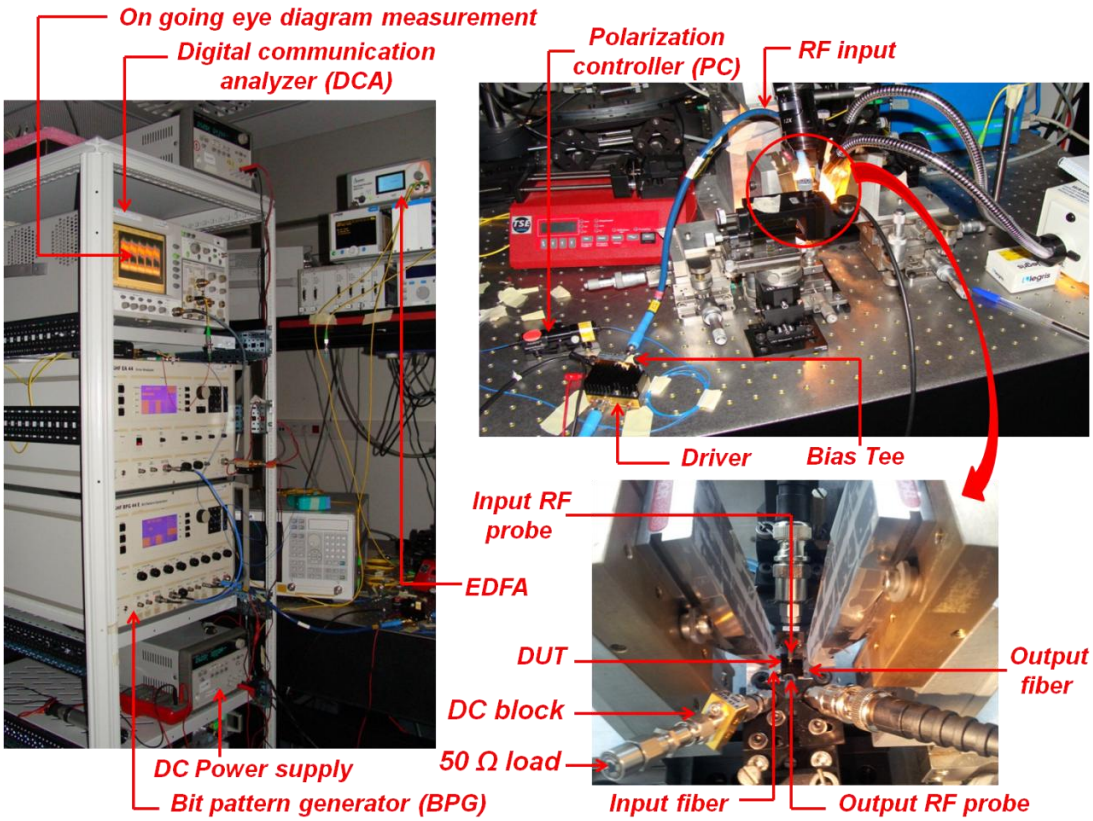

Figure 2-42: Pictures of the characterization setup for the eye diagram acquisition.

2.4.2. Small signal measurements

On the other hand, the set-up used for small signal characterization has been shown in section 2.2.3.2 for the RAMZI modulator. Small signal measurements consist basically on the determination of the electrical and electro-optical frequency response of a given electrical or electro-optical device via the calculation of the scattering parameters. Therefore, such characterization is necessary to estimate the S_{21} electro-optical parameters to obtain the 3-dB roll-off bandwidth of the RAMZI modulator and the main component for such purpose is the vector network analyzer (VNA).

So, Figure 2-43 shows the experimental set-up (and real pictures of each component) for measuring the high speed optical frequency response. Light is coupled from an ECL to the chip via a lensed fiber (details in appendix A) after polarization control (PolaRITE™ General Photonics). The small electrical signal delivered by the port 1 of a RF vectorial network analyzer (Agilent PNA-X N5247A) is coupled a DC bias voltage supplied by a DC Power Source (Agilent E3647A) using a bias-Tee (SHF BT-110) and applied to the lumped electrodes through high speed GSG probes to the RAMZI modulator. The output modulated signal is amplified with an EDFA (Amonics AEDFA-18-B-FA) and photo-detected by a high speed photodiode (u2t 50GHz XPDV2120R) connected to the port 2 of the RF VNA in order to extract the electro-optical S_{21} transfer

function. The signal generator is swept from 100MHz to 50GHz and the photo-receiver output is normalized by the input drive voltage for all frequencies

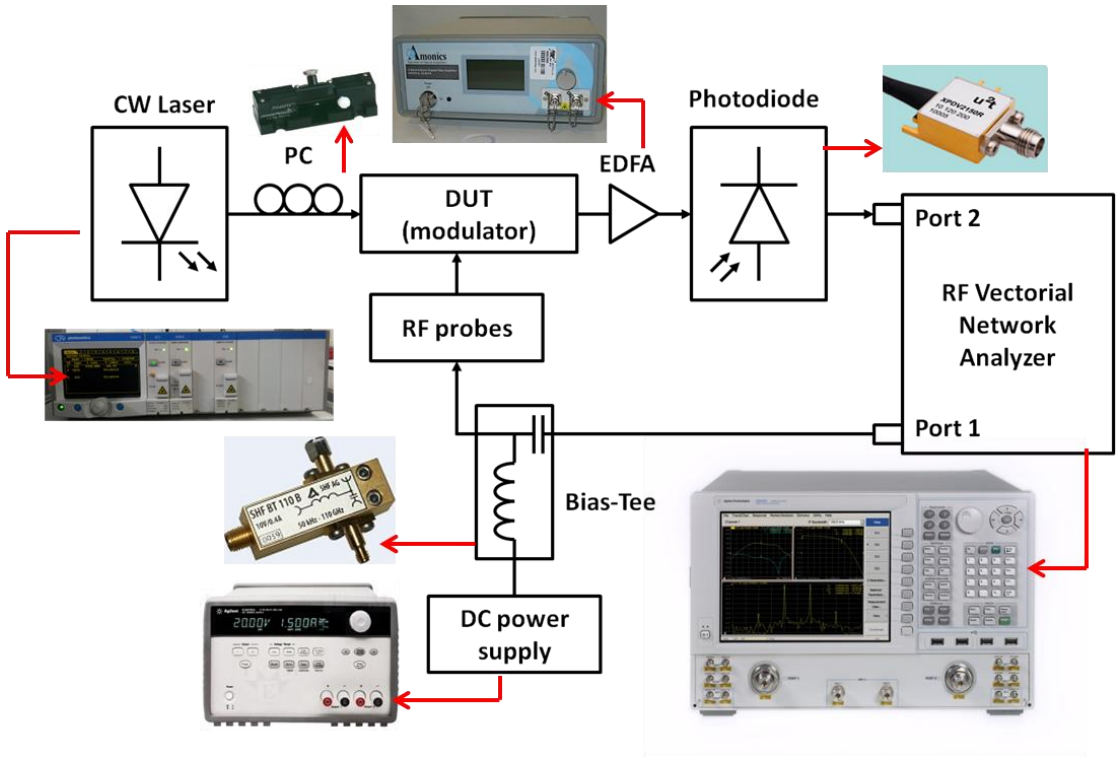

Figure 2-43: Schematic of the characterization setup and pictures of each component used in section 2.3.3.2 to measure 3dB frequency roll-off of the silicon-based RAMZI modulator.

Chapter 3

Analog applications

3.1. Introduction: Microwave Photonics

As an emerging technology, many definitions of microwave photonics (MWP) have been described in the past few years: “MWP is a discipline which brings together the world of radio-frequency engineering and optoelectronics” [MAR12], “MWP is the study of photonic devices operating at microwave frequencies and their applications to microwave and optical systems” [CAP07], “MWP is an area that studies the interaction between microwave and optical waves” [YAO12], “Microwave photonics is a rapidly-growing interdisciplinary field linking microwave and optical technologies” [BER10]. The body of work referred to as analog photonics, microwave photonics, RF photonics, and analog optics is generally focused on the optical encoding of electronic signals and the transmission or manipulation of such signals in the optical domain.

Analyzing the previous definitions one can easily to get an idea of the basic concept of a MWP link, shown in Figure 3-1(a), which consists of: analog electrical signals at microwave frequencies are transported over a photonic link composed by optical fiber. In its simplest form, an MWP link consists of an electrical-to-optical (E/O) conversion of the RF signal by a modulation device and an optical-to-electrical (O/E) reconversion of the optical signal by a photodetector once it has been transported. Further, when processing signal (as time delay, phase shift, filtering or frequency conversion) in the optical domain between the two conversions is added, we are referring to a MWP system, which is shown in Figure 3-1(b).

Considerable numbers of applications are involved in the research activity in the MWP field, as satellite and radio-astronomy communications, sensor networks, cable television system, medical imaging, antenna remoting in radar systems, and the leading

from the consumer point of view, broadband wireless access networks, for example, attaining in-home fiber networks supporting wireless communications at data rates of multiple Gbit/s. The increasing demand in speed, bandwidth, and dynamic range as well as small and lightweight devices are some of the reasons for that MWP has attracted great interest. So, MWP enables the realization in microwave systems that are becoming complex or even not possible in RF domain, exploiting the unique capabilities of photonics in terms of size, power, cost, high data-transfer capacity and immunity to electromagnetic interference.

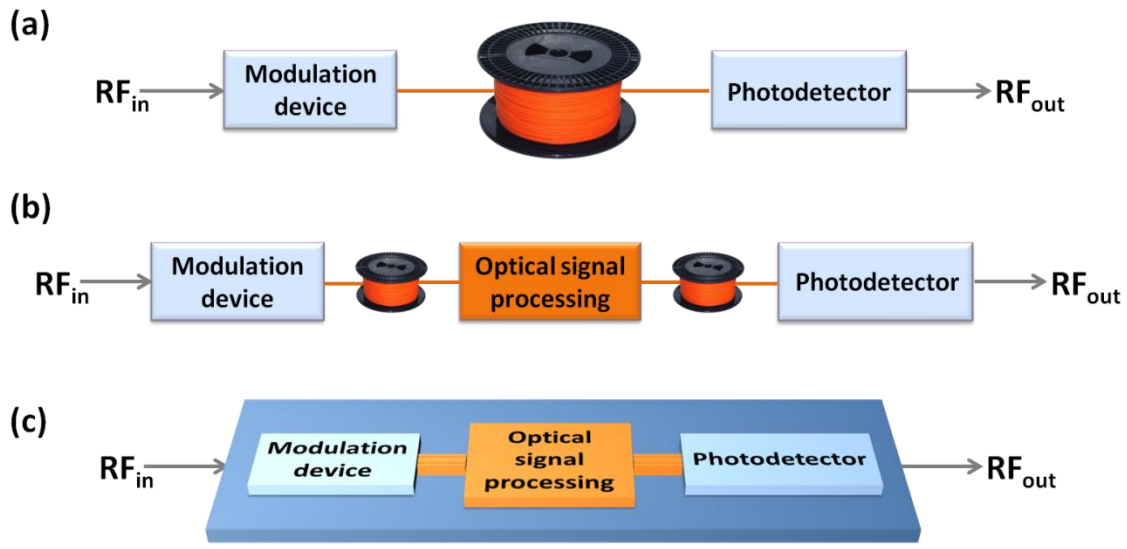

Figure 3-1: Schematic of the fundamental concept of (a) an MWP link, (b) a MWP system and (c) an IMWP chip.

Despite the potential of MWP, there are several factors that still distance the MWP solutions to replace traditional microwave solutions. The dynamic range and the reliability are still insufficient and the cost and power consumption are still too high. On one hand, the use of discrete components as lasers, modulators and detectors, leads to the system to be bulky, expensive and high power consumer. On the other hand, the interconnections with fiber pigtails reduce the robustness of the system. The most efficient solution so far to overcome these mentioned drawback factors, is the RF and photonics integration [MAR12], that is, the use of photonic integrated circuits (PICs) to address MWP functionalities, which makes arise a new technology so-called Integrated Microwave Photonics (IMWP). With the incorporation of MWP components in photonic circuits, and therefore the use of the IMWP technology, one can achieve a reduction in: footprint, inter-element coupling losses, packaging cost as well as power dissipation. This concept, shown in Figure 3-1(c), is very much in line with the recent trend, already commented in the introduction of this thesis, of large scale PIC technology for the future photonic network-on-chip (NoC) in scaled chip multiprocessors systems [COL11, SMI12, LEE10] in digital approach, but it must be taken into account that, due to the stringent requirements in the management of analog signals, PIC technology for integrated MWP should show higher performance than the

one expected from the digital applications. For this reason less attention has been paid to analog applications, and so far, MWP has addressed lower-volume market, and therefore lower volume PIC productions [MAR12].

In general terms, we can summarize the main functionalities covered by microwaves photonics as follow:

- Photonic generation of microwave signals, obtaining large frequency tunability and reaching very high frequencies up to the THz region.
- Photonic control and processing of microwave signals, in which two of the key functionalities required for the future photonic processors are frequency up and down conversions and microwave photonic filtering.
- Photonic distribution or transmission of microwave signals replacing the coaxial cables links which means improvements in size, weight, flexibility and attenuation. In this area, radio-over-fiber (RoF) systems which consist on transport and distribution of wireless signals over optical fiber, has special mention. High fidelity of signals is required in these applications, which is translated in high linear E/O conversions.
- Photonic analog-to-digital conversion, overcoming the conventional analog-to-digital conversers limits in speed and resolution which become more severe at higher frequencies.

One of the available platforms frequently used to demonstrate IMWP features is the silicon-on-insulator (SOI) technology which allows much MWP functionalities to be addressed in a single chip. SOI integration based devices is therefore a hot topic in the area of IMWP as its state of art is mature and compatible with CMOS technology, which provides it the capability to monolithically integrate optical and microelectronic components. Moreover it provides immunity to electromagnetic interference, besides that the miniaturization of the devices due to its high index contrast between Si and SiO_2 which allows large-scale integration [JAL06].

Among the numerous building blocks required to enable a fully functional PIC chip along with high speed electronics, electro-optic modulators are essential. These are just the devices employed in MWP links for converting the RF signals into the optical format, that is, they are the responsible of E/O conversions and therefore of paramount importance for achieving high performance links. As it has already been explained in the first chapter of the thesis, the leading approach for developing electro-optical modulators in silicon photonics is currently via the plasma dispersion effect which consists of varying the free-carrier concentration in a doped silicon waveguide [REE10, SOR87]. Significant milestones in modulation devices have been achieved during recent years through the plasma dispersion effect in silicon although mostly for digital applications [BRI12A, THO12, BRI12B, AKI12B, ZIE12] as it has been reviewed in chapter 2. But, until recently, less attention has been paid to analog applications due to the fact that IMWP is a much younger emerging discipline which is experiencing its impulse in the last years.

Chapter 3: Analog applications

This chapter presents different researches carried out in the analog scope for application in the field of IMWP, all of them using CMOS-compatible electro-optic SOI modulators which validate the potential of silicon CMOS photonics as a promising approach for enabling large scale photonic integration driving the development of integrated microwave photonics applications.

One of the impediments for MWP link to reach higher performance and replace the traditional microwave solutions is the distortion added by the E/O and O/E conversions and moreover, if the electro-optic conversion is carried out by a nonlinear-material modulator as silicon-based. Besides, from the perspective of system performance, silicon modulators cannot yet provide the stringent requirements of MWP in the management of analog signals; hence most of the advantages in silicon photonics for MWP have been focused on exploiting the optical nonlinearities [MAR12] but also on enhancing the linearity of the silicon devices. For these reasons, an analytical model to obtain distortion closed expressions of the most widely used modulator structure that is the Mach-Zehnder Interferometer (MZI), is theoretically developed and experimentally validated in the section 3.2. Further, the model allows the designer to set a proper choice of modulator parameters to linearize the device or to enhance the nonlinearities giving a potential tool to predict the nonlinear modulator performance and the parameters needed for a full study of a microwave photonic link [GUT13B].

The following sections 3.3 and 3.4 review two of the above mentioned MWP applications in which we have used a silicon-based electro-optic modulator, explaining more deeply in each case the basic principles and showing our experimental measurements. First, the section 3.3 is devoted to describe and demonstrate experimentally a method for photonic-mixing of microwave signals exploiting the nonlinearities produced by a silicon-based slow-light MZI modulator enhanced via slow-light propagation, which is used to successfully demonstrate an up-conversion process [GUT12C]. Finally, in section 3.4, a photonic-based integrated filter for the processing of RF signals is implemented by a silicon-based simple MZI modulator [GUT13A]. In both sections, a review of the basic theory and, additionally, the state-of-the-art of SOI devices used in the corresponding application are provided and the experimental results obtained showing the potential of using CMOS silicon-based modulators for IMWP technology. Finally, in section 3.5 the set-ups used for the RF characterization are explained in detail describing the equipment models and showing pictures of the real set-ups in the Nanophotonics Technology Center facilities.

3.2. Analytical model for silicon-based MZIs nonlinear distortion

In this section, an analytical model for calculating the distortion for RF signals added by silicon-based electro-optic MZI modulators is developed by considering the nonlinearity on the effective index change curve with the operation point and the device structure simultaneously. Distortion expressions are obtained and theoretical results are presented showing that optimal modulator parameters can be found to linearize it. Moreover, the harmonic distortion of a silicon-based asymmetric MZI is RF characterized and used to corroborate the theoretical results. Based on the present model, the nonlinear distortion in terms of bias voltage or operating wavelength is calculated and validated by comparing with the experimental data, showing a good agreement between measurements and theory. Analog photonic link quality parameter like carrier-to-distortion is one of the parameters that can be found with that model. Finally, the modulation depth is measured to assure that no over-modulation is produced. Here and for the development of our model, we assume that the analog photonic link (APL) nonlinearity is dominated only by the modulation device (by the E/O conversion). Thus, we assume that other devices in the APL, such us the photo-detector (the O/E conversion), are linear. These components also contribute to APL nonlinearities but generally their contributions are much smaller compared to that of the modulation devices [MAR09] and, hence, most of the time can be neglected. It can be pointed now that, the aim of this section is to demonstrate the potential and wide capability design that provides you having closed equations for the calculation of the distortion and demonstrate the accuracy of the model with experimental results [GUT13B].

3.2.1. Introduction: state-of-art

As mentioned in the introduction of this chapter, the heart of any MWP system is the MWP link which basically consists of a modulation device for E/O conversion connected by an optical fiber to a photodetector that does the O/E conversion. These conversions in the MWP link add nonlinear optical distortions to the output RF signal which must be reduced or exploited depending on the application to carry out in the system. On one hand, high linearity is required for photonic RF signal transmission, so the nonlinear distortions due to these E/O-O/E conversions are a limiting factor for this purpose. In this case, the distortion terms closest to the frequency of the transmitted signal have to be reduced or ideally eliminated. Two important performance metrics for measuring the linearity of an analog optical link is the spurious-free dynamic range (SFDR) and carrier-to-distortion ratio (CDR). The former is defined as the signal-to-noise ratio of a carrier when the largest spur signal is at the noise floor level.

A lot of methods to improve the commercial $LiNbO_3$ modulators linearity have been published. The general idea in these linearization schemes is to introduce certain pre-distortion to compensate for the existing ones with the cost of increased system

complexity. Improved linearity has been demonstrated by predistorting the optical signal using complex MZMs. Among them are the dual-polarization technique [JOH88], parallel MZI scheme [KAR07, BRID95] and cascade MZI scheme [SAB95, BET96, KAR08]. These schemes show difficulties of implementation and strict requirements placed on the precise control of lengths and voltages on multiple electrodes, so complex modulators are unstable and difficult to control at arbitrary operating points. Alternatively, the linearization can be performed in electronic domain by predistorting the EOM driving voltage [JAL98, WILL99], but that method requires high speed nonlinear electronic devices. Other approach on which has been paid little attention to reduce the modulator nonlinearities is the post-compensation. In [ZHA12] a post-compensation method without any pre-distortion is proposed and experimentally demonstrated to compensate in optical domain for the nonlinearity of an MZM in RoF systems.

In silicon, a thorough study of the nonlinearities of a Mach-Zehnder Modulator (MZM) and a modulator linearization scheme was reported in [KHI11], showing a silicon-based modulator with superior linearity with respect to a conventional MZI modulator. In that work, the modulator linearity is analyzed theoretically, using models and numerical simulations. However, the expressions presented are limited to a symmetric push-pull configuration which automatically cancels some distortion terms of the phase response. Moreover, other silicon-based modulators have been used for RoF transmission allowing very high linear features such operating points with 50dB [VAC10] or 57dB [SON10] of carrier-to-distortion ratio for MZM and microring-based modulators respectively, showing significant advantages for emerging RoF applications. In the former, the SFDR value was not reported and in the second one a 96dB.Hz$^{2/3}$ value of SFDR was demonstrated. Additionally, in [AYA12] the nonlinearities of another silicon ring modulator were characterized and they found a SFDR of 84 dB.Hz$^{2/3}$, and recently, in [STR13] it was demonstrated that the linearity of a silicon MZM can be improved by differentially driving it in a push-pull configuration allowing a high SFDR of 97 dB.Hz$^{2/3}$. The measurements of all these published works are verified by simulation results showing the same trend but no closed analytical expressions of the nonlinearities are presented. These results are summarized in the next Table 3-1.

Reference	Optical structure	$SFDR_{HD}$(*) [dB.Hz$^{1/2}$]	$SFDR_{IMD}$(*) [dB.Hz$^{2/3}$]	Noise Floor [dBm/Hz]	CDR [dB]
[AYA12]	Microring	64.5	84	-169	-
[VAC10]	MZI	-	-	-	50
[SON10]	Microring	80	96	-165	57
[STR13]	MZI	82	97	-165	-

Table 3-1: Reported results in photonic transmission of RF signals in the scope of MWP field, (*) In the next section 3.3.1 it will be explained the difference between harmonic distortion (HD) and intermodulation distortion (IMD).

In contrast with the plain analog signal transport, some nonlinear applications such as mixing or frequency conversion have been demonstrated in the IMWP field [GUT12C]. In these cases, the nonlinear operation of the modulator is exploited, taking advantage of the distortion produced by the nonlinearities. In the section 3.3 we will center in this kind of application. The purpose of naming them at this point is to highlight the fact that the study of the distortion properties of silicon electro-optic modulators is an important question for all silicon IMWP applications.

3.2.2. Electro-optic MZI modulator linearity

The most common way to characterize the modulator linearity is to perform a tone modulation which can be classified into two categories: single-tone or multi-tone modulation. Obviously, they differ in the number of carrier frequencies included in the modulating signal and they produce different types of distortion. Harmonic distortion can be defined as a single-tone (only a single frequency carrier is used as modulating signal) distortion product caused by device nonlinearity.

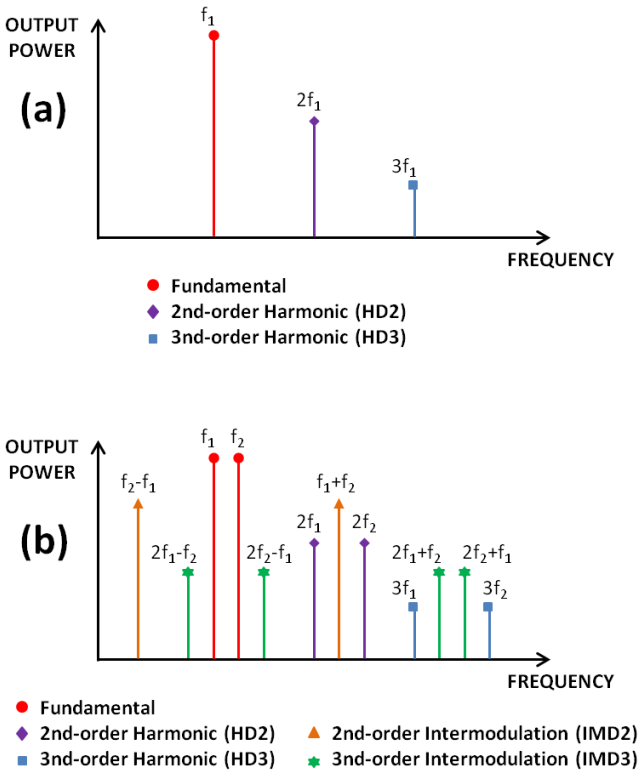

Figure 3-2: (a) Single-tone and (b) two-tone output spectrum diagram of a nonlinear device showing the frequency and the names of the generated distortion products.

When a nonlinear device is stimulated by a signal at frequency f_1, spurious output signals can be generated at the harmonic frequencies $2f_1$, $3f_1$, $4f_1$, i.e. at Nf_1. The order of the distortion product is given by the N frequency multiplier. On the other hand, intermodulation distortion is a multi-tone distortion product that results when two or more signals are present at the input of a nonlinear device. The 2^{nd}-order

intermodulation products of two signals at f_1 and f_2 (two-tone modulation) would occur at f_1+f_2, $f_2–f_1$, $2f_1$ and $2f_2$ and 3rd-order at $2f_1+f_2$, $2f_1-f_2$, f_1+2f_2 and f_1-2f_2, that is, at $Nf_1\pm f_2$ or $f_1\pm Nf_2$ with N=1 for the 2nd-order terms and N=2 for the 3rd ones. In Figure 3-2 a representation of a single-tone (a) and two-tone (b) test output spectrum diagrams of a nonlinear device are illustrated. The two-tone test is the most widely implemented to fully characterize the nonlinear distortion. As it can be observed in Figure 3-2(b), if the modulator is used in broadband application, the second harmonic distortion is the most dominant distortion that needs to be studied. Many of the analog microwave applications however, have bandwidths less than an octave, in which the second order distortion is not a problem and third-order intermodulation distortion has to be taken into account.

It is well known from theory and many published works [COX04, MAR09] that linear material-based modulators such $LiNbO_3$, in which the distortion is produced only by the nonlinear modulator transfer function, which is periodic and usually have the same performance with the bias point. This periodic function is a nonlinear cosine-squared and at quadrature bias point (QB), all even order distortion terms ideally vanish (in practice they are minimized), while fundamental signal and odd order terms maximize; by contrast, at maximum (MATB) or minimum transmission bias point (MITB), the odd order distortion terms are suppressed (again ideally) and the even ones are maximized. Figure 3-3 shows a spectrum diagram example for a single-tone test in the three key points of the modulator transfer function for a linear-material modulator.

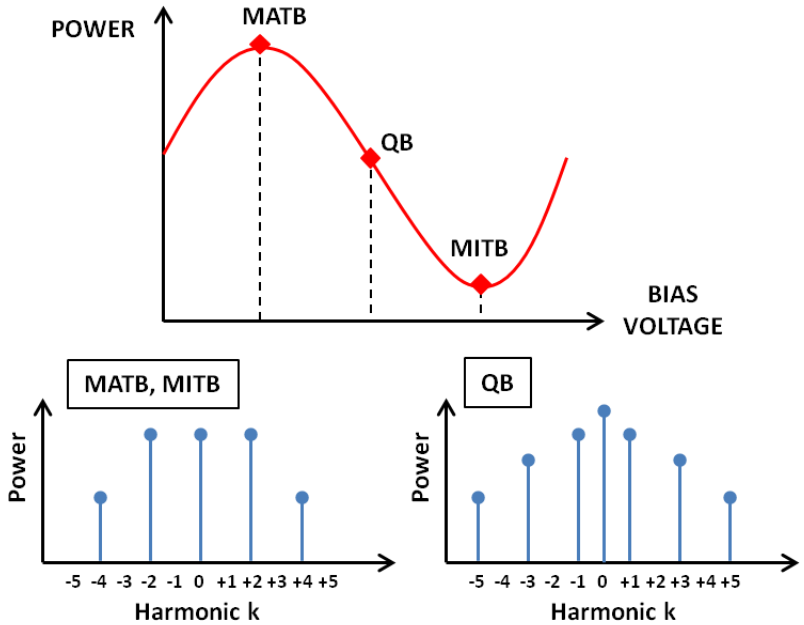

Figure 3-3: Output spectrum diagram example for a single-tone test modulation in a linear-phase modulator for the three key points of the transfer function: MATB, QB and MITB.

Although the work of in this thesis is focused in integrated SOI modulators, the distortion of a commercial LiNbO3 electro-optic modulator has been characterized, with the aim of corroborating the distortion behavior explained above. The device used was

40Gbit/s modulator from Corning OTI Inc. and the setup used for the measurements is shown in Figure 3-4.

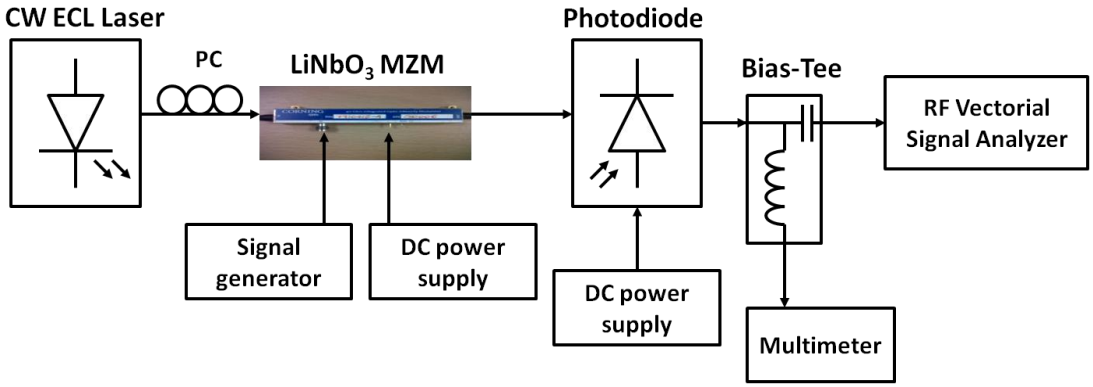

Figure 3-4: Schematic of the setup used to carry out the distortion characterization of a commercial $LiNbO_3$ modulator.

The laser used in this measurement was an external cavity laser (ECL) with a wavelength of 1550 nm and an optical output power of 8dBm. The laser is pigtailed with a standard single mode fiber and the polarization is optimized via the use of a polarization controller (PC). The MZM bias voltage was controlled with a voltage supply and the RF signal was supplied to the modulator using a RF signal generator. The modulated optical power from the modulator was then detected using a photodetector. The detector output was connected to a bias-Tee and the DC output is connected to a multimeter, while the RF output was connected to an RF spectrum analyzer (detail of all components and measurement devices in section 3.5).

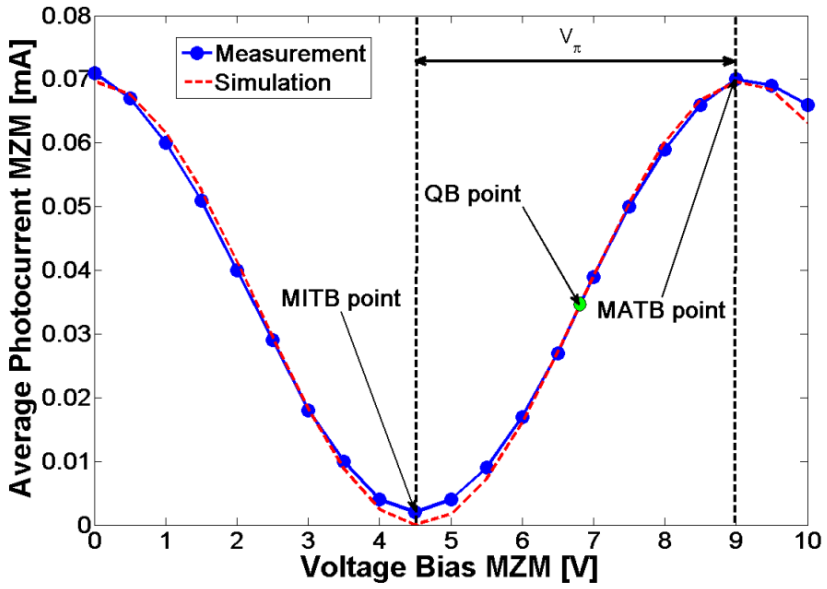

Figure 3-5: Theoretical [MAR09] and experimental average photocurrent as a function of the bias voltage of a commercial $LiNbO_3$ MZI modulator.

DC MZM characterization was done by means of varying the modulator bias voltage. The average detected photocurrent was measured for every bias voltage using a multimeter obtaining the typical modulator V/I curve as shown in Figure 3.5. In such

Figure are also shown the three key bias operation points: MATB, QB and MITB. Moreover, the measurements results were compared with the simulation results from analytical expressions developed in [MAR09]. From the average photocurrent measurements, we found that the value of the half-wave voltage V_π was 4.5V.

On the other hand, the distortion characterization was performed by means of a single-tone test in which the RF signal frequency was set to be 2 GHz and with a RF power of 10dBm. For each modulator bias voltage, the fundamental signal, the second-order harmonic distortion, HD2 (at $2f_{RF}$) and the third-order harmonic distortion, HD3 (at $3f_{RF}$) powers were measured (and shown in Figure 3-6) using the RF spectrum analyzer at the frequencies of f_{RF}=2 GHz, $2f_{RF}$=4 GHz and $3f_{RF}$=6 GHz, respectively. Again the measurements were validated by the analytical expressions presented in [MAR09] and a perfect matching between theory and practice were obtained.

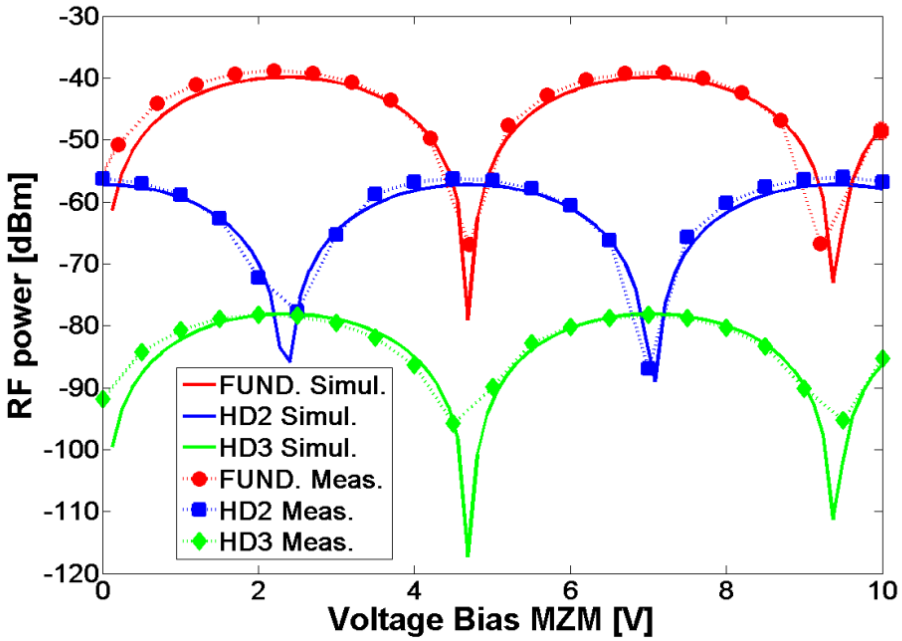

Figure 3-6: Theoretical and experimental fundamental and 2nd and 3rd harmonic distortion powers as a function of the bias voltage of a commercial $LiNbO_3$ MZI modulator.

We can easily identify in the above figure by comparing with the previous I/V curve shown in Figure 3.5, the QB point (around 2.25V and 6.75V) as the bias voltage that gives minimum HD2 power and the MITB (around 4.6V) and MATB (around 9.3V) points as bias voltages for which the fundamental and the HD3 powers are minimized, corroborating the distortion feature explained at the beginning of this section for the linear-material electro-optic modulators.

In contrast with linear material-based modulators such $LiNbO_3$, for a nonlinear material such silicon, the distortion depends on additional factors besides the DC bias voltage as we will see later. Moreover, the index change caused by the plasma dispersion effect, which it has been mentioned several times along this thesis to be the most adopted electro-optic effect in silicon, is a nonlinear effect, as it can be observed in

the Soref equations [SOR87]. This nonlinear dependency of the index change with the applied voltage also produces intermodulation and harmonic distortion terms. So, this is the main motivation for the development of a model with analytical expressions which can help the designer to predict the distortion performance in a silicon-based MZI modulator.

3.2.3. Analytical model development

The starting point of the model is the effective index change with the applied DC voltage. In a silicon-based modulator under plasma dispersion effect, in this case carrier depletion effect, one can derive such effective index change from the depletion width of the *PN* en junction. For an asymmetrically doped junction, meaning that the n-doping concentration is higher than the p-doping, the depletion width can be represented as:

$$W_D = \sqrt{\frac{2\varepsilon\ \ V_b + V_{app}}{eN_A}} \tag{3.1}$$

Where W_D is the depletion width, ε is the permittivity of silicon, e is the electron charge, N_A is the acceptor concentration, V_b is the built-in voltage (contact potential) and V_{app} is the applied voltage. On the other hand, the effective index modulation (dn) due to the bias voltage change (dV_{app}) can be described by the following Equation (3.2) [VAC10, CHU95]:

$$\frac{dn}{dV_{app}} = \frac{\delta}{e\varepsilon A^2} C_J^2 \tag{3.2}$$

$$C_J = \frac{\varepsilon A}{W_D} \tag{3.3}$$

Where n is the effective refractive index of the waveguide, δ is a empirical constant that accounts for both confinement effect (overlap between the optical mode and the spatial distribution of free carrier density change in the waveguide phase shifter) and the coefficient of charge density induced refractive index change, C_J is the junction capacitance and A is the area of the capacitor. From (3.1) to (3.3) we find by integration that the effective index change with the applied voltage can be approximated by a logarithmic curve as shown in Equation (3.4). As we have already mentioned, this dependency has a nonlinear form for a silicon-based modulator.

$$\Delta n_{eff} = k \ln\left(1 + \frac{V_{app}}{V_b}\right) \tag{3.4}$$

where $k=\delta N_A/2$ (dimensionless) and V_b (in volts) are constants. In our case, we will use

these parameters to fit the curve with the DC performance experimental results of the effective index variation. This effective index change induces a phase shift that accomplishes the Equation (3.5) already described in Chapter 1.

$$\Delta\Phi = \frac{2\pi}{\lambda}\Delta n_{eff} L_{ACT} \tag{3.5}$$

where λ is the wavelength, Δn_{eff} is the effective index change and L_{ACT} is the phase shifter length.

Furthermore, in case of having a length difference between two arms of the MZI also induces an additional phase shift proportional to this length difference. Thereupon, we can regard that the total induced phase shift is due to two factors: the device structure, related with modulator transfer function, which has been called $\Delta\Phi_{\text{Bias}}$ and allows driving the modulator to the appropriate operation bias point; and the silicon in the active area, which has been named as $\Delta\Phi_{\text{Si}}$, and it is described in Equation (3.7). So, the final phase shift expression can be written as:

$$\Delta\Phi_{TOT} = \Delta\Phi_{Si} + \Delta\Phi_{Bias} \tag{3.6}$$

where:

$$\Delta\Phi_{Si} = \frac{2\pi}{\lambda}\Delta n_{eff} L_{ACT} \tag{3.7}$$

The detected optical power at the output of a MZI modulator is:

$$P_{out} = P_{in}\cos^2\left(\frac{\Delta\Phi_{TOT}}{2}\right) \tag{3.8}$$

where P_{in} is the input optical power to the modulator. If we substitute the total phase shift described by (3.6) in (3.8) and expand the cosine, using the next trigonometric relations:

$$\cos^2 x = \frac{1}{2}\left(1+\cos 2x\right) \tag{3.9}$$

$$\cos(x+y) = \cos x \cos y - \sin x \sin y \tag{3.10}$$

we can state the output power as:

$$\begin{aligned} P_{out} &= P_{in}\left(\frac{1+\cos\Delta\Phi_{TOT}}{2}\right) = P_{in}\left(\frac{1+\cos(\Delta\Phi_{Si}+\Delta\Phi_{Bias})}{2}\right) = \\ &= P_{in}\left(\frac{1}{2}+\frac{1}{2}\cos\Delta\Phi_{Si}\cos\Delta\Phi_{Bias} - \frac{1}{2}\sin\Delta\Phi_{Si}\sin\Delta\Phi_{Bias}\right) \end{aligned} \tag{3.11}$$

Also, the phase shift due to the silicon including the Equation (3.4) of the effective index change into the Equation (3.7) results:

$$\Delta\Phi_{Si} = \frac{2\pi}{\lambda} L_{ACT} \Delta n_{eff} = \sigma \ln\left(1 + \frac{V_{app}}{V_b}\right) \tag{3.12}$$

where we have defined the design parameter σ (in radians) as shown in the Equation (3.13):

$$\sigma = \frac{2\pi}{\lambda} L_{ACT} k \tag{3.13}$$

On the other hand, in a two-tone test, the input RF signal takes the form:

$$V_{rf} = V_{RF_1} \cos\ \omega_1 t\ + V_{RF_2} \cos\ \omega_2 t \tag{3.14}$$

where V_{RF1} and V_{RF2} are the RF signals amplitudes and $\omega_1=2\pi f_1$ and $\omega_2=2\pi f_2$ are the angular modulating frequencies of the two input tones. Thus, the total applied voltage to the electro-optic modulator is the sum of one DC term and one RF term, as:

$$V_{app} = V_{DC} + V_{rf} = V_{DC} + V_{RF_1} \cos\ \omega_1 t\ + V_{RF_2} \cos\ \omega_2 t \tag{3.15}$$

If we make a compilation of the above equations and we substitute each equation into each other, we realize that the final expression for the silicon phase shift results:

$$\begin{aligned}
\Delta\Phi_{Si} &= \sigma \ln\left(1 + \frac{V_{DC} + V_{RF_1} \cos\ \omega_1 t\ + V_{RF_2} \cos\ \omega_2 t}{V_b}\right) = \\
&= \sigma \ln\left(1 + \frac{V_{DC}}{V_b} + \frac{V_{RF_1}}{V_b} \cos\ \omega_1 t\ + \frac{V_{RF_2}}{V_b} \cos\ \omega_2 t\ \right) = \\
&= \sigma \ln\left(X_{DC} + \frac{V_{RF_1}}{V_b} \cos\ \omega_1 t\ + \frac{V_{RF_2}}{V_b} \cos\ \omega_2 t\ \right) = \\
&= \sigma \ln\left[X_{DC}\left(1 + \frac{V_{RF_1}}{V_b X_{DC}} \cos\ \omega_1 t\ + \frac{V_{RF_2}}{V_b X_{DC}} \cos\ \omega_2 t\ \right)\right] = \\
&= \sigma \ln\left[X_{DC}\left(1 + X_{RF_1} \cos\left(\omega_1 t\right) + X_{RF_2} \cos\left(\omega_2 t\right)\right)\right]
\end{aligned} \tag{3.16}$$

where:

$$X_{DC} = 1 + \frac{V_{DC}}{V_b} \tag{3.17}$$

$$X_{RF_1} = \frac{V_{RF_1}}{V_b X_{DC}} \tag{3.18}$$

$$X_{RF_2} = \frac{V_{RF_2}}{V_b X_{DC}} \tag{3.19}$$

For simplicity, the model has been developed under the assumption that the two tone input signals are of equal amplitude and the small signal approximation $V_{RF} << V_b$, so:

$$X_1 = X_2 = X = \frac{V_{RF_1}}{V_b X_{DC}} = \frac{V_{RF}}{V_b\left(1+\frac{V_{DC}}{V_b}\right)} = \frac{V_{RF}}{V_b + V_{DC}} << 1 \tag{3.20}$$

Now, we can apply the relation *ln(a.b)=ln(a)+ln(b)*, so:

$$\Delta\Phi_{Si} = \sigma \ln\ X_{DC}\ + \sigma \ln\left[1 + X\ \cos\ \omega_1 t\ + \cos\ \omega_2 t\ \right] \tag{3.21}$$

Finally, we can write the silicon phase shift as described in the Equation (3.22):

$$\Delta\Phi_{Si} = \sigma\ Y_{DC} + \ln\ 1+Y \tag{3.22}$$

where Y and Y_{DC} are given by Equation (3.23) and (3.4) respectively:

$$Y = X\ \cos\ \omega_1 t\ + \cos\ \omega_2 t \tag{3.23}$$

$$Y_{DC} = \ln\ X_{DC}\ = \ln\left(1+\frac{V_{DC}}{V_b}\right) \tag{3.24}$$

Now, the silicon phase shift can be expanded into the natural logarithm Taylor series as follows:

$$\ln\ 1+Y\ = \sum_{n=1}^{\infty} -1^{\ n+1}\frac{Y^n}{n} = Y - \frac{1}{2}Y^2 + \frac{1}{3}Y^3 \ldots \tag{3.25}$$

The silicon phase shift resulted of this Taylor series will consist of a DC component which does not depend on ω, and a set of harmonics and intermodulation distortion terms as it is shown in the Equation (3.26):

$$\Delta\Phi_{Si} = \sigma \begin{pmatrix} -\frac{1}{2}X^2 + \left(X + \frac{3}{4}X^3\right)\cos\ \omega_1 t \\ -\frac{1}{4}X^2\cos\ 2\omega_1 t\ + \frac{1}{12}X^3\cos\ 3\omega_1 t \\ -\frac{1}{2}X^2\cos\ \ \omega_1 \pm \omega_2\ \ t\ + \frac{1}{4}X^3\cos\ \ 2\omega_1 \pm \omega_2\ \ t \end{pmatrix} \tag{3.26}$$

Including this expression of the silicon phase shift into the Equation (3.11) of the output optical power we can perform another Taylor expansion of the cosine and sine which are as follow:

$$\sin\ x\ = \sum_{n=0}^{\infty} \frac{-1^{\ n}}{2n+1\ !} x^{2n+1} = x - \frac{x^3}{3!} + \frac{x^5}{5!} \ldots \tag{3.27}$$

$$\cos\ x\ = \sum_{n=0}^{\infty} \frac{-1^{\ n}}{2n\ !} x^{2n} = 1 - \frac{x^2}{2!} + \frac{x^4}{4!} \ldots \tag{3.28}$$

The result is again a set of harmonic and intermodulation products. The amplitudes of all these components will be sums of linear combinations of X, Y_{DC} and σ. The desired expressions that describe the modulator amplitudes nonlinearities are finally obtained and described by the Equations (3.29)-(3.31) in which the sub-index '*c*' is referring to cosine and '*s*' to sine:

$$P_{FUND.}\ \ \omega_1\ = \frac{1}{2}\cos\ \Delta\Phi_{Bias}\ \ \Phi_{FUNDc} X\ - \frac{1}{2}\sin\ \Delta\Phi_{Bias}\ \ \Phi_{FUNDs} X \tag{3.29}$$

$$P_{IMD2}\ \ \omega_1 \pm \omega_2\ = \frac{1}{2}\cos\ \Delta\Phi_{Bias}\ \left[\Phi_{IMD2c} X^2\right] - \frac{1}{2}\sin\ \Delta\Phi_{Bias}\ \left[\Phi_{IMD2s} X^2\right] \tag{3.30}$$

$$P_{IMD3}\ \ 2\omega_1 \pm \omega_2\ = \frac{1}{2}\cos\ \Delta\Phi_{Bias}\ \left[\Phi_{IMD3c} X^3\right] - \frac{1}{2}\sin\ \Delta\Phi_{Bias}\ \left[\Phi_{IMD3s} X^3\right] \tag{3.31}$$

As we can observe, the fundamental, 2nd-order and 3rd-order amplitudes are the terms with linear, quadratic and cubic dependence on the modulating signal V_{RF}, respectively. Finally, the cosine phase expressions are:

$$\Phi_{FUNDc} = -Y_{DC}\ \ \sigma^2 \tag{3.32}$$

$$\Phi_{IMD2c} = \left(\frac{1}{2}Y_{DC} - \frac{1}{2}\right)\sigma^2 \tag{3.33}$$

$$\Phi_{IMD3c} = \left(-\frac{1}{4}Y_{DC} + \frac{3}{8}\right)\sigma^2 \tag{3.34}$$

And the sine phase expressions:

$$\Phi_{FUNDs} = \sigma - \left(\frac{1}{2}{Y_{DC}}^2\right)\sigma^3 \tag{3.35}$$

$$\Phi_{IMD2s} = \left(-\frac{1}{2}\right)\sigma + \left(\frac{1}{4}{Y_{DC}}^2 - \frac{1}{2}Y_{DC}\right)\sigma^3 \tag{3.36}$$

$$\Phi_{IMD3s} = \left(\frac{1}{4}\right)\sigma - \left(\frac{1}{8}{Y_{DC}}^2 - \frac{3}{8}Y_{DC} + \frac{1}{8}\right)\sigma^3 \tag{3.37}$$

The IMD amplitudes differ from the HD amplitudes even though they are basically generated by the same mechanism. It has been found that the IMD2 amplitude is twice that of the HD2 amplitude while the IMD3 amplitude is three-times the HD3 amplitude. However, the powers of these components rather than the amplitudes are usually measured. If we regard the amplitude to be either a current or a voltage, then the power considered here is an electrical or an RF power. Thus we can easily identify that the powers of the distortion terms are proportional to the square of their amplitudes. So, we can deduce that the power of the HD2 terms expressed in decibels are approximately 6 dB lower compared to the IMD2 powers, and the HD3 powers are approximately 9.5 dB lower relative to the IMD3 powers. Therefore, we can affirm that:

$$P_{HD2} \approx P_{IMD2} - 6dB \tag{3.38}$$

$$P_{HD3} \approx P_{IMD3} - 9.5dB \tag{3.39}$$

In the above equations, higher order terms than 3 have been simplified (in the original, there are terms up to order 7). The deviation suffered by this simplification can be neglected. As proof, the next Figure 3-7 represents the 2nd and 3rd harmonic and intermodulation products of a 1mm-long silicon-based MZI, in which the dotted line corresponds to the distortion obtained with the original equations without simplification and the solid line to the same obtained from the simplified ones. As it can be observed, the highest deviation of only 0.05nm is produced in the fundamental term which is an acceptable value. Moreover, in that figure one can confirm the relation between harmonic and intermodulation products (Equations 3.38 and 3.39).

As we can observe in the Equations (3.32)-(3.37), all amplitudes are function of σ, so one can set to zero and cancel the desired nonlinearity with an optimum design parameter for this purpose. Therefore, the model provides a wide range of possibilities of linearization including all design parameters of the modulator. Also, since the model starts from the effective index change versus DC bias voltage, any difference in dimensions or diode doping profile respect to the design values due to fabrication variations will change the curve and will be taken into account.

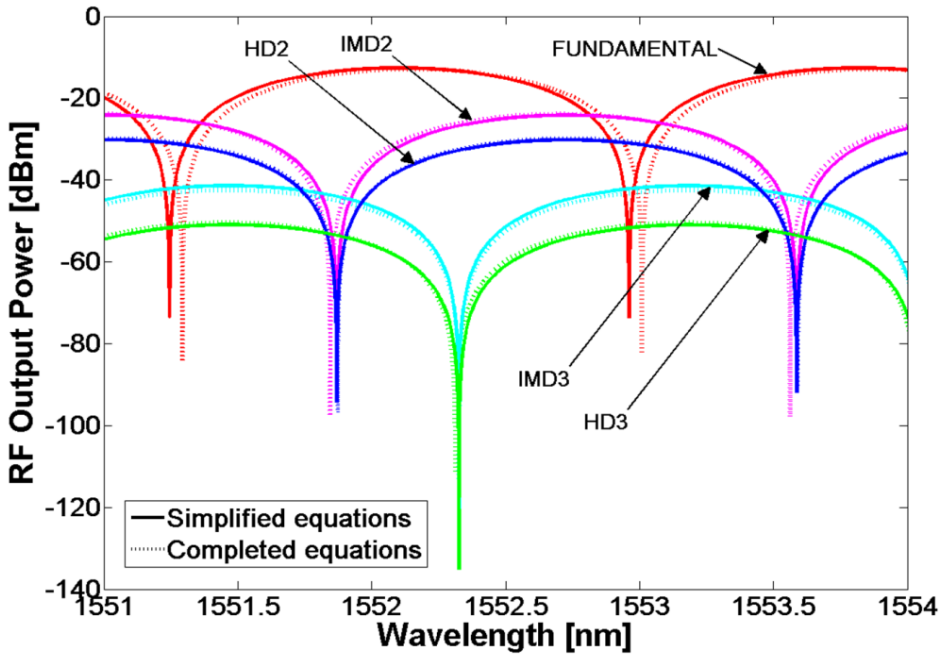

Figure 3-7: Distortion as a function of the wavelength in a 1mm-long silicon-based MZI with 180μm of length difference between their arms, for a V_{DC}=1V. Dotted line corresponds to the distortion obtained with the original equations and the solid line to the same obtained from the simplified ones.

As it can be observed from the dependency of distortion amplitudes on the parameter σ in the obtained analytical expressions, the phase shifter length is a parameter which strongly affects the distortion. So, there will be an optimum phase shifter length which allows linearizing the modulator cancelling the 3rd-order intermodulation product (dominant for less than one octave systems).

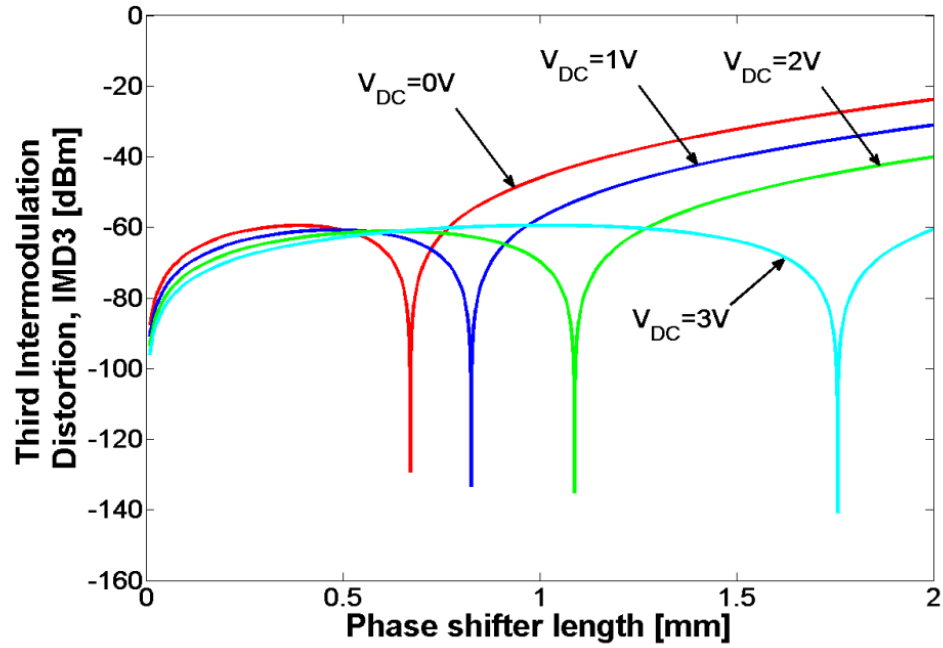

Figure 3-8: Third-order intermodulation product power as a function of the phase shifter length in a $\Delta\Phi_{Bias}=\pi/2$ modulator with a wavelength laser of 1550nm.

For example, starting from a nonlinear effective index change curve as a function of DC bias voltage with $k=0.52.10^{-3}$ and $V_b=8V$ in the Equation (3.4), in a quadrature bias modulator (modulator is designed such that the bias phase shift between the two arms at $V_{DC}=0$ and $V_{RF}=0$ is $\pi/2$), one can linearize the modulator cancelling the 3rd-order nonlinearity knowing the optimum phase shifter length. Figure 3-8 shows the lengths of the phase shifter which yield the most linear performance for several DC voltages. It can be observed, for example, that for a DC voltage of 1V the modulator phase shifter length must be 825.5µm.

Furthermore, as it can be deduced from the Equations (3.29)-(3.31), the nonlinearity of a silicon modulator also depends on the bias phase. Figure 3-9 shows this dependency for a 1mm MZI phase shifter length. This figure represents a contour of the 2nd-order (Figure 3-9(a)) and 3rd-order (Figure 3-9(b)) intermodulation distortions, P_{IMD2} and P_{IMD3} respectively, as a function of the DC voltage and bias phase. For example, for 1V of DC we can eliminate the 3rd order term if the bias phase is 0.47π. In such case, the 2nd order intermodulation product would have a value of -26.54dBm. In the same way, for 4V a bias phase shift of 0.15π would result in the 3rd order intermodulation term cancellation.

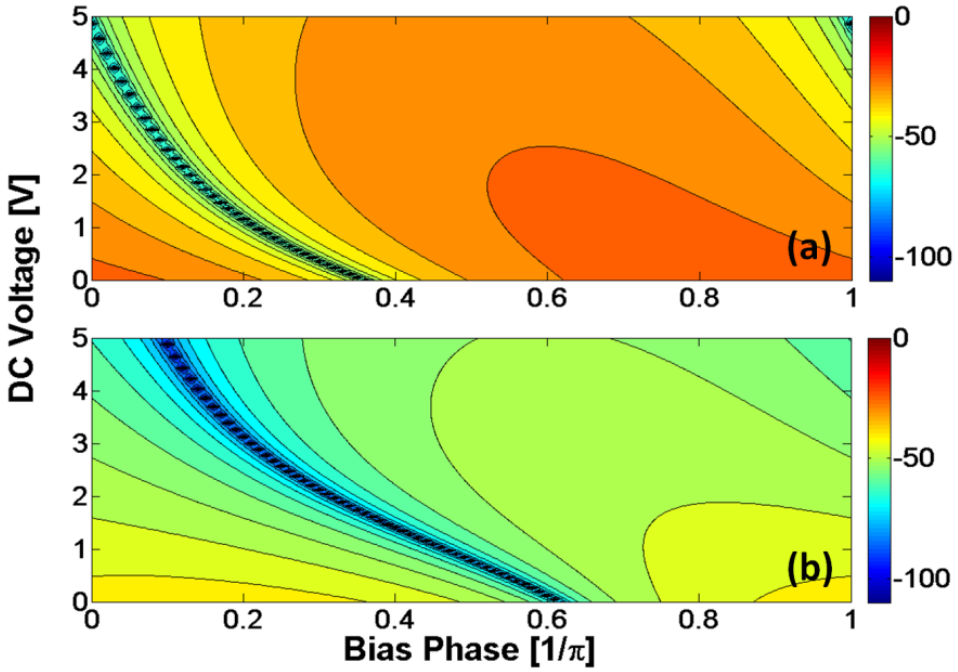

Figure 3-9: Contour of 3rd order (a) and 2nd (b) intermodulation products power as a function of bias phase and DC bias voltage for a MZI with a phase shifter length of 1mm and λ=1550nm.

In order to corroborate our analytical model, we have performed a simulation in which the signal at the modulator output (time domain waveform) is converted to the frequency domain by performing a Fourier Fast Transfer. Then, one can select the desired frequency components and obtain its amplitude. This simulation allowed us to check the correct model performance since both simulation and analytic model show similar results. This can be observed in Figure 3-10 where only some level error can be

appreciated between simulation and our analytical model, but curves follow the same trend. In any case, the analytical expressions always overestimate the simulation results.

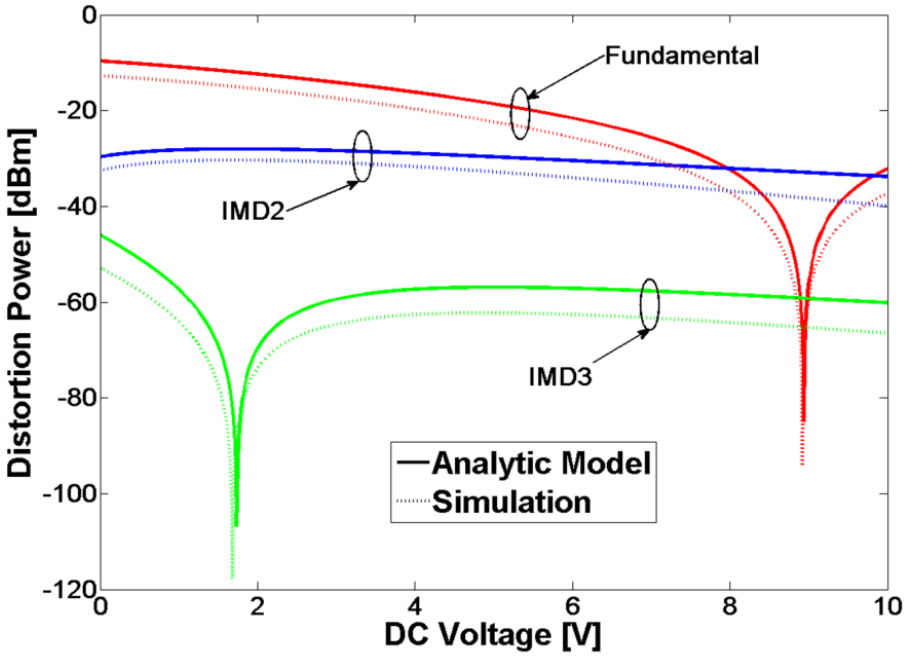

Figure 3-10: Fundamental and intermodulation products power as a function of DC voltage in a fixed wavelength of 1550nm for a 1mm MZI under the condition $\Delta\Phi_{Bias}=\pi/2$.

For a fixed quadrature modulator with an active length of 1mm and a fixed 1550nm wavelength, we can obtain from Figure 3-9 that approximately 1.7V is the optimum DC voltage for cancelling the 3rd order intermodulation term. Moreover we can observe in such figure another point of view of the model application: for a DC voltage around 8.9V the fundamental term vanishes and the 2nd order intermodulation product is maximized. This point could be useful for a frequency up-conversion process. The input signal can be set in the fundamental frequency and the signal information can be received in the 2nd order term ensuring a good level of power in such signal.

It should be noticed that the free carrier concentration variation due to the plasma dispersion effect alters the imaginary part of the refractive index thus introducing absorption losses in the material. Such absorption losses usually depend on the applied voltage in a nonlinear form, which also needs to be taken into account in the nonlinear distortion analysis.

First, the effect of constant optical losses in the arms of the MZI on the nonlinear distortion has been analyzed by means of simulations. It has been obtained that having an unbalanced power distribution at the arms of the MZI only affects to the absolute value of the RF output power but the transmission response remains unaltered so, quality parameters as CDR or SFDR are not affected.

On the other hand, the dependency of absorption losses with voltage can also be approximated by a logarithmic form. Simulation results show that in this case the transmission response of the intermodulation products is red-shifted with respect to the response obtained with the developed model, i.e. the case of having no loss. Therefore, the variation of absorption losses ($\Delta\alpha=\alpha_{max}-\alpha_{min}$) with voltage will reduce the accuracy of the model. However, the effect introduced by losses can be compensated in a real case by adjusting the bias (Φ_{bias}) for the target V_{DC}.

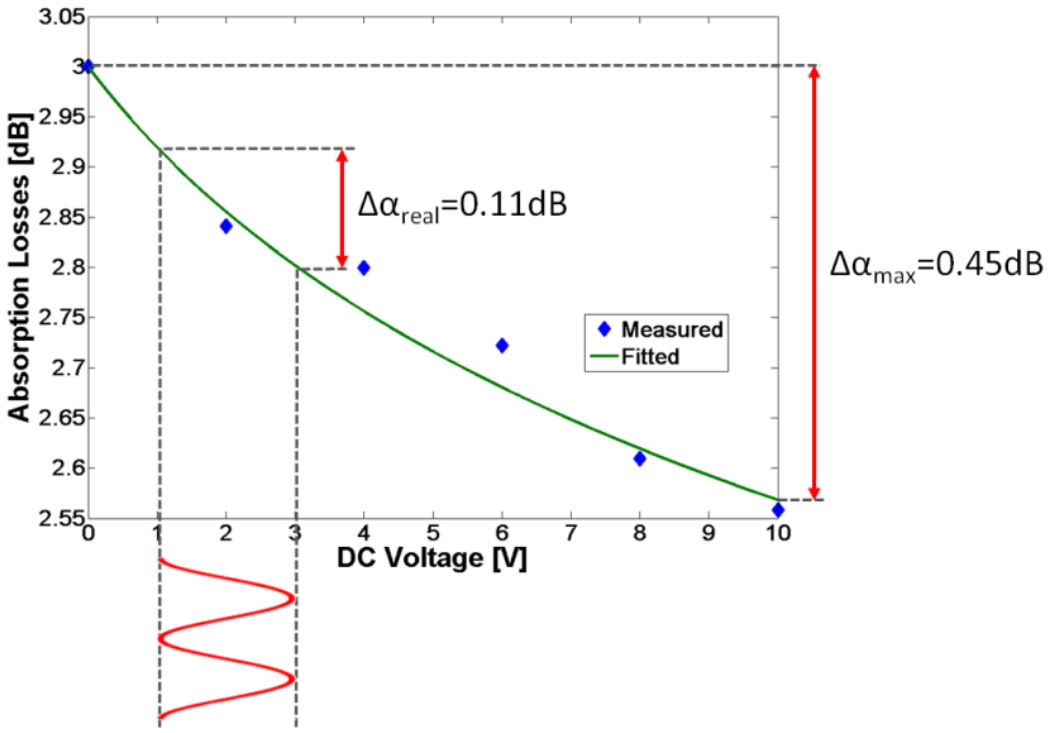

Figure 3-11: Absorption losses variation with the DC voltage. The fitted curve is obtained from a logarithmic nonlinear approximation. It is shown both the maximum variation of absorption losses between 0V and 10V and the absorption losses variation with the voltage for $2V_{pp}$ of RF modulation voltage.

In the specific case of a 1mm silicon MZI modulator which will be used to validate the analytical model, the measured voltage-dependent absorption losses are very low so the effect is almost negligible. It has been obtained that the maximum variation is $\Delta\alpha$=0.45dB between 0 and 10V, that is, for ΔV=10V. So, if the RF modulation voltage is around $2V_{pp}$, the variation of absorption losses with voltage will be of the order of 0.11dB, as shown in Figure 3-11.

Figure 3-12 shows the simulated RF output power of the IMD3 intermodulation product as a function of the bias phase and DC voltage. It can be seen that the effect of losses are almost negligible for the case of $\Delta\alpha$=0.45dB but discrepancies are more noticeable as losses increases. However, if, for example, the IMD3 is minimized for V_{DC}=2V and a $\Phi_{bias}=0.5\pi$. The effect of losses could be compensated just by slightly increasing Φ_{bias} to 0.65π for a worst-case scenario of $\Delta\alpha$=2dB. Therefore, the developed model remains as a powerful tool for analyzing nonlinear distortion in silicon MZI modulators.

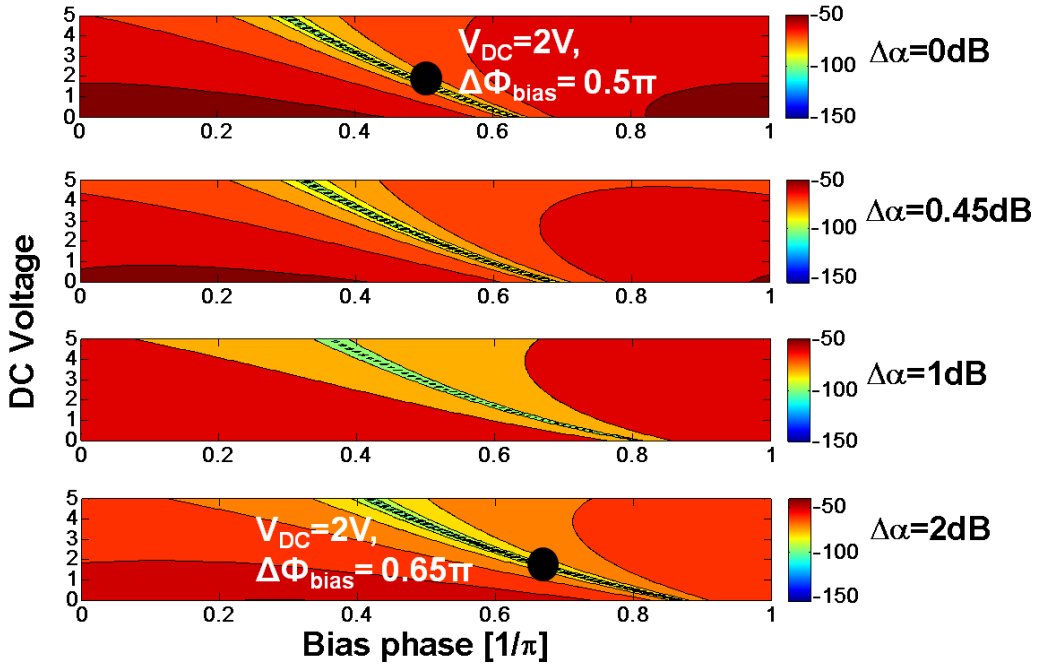

Figure 3-12: Simulated RF output power of the IMD3 intermodulation product as a function of the bias phase and DC voltage for different values of absorption losses variation. The absorption losses compensation through Φ_{bias} parameter in a specific case for modulation linearization it is also shown.

3.2.4. Experimental validation of the model

The silicon-based modulator used to experimentally validate the analytical model consists of an asymmetric MZI (as shown in Figure 3-13) and the optical phase modulation is achieved by depleting the majority carriers from a reverse biased *PN* junction located in the middle of the waveguide (Figure 3-14(a)) and embedded in the shorter arm of the MZI. The length of the shorter arm (L_{ACT}) of the MZI is 1mm and the length difference between both arms (ΔL) is 180µm with MMI coupler splitter and combiner in the input and output respectively. The silicon waveguides of dimensions of 220nm x 460nm have been partially dry etched to leave a 100nm thick slab. Doping concentrations in the p- and n-type regions of the diode are 4.10^{17} cm^{-3} and 5.10^{17} cm^{-3} respectively. The travelling wave electrodes are formed by depositing a compound AlCu layer on top of the highly doped p+ and n+ regions with concentrations of 1.10^{20} cm^{-3} in order to obtain low resistive contacts. These are placed 450nm and 500nm for p+ and n+ respectively away from the rib edges to minimize the overlap between the optical mode and therefore reduce optical losses. As can be observed from Figure 3-13, the incoming coherent light is coupled vertically to the chip via grating couplers (detail of the vertical coupling in Appendix A). A traveling-wave ground–signal–ground (GSG) coplanar design has been used to enable further high-speed radio-frequency measurements (Figure 3-14(b) and (c)).

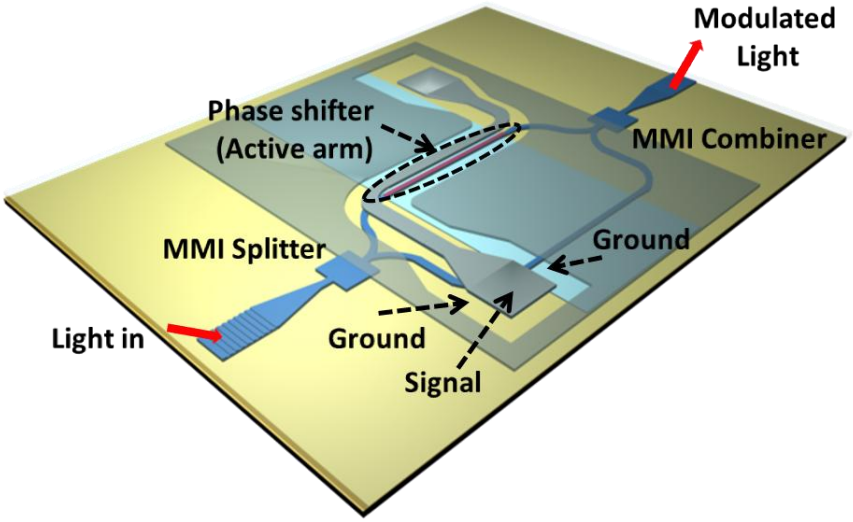

Figure 3-13: Schematic of the fabricated silicon-based electro-optic MZI modulator. The MZI is asymmetric with a length difference of 180µm and the phase shifter in the shorter arm is 1mm of length. MMI are used for divide the input light and combine the output modulated signal.

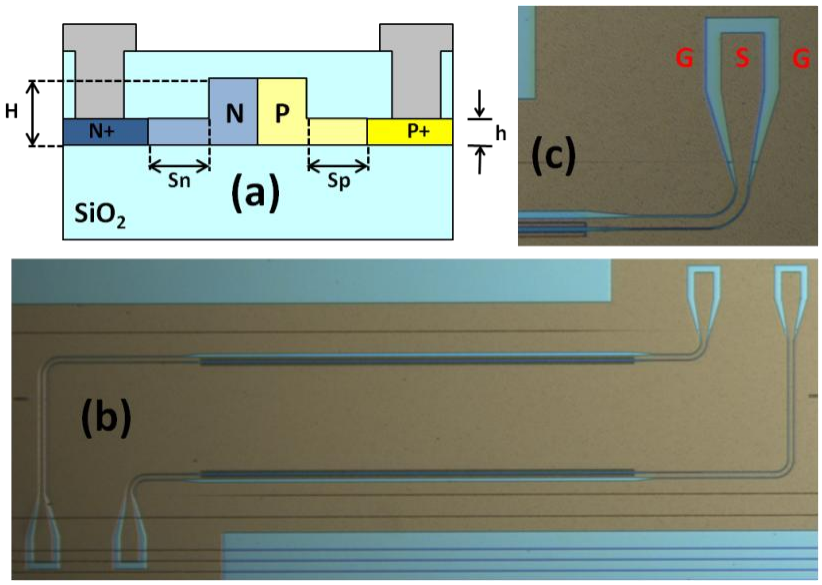

Figure 3-14: (a) Schematic of the PN junction located at the middle of the active waveguide phase shifter, (b) Optical microscope image of the fabricated modulator with a clear view of the traveling-wave ground–signal–ground (GSG) coplanar, electrodes, (c) Detail of the GSG electrode.

As it was already mentioned, the model starts from the effective index change measurement, so, first of all, static and DC performance measurements have been carried out. The spectrum of the silicon-based MZI exhibits a free-spectral range (*FSR*) of 2.42nm and a 10dB drop in transmission at the resonant wavelength around 1552nm. Figure 3-15 shows the MZI normalized transmission spectrum for varying DC voltages from 0V to 10V.

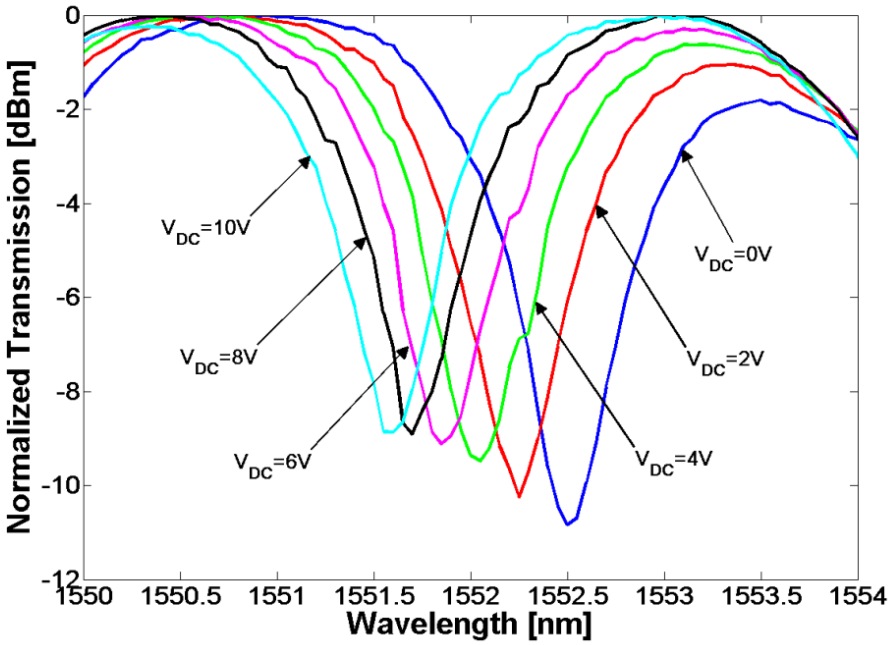

Figure 3-15: Normalized DC transmission spectrum of the MZI modulator for different applied DC voltages.

As the modulator is asymmetric we have had to take into account this asymmetry in the bias phase as follows:

$$\Delta\Phi_{Bias} = \Phi_{Offset} - \Delta\Phi_{Asym.} \tag{3.40}$$

with:

$$\Delta\Phi_{Asym.} = \frac{2\pi}{\lambda} n_g \Delta L \tag{3.41}$$

where n_g is the group index and ΔL is the length difference between both MZI arms. Moreover, the minus sign is because the active area is located in the shorter arm and thus the resonance shifts to lower wavelengths with the DC voltage. Finally, we have added an offset term (Φ_{offset}) which is required to fit the theoretical spectrum with the experimental one (in DC measurements). So, for a fixed arm difference, the bias point of the modulator can be tuned either through acting on the DC voltage or on the operation wavelength and vice-versa. Taking into account these Equations (3.40) and (3.41) and including them into the fundamental and intermodulation distortion described in Equations (3.29)-(3.31), one can obtain the optimum length difference and DC voltage for cancelling the desired intermodulation distortion. From the measured FSR, the group index has been calculated to be 3.9. Moreover, we obtain an offset phase of 0.36π to match the theoretical and experimental DC measurements and this Φ_{offset} value will be used in the Equation (3.40) to the model experimental validation for our fabricated modulator. On the other hand, the voltage-induced wavelength shift ($\Delta\lambda$) in the MZI modulator output spectrum and the index group can be used to extract the effective index variations (Δn_{eff}), through the next equation (3.42):

$$\Delta n_{eff} = \frac{\Delta\lambda}{\lambda} n_g \frac{\Delta L}{L_{ACT}} \tag{3.42}$$

Figure 3-16 depicts the calculated and fitted effective index variation as a function of applied DC voltage. The fitted curve has been obtained from the nonlinear approximation described in the equation (3.4).

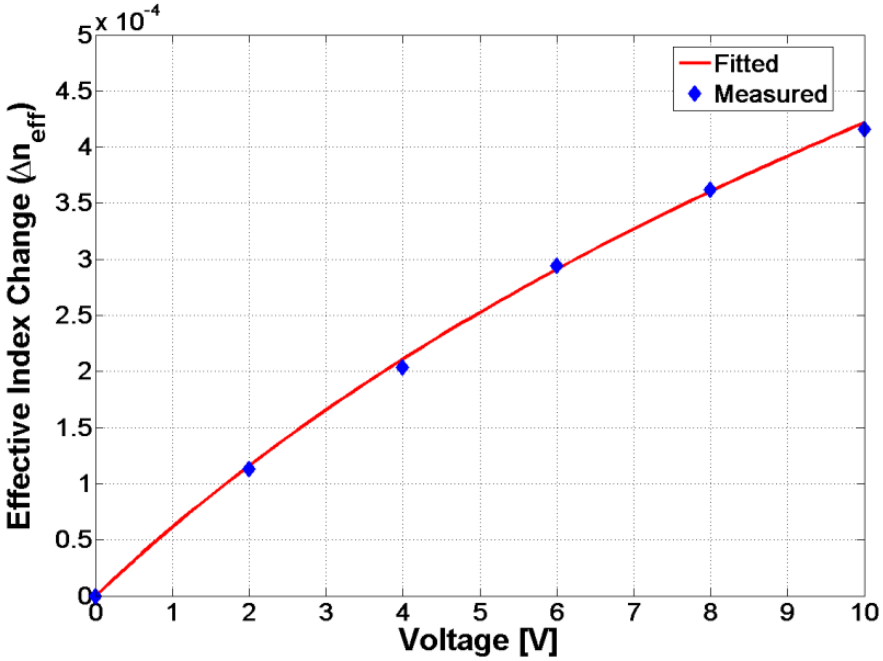

Figure 3-16: Effective index change with the voltage. The measured data are obtained from the measured voltage-induced wavelength shift through equation (3.42). The fitted curve is obtained from nonlinear approximation described in the equation (3.4).

To validate the analytical model with experimental measurements we have performed a single-tone test and analyzed the harmonic distortion. The experimental set-up used for the RF analysis of the silicon-based electro-optic MZI modulator is shown in Figure 3-17. The input light emitted by an External Cavity Laser (ECL) is coupled from standard single mode fibers to the chip via grating couplers (details in Appendix A). The polarization is optimized via the use of a polarization controller. One signal generator operating at f_{RF} is coupled to a DC voltage using a bias-Tee and applied through high speed GSG probes to one port of the silicon MZI modulator while the other port is terminated with a 50Ω load. The output modulated signal is amplified with an erbium-doped fiber amplifier (EDFA), filtered by a tunable optical filter (OF) and split with a 50/50 optical splitter with the aim of photo-detecting and measuring the optical output by an optical power meter simultaneously. Finally, an electrical hybrid is used to separate the photo-detected signal to a vectorial signal analyzer for measuring the electrical received signal in terms of frequency and to a digital communication analyzer for measuring the temporal signals. The equipment models and images of the set-up are given in section 3.5.

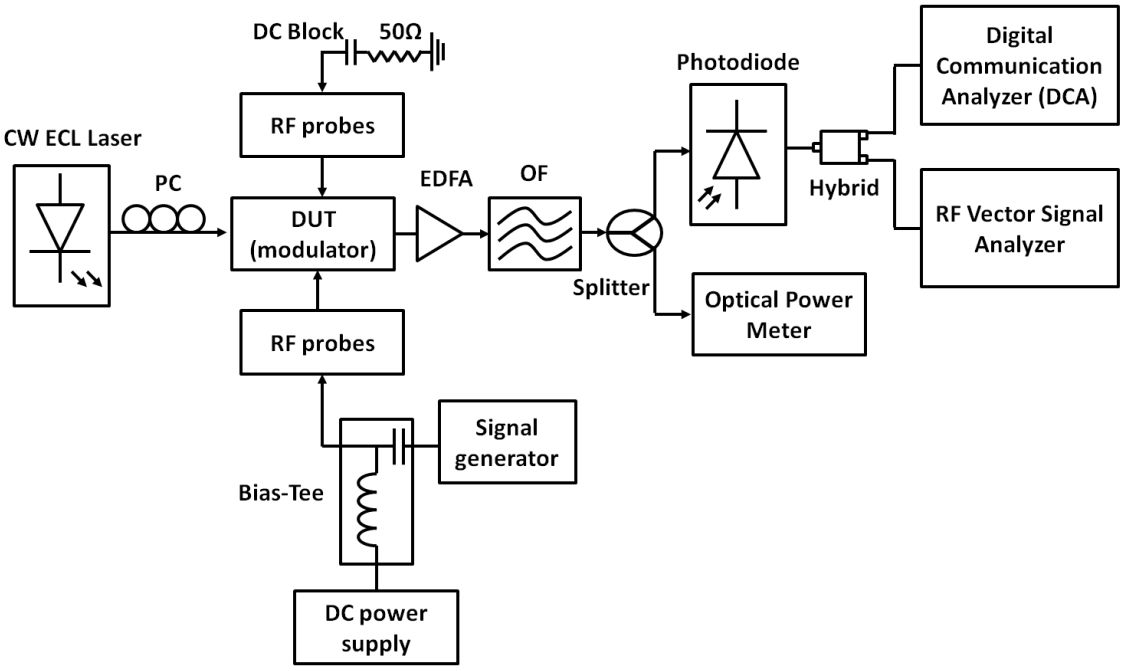

Figure 3-17: Schematic of the experimental set-up for the single-tone test carried out to experimental validation of the model.

As mentioned previously, due to the asymmetric MZI structure and the material in the active area, the bias point of the modulator can be tuned either through acting on the DC voltage or on the operation wavelength in contrast with conventional $LiNbO_3$ modulators in which the bias point is driven only with a DC voltage. So, for a given wavelength, linear or nonlinear optimum operation can be achieved by adjusting the DC voltage and vice-versa. Thereby, representations of the distortion as a function of DC voltage and wavelength can help the designer to obtain the optimum combination wavelength-DC voltage point.

Figure 3-18 shows a contour of fundamental ($P_{FUNDAM.}$) in (a), 2nd harmonic (P_{HD2}) in (b) and 3rd harmonic (P_{HD3}) in (c), obtained from analytical expressions for our fabricated device. So, from the above Figure 3-18 we can obtain that for 1V of V_{DC} the HD2 is minimized at around 1551.25nm and HD3 at 1551.75nm. To validate these results, we first tested the model by measuring the harmonic distortion utilizing a fixed DC voltage of 1V (Figure 3-19) and tuning the operating wavelength. As it can be observed in such figure, the measurements show the same trends and are in very good agreement with the analytic model corroborating the results obtained from Figure 3-18. Moreover, it must be highlighted that the experimental curves are affected by the band-pass of the optical filter shape. With this graphic one can realize that fundamental and 3rd-order harmonic distortion, have not the same performance with the bias parameter (in this case, the operation wavelength) as it occurred in linear-material modulators and it was corroborated with Figure 3-6 for a $LiNbO_3$ modulator.

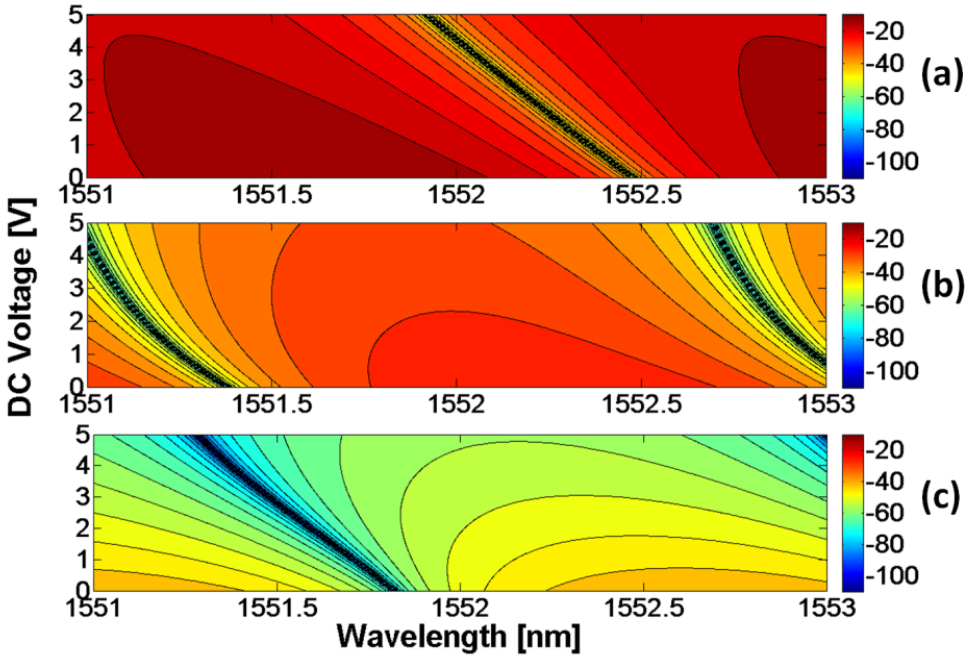

Figure 3-18: Contour of the fundamental (a), the 2nd (b) and the 3rd order (c) harmonic products powers as a function of DC voltage and wavelength for our fabricated MZI.

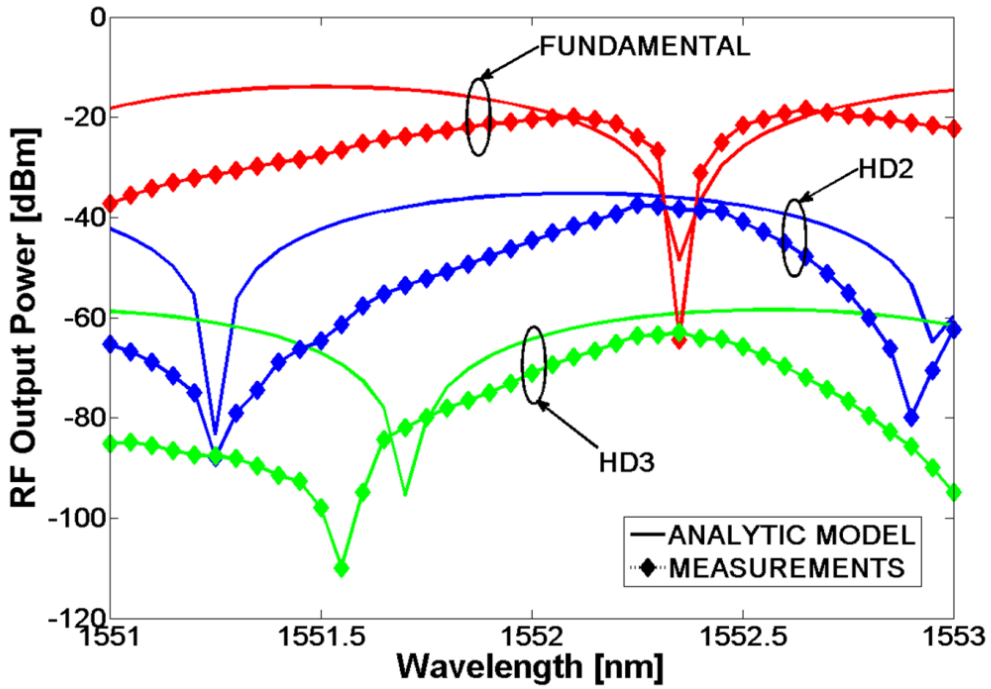

Figure 3-19: Measured values and obtained curves from the analytical expressions of the fundamental and harmonic distortion performance as a function of the wavelength for a DC bias voltage of 1V. The RF input power of the single-tone is 10dBm ($2V_{pp}$).

The level of distortion using the carrier-to-distortion parameter can also be evaluated. Defining it as the ratio between the harmonic distortion product power and the received power fundamental tone:

$$CDR_2 = \frac{P_{HD2}}{P_{FUNDAM.}} \tag{3.43}$$

$$CDR_3 = \frac{P_{HD3}}{P_{FUNDAM.}} \tag{3.44}$$

Figure 3-20 shows the experimental CDR (a), theoretical CDR_2 (b) and CDR_3 (c) as a function of the wavelength for 1V of DC voltage. From that figure we can see that according to the analytical expressions, for 1V maximum CDR, around 20dB for CDR_2 and around 1dB for CDR_3, appears at 1552.4nm as expected from Figure 3-19 in which the fundamental is minimized. In contrast, minimum CDR, around -56dB for CDR_2 and -83.5dB for CDR_3 (obviously, the slight error displacement in HD3 appears again) are obtained at 1551.25nm where HD2 is reduced and at 1551.55nm where HD3 is reduced, respectively. So, we can affirm that the analytically estimated CDR is found to be in good agreement with the experimental one.

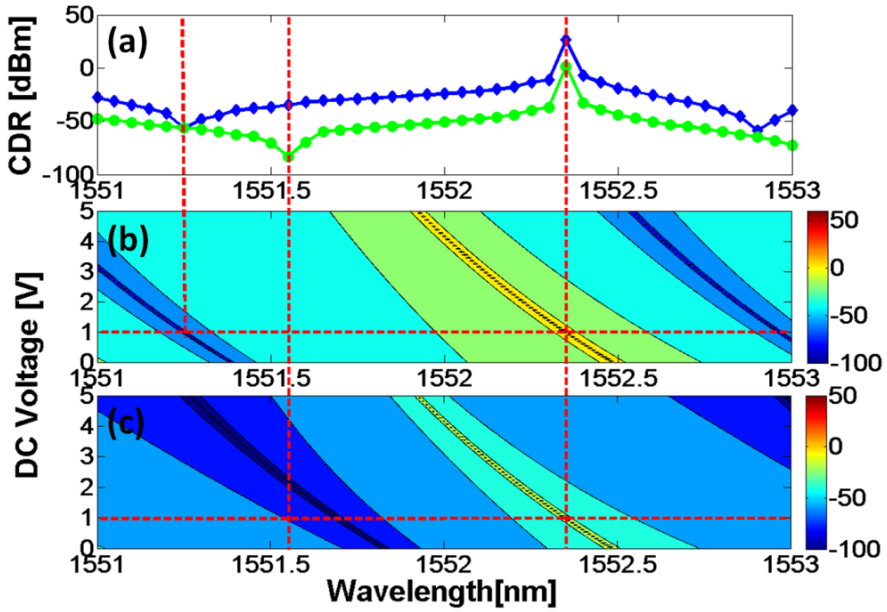

Figure 3-20: Carrier-to-distortion ratio (a) from the experimental measurements and (b) CDR2 and (c) CDR3 from the analytical model. The RF input power of the single-tone is 10dBm ($2V_{pp}$).

Another type of measurement consists of the electrical response of the harmonic distortion as a function of the RF input power and fixing the operating wavelength and DC voltage. These results are shown in Figure 3-21 for 1V of DC bias at λ=1552.1nm (a) which is the wavelength where the measured fundamental signal is maximum and λ=1552.4nm (b) where it is minimum, both for a RF input power of 10dBm. As it can be observed, the fitted curves obtained from the analytical model fit with the experimental data. For example, in 1552.4nm for an input RF power of 10dBm, the fundamental tone remains under HD2 more than 20dB and at around the same level power of HD3 as expected from Figures 3-19 and 3-20.

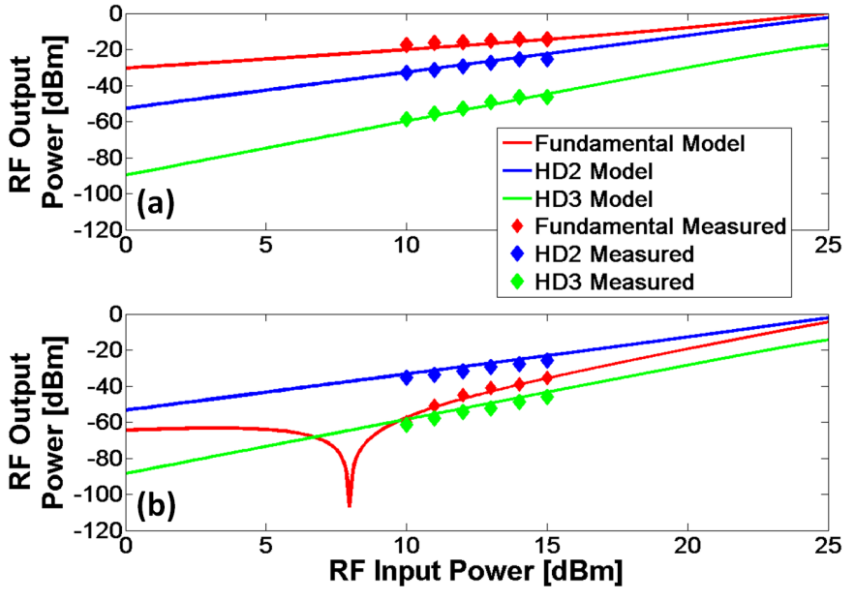

Figure 3-21: Fundamental, HD2 and HD3 powers as a function of the modulating RF input power for (a) λ=1552.1nm and (b) λ=1552.4nm. Curves are obtained from the analytical model and V_{DC}=1V.

Finally, the modulation depth was measured. It is well known that over-modulating a modulation device, which occurs when the RF modulating signal swing is too high, produces high distortion levels which strongly affect the signal output creating undesired harmonics. So, the modulation depth as a function of the RF input power was obtained through the output temporal signals to corroborate that the measured harmonics in our fabricated device were only due to the modulator nonlinear feature and not due to over-modulation. This can be observed in Figure 3-22(b) for λ=1552.1nm. No modulation depth higher than the unit is obtained in the whole range of RF input powers measured. Figure 22(a) inset shows an example of the measured temporal signal. In particular it corresponds to the case of 12dBm of RF input power which results in a modulation depth of around 50%.

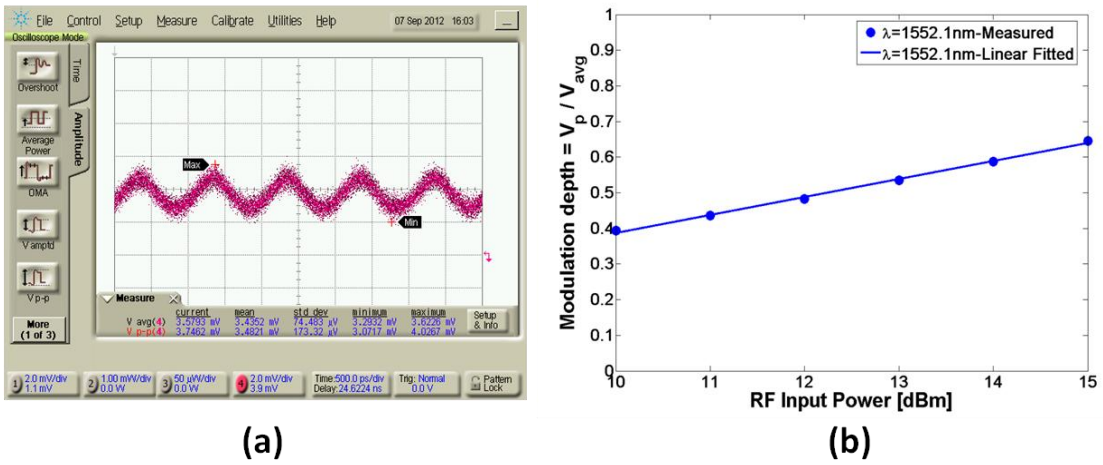

Figure 3-22: (a) Measured temporal signal for the case of 12dBm of RF input power and (b) modulation depth as a function of the RF input power for the case of λ=1552.1nm and V_{DC}=1V. It is observed that no over-modulation is produced.

We have developed analytical expressions for the harmonic and intermodulation nonlinear distortions of a silicon-based electro-optic MZI modulator due to the nonlinear feature of the silicon and the modulator transfer function. Distortion equations are estimated analytically and found to be in good agreement with numerical simulations. Some of the model applications have been shown as obtaining the optimal phase shifter length or length difference between the MZI arms for cancelling the 3rd-order intermodulation distortion, allowing a linearized modulator. Finally, the harmonic distortion calculated by the analytical model has been validated by experimental results including the carrier-to-distortion parameter showing excellent matching between the model results and experimental data. Given the growing advantages of silicon photonics and therefore of silicon modulators for emerging IMWP applications, this model gives a potential tool to predict the nonlinear modulator performance and the parameters needed for a full study of an analog photonic link.

3.3. Frequency mixing application

As we have already commented in the introduction of this chapter, compared to conventional electronic links operating over coaxial cable, photonic links operating over optical fiber can provide significant advantages in the areas of bandwidth, propagation loss and immunity against electromagnetic interferences. Among the large panel of functions needed in these systems, mixing appears to be an interesting candidate for an optical implementation to overcome the microwave mixers and conventional electrical frequency conversion schemes limitations above mentioned. So, on-chip microwave frequency conversion appears as another emerging and potential application which contributes to the advance of the availability of PIC technologies in the IMWP field. In this approach, RF frequency mixing for signal up-conversion or down-conversion is performed in a photonic integrated circuit. In this thesis, we report a contribution to this emerging application describing and experimentally demonstrating a frequency up-conversion process by using by using a single silicon electro-optical MZI modulator enhanced via slow-light propagation as photonic mixer [GUT12C].

3.3.1. Introduction: state-of-art

In contrast with the plain analog signal transport, frequency mixing is a nonlinear application. As we will explain in more detail later, when the mixing process is carried out at the modulation side (instead at the detection side), a non-linear device has to be inserted in the optical transmission link to generate a mixing signal at the output of the link. Generally, two different configurations for mixing have been applied in the literature by using linear commercial $LiNbO_3$ modulators: two cascaded linear modulations (or one of them operating in nonlinear regime) or two modulations of a single device working in a nonlinear regime. So, in this application, the nonlinear operation of the modulator is exploited, taking advantage of the nonlinearities to

frequency convert an RF signal with a conversion losses as low as possible. The objective this time is to maximize the farthest distortion terms.

Many works have been published about frequency mixing techniques using commercial $LiNbO_3$ modulators, but silicon photonics mixers had not been reported so far. In [GOP93] and [KAR08] microwave optical mixing in different configurations of MZI modulators (single MZI and a cascade interferometric modulator pair) was investigated. The authors demonstrated that the modulators could be employed for down-converting anywhere over a 15GHz [GOP93] and 18GHz [KAR08] frequency span, but both with large conversion losses (CL). The up-converting RF frequency feature of a single MZI was simulated and tested at 28GHz in [MART00] this time with lower CL. We can now consider, for example, applications of microwave photonic mixing to RoF mobile communications and WLANs, where the desired mixing frequency at the output of the system can be in the 60GHz range. In this field, much study has been done on optical transmission of UWB signals. For a UWB signal at high frequency, one first attempt at up-conversion was made at around 40GHz with cascaded modulators but with again large CL [NGU07]. Later, generation of a 60GHz UWB signal over fiber by up-conversion using cascaded EOMS was demonstrated by the same authors in [NGU09] with a suitable error vector magnitude value of 12.6%. Recently, a down-conversion frequency process with a new RoF architecture by using a combination of two optical phase modulators (OPM) and optical filtering has been demonstrated high frequency-conversion features [PAG11]. A thoroughly overview of optical techniques used for frequency conversion or mixing can be found in [CAB10], which gives the advantages and drawbacks of all techniques presented as well as the research results. The next Table 3-2 summarizes the CL results obtained in these works (it must be remembered that all of them are based on $LiNbO_3$ commercial modulators).

[ref]	Configuration	Frequency	CL [dB]
[GOP93]	Single MZI	15.5GHz-40Mhz	56
	Cascaded MZIs	15.5GHz-40Mhz	66
[KAR08]	Cascaded MZIs	2GHz-500MHz 18GHz-500MHz	15 20
	Dual-series MZIs	2GHz-500MHz 13GHz-500MHz	26 34
[MART00]	Single MZI	1GHz-28GHz	6.26
[NGU07]	Cascaded MZIs	4GHz-36GHz	56
[NGU09]	Cascaded MZI	3.4GHz–56.5GHz	30
[PAG11]	Cascaded OPM	20GHz-400MHz	13.8

Table 3-2: Reported results of the conversion losses in microwave photonic frequency conversions by using commercial EOMs.

Regarding to frequency mixing based on integrated devices, in [JIN12] the authors proposed a RF-photonic link on chip PIC (based on a AlGaInAs Multi-Quantum-Well structure) which can operate in a linear mode (as an MWP link) or a nonlinear mode (as

MWP mixer) and a frequency down-conversion from 1.05GHz to 50MHz with low conversion losses of 10dB was reported. In silicon, two down-converting links were demonstrated based on a compact and fully tunable silicon optical filter [YU13, TU10] but no silicon photonic mixer as device was used.

3.3.2. Basic principle of RF/photonic mixers

First of all, let us to review de basic principle of RF mixers. These are 3-port active or passive devices and are designed ideally to yield both, a sum and difference frequency at a single output port when two different input frequencies are inserted into the other two ports. To produce these new frequencies (the sum and the difference frequency) a nonlinear device is required. The nomenclature for the 3 mixer ports are the Local Oscillator (LO) port, the Radio Frequency (RF) port, and the Intermediate Frequency (IF) port. The LO port is typically driven with either a sinusoidal continuous wave (CW) signal or a square wave signal. The choice to apply a CW or square wave signal depends on the application and the mixer. The LO port is usually used as an input port. The other 2 ports of the mixer, the RF and IF, can be interchanged as either the second input or the output.

In a mixing process if we want to produce an output frequency that is lower than the second input signal frequency, then the process is called *down-conversion* and the RF is the input and the IF is the output. On the other hand, if we want to produce an output signal that is at higher frequency than the second input signal, it is referred to as *up-conversion* and the IF is the input and RF is the output. Figure 3-23 illustrates a frequency domain representation of down-conversion (a) and up-conversion (b) processes. As Figure 3-23 depicts, IF/RF signals tend to be information bearing signals (as denoted by the broadened spectra surrounding the RF and IF center frequencies). During the frequency conversion, the information carried by the RF (IF) signal is frequency translated to the IF (RF) output.

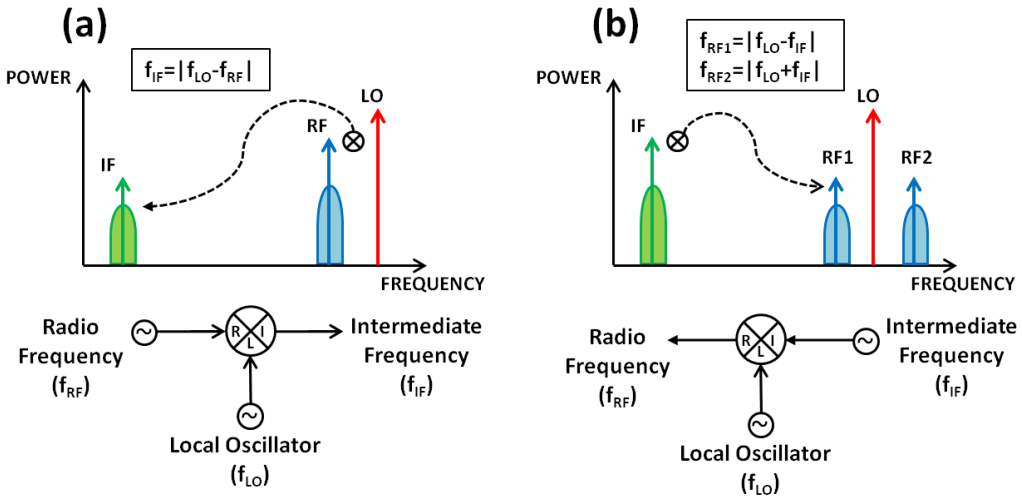

Figure 3-23: Definitions of frequency down-conversion (a) and frequency up-conversion (b) mixing processes.

To produce a new frequency (or news frequencies) a nonlinear device is required and in principle any nonlinear device can be used to make a mixer circuit. These nonlinearities will be responsible for the generation of many additional frequencies other than the pure sum and difference frequencies. So that, electro-optic modulator can be a simple but efficient method of generating mixing products and converting frequency in a microwave photonic link by taking advantage of their nonlinear transfer function (and the nonlinearity produced by the material in the case of silicon-based modulator) which brings several harmonic and intermodulation products as it has been studied in the previous section 3.2.

As explained in the basic operation of a frequency conversion scheme, usually the desired output frequency is the sum or difference of the input frequencies. Now, when a linear-phase modulator as $LiNbO_3$ is used for photonic mixing applications, taking advantage of the fact that the distortion has the same behavior with the operating bias point, one can choose another output frequency than the sum or the difference (which they would be the second-order intermodulation frequency produced by the modulator) depending on the operating point. That is, at QB point the even terms are normally minimized; maximizing the odd ones, therefore, these odd terms could be used to up-convert or down-convert the desired frequency. By contrast, when the modulator is biased at MITB or MATB points, the odd terms are minimized and the even ones are maximized, therefore in this case, the desired frequency could be converting to one of these even terms. As demonstrated with the analytical model developed in previous section, this do not happens when the material in the phase shifter is nonlinear (as it happens with the silicon phase shifters). That is why we will study the frequency conversion behavior in terms of conversion loss in both MITB and QB.

3.3.3. Experimental slow-wave photonic mixer

In this thesis, we experimentally demonstrated a silicon-based photonic mixer for up-frequency conversion. The silicon-based MZI modulator enhanced via slow-light propagation presented in Chapter 2 (and shown again in Figure 3-24) is used to generate the mixing signal. We remember from Chapter 2 that the slow light propagation in the modulator is achieved through the use of a 1D periodic structure consisting of a laterally corrugated waveguide, the optical phase modulation is achieved by depleting the majority carriers from a reverse biased *PN* junction located in the middle of the waveguide and connected to highly doped p+ and n+ regions and finally, the optical phase modulation in the slow-wave waveguide is converted into amplitude modulation via the use of an asymmetric MZI structure. As demonstrated in [BRI11A] and section 2.2 for digital measurements, the slow-light effect enhanced the modulation efficiency, allowing modulation data rates up to 40 Gb/s over an interaction length of only 500µm at a group index of ~11.

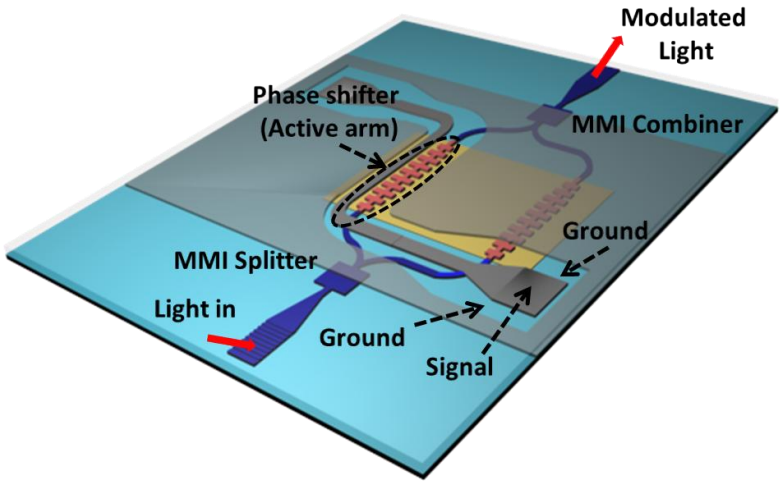

Figure 3-24: Schematic of the slow-wave MZI modulator used for mixing. The MZI is asymmetric with a length difference of 180µm and the phase shifter in the shorter arm is 1mm of length. MMI are used for divide the input light and combine the output modulated signal.

Mixing is achieved by exploiting the modulator nonlinearity which depends basically on the operating bias point of the MZI transfer function but also on the intrinsic nonlinear response to the material in the active region. However, in our case, slow-light propagation also plays a prominent role in the mixing performance. As we know from Chapter 2, slow-light relies on decreasing the group velocity of the light. This decrease in the group velocity favours light-matter interaction offering additional control possibilities over light as well as enhancing nonlinearities [BLA09]. So, we take advantage of this nonlinearities enhancement due to the slow-light effect to achieve a frequency mixing process as we will see below.

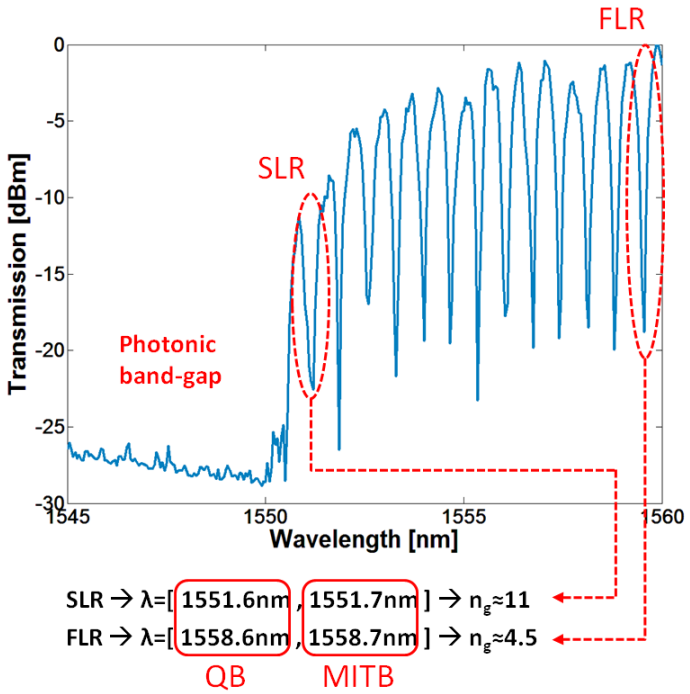

Figure 3-25: Measured transmission spectrum of the slow-wave silicon-based modulator. The photonic band-gas and both slow-light and fast-light resonances chosen from the experiment are clearly differenced.

Due to the asymmetric MZI structure used for the experiment, the bias point can be tuned either through acting on the DC voltage or on the operation wavelength in the same way that in the asymmetric MZI used in previous section 3.2. In this case, the experimental measurements were carried out by tuning the wavelength to drive the modulator to the appropriate bias operating point and utilizing a fixed 2V DC voltage. Thus, if we observe the measured modulator transmission spectrum, illustrated in the Figure 3-25, we can distinguish the operating wavelength in the slow light region for QB and MITB, close to the photonic band-gap due to the of slow-light effect, where the measured group index is around 11, from the operating wavelength in the fast-light region also for quadrature and minimum transmission, away from the band-gap, and where the measured group index is around 4.5.

To study and measure the frequency up-conversion, the IF and OL frequencies are set to 1GHz and 9.25GHz respectively. The experimental setup used is shown in Figure 3-26. The input light emitted by an ECL is coupled from standard single mode fibers to the chip via grating couplers (vertical coupling explained in Appendix A). The polarization is optimized via the use of a PC. Two signal generators operating at f_{IF}=1GHz and f_{OL}=9.25GHz are power combined and the two tone input is coupled to a DC bias of 2V using a bias-Tee and applied through high speed GSG probes to one port of the slow-light MZI modulator while the other port is terminated with a 50Ω load. The output modulated signal is amplified with an EDFA, filtered by a tunable OF and photo-detected by a high speed photodiode. Finally, a vectorial signal analyzer is used to measure the received signal. Electrical amplification is performed with a low noise amplifier featuring 26dB RF gain and 6dB noise figure (details in section 3.5).

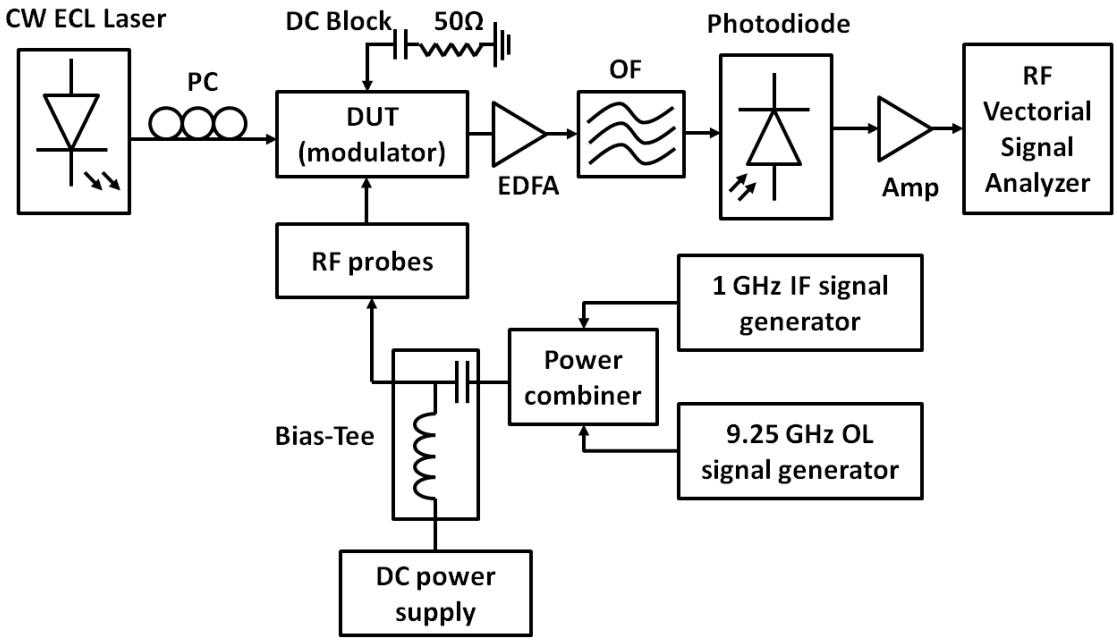

Figure 3-26: Schematic of the experimental set-up used for measuring the frequency up-conversion mixing process.

To evaluate the mixing process performance of our silicon modulator, we defined the CL as the ratio between the photo-detected electrical power at f_{IF} and the photo-detected electrical power of the considered intermodulation term at $f_{RF}=Nf_{IF}+f_{OL}$ (N=1 for IMD2 and N=2 for IMD3) as in [MART00].

$$CL = \frac{P_{f_{IF}}}{P_{f_{RF}}} = \frac{P_{f_{IF}}}{P_{Nf_{IF}+f_{OL}}} \tag{3.45}$$

According to this definition, when a given intermodulation product power is maximized with the bias point, the conversion losses of the product should be minimized. Initially, we investigated the nonlinear performance and CL at QB. Conversely to $LiNbO_3$ modulators, we obtained large CL (around 58dB for +15dBm IF input power) for the IMD3 ($2f_{IF}+f_{OL}$=11.25GHz). Furthermore, lower CL were measured (34dB for +15dBm IF input power) for the IMD2 ($f_{IF}+f_{OL}$=10.25GHz), as shown in Figure 3-27. Based on these results, the modulator was biased at MITB, where usually the IMD2 products are maximized and dominate over the third-order and the fundamental terms. In this case, CL for IMD2, also shown in Figure 3-27, were reduced by more than half (around 12dB for +15dBm IF input power) and therefore a significant improvement results in conversion losses (~20dB) between biasing the modulator at QB or MITB.

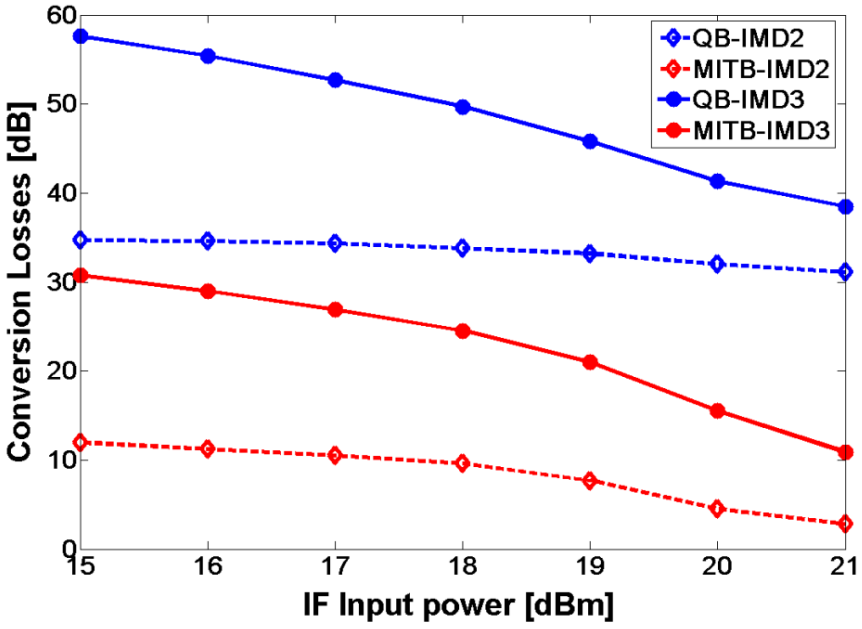

Figure 3-27: Conversion losses at QB and MITB bias points for both slow and fast-light regions at IMD2 intermodulation frequency. OL input power was set to be +20dBm.

On the other hand, lower conversion losses were also obtained in the slow light region (SLR) when compared to the fast light region (FLR), ~2-4dB more at MITB and ~1dB at QB, as depicted in Figure 3-28. As a result, the IMD2 frequency (10.25GHz) and MITB operation point was chosen to up-convert a vector modulated signal.

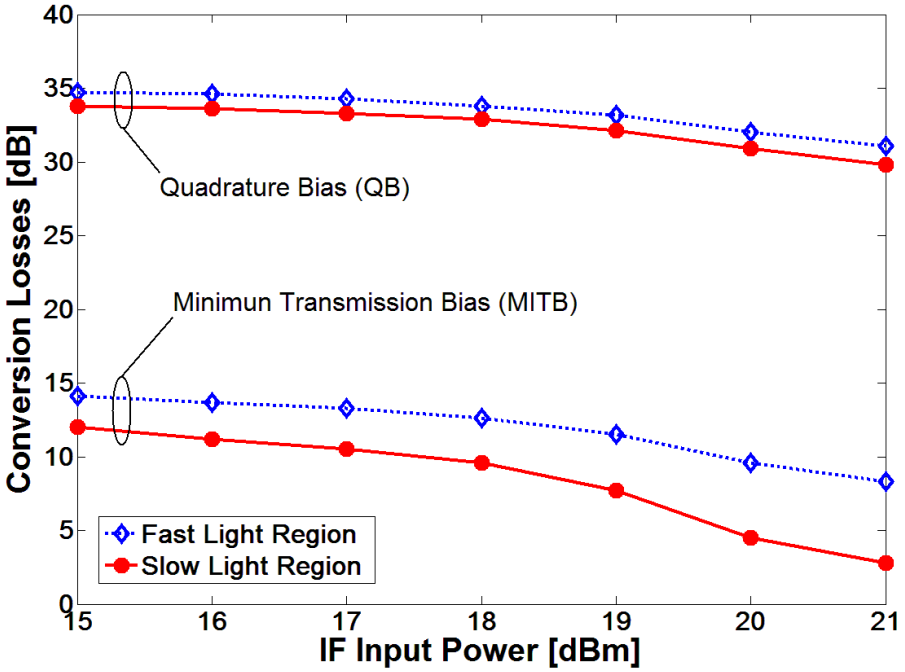

Figure 3-28: Conversion losses at QB and MITB bias points for both slow and fast-light regions at IMD2 intermodulation frequency. OL input power was set to be +20dBm.

Moreover, the SFDR, defined as the range of output powers over which no intermodulation signal is above the noise level implying that no disturbance of the desired signal is produced, was also measured. For our mixing functionality, we consider that the signal to which we will later up-convert a modulated signal is the $f_{IF}+f_{OL}$ product (IMD2). Therefore, if one qualitatively observes the output frequency spectrum diagram of a mixer (Figure 3-29), it is realized that the critical combination product in that case is $2f_{IF}+f_{OL}$ (IMD3) since it is the closest and therefore the most difficult to filter.

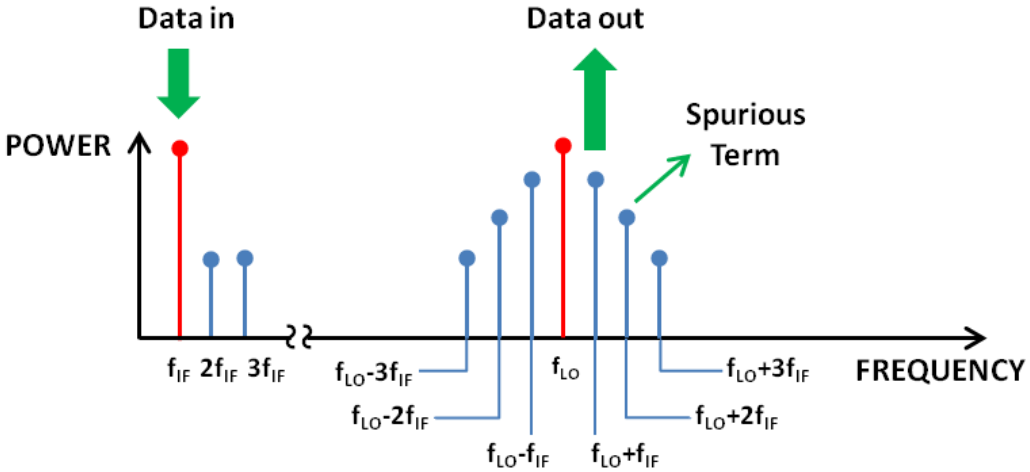

Figure 3-29: Output frequency spectrum diagram of a mixer in which the OL frequency is very higher than IF frequency.

As illustrated in Figure 3-30, our SFDR is the output power difference between the intersection of the IMD3 power signal at 11.25GHz with the noise floor and the IMD2

power signal at 10.25GHz. SFDR values of 62.8dB.Hz$^{2/3}$ and 60.2dB.Hz$^{2/3}$ for the slow and fast light regimes have been measured respectively.

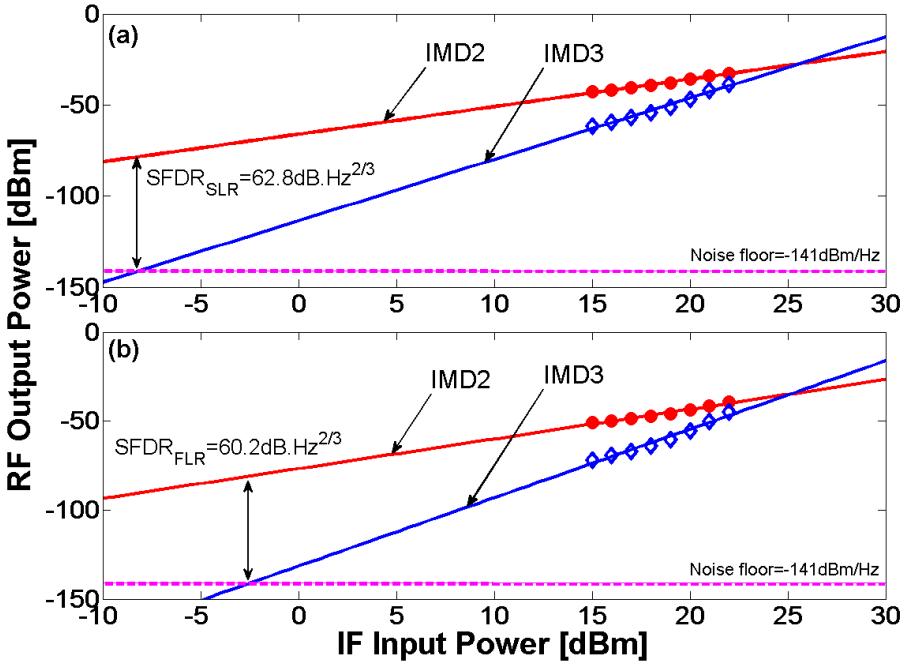

Figure 3-30: IMD2 and IMD3 powers as a function of the IF input power at MITB. SFDR for both (a) slow and (b) fast light region are represented. Noise floor level has been measured at -141dBm/Hz. OL input power was set to be +20dBm.

These results confirm again the enhanced performance brought by the slow-light regime of the modulator. In both cases, a third order intercept point around ~25dBm has been measured. For completeness, we note that intermodulation terms grow as the square and the cube of the input power for IMD2 and IMD3, respectively. It must be stated here that, obviously, lower SFDR values have obtained with respect the reported values in Table 3-2 with commercial $LiNbO_3$, due to the high system noise floor obtained, but by contrast excellent conversion losses are obtained, so, there is a good trade-off between them, besides the advantages of our silicon-based photonic mixer in terms of CMOS compatibility and fully integration capability.

Apart from the SFDR, another performance figure typical to characterize MWP links is the error vector magnitude (EVM) which is measured at the receiver and gives a good indication of the signal quality. The EVM parameter is used in most wireless system standards such as IEEE802.11g/b, UMTS, WiMAX, etc. to calculate the performance of a transmitter/modulator or receiver/demodulator implementing the respective standard. Following the optical transmission, the lower EVM, the lower deterioration the signal will have suffered. An error vector is a vector in the I-Q plane between the ideal transmitted constellation point and the point received by the receiver. In other words, it is the difference between actual received symbols and ideal transmitted symbols as shown in Figure 3-31. The average power of the error vector, normalized to signal power, is the EVM.

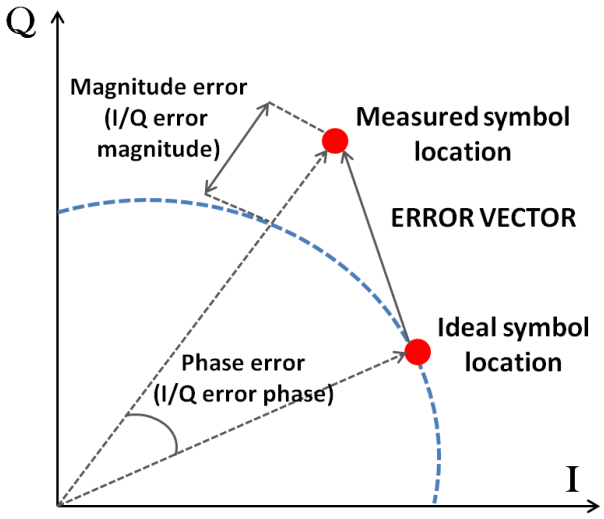

Figure 3-31: Definition the error vector magnitude in the I/Q plane.

Some examples of EVM requirements can be found. ZigBee (IEEE 802.15.4) tolerate an EVM of up to -9dB (35%) [INS07]. The IEEE 802.16e-2005 standard prescribes that a Mobile WiMAX transmitter must have a minimum EVM of -15dB (17.7%) for a QPSK½ modulation and -20.5dB (9.4%) for 16_QAM½. [IEEE05] Finally, EVM threshold to ensure communication between Ultra Wideband (UWB) devices is -14.4 dB (19%) as [ECMA368]. As example, the silicon-based MZM examined in [VAC10] allows converting 802.11 QAM modulated OFDM signals to optical domain achieving an EVM of -30dB (3%) a data rate of 54Mb/s.

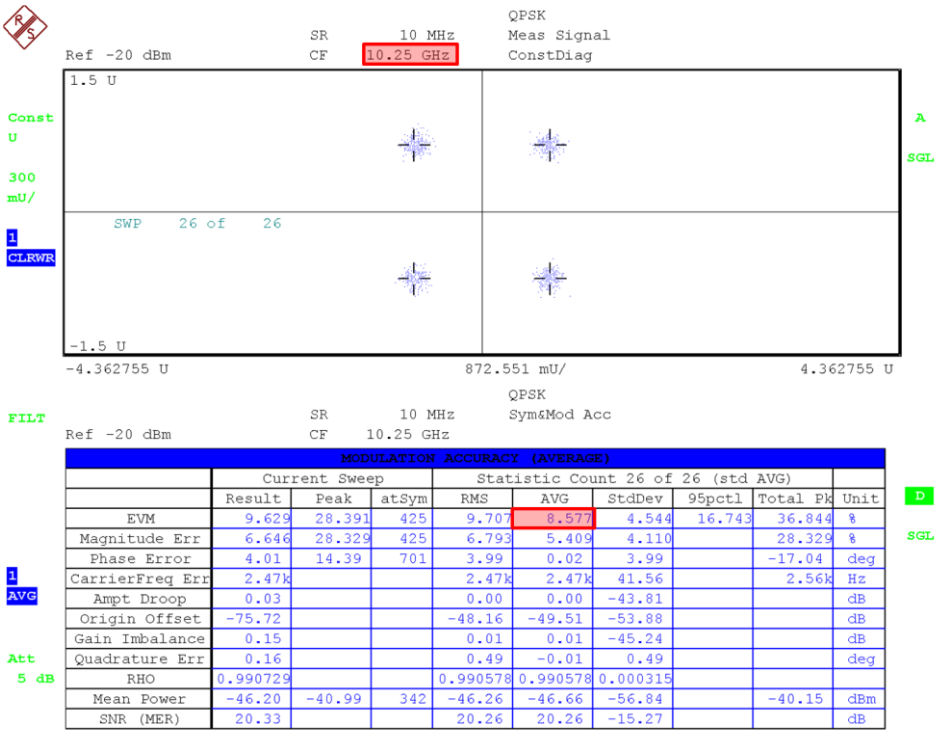

Figure 3-32: Image obtained from the signal analyzer of the received constellation at 10.25GHz in the slow-light region for 17dBm of IF input power. It is highlighted the average value of the EVM parameter and the frequency.

For the EVM measurements and for the test scenario presented here, we choose an I/Q modulated signal at the IF frequency of f_{IF}=1GHz under a digital modulation scheme of QPSK with 20Mbps up-converted to a frequency of $f_{IF}+f_{OL}$=10.25GHz with the electro-optic modulator biased at MITB point. The experimental setup is the same to that depicted in Figure 3-26 with the IF signal generator and vectorial signal analyzer properly programmed for such measurements. Figure 3-32 depicts an image of the received constellation at 10.25GHz obtained from the vector signal analyzer.

Finally, Figure 3-33 shows the measured EVM (in dB in the left axis and in % in the right axis) in both slow and fast light regions. It is clear from the figure that enhanced performance in terms of EVM is obtained in the slow light regime over the entire range of IF input powers. Outstanding results have been obtained with a very low optimum EVM of 8.5% and 12% for both slow and fast light regimes, respectively, allowing a very clean constellation. This suggests that the received signal is of excellent quality. Furthermore, the curve meets the expected behavior and decreases for low IF input power (due to the electrical noise) since an optimum point is utilized. It should be noticed that from this optimum IF input power point (17dBm), the curve increase due to the IF power source saturation.

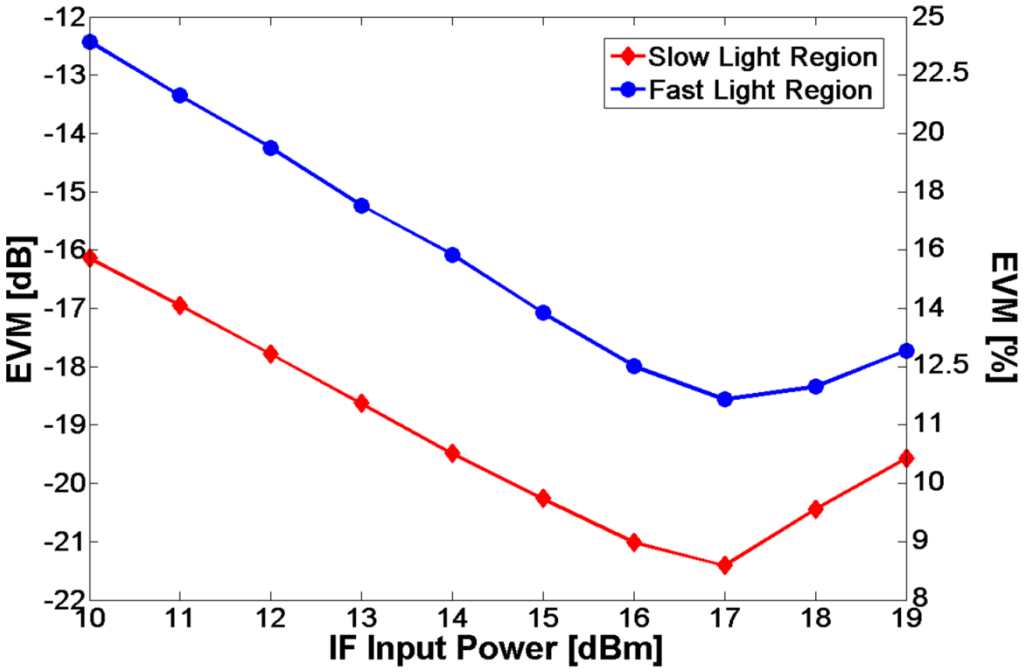

Figure 3-33: EVM as a function of IF Input Power for both fast and slow light propagation. Inset shows received constellation in the slow light region case at the optimum point of IF input power (+17dBm).

We have shown in this section a very efficient method of generating mixing products in a silicon modulator exploiting the nonlinearity produced by both the MZI transfer function and the plasma dispersion effect in silicon. Furthermore, the conversion efficiency has been enhanced via slow-light propagation in the active region of the modulator appearing the slow-light effect as a potential technology for building

microwave devices. Optimum performance has been achieved at MITB with low conversion losses around 7dB and large SFDR of 62.8dB.Hz$^{2/3}$. As a matter of evaluation, a 20Mbps QPSK signals at 1GHz frequency has been successfully up-converted to 10.25GHz without the need for high-frequency complex RF components. A minimum EVM of about 8% has been achieved, meeting well enough the EVM requirements for an acceptable quality of the received constellation. Overall, this simple photonic silicon slow-light based mixer scheme can implement a promising functionality for future broadband microwave-millimeter-wave communication applications in the IWMP scope.

3.4. Microwave photonic filtering application

In addition to frequency mixing application, another important functionality within the photonic control and processing of microwave signals field is the microwave photonic filtering. In this thesis, a photonic microwave filter implemented by a SOI electro-optic modulator is demonstrated. The modulator is based on a single silicon-based asymmetric MZI and the wavelength-dependent modulator response due to the asymmetry in combination with the π-phase inversion effect are exploited to achieve positive and negative taps and so a fully reconfigurable device [GUT13A]. Two filter responses with two and three taps are experimentally demonstrated showing a good agreement with theory for frequencies up to 10 GHz and thus going one step further towards a fully integration of the complete filter device in the CMOS-compatible silicon photonics platform.

3.4.1. Introduction: state-of-art

An MWP signal processor is a photonic subsystem designed with the aim of carrying equivalent tasks to those of an ordinary microwave filter within an RF system or link. In addition, with the development of the increasingly complex analog photonic link (APL) [UR11], more advanced functionalities are required to be explored such as high selectivity and tunable filtering. So, significant efforts have been focused on the implementation of flexible filters free from bandwidth constraints which generally are required to be reconfigurable filters with narrow bandwidth and wide FSR. Although the electronic-based designs report high performance they usually cannot offer wideband responses with high reconfigurability. Moreover, the possibility of integrating MWP filters in a single chip is highly attractive since it will open the way to structures with reduced footprint, lower power consumption, higher stability, reliability and cost reduction due to the possibility of mass production. Thereby, the silicon-based MWP signal processors are believed to be a promising solution to these challenges in the complex APL. In this way, silicon photonics is currently one of the most preferred

technology platforms for implementing low-cost and compact solutions for reconfigurable optical filtering.

All-optical signal processing in SOI lattice filters can support the fully reconfigurable optical transfer function by cascading many identical unit cells in different ways. A unit cell is a basic building block used to construct higher-order filters. Thereby, the versatility and operability of the filter depends on the functionality of the unit cell that can be configured to have any first order optical transfer function with any filter taps configuration. In the last five years, several integrated SOI-based microwave photonics filters have been reported [RAS07, FEN10, DON10, ALI11, IBR11, YU13] carrying out the task of filtering in the optical domain.

Another approach for developing microwave photonic filters [VID05, VID06, CAP03], similar to that developed in this thesis and more stable solution than the above mentioned, consists on performing the filtering in the RF domain, after photo-detection. In this approach a MWP filtering scheme based on a single photonic device is performed and the tuning control mechanism is based on the fine adjustment of the different emission wavelengths to implement complex-value taps of the filter. In [LLO11], the periodic spectrum of an integrated SOI MRR is employed to demonstrate a tunable complex-value multi-tap microwave photonic filter, but apart from the modulator device. The photonic microwave filter proposed in this thesis is based on a single asymmetric SOI MZM. The asymmetry, which is achieved by introducing a length difference between the MZM arms, is used to obtain positive and negative taps at the 1550nm wavelength band (C-band) thanks to the associated strong wavelength dependence of the modulator response in combination with the π phase inversion after photo-detection. Bipolar filter taps allow the implementation of a wide range of filter responses without the limitations of pure positive designs while keeping the inherent stability of incoherent operation. This same technical approach was also followed in [CAP03] but two commercial $LiNbO_3$ were required. Further, unlike previous proposals using a single $LiNbO_3$ modulator [VID06], the proposed technique of exploiting the asymmetry of a silicon-based MZI avoids the need of combined 1300 nm and 1550 nm optical sources. Therefore the new approach simplifies the filter architecture, and allows its use with EDFAs as well as integrated dispersive delay lines (such as [SAN12]) which can lead to the development of fully integrated photonic microwave filters.

3.4.2. Basic principle of microwave photonic filters

A microwave photonic filter is a photonic structure whose objective is to replace a standard RF microwave filter (which is basically a device that selects or removes the wanted or unwanted components or features from a signal) taking advantages inherent to photonics such as low loss, high bandwidth, and immunity to electromagnetic interference and providing features which are very difficult to achieve with traditional technologies, such fast tunability and reconfigurability [CAP06].

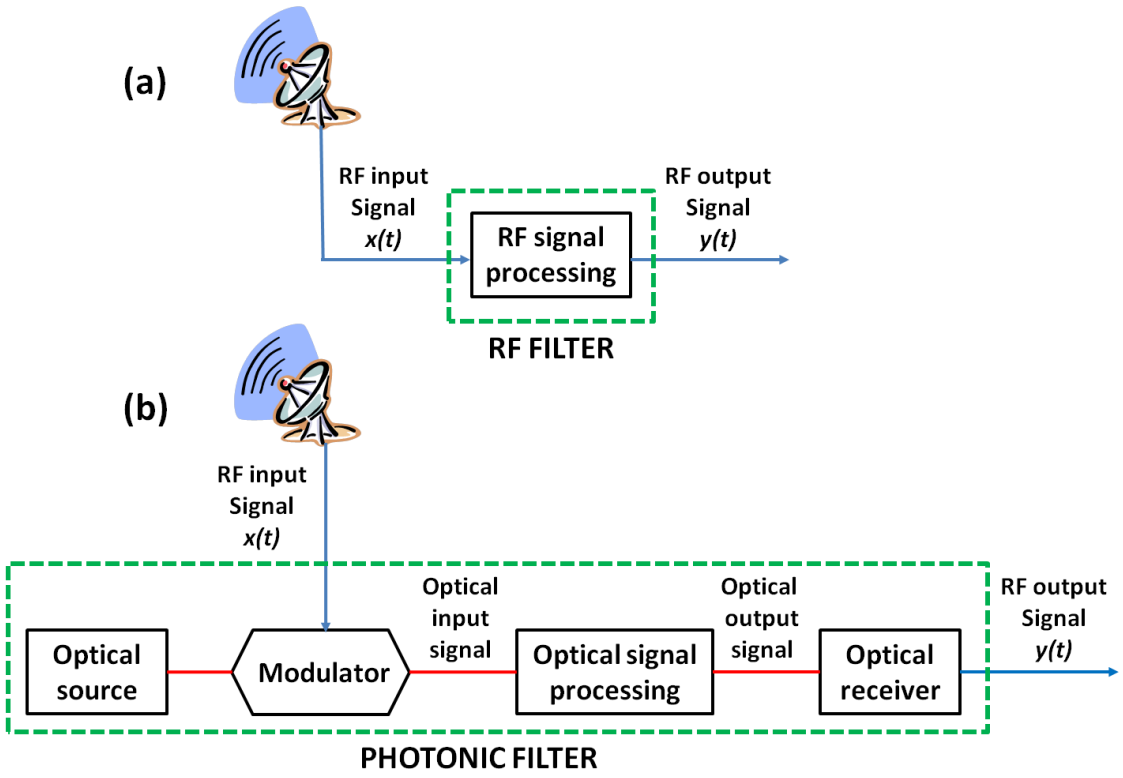

Figure 3-34: General concept diagram of (a) traditional RF filter and (b) microwave photonic filter.

In the traditional approach of RF microwave filter an RF signal originating at an RF source or coming from antenna is fed into an RF circuit that performs the signal processing task. In contrast, in the photonic approach the RF signal, again originating at an RF source or coming from antenna, that now modulates an optical carrier is directly processed in the optical domain by a photonic filter based on fiber and photonic devices and circuits. In both cases, the output RF signal once processed is ready to be sent to a receiver or to be reradiated. Figure 3-34 shows the comparison between the general concepts of these two approaches: traditional RF approach (Figure 3-34(a)) and photonic approach (Figure 3-34(b)) both in the case that the RF signal is detected from an antenna.

Referring to the microwave photonic filter, the RF to optical conversion is achieved by modulating (directly or externally as in the Figure 3-34(b)) either a single CW source or a CW source array. Then, the composite signal composed by the RF signal and the optical carrier(s) is fed to a photonic circuit that samples the signal in the time domain, weights the samples and combines them using optical delay lines and other photonic elements like couplers, fiber Bragg gratings, amplifiers, etc. At the output, the resulting signal is optically RF converted by means of a single optical receiver (photodetector) or an array of receivers producing the output RF signal. The dotted line represents an equivalent black-box of the aimed performance of the filter. It is expected to relate the input and output RF signals by means of an impulse response $h(t)$ in the time domain or by a frequency response $H(\omega)$ in the frequency domain. The most powerful approach for the implementation of the microwave photonic filter is that based on discrete-time

signal processing where a number of weighted and delayed samples of the RF signal are produced in the optical domain and combined upon detection. According to the number of samples N, the filter can be classified as either a finite impulse response (FIR) filter which combines at their output a finite set of delayed and weighted taps of the input signal or an infinite impulse response (IIR) filter which is based on recirculating cavities to provide an infinite number of delayed and weighted replicas of the input signal. In this thesis, we will demonstrate a silicon-based FIR filter so we will center in this kind of filters.

Provided that the nonlinearity in the system is small and negligible, the entire system can be considered as linear and time-invariant, in which the output *y(t)* can be written as:

$$y(t) = \sum_{n=0}^{N-1} a_n x(t - nT) \tag{3.46}$$

where *x(t)* is the RF input signal, *T* is the time delay difference between two adjacent taps and a_n is the coefficient or weight of the n-*th* tap (if all taps have the same absolute value the filter is uniform). Applying the Fourier transform, the FIR filter transfer function is then obtained,

$$H(\omega) = \sum_{n=0}^{N-1} a_n e^{-j\omega nT} \tag{3.47}$$

where $\omega = 2\pi f_{RF}$. The equation (3.47) shows that the filter spectrum is periodic with a period given by $f_{RF}=1/T$ and known as free spectral range (FSR). The selectivity of any of the pass-bands or resonances is given by the -3dB bandwidth and the filter rejection is obtained through the relation between the main to secondary sidelobe ratio (MSSR). Figure 3-35 shows an example of a microwave photonic filter spectrum with the most important parameters.

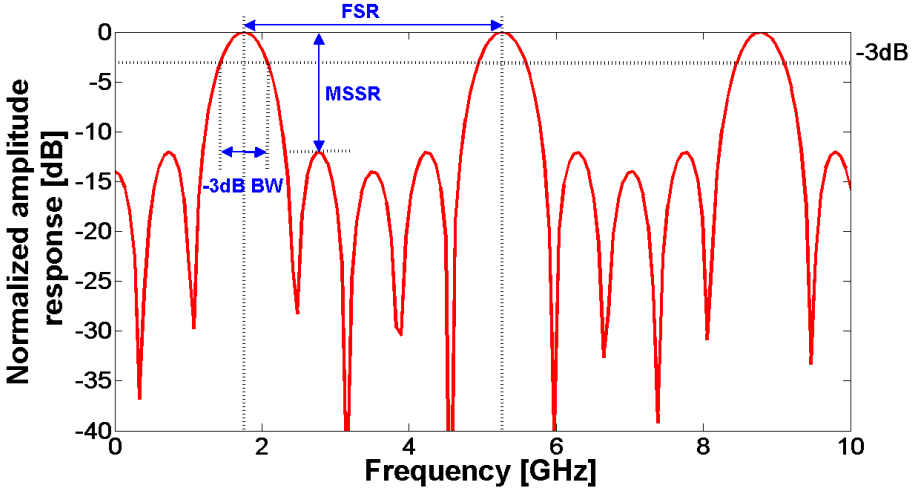

Figure 3-35: Typical response of a uniform 5-tap ([1 -1 1 -1 1]) photonic microwave filter showing the most important parameters.

Moreover, it can be pointed that the MWP filter flexibility, which is achieved by acting over the different parameters in equation (3.47), is evaluated in terms of tunability, reconfigurability and selectivity. The first one refers to the possibility to dynamically change the position of filter resonances (the central filter frequency). To provide tunability it is necessary to alter the value of the sampling period T and therefore the FSR. The reconfigurability refers to the possibility to dynamically change the values of coefficients a_n which results in a reduction of the sidelobes and therefore in a filter shape change (changing the MSSR). Finally, the filter selectivity is dictated by the number of samples (N=2 provides a notch filter and N>2 a band-pass filter) which can be increased by cascading the filter unit cell. The effect of the relevant parameters on the filter response is illustrated in the next Figure 3-36.

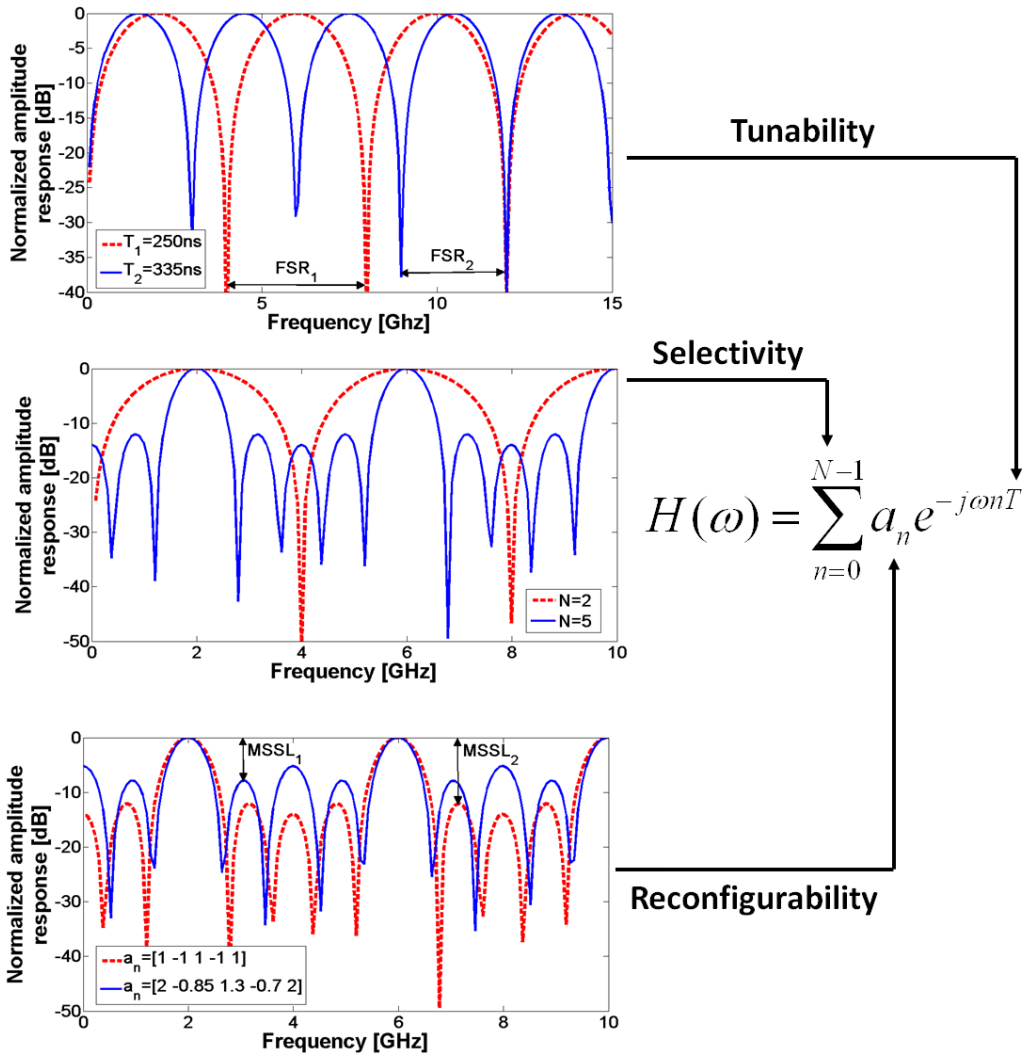

Figure 3-36: Examples of filter flexibility changing sample parameters to obtain tunability (T), selectivity (N) and reconfigurability ($|a_n|$)

Broadly, the usual implementation of microwave photonic FIR filters can follow two approaches. The first one is based on a single optical source in combination with multiple delay-lines implemented, for example, by a set of optical fibers or waveguides. This simple scheme does not allow tuning as this would require changing the T value

and the weight of the n-*th* tap (a_n) is changed by inserting loss or gain devices in the fiber. The other one, followed in this thesis, is based on the combination of a dispersive delay line and different optical carriers where the T value is changed by tuning the wavelength separation among the carriers, thereby allowing tunability and a_n is readily adjusted by changing the optical power emitted by the optical sources. The last, is considered a wavelength-division-multiplexing architecture.

Moreover, filters can operate under *incoherent regime*, where a_n coefficients in Equation (3.47) correspond to optical intensities and are thus positive or under *coherent regime* where the taps in the same equation can be complex-valued in general. Most of the proposed photonic microwave filter architectures work under incoherent regime since incoherent optical processing is insensitive to environmental conditions and, therefore, very robust and stable against vibrations or changes in temperature and polarization. However, based on signal processing theory, an all positive coefficient microwave filter can only operate as a low-pass filter. Besides that, filters with positive coefficients always have a resonance placed at the baseband. To overcome these limitations, considerable efforts have taken to design and implement photonic microwave filters with negative or complex coefficients, to achieve band-pass filtering functionality in the incoherent regime. A straightforward solution to generate negative coefficients is to use a MZM considering the wavelength dependence nature of their transfer function and a proper bias point choice which makes the modulator operate at complementary slopes of the transfer function. This is the solution followed in this thesis to implement a silicon-based microwave photonic FIR filter with negative coefficients and it will be explained in more detail in the next section.

3.4.3. Experimental microwave photonic filter

The silicon-based MZI modulator is that we already used for the distortion analytical model validation in section 3.2 and it is shown again in Figure 3-37(a). Static performance measurements have been firstly carried out to characterize the modulator. Figure 3-37(b) shows the effect of varying DC voltages from 0V to 10V on the normalized transmission spectrum of the modulator. It is shown that a large static extinction ration close to 30 dB is achieved at wavelengths around 1551.5 nm. The voltage-induced wavelength shift, $\Delta\lambda$, is used to calculate the effective index variation from the Equation (3.42) with L_A=1mm as the modulation length. We obtained that the effective index variation changes from 0 to 3.10^{-4} when the voltage increases from 0V to 10V. The $V_\pi L_\pi$ product, commonly used to evaluate the efficiency of the modulator, has also been calculated from such effective index variations obtained from the voltage-induced wavelength. A nearly constant $V_\pi L_\pi$ value around 2.25 V.cm has been obtained. The insertion loss of the modulator is around 12dB which includes the MMI losses.

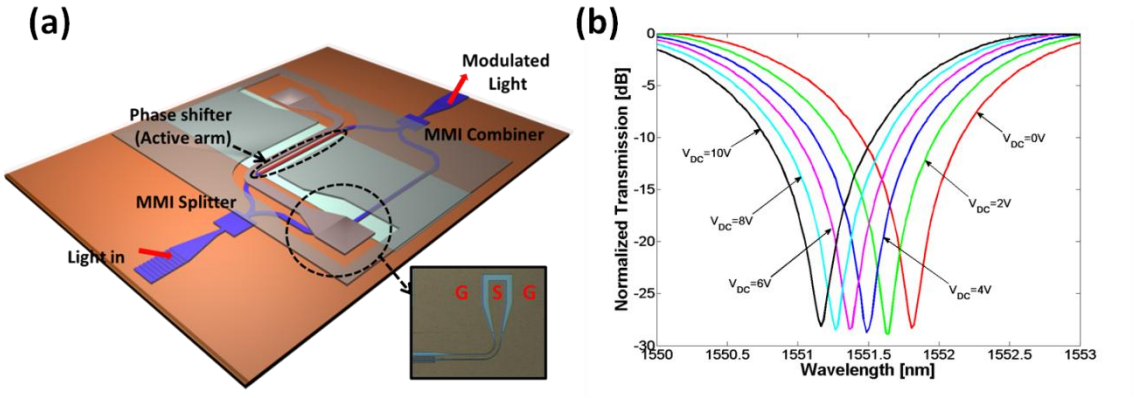

Figure 3-37: (a) Schematic of the silicon-based 1mm MZI electro-optic modulator for implementing the proposed photonic RF filter. The length difference between both arms is 180μm. Inset shows an optical microscope image of the traveling-wave ground–signal–ground (GSG) coplanar electrodes, (b) Normalized transmission spectrum variation with the DC voltage.

Figure 3-38 shows the block diagram of the proposed dispersion-based photonic microwave filter. This filter architecture already mentioned in the previous point is well-known for optical processing of RF signals. The principle of operation is based on modulating a multi-wavelength optical source with the input microwave signal (RF_{in}). The modulated signal is then propagated through a dispersive medium and photo-detected to obtain the filtered microwave signal (RF_{out}). Hence, each optical source implements a filter sample that is selectively delayed by employing the dispersive medium. The amplitude of each sample can be changed by using different techniques but the simplest way is controlling the output power of the optical sources as it has been already commented in the theory section. In such a way, a FIR filter can be implemented with transfer function expressed by Equation (3.47).

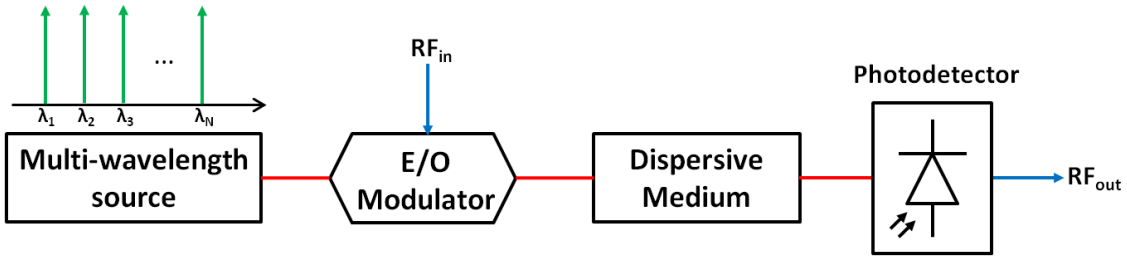

Figure 3-38: Block diagram of the dispersion-based photonic microwave filter.

The main advantage of this filter architecture is a very stable response due to operation in the incoherent regime. Furthermore, the filter transfer function can be reconfigured by dynamically changing the relative power of the optical wavelengths and it can be tuned by controlling the dispersive medium [VID03]. However, positive and negative filter coefficients are needed to allow a full versatility in the transfer function thus enabling flat-pass bands or high out-of-band suppression [CAO03, VID06]. The equivalent of positive and negative coefficients can be obtained by using opposite slopes of the modulation transmission response. The principle of the technique used is

based on the π-phase inversion which happens in the Mach-Zehnder modulators. The relative sign experienced by the microwave signal depends on the slope of the modulator transmission spectrum. If two optical carriers modulated by a microwave signal are placed at wavelengths that correspond with opposite slopes in the modulator response, as depicted in Figure 3-39, the microwave signals after photo-detection will show the same average power but a π-phase shift. In this way, positive and negative coefficients for a FIR filter can be obtained while keeping the stability inherent to incoherent operation if the input microwave signal is modulated over both slopes.

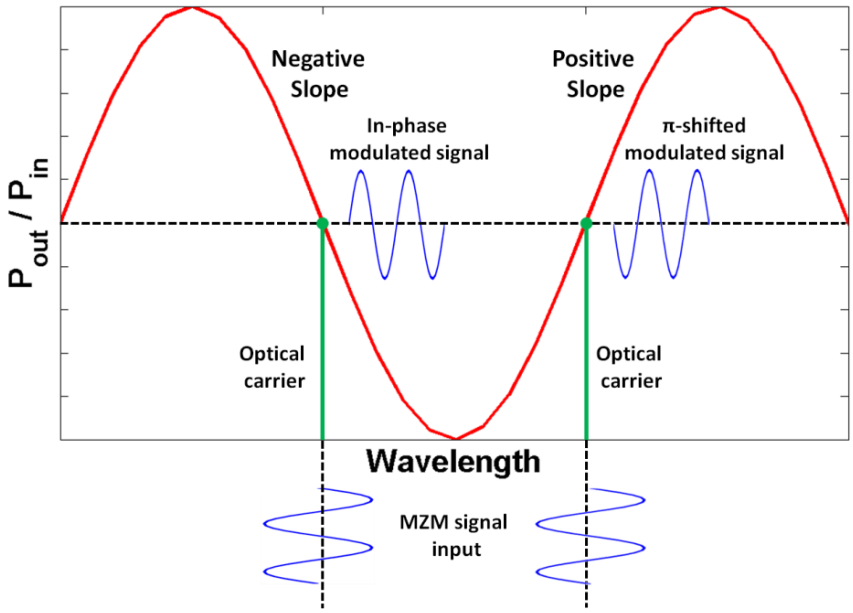

Figure 3-39: Concept of the π phase inversion suffered by a microwave modulating signal over the optical transfer function of a MZM as a function of the wavelength for a fixed DC voltage.

This technique has been employed with only one single $LiNbO_3$ Mach-Zehnder modulator by exploiting the V_π dependence with wavelength [VID06]. However, this dependence was very weak and optical sources with a very large separation (1300 and 1550 nm) were required. That makes the filter implementation complex, introduces high loss at 1300 nm (more than 20 dB) since the modulator is not optimized for operation at both 1550 and 1300 nm, prevents the use of EDFAs and limits further integration with other subsystems such as on-a-chip dispersive delay lines [SAN12].

In this work, we propose this approach for achieving positive and negative coefficients but this time based on exploiting the asymmetry of a silicon-based MZM. The asymmetry of the modulator is achieved by introducing a length difference of only 180 μm between the MZM arms. Such asymmetry introduces a strong dependence with wavelength in the modulator response. If, for instance, two optical carriers modulated by a microwave signal are placed at wavelengths that correspond with opposite slopes in the modulator response, the microwave signals after photo-detection will show a π-phase shift. So, by properly choosing the wavelength of the optical carriers, it is possible to control the sign of the corresponding filter coefficient. For our experiment, we choose a 4V of DC voltage and over the transmission spectrum for this voltage we

choose the wavelengths such that correspond with opposite slopes in the 4V modulator response. For the two-tap experiment we used two optical lasers emitting at λ_1=1550.75nm and λ_2=1552.30nm while for the three-tap one we used an array of lasers emitting at λ_1=1547.51nm, λ_2=1549.13nm and λ_3=1550.75 nm (Figure 3-40). The L=10km fiber coil provides a dispersion of D=17ps/km.nm which, for a wavelength separation between the two optical carriers of 1.55nm for the two-tap case, corresponds to a time delay between adjacent samples of T=263.5ps (T=D.L.Δλ) or in other words a free spectral range of FSR=1/T=3.8GHz.

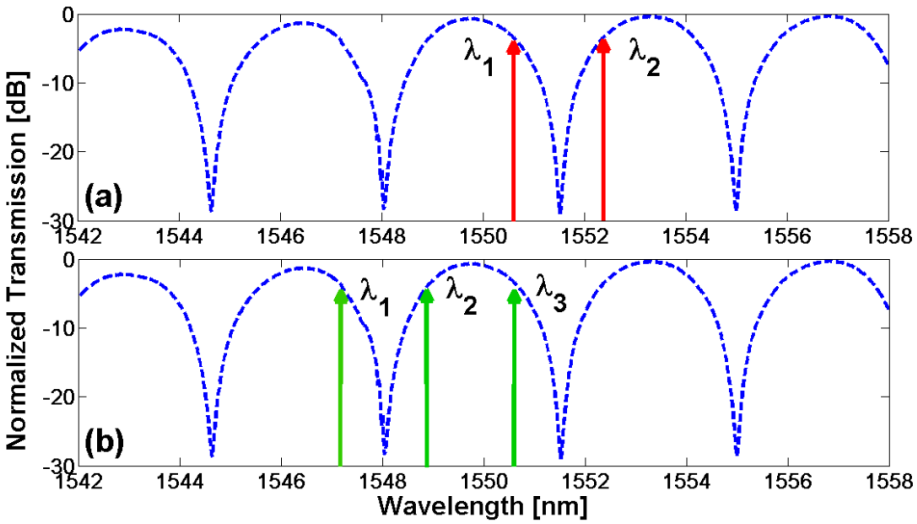

Figure 3-40: Normalized modulator transmission spectrum for a fixed 4V applied DC voltage showing the chosen wavelengths for (a) two-tap experiment and (b) three-tap experiment.

The experimental setup used for the experiment is shown in Figure 3-41.

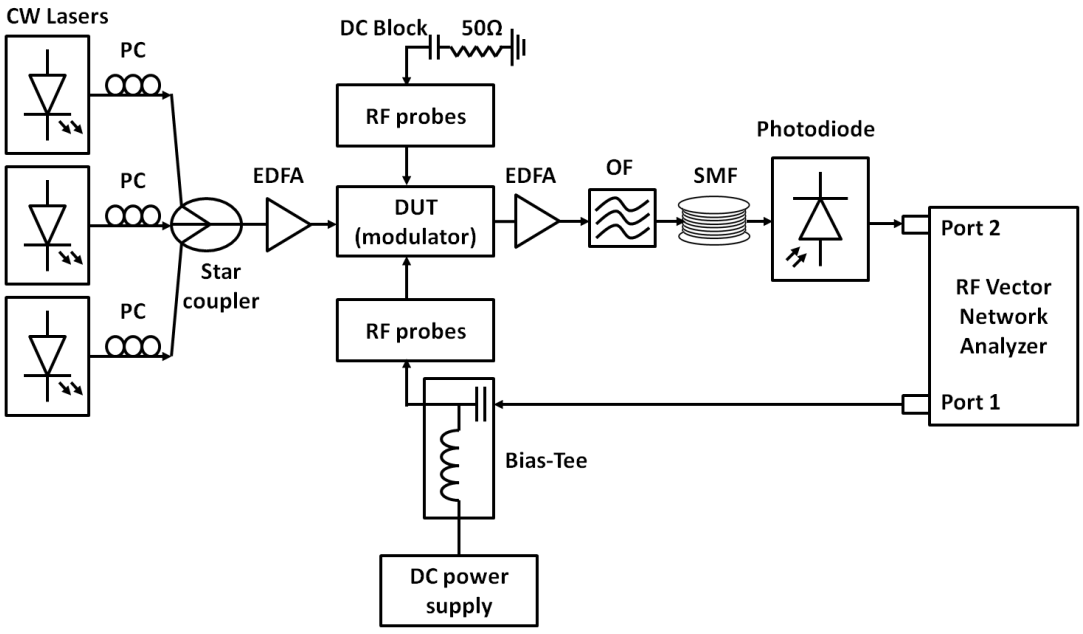

Figure 3-41: Experimental setup used to characterize the photonic RF filter performance.

A set of optical CW carriers are modulated by the silicon modulator. The RF signal from a vector network analyzer is combined with the DC voltage using a bias-Tee and applied to the modulator through a broadband GSG probe. The output of the electrode is terminated by a DC-block and a 50Ω load using another GSG probe. After modulation, the signals are amplified with an EDFA, filtered by a tunable OF and launched to a dispersive medium (a reel of 10 km of single-mode fiber). Chromatic dispersion in the fiber will introduce a time delay between the optical carriers. Then the optical signal at the output of the fiber coil is photo-detected and the delayed electrical signal is injected into the vector network analyzer. If a sweep of the frequency of the modulating electrical signal is carried out, the photonic microwave filter response is measured through the S_{21}.

Figure 3-42 shows the normalized filter response between 0-15 GHz for a 4V applied DC voltage when two optical carriers (λ_1=1550.75nm and λ_2=1552.30nm) enter the modulator with the same output power at the input of the photodiode. These wavelengths are placed at opposite slopes of the modulator response as it is shown in the Figure 3-40(a), resulting in filter coefficients [a1 a2]=[-1 1]. A very good agreement between theory, described by Equation (3.47), and measurements can be seen in such figure, demonstrating that two coefficients of opposite sign have been obtained.

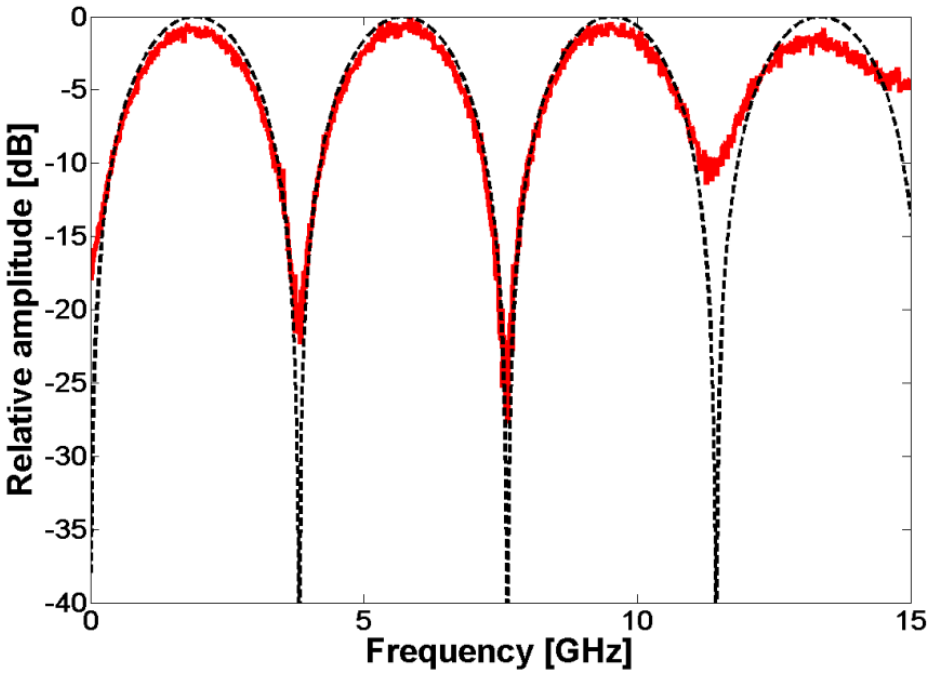

Figure 3-42: Experimental two-tap filter response with amplitude distribution [1 -1]. The solid line represents the experimental results and the dotted the theoretical estimation.

Figure 3-43 depicts the filter response when three optical carriers (λ_1=1547.51nm, λ_2=1549.13nm and λ_3=1550.75nm) are fed to the modulator with 4V applied DC voltage. The filter response agrees again very well with the theoretical response corresponding to the amplitude distribution [a1 a2 a3]=[-1 1 -1] (Figure 3-40(b)) for frequencies up to 10 GHz.

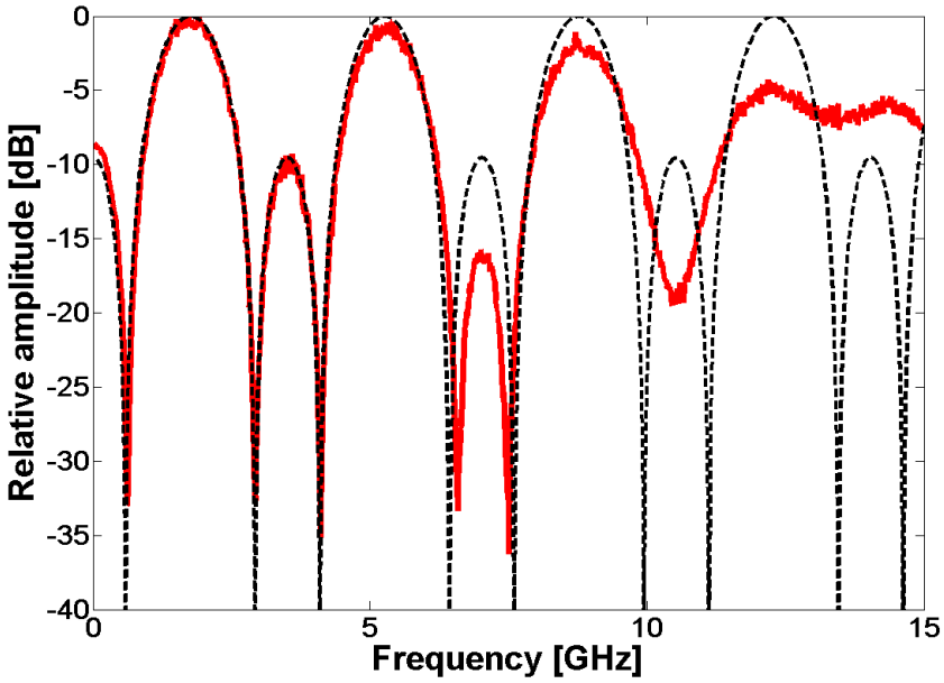

Figure 3-43: Experimental three-tap filter response with amplitude distribution [1 -1 1]. The solid line represents the experimental results and the dotted the theoretical estimation.

By changing the number of taps (that is, increasing the number of optical carriers) we have demonstrated the selectivity of the filter. Also, since the output powers (amplitude of each tap) of the lasers can be adjusted independently at high speed, the shape of the filter transfer function can be changed therefore showing the reconfigurability allowed by the filter. Further, in this case tunability by changing the T delay between optical carriers through the change of de wavelength difference between optical carriers is not possible due that they must be properly set in the wavelengths which correspond to QB bias (3dB respect to the maximum) of the MZI response. However, an alternative way to achieve filter discrete tuning consists on changing the length of the fiber path thorough a switched dispersion matrix (SDM) as in [VID03]. Therefore, since the filter tuning performance depends on the length of the fiber paths, it is also possible to choose the fiber lengths allowing discrete tuning over the whole filter spectral response margin. Furthermore, this additional component (SDM) could be integrated together with the proposed silicon modulator for building a CMOS-compatible PIC.

In conclusion, a novel photonic microwave filter implementation based on an asymmetric silicon-based MZI modulator has been demonstrated. A method for achieving positive and negative filter coefficients at the 1550nm wavelength based on exploiting the asymmetry of the MZI structure has been proposed. Furthermore, the obtained results show the capability of the silicon photonics platform not only to open up the path to full integration of photonic microwave filters in a chip scale but also to enable the implementation of advanced functionalities.

3.5. Active RF characterization set-ups

During the chapter, a brief overview of the set-ups used for experimental measurements has been provided. However, it is important to describe in more detail the experimental setup as well as the function of each component used for characterizing the fabricated electro-optic modulators acting in each case on different way. Two main types of active characterization set-ups have been presented and used along the chapter.

3.5.1. Distortion products measurements

In this point, the set-up used for the distortion products (both harmonic and intermodulation) measurements is reviewed in detail. For such task it is necessary to visualize and measure the frequency spectrum of the signals. For that, the main component used is the vectorial signal analyzer (VSA) which allows us to display features of the spectrum of the signal showing all distortion products and their power levels (for the SFDR, CDR and CL measurements), the constellation diagram of received signals and error vector magnitude measurements. This is the main set-up used in section 3.2 for the MZI distortion analytical model validation and the analog applications of frequency mixing by using a slow-wave MZI in section 3.3, although slight differences are shown between them. We are going to explain in detail the set-up used for the analytical distortion model validation since it is the most complex of both.

Light emitted by a CW laser is injected into the modulator via grating couplers (vertical coupling). The transmitted power is optimized through the use of a polarization controller (PolaRITE™ General Photonics). The description of coupling techniques as well as the passive characterizations set-ups is given in Appendix A.

A single tone test was performed so, a RF signal operating at f_{RF} is delivered by a RF signal generator (R&S SMR-50 with pulse modulation capability). If two-tone is required, as in section 3.3, two RF signals operating at f_{IF} and f_{OL} delivered by two RF signal generators are power combined by an electrical hybrid (Aeroflex Weinschel 1575). The single (or two) tone input is coupled a DC bias voltage supplied by a DC Power Source (Agilent E3647A) via a bias-Tee (SHF BT-110) and applied through high speed ground-signal-ground (GSG) input probes to the travelling wave electrodes terminated externally by a 50 Ω load coupled to a DC block (SHF DCB-110) through high speed GSG output probes to avoid reflexions (in section 3.3 neither GSG output probes nor DC block are used since the electrode configuration is lumped electrode).

The output modulated signal is amplified with an erbium-doped fiber amplifier (Amonics AEDFA-18-B-FA), filtered by a tunable optical filter (Tecos bandpass-OF) to isolate the selected resonance of the modulator optical transmission spectrum and split with a 50/50 optical splitter with the aim of photo-detecting by a photodiode (50GHz u2t XPDV2120R) and measuring the optical output by an optical power meter

(Thorlabs PM320E) simultaneously. Electrical amplification is performed (as needed) with a low noise (6dB) amplifier featuring 30dB RF gain (SHF 810). Finally, an electrical hybrid (Aeroflex Weinschel 1575) is used to separate the photo-detected signal to a VSA (R&S FSQ40 VSA) for measuring the electrical received signal in terms of frequency and to a digital communication analyzer (Agilent Infiniium DCA-J 86100C) for measuring the temporal signals with the aim of obtaining the modulation depth.

With the vector signal analyzer we display the spectrum of the electrical received signal and we can measure the fundamental and distortion products levels which allow us to obtain the SFDR, the CDR and the CL (in the case of the mixing application). Further, for the EVM measurements we must obtain the received constellations of an I/Q modulated signal. In such case, we properly programme the RF signal generator and vector signal analyzer.

The next Figure 3-44 depicts again the schematic of the set-up but this time showing a real picture of each component used.

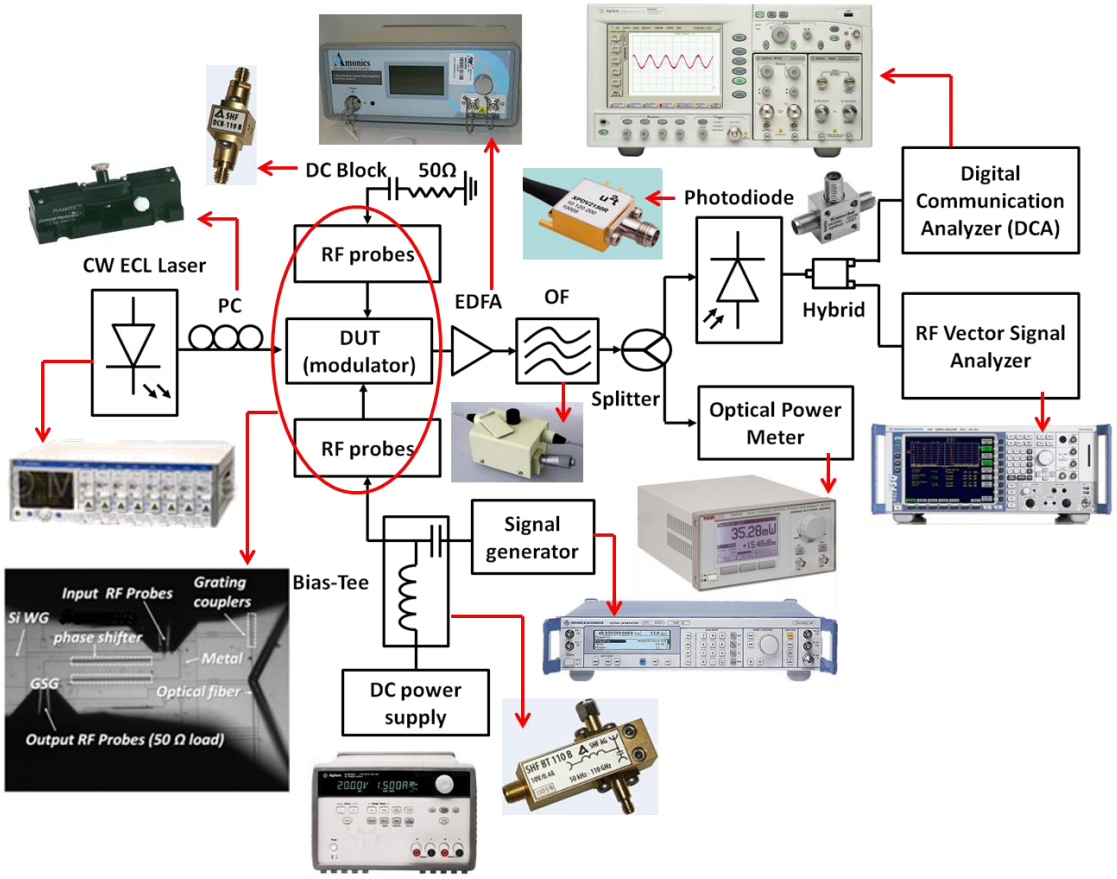

Figure 3-44: Schematic of the characterization setup and pictures of each component used in section 3.2 for distortion analytical model validation to evaluate the distortion products. The setup used in section 3.3 for the frequency mixing applications respectively is part of this one.

For completeness, pictures of the entire real set-up used in the Nanophotonics Technology Center facilities are shown in Figure 3-45.

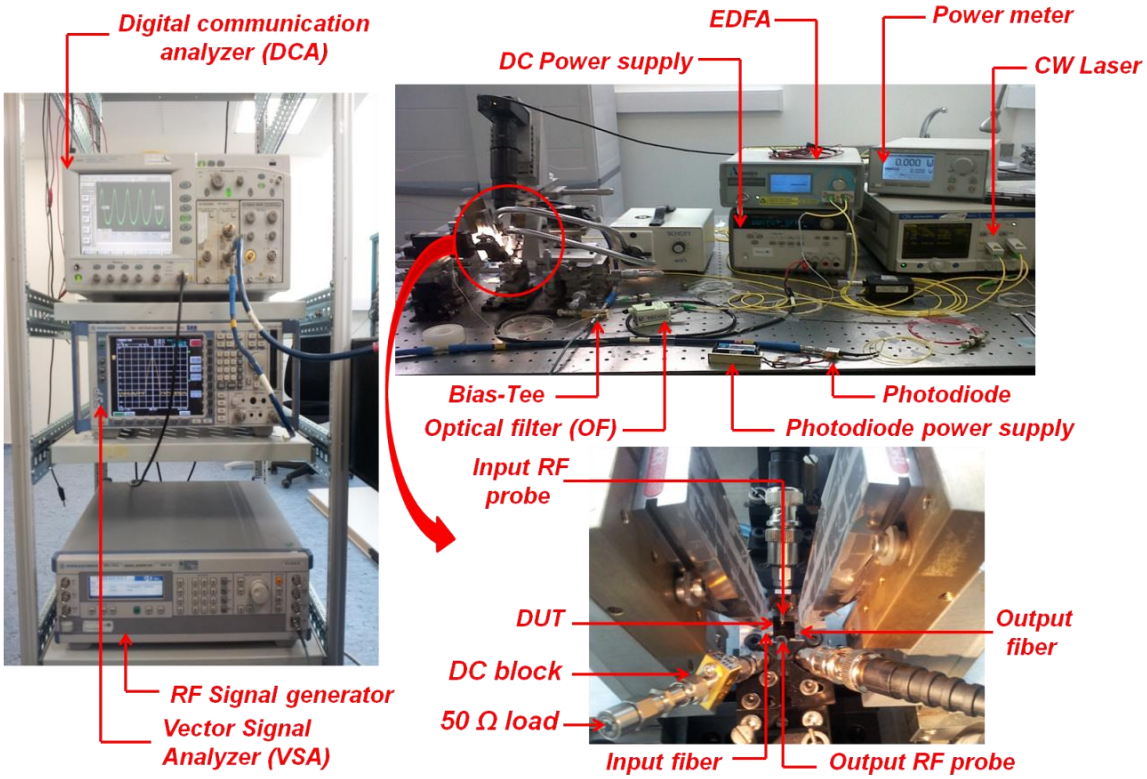

Figure 3-45: Pictures of the characterization setup used in section 3.2-3.3 for the distortion products measurements (and modulation depth in section 3.2 through temporal signals using the DCA).

3.5.2. Filter response measurements

On the other hand, the set-up used for small signal characterization has been used in section 3.4. Such characterization was necessary to demonstrate the filtering application (by using a silicon-based MZI). Small signal measurements consist basically on the determination of the electrical and electro-optical frequency response of a given electrical or electro-optical device via the calculation of the scattering parameters. In our case, we were interested on measure the S_{21} parameter to visualize the filter response. For such purpose, the main component used is the vector network analyzer.

The experimental setup used for the experiment is shown in Figure 3-46 (and real pictures of each component). A set of optical CW carriers emitted by a set of CW lasers are combined by an optical star coupler, amplified by an EDFA (Keopsys BT2-C-18-BO-FA) and injected into the modulator via grating couplers (the description of vertical coupling is given in Appendix A). The transmitted power emitted by each CW laser is optimized through the use of a polarization controller (PolaRITE™ General Photonics). The small electrical signal delivered by the port 1 of the RF vector network analyzer

(Agilent PNA-X N5247A) is coupled to a DC voltage supplied by a DC Power Source (Agilent E3647A) using a bias-Tee (SHF BT-110) and applied to the modulator through a high speed GSG probes. The output of the electrode is terminated by a DC-block (SHF DCB-110) and a 50Ω load using another GSG probes. The output modulated signal is amplified again by with an EDFA (Yenista/ NetTest/ Photonetics 93/3615/EOG/01 module), filtered by a tunable optical filter (Tecos bandpass-OF) to isolate the selected resonance of the modulator optical transmission spectrum and launched to a dispersive medium (a reel of 10 km of single-mode fiber). Then the optical signal at the output of the fiber coil is photo-detected by a high speed photodiode (u2t 50GHz XPDV2120R) and the delayed electrical signal is injected into the port 2 of the vector network analyzer. If a sweep of the frequency of the modulating electrical signal is carried out, the photonic microwave filter response is measured through the S_{21}.

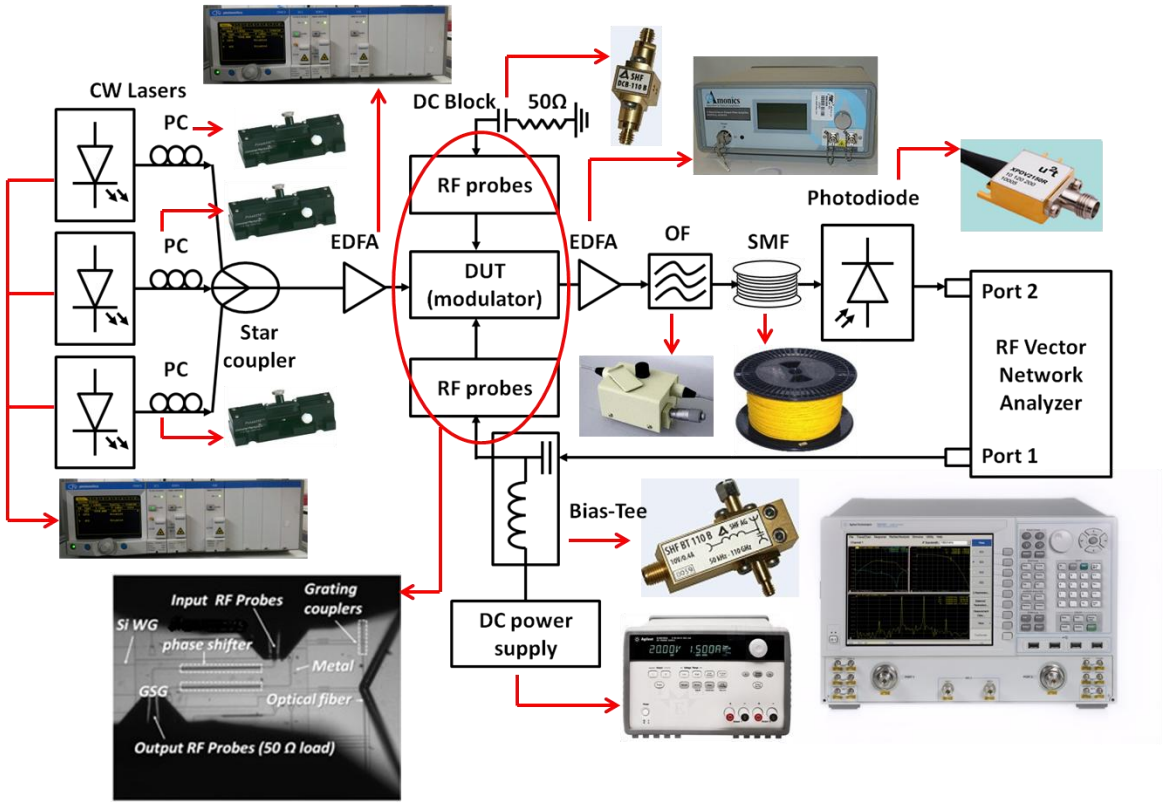

Figure 3-46: Schematic of the characterization setup and equipment pictures used in section 3.4 for obtaining the filter response thought the S_{21} parameter measurement.

For completeness, pictures of the entire real set-up used in the Nanophotonics Technology Center facilities are shown in Figure 3-47.

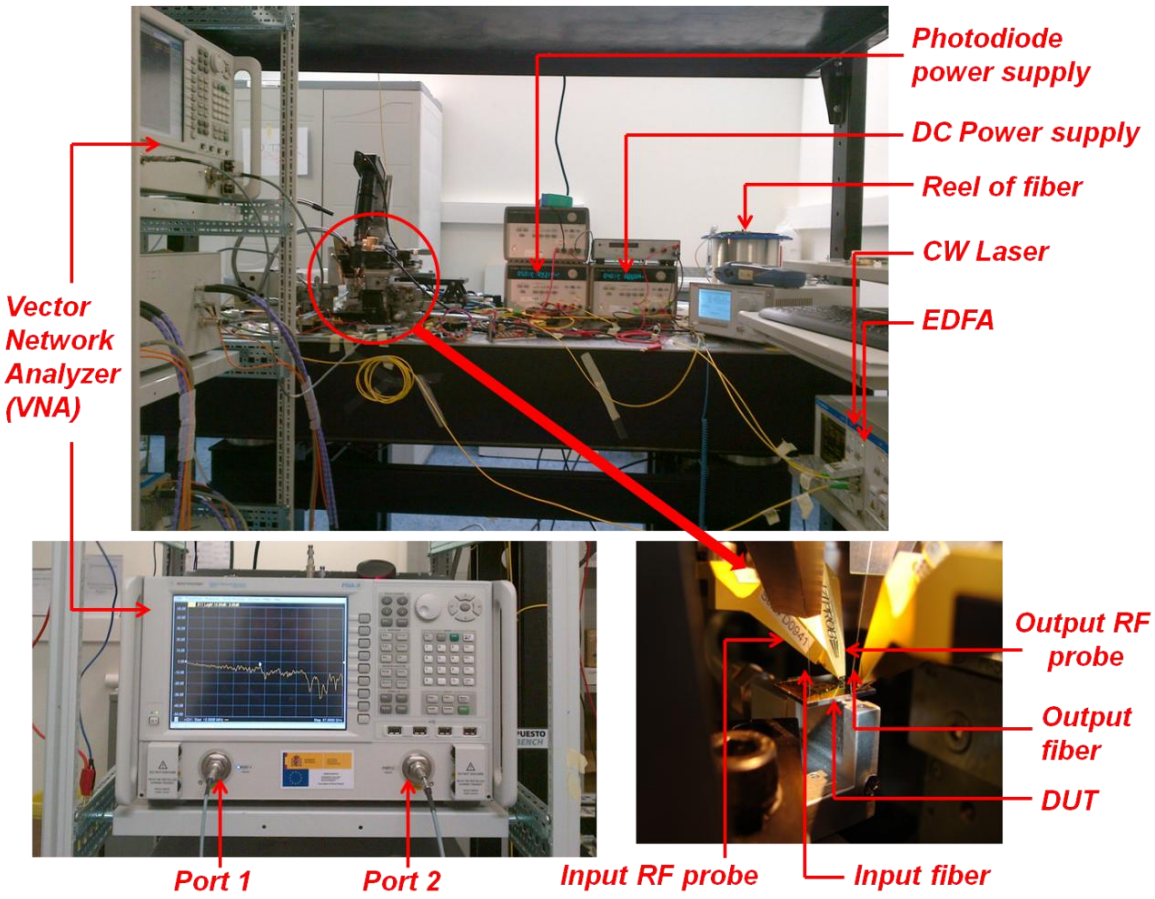

Figure 3-47: Pictures of the characterization setup used in section 3.4 for the filter response measurements (through the S_{21} parameter).

Chapter 4

Conclusions and future outlook

This thesis provides a contribution in the field of silicon photonics through demonstrating high-speed modulation in silicon devices to achieve more complex building blocks and thus going one step further towards a fully integration of modulators devices in the CMOS-compatible silicon photonics platform for digital and analog applications.

The objective of the chapter centered in digital applications was to develop silicon modulation structures in order to enhance the performance of conventional MZI modulators and to demonstrate that the incorporation of optical phase modulators into slow-wave and resonant structures can offer advantages in both reduced device footprint and power consumption meanwhile high speed operation is maintained. This will offer the prospect of compact optoelectronic devices integrated with CMOS circuits on the same silicon substrate. This objective has been successfully accomplished based on the obtained results, which can be summarized as:

- We have reported high speed silicon MRR-based modulators fabricated with a standard CMOS-compatible process. On one hand, we have presented a 40µm radius MRR modulator in which the modulation is achieved by carrier depletion effect in a *PIPIN* diode structure. On the other, a high speed silicon RAMZI (MRR+MZI) modulator has been reported. This RAMZI modulator features the potential for high speed performance and higher robustness against fabrication deviations than its standalone MRR based intensity modulator counterpart as the MRR does not require being at the critical coupling operation point. In our devices, modulation is achieved by carrier depletion in a *PIPIN* diode structure over RF/optical micrometer-scale interaction lengths featuring data transmissions up to 20Gbit/s.

- The performance of slow-light modulators has been analyzed in terms of insertion loss, modulation efficiency, and dynamic operation. The high modulation efficiency provided by the slow-light phase shifters with *PN* junctions allowed data transmission rates up to 40Gbit/s. Moreover, the promising combination of high modulation efficiency, low drive voltage, relatively low insertion loss, compactness, and high-speed operation gives all the more reasons for slow-light modulators to be used in more complex silicon photonic systems.
- Finally a method for measuring the propagation and insertion losses, since it is one of the main drawbacks derived by the use of the slow-light structures, is developed. Such method is proposed and demonstrated experimentally to be independent of the fiber-to-chip coupling losses. The method is based on the analysis of the transmission spectra of asymmetric MZIs, which enables the calculation of the propagation losses as well as the power imbalance of the branching structure of a MZI. First of all, the method is developed for conventional rib waveguides MZIs and then it is extended to slow-light photonic waveguiding structures.

As future work in the digital approach, it is proposed the CMOS integration of drivers and DC circuitry and the assembling and packaging of the silicon modulators. Respect to slow-light modulators the optimization of the travelling wave electrodes for the modulator operation in the slow-light regime and investigate alternative designs to increase the optical bandwidth with use of engineered slow-light structures are some of the future directions proposed. On the other hand, for the RAMZI modulator, a possible enhancement can be adding an additional ring placed in the other arm of the MZI. This structure will be useful to overcome the difference of attenuation between both arms of the MZI and so maximize the extinction ratio.

The chapter devoted to analog applications presents different researches carried out in the analog scope for application in the field of IMWP, all of them using CMOS-compatible electro-optic silicon-based MZI modulators which validate the potential of silicon CMOS photonics and SOI technology as a promising approach for enabling large scale photonic integration driving the development of integrated microwave photonics applications. The work achieved in this scope can be summarized as follows:

- We have developed analytical expressions for the harmonic and intermodulation nonlinear distortions of a MZI modulator due to the nonlinear feature of the silicon and the modulator transfer function. Distortion equations are estimated analytically and found to be in good agreement with numerical simulations. Another excellent feature of the presented model is the possibility to linearize the modulator at the time of designing it. Given the growing advantages of silicon photonics and therefore of silicon modulators for emerging IMWP applications, this model gives a potential tool to predict the nonlinear modulator performance and the parameters needed for a full study of

an analog photonic link.

- We have shown also in this chapter a very efficient method of generating mixing products in a silicon modulator exploiting its nonlinearity. Furthermore, the conversion efficiency has been enhanced via slow-light propagation in the active region of the modulator appearing the slow-light effect as a potential technology for building microwave devices.
- Finally, a novel photonic microwave fully reconfigurable filter implementation based on an asymmetric silicon-based MZI modulator has been demonstrated. The obtained results show the capability of the silicon photonics platform not only to open up the path to full integration of photonic microwave filters in a chip scale but also to enable the implementation of advanced functionalities.

As possible direction for further research in this scope it can be suggested that it would be interesting to demonstrate the performance enhancement techniques presented here at a higher frequency range, i.e. at microwave or millimeter-wave frequency range, since nowadays the trend in microwave photonics systems are moving toward high frequencies.

Overall, we believe that the results presented in this work may have both scientific and commercial importance as proof of concept. It explores silicon photonic modulation devices through extensive empirical validation and characterization, as part of the requited photonic building blocks for use in analog and digital communication systems.

Appendix A

Horizontal & vertical coupling and passive characterization

Conventional single-mode SOI nanophotonic waveguides are about 220 nm thick and 500 nm wide. However, standard single-mode fibers (SMF) are very large size compared to nanophotonic SOI waveguides. Typical core diameter size of a standard SMF is about 8μm. Thus, coupling light from an optical fiber to a nanophotonic waveguide becomes a difficult task. The high difference in the dimensions between the fiber and the waveguide causes a high mismatch between their optical modes. Due to this mismatch, a coupling structure is needed to adapt a wide fiber to a narrow silicon waveguide improving the coupling loss. To solve the fiber-chip coupling problem, two main strategies have appeared in literature, depending on the physical direction in which the fiber is coupled to the chip: vertical and horizontal coupling techniques.

A.1. Horizontal coupling

Horizontal coupling, also known in literature as end-fire or butt-coupling, involves coupling light onto the end of the waveguide. Due to the great difference between dimension of waveguide and fiber, this form implies very high coupling losses. A solution for an efficient butt-coupling relies on the use of tapers, which consist on a waveguide whose dimensions change along the propagation direction from chip to fiber, creating a transition from a small to a large mode. It is so able to convert the small size optical mode of the nanophotonic waveguide into a larger size optical mode, and vice-versa. The most widely used taper structure is an inverted taper planar structure, which, due to its planar geometry (constant height), can be fabricated using conventional CMOS compatible techniques. Moreover, this technique is highly dependent upon the

facet quality and the use of lensed fibers may improves the coupling efficiency. A schematic of configuration is shown in Figure A-1.1:

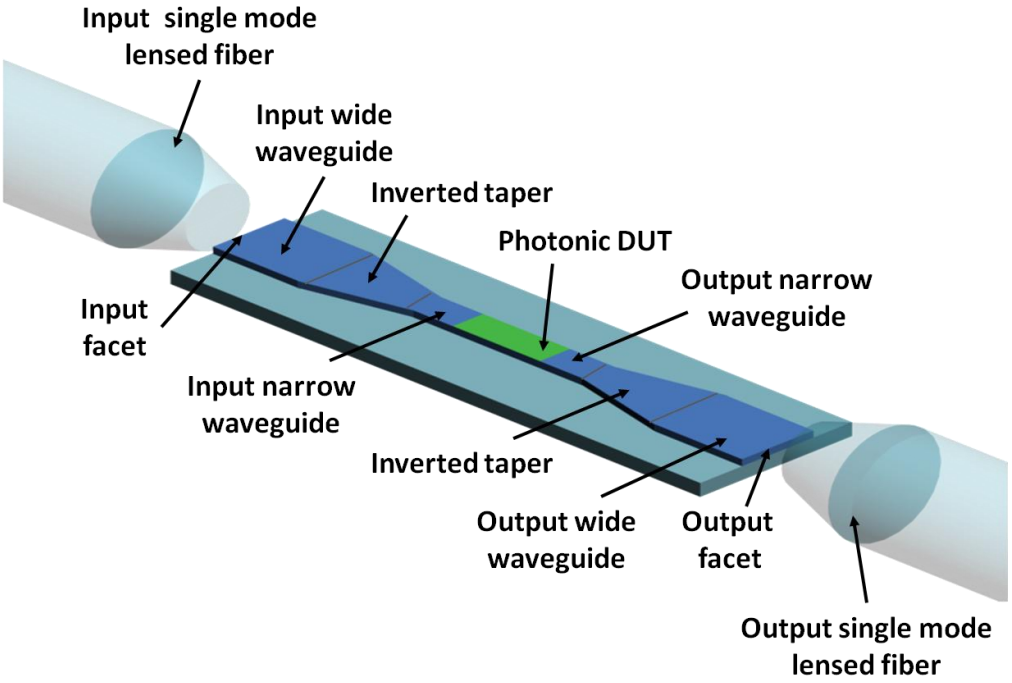

Figure A-1.1: Standard fiber-to-chip horizontal coupling technique by using lensed fibers and inverted taper.

In the Figure A-1.2, a schematic of the basic set-up with horizontal coupling for passive characterization (optical measurements) is shown.

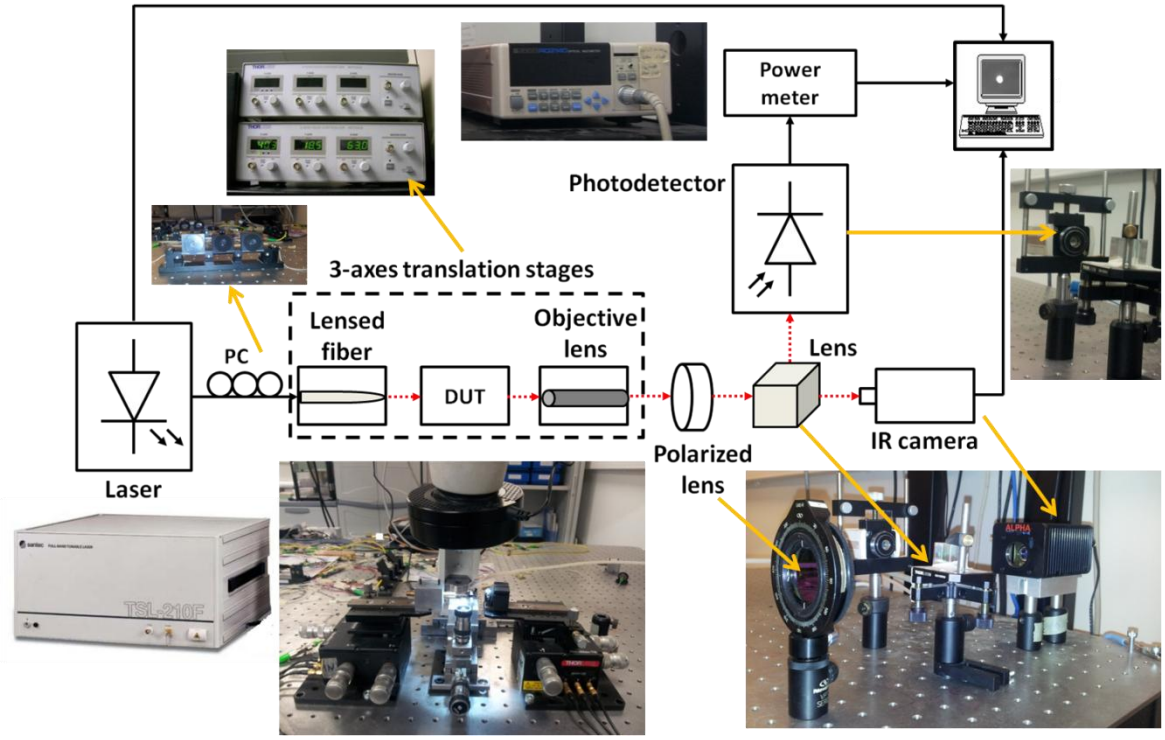

Figure A-1.2: Schematic of the passive characterization set-up with horizontal coupling. Picture of each component is also shown.

As excitation source, a broadband laser (SANTEC TSL-210F) is used. After the laser, a polarization controller (PC) is placed. Because the photonic devices under test (DUT) are polarization-sensitive, we must control the polarization of the light incident upon it in order to check its correct performance. After the polarizer, the light is injected into the chip with the selected polarization, through a lensed fiber. With the output polarizer lens, the polarization to be measured can be selected, being in a horizontal position for measuring the TE polarization and in a vertical position for the TM one. Next we place a lens that splits the received light to a power meter (Q2140 ANDO) and to an infrared camera, which were connected to a computer by a GPIB bus, in order to visualize the light spot and measure the received power at the same time. The 3-axes translation stages are connected to a piezoelectric controller so a finer adjustment in alignment process between the fiber, the sample and the objective lens may be done. Moreover, a microscope allows you to align more easily and check that the chip and the fiber not touch and therefore no damage is produced in the sample

The next pictures in the Figure A-1.3 are (a) the entire set-up, (b) the holders where the sample is positioned and the 3-axes translation stages and (c) a detail of the fiber-chip-objective configuration.

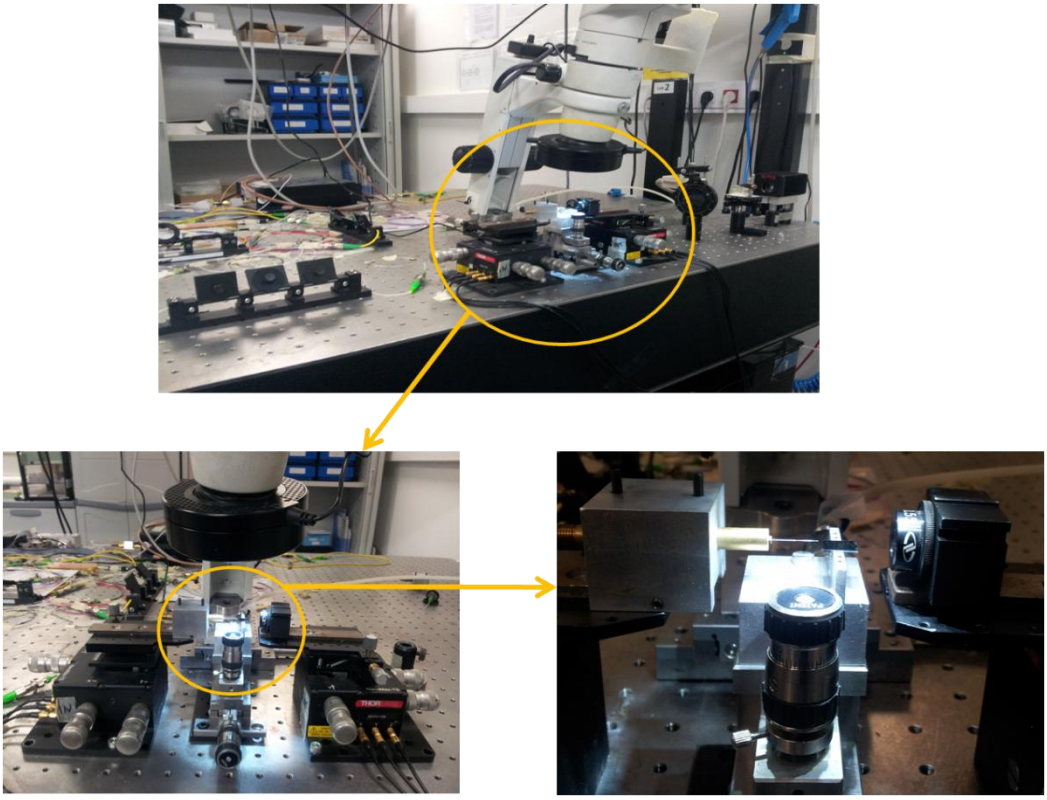

Figure A-1.3: Pictures of the horizontal coupling set-up used in the Nanophotonics Technology Center laboratories during the thesis development.

A.2. Vertical coupling

In vertical coupling techniques, light is injected onto the surface of the waveguide at a specific angle. We call them vertical coupling techniques because the optical fiber is vertically placed over the waveguide. The most important vertical coupling technique is the grating coupler. A grating coupler is basically a one dimensional (1D) diffractive structure that can be designed for coupling light onto the waveguide surface by means of one of its orders of diffraction. A schematic of configuration is shown in Figure A-2.1:

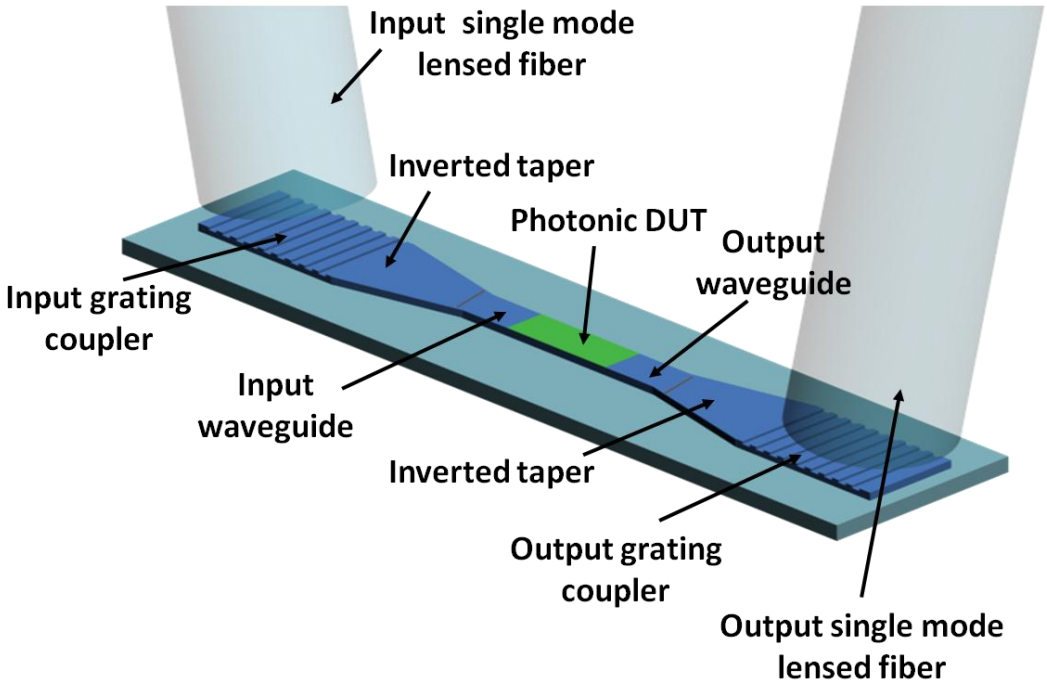

Figure A-2.1: Standard fiber-to-chip vertical coupling technique by using grating couplers.

As excitation source, an external cavity laser (ECL Photonetics) is used. After the laser, in the same way that horizontal coupling, the input polarization state is firstly set by adjusting an external polarization controller (PC). After the polarizer, the light is injected into the chip with the selected polarization, through vertical coupling with a single mode fiber tilted under an angle of 13 degrees relative to the surface normal of the grating. Next we place an optical power meter (THORLABS PM320E) to monitoring the received power, which were connected to a computer by a GPIB bus, in order to measure it. The next Figure A-2.2 shows again the basic set-up with vertical coupling for passive characterization (optical measurements) and, for completeness, Figure A-2.3 shows pictures of the entire setup are also shown

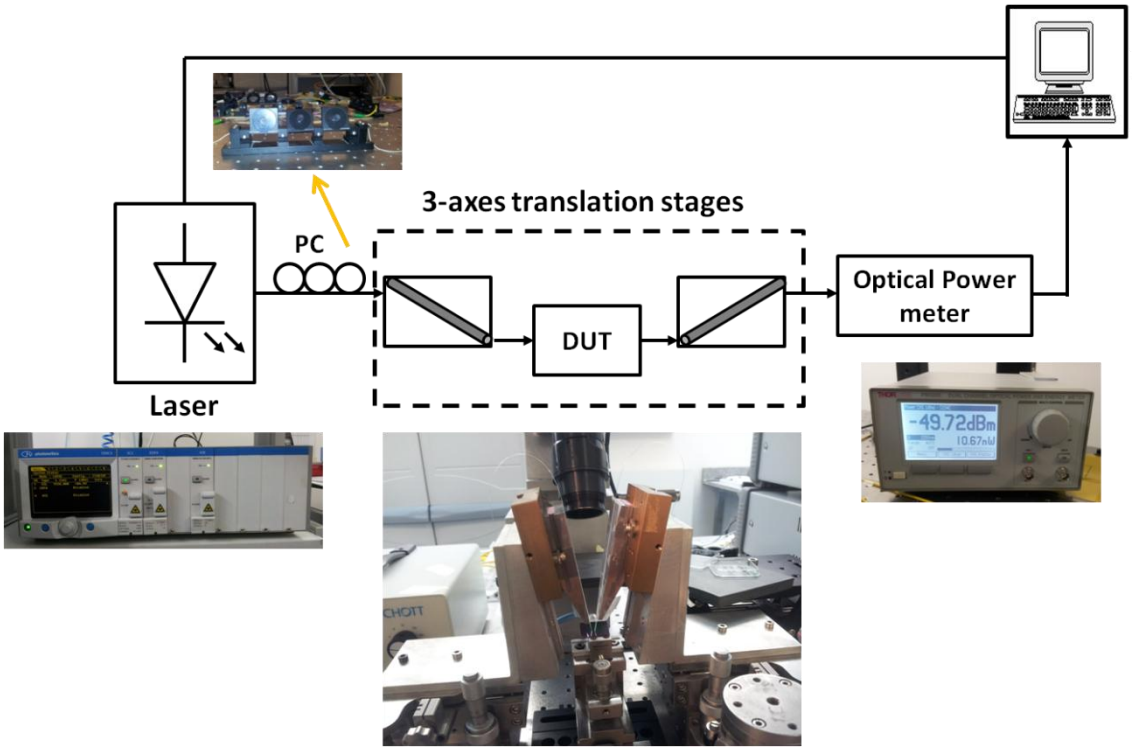

Figure A-2.2: Schematic of the passive characterization set-up with vertical coupling. Picture of each component is also shown.

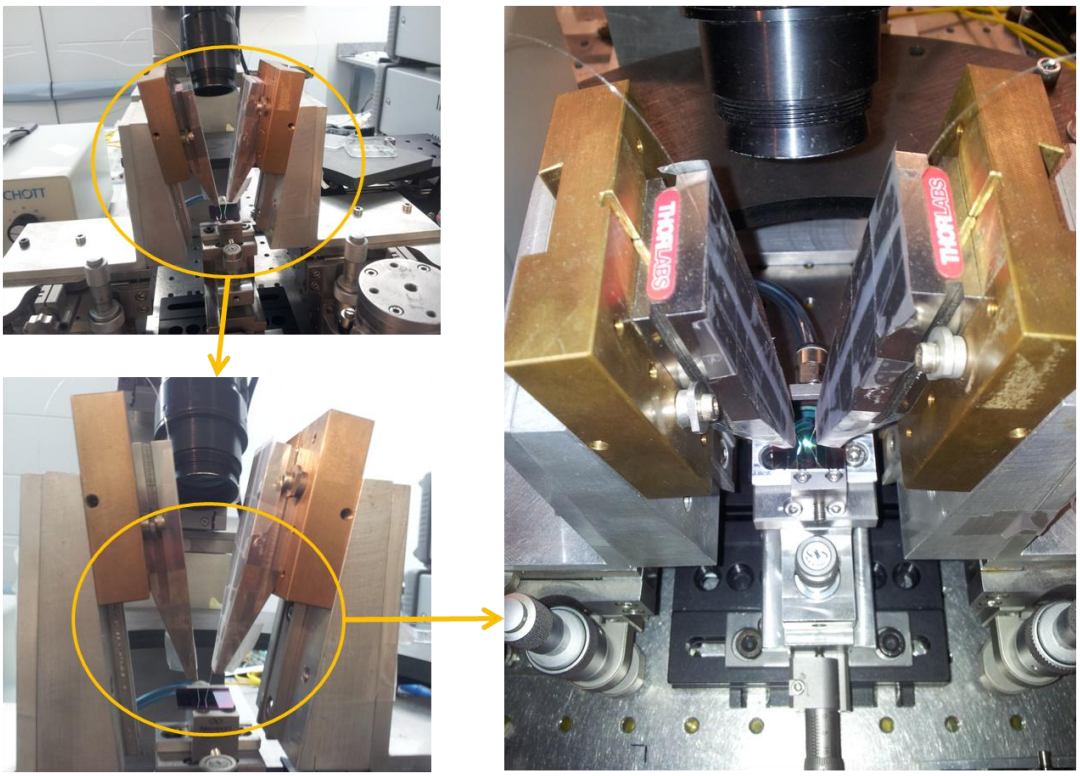

Figure A-2.3: Pictures of the vertical coupling set-up used in the Nanophotonics Technology Center laboratories during the thesis development.

List of publications

JOURNAL PUBLICATIONS

[J.1] **A. M. Gutierrez**, A. Brimont, J. Herrera, M. Aamer, D. J. Thomson, F. Y. Gardes, G. T. Reed, J. M. Fedeli, and P. Sanchis, "Analytical Model for Calculating the Nonlinear Distortion in Silicon-Based Electro-Optic Mach-Zehnder Modulators," *to be published in Journal of Lightwave Technology*, 2013.

[J.2] **A. M. Gutiérrez**, B. Vidal, A. Brimont, D. J. Thomson, F. Y. Gardes, G. T. Reed, J.-M. Fedeli and P. Sanchis, "A photonic integrated microwave filter based on a silicon carrier depletion modulator," *to be published in IEEE Photonics Journal*, 2013.

[J.3] **A. M. Gutiérrez**, A. Brimont, J. Herrera, M. Aamer, J. Martí, D. Thomson, F. Gardes, G. Reed, J. Fedeli, and P. Sanchis, "Silicon slow-light-based photonic mixer for microwave-frequency conversion applications," *Optics Letters*, vol. 37, pp. 1721-1723, 2012.

[J.4] **A. M. Gutierrez**, A. Brimont, M. Aamer, and P. Sanchis, "Method for measuring waveguide propagation losses by means of a Mach–Zehnder Interferometer structure", *Optics Communications*, vol. 285, no. 6, pp. 1144-1147, 2012.

[J.5] **A. M. Gutierrez**, A. Brimont, G. Rasigade, M. Ziebell, D. Marris-Morini, J.-M. Fedeli, L. Vivien, J. Marti, and P. Sanchis, "Ring-Assisted Mach–Zehnder Interferometer Silicon Modulator for Enhanced Performance," *Journal of Lightwave Technology*, vol. 30, no. 1, pp. 9-14, 2012.

[J.6] G. Rasigade, M. Ziebell, D. Marris-Morini, A. Brimont, **A. M. Gutierrez**, P. Sanchis, J. Fedeli, G. Duan, E. Cassan, and L. Vivien, "10-Gb/s Error-Free

Silicon Optical Modulator for Both TE and TM Polarized Light," *IEEE Photonics Technology Letters*, vol. 23, no. 23, pp. 1799-1801, 2011.

[J.7] A. Brimont, **A. M. Gutierrez,** , M. Aamer, D.J. Thomson, F.Y. Gardes, J.M. Fedeli, G.T. Reed, J. Marti, and P. Sanchis, "Slow-Light-Enhanced Silicon Optical Modulators Under Low-Drive-Voltage Operation," *IEEE Photonics Journal*, vol. 4, no. 5, pp. 1306-1315, 2012.

CONFERENCE PUBLICATIONS

[C.1] **A. M. Gutiérrez**, P. Sanchis, A. Brimont, D. J. Thomson, F. Y. Gardes, G. T. Reed, J.-M. Fedeli, and B. Vidal, "Chirp Characterization of a Single-arm Asymmetric Silicon Carrier Depletion Modulator," Accepted in IEEE International Topical Meeting on Microwave Photonics (MWP), Alexandria, Virginia (USA), October 28-31, 2013.

[C.2] **A. M. Gutierrez**, A. Brimont, J. Herrera, M. Aamer, D. J. Thomson, F. Y. Gardes, G. T. Reed, J-M. Fédéli, and P. Sanchis, "Modeling of the nonlinear distortion in an electro-optic silicon-based Mach-Zehnder modulator," Accepted in *10th IEEE International Conference on Group IV Photonics (GFP)*, Seoul (Korea), August 28-30, 2013.

[C.3] **A. M. Gutiérrez**, J. V. Galan, J. Herrera, A. Brimont, M. Aamer, J. Martí, D. Marris-Morini, L. Vivien, J-M. Fédéli, D. J. Thomson, F. Y. Gardes, G. T. Reed, and P. Sanchis, "Silicon-Based Electro-Optic Modulators for Linear and Nonlinear Radio-over-Fiber Applications," *IEEE International Topical Meeting on Microwave Photonics (MWP)*, Noordwijk (Holland), September 11-14, 2012.

[C.4] **A. M. Gutierrez**, A. Brimont, M. Aamer, J. Martí, P. Sanchis, D. Thomson, F.Y. Gardes, G. T. Reed, and J. M. Fedeli, "A slow light silicon-based Mach-Zehnder Interferometer for frequency mixing applications," *16th European Conference on Integrated Optics and Technical Exhibition (ECIO)*, Sitges (Spain), April 18-20, 2012.

[C.5] A. Brimont, **A. M. Gutierrez**, M. Aamer, D. J. Thomson, F. Y. Gardes, J. M. Fedeli, G. Reed, J. Martí and P. Sanchis, "Recent progress on high contrast 40Gb/s and low drive voltage 10 Gb/s slow light-based silicon photonic modulators," *Conferencia Española de Nanofotonica*, Carmona (Spain), October 1-4, 2012.

OTHER PUBLICATIONS

[O.1] M. Aamer, D. J. Thomson, **A. M. Gutiérrez**, A. Brimont, F. Y. Gardes, G. T. Reed, J. M. Fedeli, A. Hakansson, and P. Sanchis, "10Gbit/s error-free DPSK modulation using a push-pull dual-drive silicon modulator", *Optics Communications*, vol. 304, pp. 107-110, 2013.

[O.2] M. Aamer, A. Griol, A. Brimont, **A. Gutierrez**, P. Sanchis, and A. Håkansson, "Increased sensitivity through maximizing the extinction ratio of SOI delay-interferometer receiver for 10G DPSK," *Optics Express*, vol. 20, pp. 14698-14704, 2012.

[O.3] M. Aamer, **A. M. Gutierrez**, A. Brimont, D. Vermeulen, G. Roelkens, J. M. Fedeli, A. Håkansson and P. Sanchis, **"**CMOS Compatible Silicon-on-Insulator Polarization Rotator Based on Symmetry Breaking of the Waveguide Cross Section," *IEEE Photonics Technology Letters*, vol. 24, no. 22, pp. 2031-2034, 2012.

[O.4] P. Sanchis, M. Aamer, A. Brimont, **A. M. Gutierrez**, N. Sotiropoulos, H. de Waardt, D. J. Thomson, F. Y. Gardes, G. T. Reed, K. Ribaud, P. Grosse, J. M. Hartmann, J.-M- Fedeli, D. Marris-Morini, E. Cassan, L. Vivien, D. Vermeulen, G. Roelkens, and A. Hakansson, "Silicon CMOS photonics platform for enabling high-speed DQPSK transceivers", *15th International Conference on Transparent Optical Networks (ICTON)*, Cartagena (Spain), June 23-27, 2013.

[O.5] M. Aamer, **A. M. Gutiérrez**, A. Brimont, and P. Sanchis, "Ring Resonator Structures for Active Applications in Silicon", Optica Pura y Aplicada, vol. 45, pp. 169-175, 2012.

[O.6] M. Aamer, A. Griol, A. Brimont, **A. M. Gutierrez**, P. Sanchis and A. Håkansson, "Increased sensitivity of delay-interferometer receiver for 10G DPSK for SOI platform," *Conferencia Española de Nanofotonica*, Carmona (Spain), October 1-4, 2012

[O.7] A. Rosa, **A. M. Gutiérrez**, A. Brimont, A. Aamer, and P. Sanchis, "A silicon-based tunable multimode interferometer using the thermo-optic effect." *European Conference on Integrated Optics (ECIO)*, Sitges (Spain), April 18-20, 2012.

[O.8] M. Aamer, A. Brimont, **A. M. Gutierrez**, A. Griol, J. Martí, and P. Sanchis, "Optimized 20 Gbps DPSK demodulator in 220nm SOI. " *16th European*

Conference on Integrated Optics and Technical Exhibition (ECIO), Sitges (Spain), April 18-20, 2012.

[O.9] M. Aamer, **A. M. Gutierrez**, A. Brimont, A. Griol, and P. Sanchis, "Experimental demonstration of an ultra compact SOI polarization rotator," *16th European Conference on Integrated Optics and Technical Exhibition (ECIO)*, Sitges (Spain), April 18-20, 2012.

[O.10] M. Aamer, **A. M. Gutierrez**, A. Brimont, and P. Sanchis, "Ring Resonator Structures for Active Applications in Silicon," *7ª Reunión Española de Optoelectrónica (OPTOEL)*, Santander (Spain), June-July 29-01, 2011.

List of figures

List of tables

Acronyms

AC	Alternating Current
APL	Analog Photonic Link
BPG	Bit Pattern Generator
CDR	Carrier-to-Distortion
CL	Conversion Losses
CW	Continuous Wave
CMOS	Complementary Metal Oxide Semiconductor
DC	Direct Current
EBL	Electron-Beam Lithography
ECL	External Cavity Laser
EDFA	Erbium-Doped Fiber Amplifier
E/O	Electrical-to-Optical
ER	Extinction Ratio
EVM	Error Vector Magnitude
FIR	Finite Impulse Response
FLR	Fast-Light Region
FSR	Free Spectral Range
GDS	Graphic Database System
GSG	Ground-Signal-Ground
HD2	2^{nd}-order Harmonic Distortion
HD3	3^{rd}-order Harmonic Distortion
IC	Integrated Circuit
IIP3	3^{rd}-order Input Intercept Point
IIR	Infinite Impulse Response
IL	Insertion Losses

IMD2	2nd-order Intermodulation Distortion
IMD3	3rd-order Intermodulation Distortion
IMWP	Integrated Microwave Photonics
LCWG	Laterally Corrugated Waveguide
MATB	Maximum Transmission Bias Point
MITB	Minimum Transmission Bias Point
MMI	Multi-Mode Interference
MOS	Metal-Oxide-Semiconductor
MRR	Micro-Ring Resonator
MSSR	Main to Secondary Sidelobe Ratio
MWP	Microwave Photonics
MZI	Mach-Zehnder Interferometer
MZM	Mach-Zehnder Modulator
NoC	Network-On-Chip
NRZ	Nonreturn-to-zero
O/E	Optical-to-Electrical
OF	Optical Filter
PC	Polarization Controller
PE	Pre-Emphasis
PhCs	Photonic Crystals
PIC	Photonic Integrated Circuit
PRBS	Pseudo-Random Bit Sequence
QB	Quadrature Bias Point
RAMZI	Ring-assisted Mach-Zehnder Interferometer
RF	Radio Frequency
SEM	Scanning Electron Microscope
SFDR	Spurious-Free Dynamic Range
SOI	Silicon-On-Insulator
SL-MZI	Slow-Light Mach Zehnder Interferometer
SLR	Slow-Light Region
UWB	Ultra Wide-Band

Bibliography

[AKI12A] S. Akiyama, T. Baba, M. Imai, T. Akagawa, M. Takahashi, N. Hirayama, H. Takahashi, Y. Noguchi, H. Okayama, T. Horikawa, and T. Usuki, "12.5-Gb/s operation with 0.29-V.cm $V_{\pi}L_{\pi}$ using silicon Mach-Zehnder modulator based-on forward-biased pin diode," *Optics Express*, vol. 20, no. 3, p. 2911, Jan. 2012.

[AKI12B] S. Akiyama, T. Baba, M. Imai, T. Akagawa, M. Noguchi, E. Saito, Y. Noguchi, N. Hirayama, T. Horikawa, and T. Usuki, "50-Gb/s silicon modulator using 250-μm-Long phase shifter based-on forward-biased pin diodes," *The 9th International Conference on Group IV Photonics (GFP)*, pp. 192–194, 2012.

[ALI11] P. Alipour, A. A. Eftekhar, A. H. Atabaki, Q. Li, S. Yegnanarayanan, C. K. Madsen, and A. Adibi, "Fully reconfigurable compact RF photonic filters using high-Q silicon microdisk resonators," *Optics Express,* vol. 19, no. 17, p. 15899, Aug. 2011.

[AYA12] A. Ayazi, T. Baehr-Jones, Y. Liu, A. E.-J. Lim, and M. Hochberg, "Linearity of silicon ring modulators for analog optical links," *Optics Express*, vol. 20, no. 12, p. 13115, May 2012.

[BAB08] T. Baba, "Slow light in photonic crystals," Nature Photonics, vol. 2, no. 8, pp. 465–473, Aug. 2008.

[BAB12] T. Baba, S. Akiyama, M. Imai, T. Akagawa, M. Takahashi, N. Hirayama, H. Takahashi, Y. Noguchi, H. Okayama, T. Horikawa, T. Usuki, T., "25-Gbps operation of silicon p-i-n Mach-Zehnder optical modulator with 100-μm-long phase shifter," *Conference on Lasers and Electro-Optics (CLEO), 2012*, pp.1, 2, 6-11 May 2012

[BAB13] T. Baba, S. Akiyama, M. Imai, N. Hirayama, H. Takahashi, Y. Noguchi, T. Horikawa, and T. Usuki, "50-Gb/s ring-resonator-based silicon modulator," *Optics Express*, vol. 21, no. 10, p. 11869, May 2013.

[BAH01] M. C. T. Bahaa and E. A. Saleh, "*Fundamentals of Photonics*.", 1991 John Wiley & Sons, Inc., p. 1010, 2001.

[BEA10] R. G. Beausoleil and A. E. Willner, "Silicon-Based Microring Resonator Modulators for Intensity Modulation," *IEEE Journal of Selected Topics in Quantum Electronics*, vol. 16, no. 1, pp. 149–158, 2010.

[BER10] T. Berceli and P. R. Herczfeld, "Microwave Photonics—A Historical Perspective," *IEEE Transactions on Microwave Theory and Techniques*, vol. 58, no. 11, pp. 2992–3000, Nov. 2010.

[BET96] G. E. Betts and F. J. O'Donnell, "Microwave analog optical links using suboctave linearized modulators," *IEEE Photonics Technology Letters*, vol. 8, no. 9, pp. 1273–1275, Sep. 1996.

[BIB12] A. Biberman and K. Bergman, "Optical interconnection networks for high-performance computing systems," *Reports on progress in physics. Physical Society (Great Britain)*, vol. 75, no. 4, p. 046402, Apr. 2012.

[BLA09] A. Blanco, E. Areizaga, and J. A. Zubia, "Slow light for microwave photonics applications," *Mediterrannean Microwave Symposium (MMS)*, pp. 1–5, 2009.

[BOY09] R. W. Boyd and D. J. Gauthier, "Controlling the velocity of light pulses," *Science (New York, N.Y.)*, vol. 326, no. 5956, pp. 1074–7, Nov. 2009.

[BRI09] A. Brimont, P. Sanchis, and J. Martí, "Strong electro-optical modulation enhancement in a slow wave corrugated waveguide," *Optics Express*, vol. 17, no. 11, p. 9204, May 2009.

[BRI10] A. Brimont, J. Vicente Galán, J. Maria Escalante, J. Martí, and P. Sanchis, "Group-index engineering in silicon corrugated waveguides," *Optics Letters*, vol. 35, no. 16, p. 2708, Aug. 2010.

[BRI11A] A. Brimont, D. J. Thomson, P. Sanchis, J. Herrera, F. Y. Gardes, J. M. Fedeli, G. T. Reed, and J. Martí, "High speed silicon electro-optical modulators enhanced via slow light propagation," *Optics Express*, vol. 19, no. 21, p. 20876, Oct. 2011.

[BRI11B] A. Brimont, "Toward compact and high speed silicon modulators," Universidad Politécnica de Valencia, 2011.

[BRI12A] A. Brimont, A. M. Gutierrez, M. Aamer, D. J. Thomson, F. Y. Gardes, J. Fedeli, G. T. Reed, J. Marti, and P. Sanchis, "Slow-Light-Enhanced Silicon Optical Modulators Under Low-Drive-Voltage Operation," *IEEE Photonics Journal*, vol. 4, no. 5, pp. 1306–1315, Oct. 2012.

[BRI12B] A. Brimont, D. Thomson, F. Gardes, J. Fedeli, G. Reed, J. Martí, and P. Sanchis, "High-contrast 40Gb/s operation of a 500μm long silicon carrier-depletion slow wave modulator," *Optics Letters*, vol. 37, pp. 3504-3506, Sept. 2012.

[BRID95] W. B. Bridges and J. H. Schaffner, "Distortion in linearized electrooptic modulators," *IEEE Transactions on Microwave Theory and Techniques*, vol. 43, no. 9, pp. 2184–2197, 1995.

[CAB10] B. Cabon, "Microwave photonic mixing," *Transactions on Computer Science & Engineering and Electrical Engineering*, vol. 17, no. 2, pp. 149–162, 2010.

[CAP03] J. Capmany, D. Pastor, A. Martinez, B. Ortega, and S. Sales, "Microwave photonic filters with negative coefficients based on phase inversion in an electro-optic modulator," *Optics Letters*, vol. 28, no. 16, p. 1415, Aug. 2003.

[CAP06] J. Capmany, B. Ortega, and D. Pastor, "A tutorial on microwave photonic filters," *Journal of Lightwave Technology*, vol. 24, no. 1, pp. 201–229, Jan. 2006.

[CAP07] J. Capmany and D. Novak, "Microwave photonics combines two worlds," *Nature Photonics*, vol. 1, no. 6, pp. 319–330, Jun. 2007.

[CHA01] C. Chaudhari, D. S. Patil, and D. K. Gautam, "A new technique for the reduction of the power loss in the Y-branch optical power splitter," *Optics Communications*, vol. 193, no. 1–6, pp. 121–125, Jun. 2001.

[CHE09] X. Chen, Y.-S. Chen, Y. Zhao, W. Jiang, and R. T. Chen, "Capacitor-embedded 0.54 pJ/bit silicon-slot photonic crystal waveguide modulator.," Optics letters, vol. 34, no. 5, pp. 602–4, Mar. 2009.

[CHU95] Shun Lien Chuang, *Physics of optoelectronic devices*, John Wiley. 1995.

[COL11] L. A. Coldren, S. C. Nicholes, L. Johansson, S. Ristic, R. S. Guzzon, E. J. Norberg, and U. Krishnamachari, "High Performance InP-Based Photonic ICs—A Tutorial," *Journal of Lightwave Technology*, vol. 29, no. 4, pp. 554–570, Feb. 2011.

[COX04] Charles Howard Cox, "Analog optical links: theory and practice," Cambridge, 2004.

[DIN12] J. Ding, H. Chen, L. Yang, L. Zhang, R. Ji, Y. Tian, W. Zhu, Y. Lu, P. Zhou, R. Min, and M. Yu, "Ultra-low-power carrier-depletion Mach-Zehnder silicon optical modulator," *Optics Express*, vol. 20, no. 7, p. 7081, Mar. 2012.

[DON10A] P. Dong, R. Shafiiha, S. Liao, H. Liang, N.-N. Feng, D. Feng, G. Li, X. Zheng, A. V. Krishnamoorthy, and M. Asghari, "Wavelength-tunable silicon microring modulator," *Optics Express*, vol. 18, no. 11, p. 10941, May 2010.

[DON10B] P. Dong, S. Liao, H. Liang, W. Qian, X. Wang, R. Shafiiha, D. Feng, G. Li, X. Zheng, A. V. Krishnamoorthy, and M. Asghari, "High-speed and compact silicon modulator based on a racetrack resonator with a 1 V drive voltage," *Optics Letters*, vol. 35, no. 19, p. 3246, Sep. 2010.

[DON12] P. Dong, L. Chen, and Y. Chen, "High-speed low-voltage single-drive push-pull silicon Mach-Zehnder modulators," *Optics Express*, vol. 20, no. 6, p. 6163, Feb. 2012.

[DON10C] P. Dong, N.-N. Feng, D. Feng, W. Qian, H. Liang, D. C. Lee, B. J. Luff, T. Banwell, A. Agarwal, P. Toliver, R. Menendez, T. K. Woodward, and M. Asghari, "GHz-bandwidth optical filters based on high-order silicon ring resonators," *Optics Express*, vol. 18, no. 23, p. 23784, Oct. 2010.

[ECMA368] International Standard, High rate ultra wideband PHY and MAC Standard, 3rd Edition, December 2008.

[EPI] "ePIXfab: http://www.epixfab.eu/."

[FAO06] L. O'Faolain, X. Yuan, D. McIntyre, S. Thoms, H. Chong, R. M. De La Rue, and T. F. Krauss, "Low-loss propagation in photonic crystal waveguides," *Electronics Letters*, vol. 42, no. 25, p. 1454, 2006.

[FAO07] L. O'Faolain, T. P. White, D. O'Brien, X. Yuan, M. D. Settle, and T. F. Krauss, "Dependence of extrinsic loss on group velocity in photonic crystal waveguides," *Optics Express*, vol. 15, no. 20, p. 13129, 2007.

[FEN08] D. J. Y. Feng and T. S. Lay, "Compact multimode interference couplers with arbitrary power splitting ratio," *Optics Express*, vol. 16, no. 10, p. 7175, May 2008.

[FEN10] N.-N. Feng, P. Dong, D. Feng, W. Qian, H. Liang, D. C. Lee, J. B. Luff, A. Agarwal, T. Banwell, R. Menendez, P. Toliver, T. K. Woodward, and M. Asghari, "Thermally-efficient reconfigurable narrowband RF-photonic filter," *Optics Express*, vol. 18, no. 24, p. 24648, Nov. 2010.

[FRAN06] L. H. Frandsen, A. V. Lavrinenko, J. Fage-Pedersen, and P. I. Borel, "Photonic crystal waveguides with semi-slow light and tailored dispersion properties," *Optics Express*, vol. 14, no. 20, p. 9444, 2006.

[FUJ10] J. Fujikata, J. Ushida, T. Nakamura, Y. Ming-Bin, Z. ShiYang, D. Liang, P. L. Guo-Qiang, and D.-L. Kwong, "25GHz Operation of Silicon Optical Modulator with Projection MOS Structure," in *Optical Fiber Communication Conference*, p. OMI3, 2010.

[GAM00] W. A. Gambling, "The Rise and Rise of Optical Fibers," *IEEE Journal of Selected Topics in Quantum Electronics*, vol. 6, pp. 1084–1093, 2000.

[GAR05] F. Y. Gardes, G. T. Reed, N. G. Emerson, and C. E. Png, "A sub-micron depletion-type photonic modulator in Silicon On Insulator," *Optics Express*, vol. 13, no. 22, p. 8845, 2005.

[GAR08] J. Garcia, P. Sanchis, A. Martinez, and J. Marti, "1D periodic structures for slow-wave induced non-linearity enhancement," *Optics Express*, vol. 16, no. 5, p. 3146, 2008.

[GAR09] F. Y. Gardes, A. Brimont, P. Sanchis, G. Rasigade, D. Marris-Morini, L. O'Faolain, F. Dong, J. M. Fedeli, P. Dumon, L. Vivien, T. F. Krauss, G. T. Reed, and J. Martí, "High-speed modulation of a compact silicon ring resonator based on a reverse-biased pn diode," *Optics Express*, vol. 17, no. 24, p. 21986, Nov. 2009.

[GER05] H. Gersen, T. Karle, R. Engelen, W. Bogaerts, J. Korterik, N. van Hulst, T. Krauss, and L. Kuipers, "Real-Space Observation of Ultraslow Light in Photonic Crystal Waveguides," *Physical Review Letters*, vol. 94, no. 7, p. 073903, Feb. 2005.

[GIL10] D. M. Gill, S. S. Patel, M. Rasras, A. E. White, A. Pomerene, D. Carothers, R. L. Kamocsai, C. M. Hill, and J. Beattie, "CMOS-Compatible Si-Ring-Assisted Mach–Zehnder Interferometer With Internal Bandwidth Equalization," *IEEE Journal of Selected Topics in Quantum Electronics*, vol. 16, no. 1, pp. 45–52, 2010.

[GNA07A] M. Gnan, D. S. Macintyre, M. Sorel, R. M. De La Rue, and S. Thoms, "Enhanced stitching for the fabrication of photonic structures by electron beam lithography," *Journal of Vacuum Science & Technology B:*

Microelectronics and Nanometer Structures, vol. 25, no. 6, p. 2034, 2007.

[GNA07B] M. Gnan, M. Sorel, D. S. Macintyre, P. Pottier, S. Thoms, and R. M. De La Rue, "Effect of lithography stitching errors on Silicon-on-Insulator photonic wires," in *2007 European Conference on Lasers and Electro-Optics and the International Quantum Electronics Conference*, pp. 1–1, 2007.

[GNA08] M. Gnan, S. Thoms, D. S. Macintyre, R. M. De La Rue, and M. Sorel, "Fabrication of low-loss photonic wires in silicon-on-insulator using hydrogen silsesquioxane electron-beam resist," *Electronics Letters*, vol. 44, no. 2, p. 115, 2008.

[GOM07] A. Gomez-Iglesias, D. O'Brien, L. O'Faolain, A. Miller, and T. F. Krauss, "Direct measurement of the group index of photonic crystal waveguides via Fourier transform spectral interferometry," *Applied Physics Letters*, vol. 90, no. 26, p. 261107, 2007.

[GOP93] G. K. Gopalakrishnan, W. K. Burns, and C. H. Bulmer, "Microwave-optical mixing in $LiNbO_3$ modulators," *IEEE Transactions on Microwave Theory and Techniques*, vol. 41, no. 12, pp. 2383–2391, 1993.

[GRE07] W. M. Green, M. J. Rooks, L. Sekaric, and Y. A. Vlasov, "Ultra-compact, low RF power, 10 Gb/s silicon Mach-Zehnder modulator," *Optics Express*, vol. 15, no. 25, p. 17106, 2007.

[GU06] L. Gu, W. Jiang, Y. Jiang, X. Chen, and R. Chen, "Photonic-Crystal-Waveguide-Based Silicon Mach-Zehnder Modulators," in *Integrated Photonics Research and Applications/Nanophotonics*, Technical Digest, Optical Society of America, 2006.

[GU07] L. Gu, W. Jiang, X. Chen, L. Wang, and R. T. Chen, "High speed silicon photonic crystal waveguide modulator for low voltage operation," *Applied Physics Letters*, vol. 90, no. 7, p. 071105, 2007.

[GUT12A] A. M. Gutierrez, A. Brimont, G. Rasigade, M. Ziebell, D. Marris-Morini, J.-M. Fedeli, L. Vivien, J. Marti, and P. Sanchis, "Ring-Assisted Mach–Zehnder Interferometer Silicon Modulator for Enhanced Performance," *Journal of Lightwave Technology*, vol. 30, no. 1, pp. 9–14, 2012.

[GUT12B] A. M. Gutierrez, A. Brimont, M. Aamer, and P. Sanchis, "Method for measuring waveguide propagation losses by means of a Mach–Zehnder Interferometer structure," *Optics Communications*, vol. 285, no. 6, pp. 1144–1147, 2012.

[GUT12C] A. M. Gutiérrez, A. Brimont, J. Herrera, M. Aamer, J. Martí, D. J. Thomson, F. Y. Gardes, G. T. Reed, J. M. Fedeli, and P. Sanchis, "Silicon slow-light-based photonic mixer for microwave-frequency conversion applications," *Optics Letters*, vol. 37, no. 10, p. 1721, 2012.

[GUT13A] A. M. Gutiérrez, B. Vidal, A. Brimont, D. J. Thomson, F. Y. Gardes, G. T. Reed, J.-M. Fedeli and P. Sanchis, "A photonic integrated microwave filter based on a silicon carrier depletion modulator," *to be published in IEEE Photonics Journal*, 2013.

[GUT13B] A. M. Gutierrez, A. Brimont, J. Herrera, M. Aamer, D. J. Thomson, F. Y. Gardes, G. T. Reed, J.M. Fedeli and P. Sanchis, "Analytical Model for Calculating the Nonlinear Distortion in Silicon-Based Electro-Optic Mach-Zehnder Modulators," *submitted for publication*, 2013.

[HEL] HELIOS Project, "http://www.helios-project.eu/"

[HUG05] S. Hughes, L. Ramunno, J. F. Young, and J. E. Sipe, "Extrinsic optical scattering loss in photonic crystal waveguides: role of fabrication disorder and photon group velocity.," *Physical review letters*, vol. 94, no. 3, p. 033903, Jan. 2005.

[IBM] Silicon Integrated Nanophotonics IBM Research http://researcher.ibm.com/researcher/view_project.php?id=2757

[IBR11] S. Ibrahim, N. K. Fontaine, S. S. Djordjevic, B. Guan, T. Su, S. Cheung, R. P. Scott, A. T. Pomerene, L. L. Seaford, C. M. Hill, S. Danziger, Z. Ding, K. Okamoto, and S. J. B. Yoo, "Demonstration of a fast-reconfigurable silicon CMOS optical lattice filter," *Optics Express*, vol. 19, no. 14, p. 13245, Jun. 2011.

[IEEE05] IEEE Standard for Local and Metropolitan Area Networks: IEEE Std. 802.16e-2005.

[IHP] IHP - Innovations for High Performance Microelectronics "http://www.ihp-microelectronics.com/"

[IME] Interuniversity Microelectronics Centre "http://www2.imec.be/be_en/home.html"

[INS07] National Instruments, "http://www.ni.com/white-paper/6631/en", 2007.

[INT] First 40 Giga bits per second Silicon Laser Modulator "http://download.intel.com/pressroom/kits/research/40G_modulator_presentation.pdf?wapkw=modulator"

[JAL98] B. Jalali, S. Garner, and W. Steier, “Broadband linearization of externally modulated fiber-optic links,” *International Topical Meeting on Microwave Photonics,* pp. 49–50, 1998.

[JAL06] B. Jalali, M. Paniccia, and G. Reed, “Silicon photonics,” *IEEE Microwave Magazine,* vol. 7, no. 3, pp. 58–68, Jun. 2006.

[JIA05] Y. Jiang, W. Jiang, L. Gu, X. Chen, and R. T. Chen, “80-micron interaction length silicon photonic crystal waveguide modulator,” *Applied Physics Letters,* vol. 87, no. 22, p. 221105, 2005.

[JIN12] S. Jin, A. Bhardwaj, P. Herczfeld, and Y. Li, “RF/Photonic Link-on-Chip PIC,” *IEEE Photonics Technology Letters*, vol. 24, no. 13, pp. 1139–1141, Jul. 2012.

[JOH88] L. M. Johnson and H. V. Roussell, “Reduction intermodulation distortion in interferometric optical modulators,” *Optics Letters*, vol. 13, no. 10, p. 928, Oct. 1988.

[KAO66] K. C. Kao and G. A. Hockham, “Dielectric-fiber surface waveguides for optical frequencies,” *Proc. IEE*, vol. 113, pp. 1151–1158, 1966.

[KAR07] A. Karim and J. Devenport, “Low Noise Figure Microwave Photonic Link,” *2007 IEEE/MTT-S International Microwave Symposium*, pp. 1519–1522, 2007.

[KAR08] A. Karim and J. Devenport, “High Dynamic Range Microwave Photonic Links for RF Signal Transport and RF-IF Conversion,” *Journal of Lightwave Technology*, vol. 26, no. 15, pp. 2718–2724, Aug. 2008.

[KHI11] A. Khilo, C. M. Sorace, and F. X. Kärtner, “Broadband linearized silicon modulator,” *Optics Express*, vol. 19, no. 5, p. 4485, Feb. 2011.

[KIM11] G. Kim, J. W. Park, I. G. Kim, S. Kim, S. Kim, J. M. Lee, G. S. Park, J. Joo, K.-S. Jang, J. H. Oh, S. A. Kim, J. H. Kim, J. Y. Lee, J. M. Park, D.-W. Kim, D.-K. Jeong, M.-S. Hwang, J.-K. Kim, K.-S. Park, H.-K. Chi, H.-C. Kim, D.-W. Kim, and M. H. Cho, “Low-voltage high-performance silicon photonic devices and photonic integrated circuits operating up to 30 Gb/s,” *Optics Express*, vol. 19, no. 27, p. 26936, Dec. 2011.

[KRA08] T. F. Krauss, “Why do we need slow light?,” *Nature Photonics*, vol. 2, no. 8, pp. 448–450, Aug. 2008.

[KUB07] S. Kubo, D. Mori, and T. Baba, “Low-group-velocity and low-dispersion slow light in photonic crystal waveguides,” *Optics Letters*, vol. 32, no. 20, p. 2981, 2007.

[KUR05] E. Kuramochi, M. Notomi, S. Hughes, A. Shinya, T. Watanabe, and L. Ramunno, "Disorder-induced scattering loss of line-defect waveguides in photonic crystal slabs," *Physical Review B*, vol. 72, no. 16, p. 161318, Oct. 2005.

[LEE00] K. K. Lee, D. R. Lim, H.-C. Luan, A. Agarwal, J. Foresi, and L. C. Kimerling, "Effect of size and roughness on light transmission in a Si/SiO_2 waveguide: Experiments and model," *Applied Physics Letters*, vol. 77, no. 11, p. 1617, 2000.

[LEE01] K. K. Lee, D. R. Lim, L. C. Kimerling, J. Shin, and F. Cerrina, "Fabrication of ultralow-loss Si/SiO_2 waveguides by roughness reduction," *Optics Letters*, vol. 26, no. 23, p. 1888, Dec. 2001.

[LEE06] B. G. Lee, B. A. Small, K. Bergman, Q. Xu and M. Lipson, "Transmission of high-data-rate optical signals through a micrometer-scale silicon ring resonator," *Optics Letters*, vol. 31, no. 18, pp. 2701-2703, 2006.

[LEE10] B. G. Lee, A. Biberman, J. Chan, and K. Bergman, "High-Performance Modulators and Switches for Silicon Photonic Networks-on-Chip," *IEEE Journal of Selected Topics in Quantum Electronics*, vol. 16, no. 1, pp. 6–22, 2010.

[LI11] G. Li, X. Zheng, J. Yao, H. Thacker, I. Shubin, Y. Luo, K. Raj, J. E. Cunningham, and A. V. Krishnamoorthy, "25Gb/s 1V-driving CMOS ring modulator with integrated thermal tuning," *Optics Express*, vol. 19, no. 21, p. 20435, Oct. 2011.

[LIA05] L. Liao, D. Samara-Rubio, M. Morse, A. Liu, D. Hodge, D. Rubin, U. D. Keil, and T. Franck, "High speed silicon Mach-Zehnder modulator," *Optics Express*, vol. 13, no. 8, p. 3129, 2005.

[LIA07] L. Liao, A. Liu, D. Rubin, J. Basak, Y. Chetrit, H. Nguyen, R. Cohen, N. Izhaky, and M. Paniccia, "40 Gbit/s silicon optical modulator for high-speed applications," *Electronics Letters*, vol. 43, no. 22, p. 1196, 2007.

[LIU04] A. Liu, R. Jones, L. Liao, D. Samara-Rubio, D. Rubin, O. Cohen, R. Nicolaescu, and M. Paniccia, "A high-speed silicon optical modulator based on a metal-oxide-semiconductor capacitor.," *Nature*, vol. 427, no. 6975, pp. 615–8, Feb. 2004.

[LLO11] J. Lloret, J. Sancho, M. Pu, I. Gasulla, K. Yvind, S. Sales, and J. Capmany, "Tunable complex-valued multi-tap microwave photonic filter based on single silicon-on-insulator microring resonator," *Optics Express*, vol. 19, no. 13, p. 12402, Jun. 2011.

[MAN07] S. Manipatruni, Q. Xu, B. Schmidt, J. Shakya, and M. Lipson, "High Speed Carrier Injection 18 Gb/s Silicon Micro-ring Electro-optic Modulator," in *LEOS 2007 - IEEE Lasers and Electro-Optics Society Annual Meeting Conference Proceedings*, pp. 537–538, 2007.

[MAR09] D. Marpaung, "High dynamic range analog photonic links□: design and implementation." University of Twente, Enschede, The Netherlands, 27-Aug-2009.

[MAR12] D. Marpaung, C. Roeloffzen, R. Heideman, A. Leinse, S. Sales, and J. Capmany, "Integrated microwave photonics," *Laser & Photonics Reviews*, Jan. 2013.

[MART00] J. Marti, V. Polo, F. Ramos, and J. M. Fuster, "Single Mach–Zehnder Modulator Electro-Optical Harmonic Mixer for Broadband Microwave/Millimetre-Wave Applications," *Wireless Personal Communications*, vol. 15, no. 1, pp. 31–42, 2000.

[MEL03] A. Melloni, F. Morichetti, and M. Martinelli, "Linear and nonlinear pulse propagation in coupled resonator slow-wave optical structures," *Optical and Quantum Electronics*, vol. 35, no. 4/5, pp. 365–379, Mar. 2003.

[MIN] Commissariat à l'énergie atomique - Laboratoire des technologies de L'information « http://www.minatec.com/."

[MOO65] G. Moore, "Cramming more components onto integrated circuits," *Electronics Mag.*, vol. 38, no. 8, pp. 114-117, 1965.

[NGU07] H. G. Nguyen, K. Merzouk, R. Gary, B. Cabon, S. B. Constant, G. Maury, and Y. Le Guennec, "IR-UWB Transmission in 40-GHz-Band using Optical Conversion by Cascaded Modulators," in *Microwave Photonics, 2007 International Topical Meeting on*, 2007, pp. 100–103.

[NGU09] H. G. Nguyen, B. Cabon, and Y. Le Guennec, "Generation of 60-GHz MB-OFDM Signal-Over-Fiber by Up-Conversion Using Cascaded External Modulators," *Journal of Lightwave Technology*, vol. 27, no. 11, pp. 1496–1502, Jun. 2009.

[NGU11] H. C. Nguyen, Y. Sakai, M. Shinkawa, N. Ishikura, and T. Baba, "10 Gb/s operation of photonic crystal silicon optical modulators," *Optics Express*, vol. 19, no. 14, p. 13000, Jun. 2011.

[NGU12A] H. C. Nguyen, Y. Sakai, M. Shinkawa, N. Ishikura, and T. Baba, "Photonic Crystal Silicon Optical Modulators: Carrier-Injection and

Depletion at 10 Gb/s," *IEEE Journal of Quantum Electronics*, vol. 48, no. 2, pp. 210–220, Feb. 2012.

[NGU12B] H. C. Nguyen, S. Hashimoto, M. Shinkawa, and T. Baba, "Compact and fast photonic crystal silicon optical modulators.," *Optics express*, vol. 20, no. 20, pp. 22465–74, Sep. 2012.

[NOT01] M. Notomi, K. Yamada, A. Shinya, J. Takahashi, C. Takahashi, and I. Yokohama, "Extremely large group-velocity dispersion of line-defect waveguides in photonic crystal slabs.," *Physical review letters*, vol. 87, no. 25, p. 253902, Dec. 2001.

[OCL11] Technologies for Optical Interconnection: Challenges and Opportunities, Silicon Photonics Workshop: "Packaging and Test Challenges or Industrialization of Silicon Photonics", Munich, 23 May 201, "http://www.siliconphotonics.eu/munich_slides/5_Oclaro.pdf"

[OKA83] Y. Okamura, S. Yoshinaka, and S. Yamamoto, "Measuring mode propagation losses of integrated optical waveguides: a simple method," *Applied Optics*, vol. 22, no. 23, p. 3892, Dec. 1983.

[PAG11] V. R. Pagán, B. M. Haas, and T. E. Murphy, "Linearized electrooptic microwave downconversion using phase modulation and optical filtering," *Optics Express*, vol. 19, no. 2, p. 883, Jan. 2011.

[POV05] M. L. Povinelli, S. G. Johnson, and J. D. Joannopoulos, "Slow-light, band-edge waveguides for tunable time delays," *Optics Express*, vol. 13, no. 18, p. 7145, 2005.

[RAI150] Raith 150 e-beam lithography software "http://www.nanophys.kth.se/nanophys/facilities/nfl/manual/"

[RAS07] M. S. Rasras, D. M. Gill, S. S. Patel, K.-Y. Tu, Y.-K. Chen, A. E. White, A. T. S. Pomerene, D. N. Carothers, M. J. Grove, D. K. Sparacin, J. Michel, M. A. Beals, and L. C. Kimerling, "Demonstration of a Fourth-Order Pole-Zero Optical Filter Integrated Using CMOS Processes," *Journal of Lightwave Technology*, vol. 25, no. 1, pp. 87–92, Jan. 2007.

[RAS10] G. Rasigade, D. Marris-Morini, L. Vivien, and E. Cassan, "Performance Evolutions of Carrier Depletion Silicon Optical Modulators: From p-n to p-i-p-i-n Diodes," *IEEE Journal of Selected Topics in Quantum Electronics*, vol. 16, no. 1, pp. 179–184, 2010.

[RAS11A] G. Rasigade, M. Ziebell, D. Marris-Morini, J. Fédéli, F. Milesi, P. Grosse, D. Bouville, E. Cassan, and L. Vivien, "High extinction ratio 10

Gbit/s silicon optical modulator," *Optics Express*, vol. 19, no. 7, pp. 5827-5832, Mar. 2011.

[RAS11B] G. Rasigade, M. Ziebell, D. Marris-Morini, A. Brimont, A. M. Gutierrez, P. Sanchis, J. Fedeli, G. Duan, E. Cassan, and L. Vivien, "10-Gb/s Error-Free Silicon Optical Modulator for Both TE and TM Polarized Light," *IEEE Photonics Technology Letters*, vol. 23, no. 23, pp. 1799-1801, Dec. 2011.

[REE92] Reed, G.T., "Methods of measurement of passive integrated optical waveguides," *IEEE Colloquium on Measurements on Optical Devices*, pp.2/1,2/7, 19 Nov 1992

[REE04] G. T. Reed and A. P. Knights, "*Silicon Photonics: An Introduction*," John Wiley & Sons, Inc., 2004

[REE10] G. T. Reed, G. Mashanovich, F. Y. Gardes, and D. J. Thomson, "Silicon optical modulators," *Nature Photonics*, vol. 4, no. 8, pp. 518–526, Jul. 2010.

[REG85] R. Regener and W. Sohler, "Loss in low-finesse Ti:LiNbO3 optical waveguide resonators," *Applied Physics B Photophysics and Laser Chemistry*, vol. 36, no. 3, pp. 143–147, Mar. 1985.

[REI06] S. Reitzenstein, A. Bazhenov, A. Gorbunov, C. Hofmann, S. Munch, A. Loffler, M. Kamp, J.-P. Reithmaier, V. D. Kulakovskii and A. Forchel, "Lasing in high-Q quantum-dot micropillar cavities," *Applied Physics Letters*, vol. 89, no. 5, 2006.

[ROE11] G. Roelkens, D. Vermeulen, S. Selvaraja, R. Halir, W. Bogaerts, and D. Van Thourhout, "Grating-Based Optical Fiber Interfaces for Silicon-on-Insulator Photonic Integrated Circuits," *IEEE Journal of Selected Topics in Quantum Electronics*, vol. 17, no. 3, pp. 571–580, May 2011.

[ROS11] J. C. Rosenberg, W. M. Green, S. Assefa, T. Barwicz, M. Yang, S. M. Shank, and Y. A. Vlasov, "Low-Power 30 Gbps Silicon Microring Modulator," in *CLEO: 2011 - Laser Applications to Photonic Applications*, p. PDPB9, 2011.

[RSO00] Rsoft Design Group, Inc., 2000 Executive Group Blvd. Ossining, NY 10562, "www.rsoftdesign.com".

[SAB95] D. J. M. Sabido, M. Tabara, T. K. Fong, and L. G. Kazovsky, "Improving the dynamic range of a coherent AM analog optical link using a cascaded

linearized modulator," *IEEE Photonics Technology Letters*, vol. 7, no. 7, pp. 813–815, Jul. 1995.

[SAN12] J. Sancho, J. Bourderionnet, J. Lloret, S. Combrié, I. Gasulla, S. Xavier, S. Sales, P. Colman, G. Lehoucq, D. Dolfi, J. Capmany, and A. De Rossi, "Integrable microwave filter based on a photonic crystal delay line," *Nature communications*, vol. 3, p. 1075, Jan. 2012.

[SAV02] N. Savage, "Linking with light [high-speed optical interconnects]," *IEEE Spectrum*, vol. 39, no. 8, pp. 32–36, Aug. 2002.

[SET07] M. D. Settle, R. J. P. Engelen, M. Salib, A. Michaeli, L. Kuipers, and T. F. Krauss, "Flatband slow light in photonic crystals featuring spatial pulse compression and terahertz bandwidth," *Optics Express*, vol. 15, no. 1, p. 219, 2007.

[SMI12] M. Smit, J. van der Tol, and M. Hill, "Moore's law in photonics," *Laser & Photonics Reviews*, vol. 6, no. 1, pp. 1–13, Jan. 2012.

[SOL02] M. Soljačić, S. G. Johnson, S. Fan, M. Ibanescu, E. Ippen, and J. D. Joannopoulos, "Photonic-crystal slow-light enhancement of nonlinear phase sensitivity," *Journal of the Optical Society of America B*, vol. 19, no. 9, p. 2052, Sep. 2002.

[SON10] M. Song, L. Zhang, R. G. Beausoleil and A. E. Willner, "Nonlinear Distortion in a Silicon Microring-Based Electro-Optic Modulator for Analog Optical Links," *IEEE Journal of Selected Topics in Quantum Electronics*, vol. 16, no. 1, pp. 185–191, 2010.

[SOR86] R. Soref and J. Larenzo, "All-silicon active and passive guided-wave components for λ = 1.3 and 1.6 μm," *IEEE Journal of Quantum Electronics*, vol. 22, no. 6, pp. 873–879, Jun. 1986.

[SOR87] R. Soref and B. Bennett, "Electrooptical effects in silicon," *IEEE Journal of Quantum Electronics*, vol. 23, no. 1, pp. 123–129, Jan. 1987.

[SPA05] D. K. Sparacin, S. J. Spector, and L. C. Kimerling, "Silicon waveguide sidewall smoothing by wet chemical oxidation," *Journal of Lightwave Technology*, vol. 23, no. 8, pp. 2455–2461, Aug. 2005.

[STR13] M. Streshinsky, A. Ayazi, Z. Xuan, A. E.-J. Lim, G.-Q. Lo, T. Baehr-Jones, and M. Hochberg, "Highly linear silicon traveling wave Mach-Zehnder carrier depletion modulator based on differential drive," *Optics Express*, vol. 21, no. 3, p. 3818, Feb. 2013.

[THO10] D. J. Thomson, F. Y. Gardes, G. T. Reed, F. Milesi, and J.-M. Fedeli, "High speed silicon optical modulator with self aligned fabrication process," *Optics Express*, vol. 18, no. 18, p. 19064, Aug. 2010.

[THO11] D. J. Thomson, F. Y. Gardes, Y. Hu, G. Mashanovich, M. Fournier, P. Grosse, J.-M. Fedeli, and G. T. Reed, "High contrast 40Gbit/s optical modulation in silicon," *Optics Express*, vol. 19, no. 12, p. 11507, May 2011.

[THO12] D. J. Thomson, F. Y. Gardes, J.-M. Fedeli, S. Zlatanovic, Y. Hu, B. P. P. Kuo, E. Myslivets, N. Alic, S. Radic, G. Z. Mashanovich, and G. T. Reed, "50-Gb/s Silicon Optical Modulator," *IEEE Photonics Technology Letters*, vol. 24, no. 4, pp. 234–236, Feb. 2012.

[TIT93] G. Tittelbach, B. Richter, and W. Karthe, "Comparison of three transmission methods for integrated optical waveguide propagation loss measurement," *Pure and Applied Optics: Journal of the European Optical Society Part A*, vol. 2, no. 6, pp. 683–700, Nov. 1993.

[TU10] K.-Y. Tu, M. S. Rasras, D. M. Gill, S. S. Patel, Y.-K. Chen, A. E. White, A. Pomerene, D. Carothers, J. Beattie, M. Beals, J. Michel, and L. C. Kimerling, "Silicon RF-Photonic Filter and Down-Converter," *Journal of Lightwave Technology*, vol. 28, no. 20, pp. 3019–3028, Oct. 2010.

[TU11] X. Tu, T.-Y. Liow, J. Song, M. Yu,, and G. Q. Lo, "Fabrication of low loss and high speed silicon optical modulator using doping compensation method," *Optics Express*, vol. 19, no. 19, p. 18029, Aug. 2011.

[URI11] V. J. Urick, F. Bucholtz, J. D. McKinney, P. S. Devgan, A. L. Campillo, J. L. Dexter, and K. J. Williams, "Long-Haul Analog Photonics," *Journal of Lightwave Technology*, vol. 29, no. 8, pp. 1182–1205, Apr. 2011.

[VAC10] F. Vacondio, M. Mirshafiei, J. Basak, M. Paniccia, and L. A. Rusch, "A Silicon Modulator Enabling RF Over Fiber for 802.11 OFDM Signals," *IEEE Journal of Selected Topics in Quantum Electronics*, vol. 16, no. 1, pp. 141–148, 2010.

[VID03] , "Photonic microwave filter with tuning and reconfiguration capabilities using optical switches and dispersive media," *Electronics Letters*, vol. 39, no. 6, p. 547, 2003.

[VID05] B. Vidal, J. L. Corral, and J. Marti, "All-optical WDM microwave filter with negative coefficients," *IEEE Photonics Technology Letters*, vol. 17, no. 3, pp. 666–668, Mar. 2005.

[VID06] B. Vidal, J. L. Corral, and J. Martí, “All-optical WDM multi-tap microwave filter with flat bandpass,” *Optics Express*, vol. 14, no. 2, p. 581, 2006.

[VLA04] Y. A. Vlasov and S. J. McNab, “Losses in single-mode silicon-on-insulator strip waveguides and bends,” *Optics Express*, vol. 12, no. 8, p. 1622, 2004.

[VLA05] Y. A. Vlasov, M. O’Boyle, H. F. Hamann, and S. J. McNab, “Active control of slow light on a chip with photonic crystal waveguides,” *Nature*, vol. 438, no. 7064, pp. 65–9, Nov. 2005.

[WEB73] H. P. Weber, F. A. Dunn, and W. N. Leibolt, “Loss Measurements in Thin-Film Optical Waveguides,” *Applied Optics*, vol. 12, no. 4, p. 755, Apr. 1973.

[WILL99] G. Wilson, “Predistortion techniques for linearization of external modulators,” in *1999 Digest of the LEOS Summer Topical Meetings: Nanostructures and Quantum Dots/WDM Components/VCSELs and Microcavaties/RF Photonics for CATV and HFC Systems*, pp. IV39–IV40, 1999.

[WON80] Y. H. Won, P. C. Jaussaud, and G. H. Chartier, “Three-prism loss measurements of optical waveguides,” *Applied Physics Letters*, vol. 37, no. 3, p. 269, 1980.

[XIA07] F. Xia, L. Sekaric, and Y. Vlasov, “Ultracompact optical buffers on a silicon chip,” *Nature Photonics*, vol. 1, no. 1, pp. 65–71, Jan. 2007.

[XIA13] X. Xiao, H. Xu, X. Li, Z. Li, T. Chu, Y. Yu, and J. Yu, "High-speed, low-loss silicon Mach-Zehnder modulators with doping optimization," *Optics Express*, vol. 21, no. 4, pp. 4116-4125, 2013.

[XU05] Q. Xu, B. Schmidt, S. Pradhan, and M. Lipson, “Micrometre-scale silicon electro-optic modulator.,” *Nature*, vol. 435, no. 7040, pp. 325–7, May 2005.

[XU07] Q. Xu, S. Manipatruni, B. Schmidt, J. Shakya, and M. Lipson, “125 Gbit/s carrier-injection-based silicon micro-ring silicon modulators,” *Optics Express*, vol. 15, no. 2, p. 430, Jan. 2007.

[XU12] H. Xu, X. Xiao, X. Li, Y. Hu, Z. Li, T. Chu, Y. Yu, and J. Yu, "High speed silicon Mach-Zehnder modulator based on interleaved PN junctions," *Opt. Express* 20, 15093-15099, 2012.

[YAO12] J. Yao, "A Tutorial on Microwave Photonics," *IEEE Photonics Society newsletter*, Apr. 2012.

[YU13] H. Yu, M. Chen, P. Li, S. Yang, H. Chen, and S. Xie, "Silicon-on-insulator narrow-passband filter based on cascaded MZIs incorporating enhanced FSR for downconverting analog photonic links," *Optics Express*, vol. 21, no. 6, p. 6749, Mar. 2013.

[ZHA12] G. Zhang, X. Zheng, S. Li, H. Zhang, and B. Zhou, "Postcompensation for nonlinearity of Mach–Zehnder modulator in radio-over-fiber system based on second-order optical sideband processing," *Optics Letters*, vol. 37, no. 5, p. 806, Feb. 2012.

[ZHE10] X. Zheng, J. Lexau, Y. Luo, H. Thacker, T. Pinguet, A. Mekis, G. Li, J. Shi, P. Amberg, N. Pinckney, K. Raj, R. Ho, J. E. Cunningham, and A. V. Krishnamoorthy, "Ultra-low-energy all-CMOS modulator integrated with driver," *Optics Express*, vol. 18, no. 3, p. 3059, Jan. 2010.

[ZIE12] M. Ziebell, D. Marris-Morini, G. Rasigade, J.-M. Fédéli, P. Crozat, E. Cassan, D. Bouville, and L. Vivien, "40 Gbit/s low-loss silicon optical modulator based on a pipin diode," *Optics Express*, vol. 20, no. 10, p. 10591, Apr. 2012.